IMAGING CURRENT IN MATERIALS

A DISSERTATION
SUBMITTED TO THE DEPARTMENT OF PHYSICS
AND THE COMMITTEE ON GRADUATE STUDIES
OF STANFORD UNIVERSITY
IN PARTIAL FULFILLMENT OF THE REQUIREMENTS
FOR THE DEGREE OF
DOCTOR OF PHILOSOPHY

Eric M. Spanton
July 2016

Acknowledgments

Graduate school is really hard in a lot of (surprising) way and I couldn't have done it without a lot of people. Apologies if I miss someone, I am characteristically doing this at the last minute! I hope to convey a fraction of how important you all are to me.

First of all, I'd like to thank my parents, Michael, and Jessica for continuing to love and support me despite definitely not calling and visiting enough.

Working in the Moler lab has been a ride. I'd like to thank KAM for being supportive and also tolerant of the ups and downs of my graduate student career. I feel like I've been able to develop a fairly strong and independent outlook as a scientist and I'm not sure that would have happened in a different lab. Thanks also to DGG, Xiaoliang Qi, and Mac Beasley for agreeing to be on my committee and for useful and engaging discussions.

I've gotten to work with so many cool people in the Moler lab. I've benefited and gained so much by working closely with a couple of former postdocs: Beena on Egon, who might hold the world record for throughput on a scanning SQUID system and taught me the ways of scanning SQUID, and Katja on Dilford, who I still today bug way too much gchat with questions and for advice. The greater Moler group culture is one of shared commiseration and support, and at point was an absolute lifeline for me. Thanks to Lan, Julie, Tom, Lisa, John, Hilary, Aaron, Phil, Chris, Johanna, and Zheng, for condolences on broken SQUIDs or MFM tips, late night heart-to-hearts, discussions of the middle east, putting up with my sometimes not so subtle swearing at soldering jobs, for sometimes doing just about anything but actually working, and more. Y'all have made grad school an unforgettable experience. Thanks to Hilary for putting up with my constant query of "do we really have to do this" while working on Dilford together.

Thanks to my friends (with whom there is a lot of overlap in the previous paragraph)! In particular: Crystal for putting up with my sporadic M.I.A-ness, for randomly pulling me out of work to hang out, keeping my love for Kanye in check, and always being up for a trip to Coconuts. Johanna and Lawrence for hosting board games, riding dinosaurs, pwning noobs, and Dungeons and

Dragons craziness. Cheers to old friends who I've managed to stay in contact with since starting grad school, specifically Chris for pulling me away from lab for an epic road trip and THE ANDIE. THE ANDIE continues to laugh at our inside jokes from high school, dance ONLY ON DANCE FLOORS, and be a genuinely awesome person.

Also, my first couple of years would not have been the same without members of my Physics/AP cohort: Crystal, Tony, Kristi, Dickson, Sho, Yonas, Max, Sam, Menyoung, Max Shapiro, Max Swiatlowski, Masha, et al. who I spent a lot of time working on homework in the basement of the Huang building (or at least distracting others from trying to do homework), or going to barbecues and get-togethers back when we did those sorts of things.

Contents

List of Tables

List of Figures

Chapter 1

Introduction

Webster's dictionary defines 'condensed matter physics' as *"none found Please try the words separately:"*. I couldn't agree more wholeheartedly: condensed matter physics is hard to define. It is at its most basic level the study of the physical properties of solids and liquids. A large subdivision of condensed matter (and the part that I have paid attention to in my Ph.D. work) is devoted to the study of how electrons behave in solids and devices made of solids.

In particular, the very academic question of "what exotic electronic states of matter can we realize inside of a solid structure?" is an interesting 'basic science' question which also occasionally bears useful fruit. By exotic, I mean states which betray our intuition about how electrons behave, or just behave in ways which have not been observed elsewhere.

Scanning superconducting quantum interference device (SQUID) is a unique magnetic probe due to its exquisite magnetic sensitivity and local susceptibility capability. Given our lab's unique capability, my guiding principle in choosing projects was "I have this really sweet hammer, what nails can I hit with it?". Hence, the rather vague title of my thesis "Imaging current in materials" and the variety of materials investigated in the thesis. The (pragmatic) guiding scientific principle of this thesis is what can scanning SQUID elucidate in the study new and exotic states of electronic matter. I am not confident this was the correct tack to take, but it has required the development of a pretty wide breadth of knowledge in a number of subfields, which I appreciate. In lieu of broad context, I've included more specific introductions to the problems and materials at hand at the beginning of each chapter.

The vegan meat substitute of this thesis consists of three major movements. The first, in Ch. 4, describes study of unexpected current flow patterns in $LaAlO_3/SrTiO_3$ heterostructures. We discovered that local conductivity of $LaAlO_3/SrTiO_3$ is modulated strongly by the underlying tetragonal

domain structure of $SrTiO_3$. This work illustrates the ability of SQUID to discover and investigate effects which would be very hard to access using bulk probes.

Secondly, I present SQUID imaging studies of current in prospective 2D topological insulators HgTe and InAs/GaSb (Chapters 5 and 6, respectively). I've taken the opportunity of thesis writing to voice my rather pessimistic views on the experimental state of the search for clear evidence of 2D topologically insulating states in these materials.

Thirdly, in Chapter 8, I outline direct measurements of the current-phase relations (CPRs) of gated InAs nanowire Josephson junctions. We observed strong fluctuations of the shape of the CPR with gate voltage and resonant-tunneling behavior at low gate voltages. I believe these measurements represent the most comprehensive study of gated CPRs to date. Interpretation of this work is still ongoing as of writing this thesis.

In addition to the main chapters, I've included a couple chapters which are more technical. In Ch. 2, I outline work I've done modeling magnetic force microscope measurements of the superconducting penetration depth, and conclude that previous modeling does not correctly represent reality. In Ch. 3 I describe the numerical techniques used in this thesis to reconstruct current from flux images. Finally, in Ch. 7, I outline an artifact in other people's measurements of current in a ferromagnetic system I discovered, which highlights the importance of considering how electric fields couple into scanning SQUID measurements.

1.1 Contributions

Here is a brief summary of my and others' contributions to the work presented in this thesis. Sample collaborators are listed and the beginning of the chapters where applicable. KAM's input was invaluable for all of the chapters.

Chapter 2 represents calculation-based work I carried out regarding MFM measurements, and I have fit data taken by Lan Luan. The results and models benefited from discussion with Lan, Ophir Auslaender, and KAM.

Chapter 3 is strongly based on code written and work done by John Kirtley and Katja Nowack.

Chapter 4 is mostly a reproduction of our paper in Nature Materials, which I took the lead in writing. A lion's share of the experimental work was performed by Beena Kalisky and I joined on the tail end of those measurements.

Chapter 5 consists of a lot of data taken by Katja Nowack for our Nature Materials paper. My

contributions were measurements of the 2nd measured Hall bar, temperature dependence, measurements of the non-inverted sample, and the attempted measurements of persistent currents. Katja and I collaborated on analysis of the later measurements and design of the persistent currents sample. I have written most of this chapter myself, but it very much based (especially in the results section) on the Nature Materials paper which Katja wrote.

Chapter 6 consists mainly of work I performed by myself, with many fruitful discussions with Katja.

Chapter 7 consists of the 'discovery' of an artifact for which I was mainly responsible. The chapter is an exact reproduction of an arXiv paper we posted on the subject. Aaron Rosenberg was very involved in helping with the measurements, analysis, and editing of the manuscript. As noted in the chapter, some of the presented data was from the original (misinterpreted) work and was taken by Yihua Wang.

Chapter 8 consists mainly of work I performed. Zheng Cui helped with measurements of hysteretic rings on the third sample, and has done more detailed analysis of the hysteresis which I haven't included here.

Chapter 2

Modeling magnetic force microscopy of bulk superconductors

2.1 Executive Summary

Magnetic force microscopy (MFM) is a unique tool which allows for spatial mapping of magnetic fields on the nanometer scale. Our group has, in the past, used MFM to measure the Meissner response of bulk superconductors in order to locally measure the penetration depth, a useful thermodynamic quantity which characterizes superconductors.

In the past, others attempted to model the magnetic tip of an MFM in order to extract the absolute value of the penetration depth from the height dependence of the MFM signal over a supercondcutor [67, 68, 69]. Here, I will show that previous modeling of the tip took approximations which, when corrected, lead to a significant shift in the extracted penetration depth away from realistic values. The sensitivity of the extracted λ to the specifics of the tip model leads me to believe that more complete information about the shape and magnetic moment of the tip (or more comprehensive data) are required to accurately extract the absolute value of the penetration depth from such measurements. Measurements of the relative change of the penetration depth are in general insensitive to such systematic errors.

2.2 Introduction to magnetic force microscopy

Magnetic force microscopy (MFM) is a method for locally probing the force a magnetic tip feels due to stray magnetic fields on the surface of a sample. For a tip which is a point dipole, the magnetic

force is given by:

$$\vec{F}(x,y,z) = \mu_0(\vec{m}\cdot\nabla)\vec{H}(x,y,z) \tag{2.1}$$

where $\vec{F}$ is the force felt by the magnetic tip, μ_0 is the permeability of free space, $\vec{m}$ is the magnetic moment vector of the tip, and $\vec{H}$ is the magnetic field due to the sample. When the tip is placed on a flexible cantilever, the force can be read out directly as a displacement of the cantilever from its equilibrium position.

In practice, it is often favorable to measure in 'AC mode', by measuring the shift of the cantilever's resonance due to an external force. By approximating the cantilever as a harmonic oscillator, the measured shift in the resonance frequency is given by

$$\Delta f \equiv f - f_0 \propto -\frac{f_0}{2k}\frac{\partial F_z}{\partial z} \tag{2.2}$$

where f is the measured resonance frequency, f_0 is the resonance frequency of the cantilever in the absence of an external force, k is the spring constant of the cantilever, F_z is the force along the direction of oscillation of the tip, z.

Most importantly, the shift in resonance frequency is directly proportional to the force gradient. Plugging this proportionality back into the equation for magnetic force, we find that the measured quantity (shift in resonance frequency) is given by

$$\Delta f \propto -\frac{\mu_0 f_0}{2k}\frac{\partial}{\partial z}([(\vec{m}\cdot\nabla)\vec{H}]\cdot\hat{z}) = -\frac{\mu_0 f_0 m_z}{2k}\frac{\partial^2 H_z}{\partial z^2} \tag{2.3}$$

where the third part of the equation is obtained by assuming that the magnetic moment of the tip points only along the z direction. Therefore, we find that measuring the shift in the resonance, for a tip which is a point dipole, is directly proportional to the second partial derivative of the field with respect to z. The rest of the equation depends only on the details of the tip, cantilever, and physical constants.

2.3 Local penetration depth measurements

Superconductors expel an applied magnetic field by developing screening currents which flow without dissipation. In a small enough uniform applied magnetic field, the field inside a superconductor goes to zero in the bulk (i.e. 'perfect diamagnetism'). Near the surface, the magnetic field is screened exponentially on a length scale given by the London penetration depth (λ). λ is given

theoretically for an isotropic single-band superconductor by

$$\lambda = \sqrt{\frac{m}{\mu_0 n_s e^2}} \tag{2.4}$$

Measuring λ allows one to directly access fundamental properties of a superconducting sample. Specifically, measurements of the absolute value of λ (as opposed to $\Delta\lambda \equiv \lambda(T) - \lambda(T_0)$) can more thoroughly investigate the symmetry of the superconducting gap of a given superconductor or compare the penetration depth between samples (e.g. as a function of doping). Accurate measurements of the absolute value of the penetration depth are much sought after.

For a perfectly homogeneous and isotropic sample, measuring the response of a superconducting sample to a uniform field would give you all the information you need. For the most interesting superconductors, one of the main tuning knobs is doping, which is an inherently random and disordered process. Due to dopant, strain, or other sorts of disorder, λ may vary as a function of space. This disorder could obscure or reduce interesting effects such as divergence of the penetration depth near a quantum critical point (e.g. in the pnictide superconductors [96], or could even shift the measured bulk penetration depth from its volume-averaged value [65]. Due to the above reasons, measuring $\lambda(x, y)$ near the surface of a superconductor could better investigate important physics in unconventional superconductors.

One way of probing the spatial variation of λ is to apply a local field to the sample and measure its diamagnetic response. Diamagnetic screening current will only flow where there is a field, so the strength of screening will depend only on the the local penetration depth near the field source. Spatial variation of λ on smaller length scales than the local field may shift the penetration depth far from its volume-averaged value, depending on the character of spatial inhomogeneity in $\lambda(x, y)$ [65].

Previously, our group has investigated the local penetration depth by using the magnetic force tip as both the locally applied field and a probe of the response of the superconductor. Such investigations were carried out on pnictide superconductors [67, 69, 68]. These papers execute measurements of the local superconducting properties looking at both the absolute value of the penetration depth (λ) and the relative penetration depth ($\Delta\lambda$). In the rest of this chapter, I will describe how we modeled the MFM tip and approximations used in previous works to extract the absolute value of the penetration depth. I will show that they are not sufficient to accurately describe the properties of our magnetic tips. In particular, extensions of the tip model which should more accurately describe the tip change the fitted penetration depth by up to $\approx 50\%$, away from the values measured by other

techniques. Therefore, I conclude that the reported values for the absolute value of the penetration depth in previous MFM studies are not necessarily accurate. Measurements of $\Delta\lambda$ by MFM are not affected by tip modeling and the main scientific conclusions of previous papers [67, 69, 68], apart from the assertion that the absolute value λ has been measured, are largely unaffected.

2.4 MFM response model

Here, I will derive the model for our magnetic tips, which are standard Si AFM tips with magnetic material (either Fe or Co) evaporated onto half of the approximately conical AFM tip. The MFM tip was magnetized at room temperature using a permanent magnet, and can be re-magnetized at low temperature using a superconducting magnet if necessary. The goal is to model the MFM tip well enough to quantitatively predict its dependence on height of the tip above the surface (z) above a superconductor of a given penetration depth, λ.

The force on a magnet with arbitrary shape over a bulk, homogeneous, isotropic superconductor in the Meissner state is given by [114]:

$$F_z = \frac{\mu_0}{4\pi}\int_0^\infty dk k^3 \frac{\sqrt{1+\lambda^2k^2}-\lambda k}{\sqrt{1+\lambda^2k^2}+\lambda k}e^{-2zk} \int_{V'} d\tau' \int_{V''} d\tau'' M(\mathbf{r}')M(\mathbf{r}'')e^{-k(z'+z'')}J_0[k\sqrt{(x'-x'')^2+(y'-y'')^2}] \tag{2.5}$$

where λ is the London penetration depth, M is the magnetization of the tip along the z direction as a function of space and J_0 is a Bessel function of the first kind. Two volume integrals are required to take into account the fact that each infinitesimal magnetic volume feels a force from the diamagnetic response generated in the superconductor by all of the moments in the tip, not just itself.

In AC mode, the MFM measures a signal proportional to the partial z derivative of the force (derivative indicated by a prime):

$$F_z' = -\frac{\mu_0}{2\pi}\int_0^\infty dk k^4 \frac{p-k}{p+k}e^{-2kz}\int_{V'} d\tau' \int_{V''} d\tau'' M(\mathbf{r}')M(\mathbf{r}'')e^{-k(z'+z'')}J_0[k\sqrt{(x'-x'')^2+(y'-y'')^2}] \tag{2.6}$$

where I have defined

$$p \equiv \sqrt{\lambda^{-2}+k^2} \tag{2.7}$$

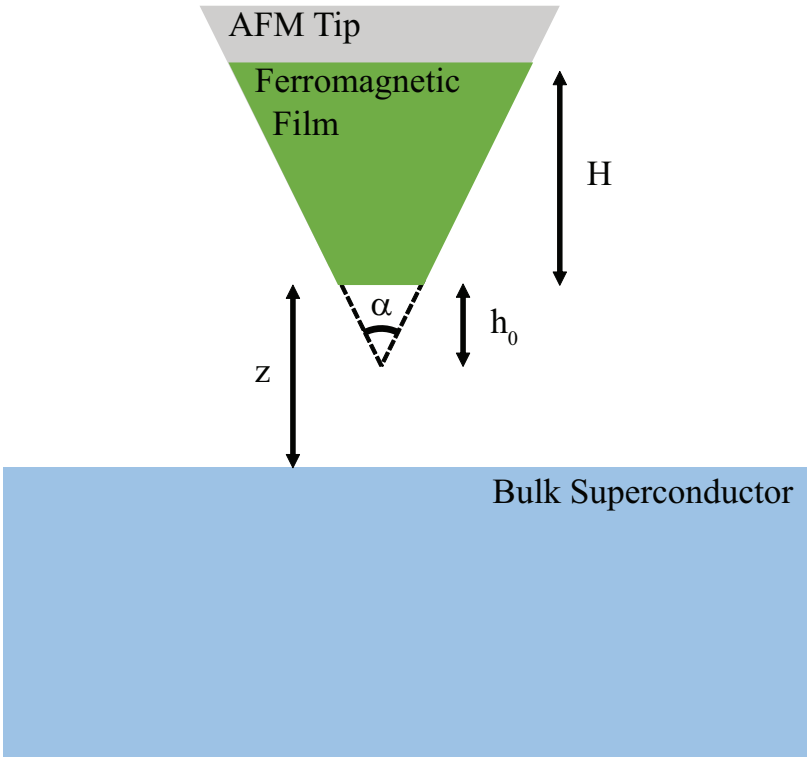

Figure 2.1: **Schematic of the MFM tip model.** We modeled the tip as a cone truncated at a height (h_0) above its hypothetical apex (dashed line). The cone has an opening angle of α. A ferromagnetic film coats the Si AFM tip from its bottom to a certain height (H). The height above the sample (z), in this case a superconductor, is measured from the truncated part of the tip.

2.4.1 "Full tip model"

We modeled the MFM tip as a half-coated cone which has been truncated at a height h_0.

The closest to reality model that is 'simple' to write down for the tip magnetization is

$$M(r') = M_0 t\delta[R' - tan(\alpha)(z' + h_0)] \tag{2.8}$$

where M_0 is the magnetic moment density of the evaporated ferromagnet, t is the thickness of the coating, R' is the radial variable in the x-y plane of the tip, z' is the height variable with respect to the tip, and α is the opening angle of the tip (see Fig. 2.1).

Using cylindrical coordinates ($d\tau' = R'dR'd\theta'dz'$) and the half-coated, truncated cone model the MFM signal is given by

$$F'_z = -\frac{\mu_0 M_0^2 t^2}{2\pi}\int_0^\infty dk k^4 \frac{p-k}{p+k} e^{-2kz}\int_0^\infty R'dR'\int_0^\infty R''dR''\int_0^\pi d\theta'\int_0^\pi d\theta''\int_0^H dz'\int_0^H dz'' \\ e^{-k(z'+z'')}\delta[R'-(z'+h_0)tan(\alpha)]\delta[R''-(z''+h_0)tan(\alpha)] \\ \times J_0[k\sqrt{R'^2+R''^2-2R'R''cos(\theta'-\theta'')}] \tag{2.9}$$

where J_0 is a Bessel function of the first kind.

Performing the integrals over R' and R'':

$$F'_z(z,\lambda) = -\frac{\mu_0 M_0^2 t^2 tan^2(\alpha)}{2\pi}\int_0^\infty dk k^4 \frac{p-k}{p+k} e^{-2kz}\int_0^\pi d\theta'\int_0^\pi d\theta''\int_0^H dz'\int_0^H dz'' \\ e^{-k(z'+z'')}(z'+h_0)(z''+h_0) \\ \times J_0[ktan(\alpha)\sqrt{(z'+h_0)^2+(z''+h_0)^2-2(z'+h_0)(z''+h_0)cos(\theta'-\theta'')}] \tag{2.10}$$

Equation 2.10 represents the closest-to-reality model for the actual half-coated MFM tip I can write down. The goal is to fit the full functional form to experimentally obtained 'touchdown' curves ($\Delta f(z)$) in order to extract λ. Eqn. 2.10 is too computationally expensive to fit to experimental curves. I will describe a range of approximations which one can make in order to make the equation more manageable.

In practice, the 'full model' already contains the following assumptions:

- The magnetic moment points only along the z direction and the tip is mono-domain.
- The magnetic moment density and thickness are uniform over the volume of the tip.
- The shape of the tip is conical (in reality it is closer to an octagonal pyramid).

2.4.2 Zero tip radius ($r_{tip} = 0$) approximation

We can get rid of both the integrals over angle by ignoring the radial position of the magnetic moments of the tip. Mathematically, this corresponds to taking the following approximation in Eqn. 2.10.

$$\theta' - \theta'' \approx 0 \tag{2.11}$$

The angle of the cone still determines the magnetic moment density as a function of height, but

the distance between infinitesimal moments in the x-y plane are ignored for calculating the response. Plugging this approximation into Eqn. 2.10 gives

$$F_z'(z,\lambda) = -\frac{\mu_0 M_0^2 t^2 tan^2(\alpha)\pi}{2}\int_0^\infty dk k^4 \frac{p-k}{p+k} e^{-2kz}\int_0^H dz' \int_0^H dz'' \\ e^{-k(z'+z'')}(z'+h_0)(z''+h_0) \tag{2.12}$$

where the Bessel function goes to 1 and the angular integrals each contribute a factor of π (because the cone is half-coated). The z' and z'' integrals can now be performed analytically and yield

$$F_z'(z,\lambda) = -\frac{\mu_0 M_0^2 t^2 tan^2(\alpha)\pi}{2}\int_0^\infty dk \frac{p-k}{p+k} e^{-2kz}[kh_0 + 1 - (k(h_0+H)+1)e^{-kH}]^2 \tag{2.13}$$

The $r_{tip} = 0$ approximation yields an equation which can be fit to in a reasonable amount of time using numerical integration (e.g. quadgk in Matlab), albeit slowly. Other approximations which simplify the expression further are possible.

2.4.3 Mirror approximation

The mirror approximation is a very intuitively useful approximation, which states that response magnetic field of the superconductor can be approximated by an 'image' magnetic tip, reflected about a mirror plane λ below the surface of the superconductor (in analogy with image charges in electrostatics problems).

The mirror approximation is equivalent to the limit $\lambda k << 1$, which allows a Taylor expansion of the first part of Eqn. 2.10

$$\frac{p-k}{p+k} = \frac{\sqrt{1+\lambda^2k^2}-\lambda k}{\sqrt{1+\lambda^2k^2}+\lambda k} = 1 - 2k\lambda + 2k^2\lambda^2 + \mathcal{O}(k^3\lambda^3) \\ = e^{-2k\lambda} + \mathcal{O}(k^3\lambda^3) \tag{2.14}$$

In the last step, the Taylor expansion of the second term is recognized to be the same as the Taylor expansion of $e^{-2k\lambda}$. The integrand of Eqn 2.10 is now proportional to $e^{-2k(z+\lambda)}$, indicating that we have replaced the full superconducting response with an image tip which is mirror at a plane λ below the surface. This approximation is the only approximation which is important when measuring the relative penetration depth ($\Delta\lambda$), because shifts in λ are equivalent to a shift in the

height of the MFM tip, which can be calibrated with experimental touchdown curves.

If we use both the mirror approximation (Eqn. 2.14) and the $r_{tip} = 0$ approximation, the result is:

$$F'_z(z,\lambda) = -\frac{\mu_0 M_0^2 t^2 tan^2(\alpha)\pi}{2}\int_0^\infty dk e^{-2k(z+\lambda)}[kh_0 + 1 - (k(h_0+H)+1)e^{-kH}]^2 \quad (2.15)$$

Working through this integral results in this overlong (but analytical!) result:

$$\begin{aligned} F'_z(z,\lambda) = -\frac{\mu_0 M_0^2 t^2 tan^2(\alpha)\pi}{2} \times \Bigg\{ & \frac{1}{2(z+\lambda)}\left[1 + \frac{h_0}{z+\lambda} + \frac{h_0^2}{2(z+\lambda)^2}\right] \\ & + \frac{1}{2(z+\lambda+H)}\left[1 + \frac{h_0+H}{z+\lambda+H} + \frac{(h_0+H)^2}{2(z+\lambda+H)^2}\right] \\ & - \frac{1}{2(z+\lambda+H/2)}\left[2 + \frac{2h_0+H}{z+\lambda+H/2} + \frac{h_0(h_0+H)}{(z+\lambda+H/2)^2}\right]\Bigg\} \end{aligned} \quad (2.16)$$

2.4.4 Infinite tip height approximation

This approximation, in combination with the $r_{tip} = 0$ and mirror approximations constitute the model utilized in Refs. [68, 67, 69]. In hindsight, this approximation is unjustified and not necessary computationally. By taking $H \to \infty$, Eqn. 2.16 goes to the previously obtained result:

$$F'_z(z,\lambda) = -\frac{\mu_0 M_0^2 t^2 tan^2(\alpha)\pi}{4(z+\lambda)}\left[1 + \frac{h_0}{z+\lambda} + \frac{h_0^2}{2(z+\lambda)^2}\right] \quad (2.17)$$

2.5 Comparison of tip models

I have plotted the four easily calculable models for the same parameters, which are typical of those found in experiment (FIG. 2.2). Both the mirror approximation and infinite height approximation have noticeable effects on the predicted touchdown curves ($\frac{\partial F_z}{\partial z}$ vs. z).

Specifically, the mirror approximation underestimates $\frac{\partial F_z}{\partial z}$ when $z < \lambda$, which is where the mirror approximation is expected to breakdown. Secondly, the infinite height approximation strongly overestimates the response measured by the tip when it is far away from the sample and significantly modifies the shape of the touchdown curve for a given λ.

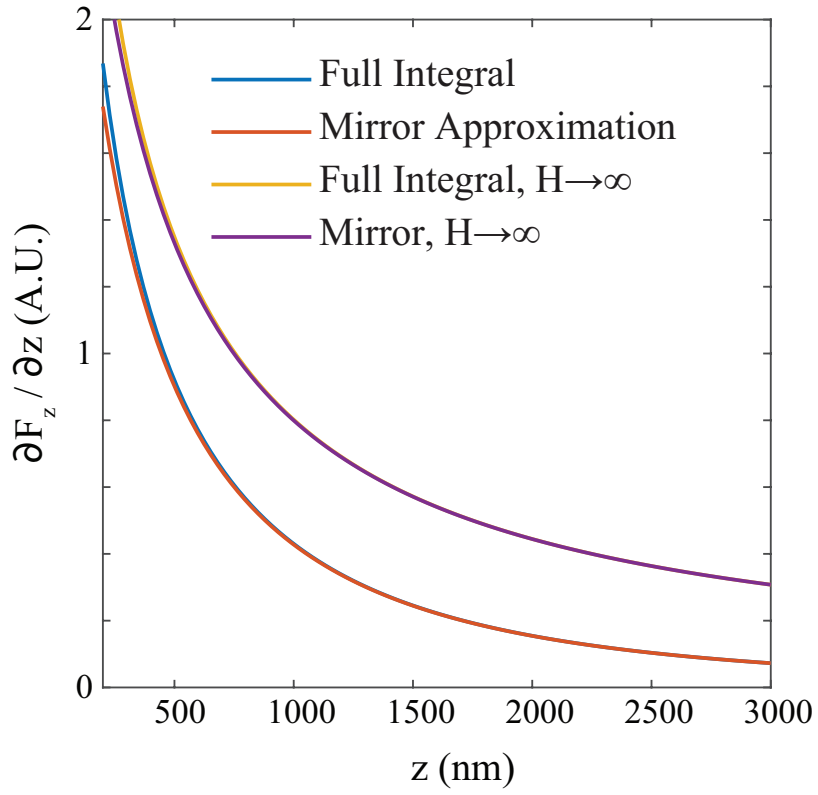

Figure 2.2: **The predicted touchdown curves ($\frac{\partial F_z}{\partial z}$ vs. z) change strongly based on the tip model** Predicted touchdown curves ($\frac{\partial F_z}{\partial z}$ vs. z) for $\lambda = 300nm$, $h_0 = 50nm$, $H = 10\mu m$ calculated from the full integral (Eqn. 2.10, blue), the mirror approximation (Eqn. 2.16, orange), the full integral with the infinite tip height approximation (yellow), and the mirror approximation + infinite tip height (2.17, purple)

2.6 Refitting data with different tip models

The mirror and infinite height approximations were used in Refs. [68, 67, 69] to extract the absolute value of the penetration depth from touchdown curves. Here I present a fit of a representative MFM touchdown curve to the different models and show that using different tip models shifts the value of the extracted penetration depth by a significant amount. Furthermore, using more accurate tip models shifts the extracted λ away from the values measured on similar samples using different techniques. This effect was observed for all touchdowns which were refit, regardless of sample.

In the absence of free parameters other than λ, fits using the infinite height approximation (Eqn. 2.17) should be obviously rejected, due to the large offset from the more realistic models. However, in order to fit actual experimental data, one must include two more free (or quasi-free) parameters, O, an overall horizontal offset which should be the measured $\frac{\partial F_z}{\partial z}$ as $z \to \infty$, and A, which is an overall amplitude which is the front factor in Eqn. 2.17, for example. The two extra free parameters make it harder to discriminate the correct model just based on the residuals of fits.

I fitted a representative touchdown curve taken over a Co-doped $BaFe_2As_2$ at 5.1% doping taken by Lan Luan (data file: 09-March-T004014.mat).

Approximations			**Best Fit Values**			
Mirror	$\mathbf{H \to \infty}$	$\mathbf{r_{tip} = 0}$	$\lambda(\mathbf{nm})$	$\mathbf{A(pN)}$	$\mathbf{O(Hz)}$	$\chi^\mathbf{2}(\mathbf{A.U.})$
x	x	x	407.5	100.75	22.36	0.009
	x	x	436.6	102.3	22.37	0.01
x		x	521.6	128.3	22.51	0.006
		x	616.7	138.4	22.50	0.006

Table 2.1: Fit Parameters for 5.1 doping at 5K (09-March-T004014) The data was truncated at a height of $z = 0.7\mu m$, $h_0 = 400nm$ was set based on SEM imaging of the tip, and $H = 20\mu m$ was estimated but not measured directly.

As shown in Table 2.1, The Mirror + $\mathbf{H} \to \infty$ model and the full integral model result in fitted λ's which differ by more than 200 nm. The difference between models is much larger than the previously estimated systematic error bars of the measurement [68, 67, 69]. The offset (O) and amplitude (A) are noticeably different depending on whether the infinite height approximation is taken or not, indicating that the 'extra' free parameters are compensating for incorrect functional forms of the touchdown curves.

The fit parameters are also very sensitive to the specific value chosen for H, the height of the ferromagnetic coating (FIG. 2.3). For a reasonable range of H's, the fitted λ varies from $\sim$ 450 to $\sim$ 1000 nm (FIG. 2.3 b). The minimum in the error of the fit (FIG. 2.3 a) sets $H \approx 15\mu m$ and

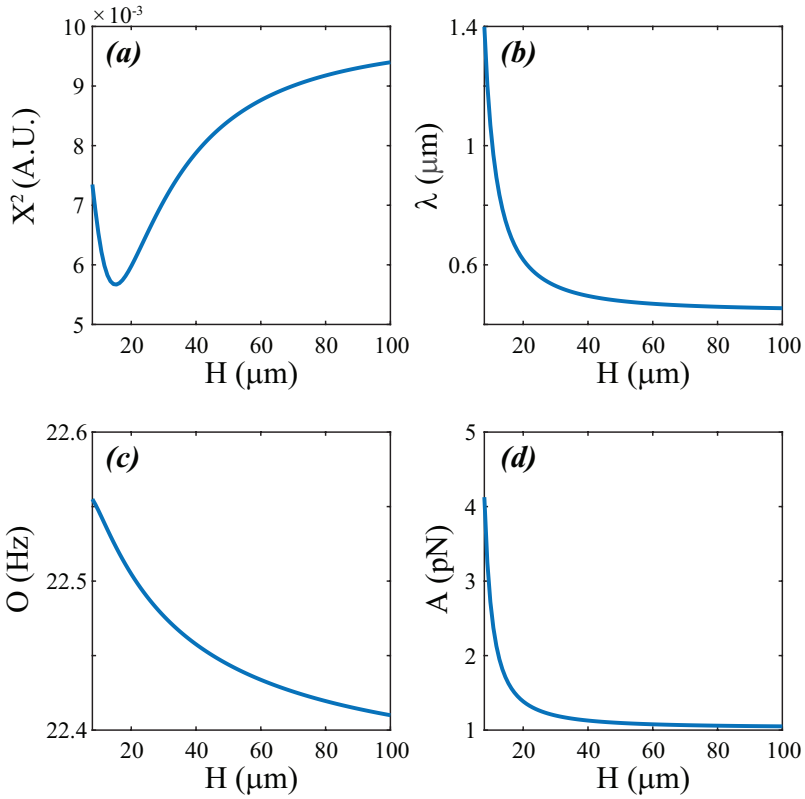

Figure 2.3: **Full integral fit parameters (Eqn. 2.10) vs. the fixed height of the ferromagnetic coating on the tip (H).** Results of full integral fits of 09-Mar-2009-T004014.mat, a touchdown curve over a 5.1 percent Co-doped Ba-122 pnictide. (a) χ^2 or mean squared error and fitted values for (b) penetration depth (λ), (c) vertical offset (O), and (d) amplitude (A) as a function of the tip height (H). The penetration depth for λ depends sensitively on the value of H, which is not known precisely.

results in a fitted $\lambda \approx 700nm$ which is much higher than the expected penetration depth from bulk measurements of penetration depth.

Similar analysis performed on touchdowns on a cuprate superconductor, YBCO, yielded similar general trends when fitting to more accurate functional forms.

2.7 MFM fitting conclusions

I've extended previous MFM modeling of the measured Meissner response by our MFM tips over a bulk superconductor ([68, 67, 69]) to include a finite height of the magnetic coating on the tip (H) and to not rely on the mirror approximation. When these improvements were included in the fit, the fitted penetration depth (λ) changed by a significant amount. Fitted values of λ appear to get farther from other reported experimental values as the model gets more accurate. This indicates that the similarity of the fitted values (using the old modeling) to bulk measurements of λ was probably accidental.

From this work, it is unclear what is required or if it is actually feasible to extract λ accurately using magnetic force microscopy and fitting. Some possibly helpful, but not necessarily sufficient improvements coudld be: better knowledge of the exact geometry and magnetic moment density of the tip, data which includes a wide enough range of z values to fix the vertical offset (O) of the fit independently, or an easier to model geometry (e.g. nanotube tips [30]).

Measurements of $\Delta\lambda$, relative changes of the penetration depth, are much less sensitive to the above considerations. Work involving measuring $\Delta\lambda$ between a reference superconductor and the superconductor of interest using the same magnetic tip may be a more robust, albeit challenging, way of extracting λ from MFM measurements [51].

Chapter 3

Point spread funtion and current reconstruction

3.1 Point-spread function basics

A point spread function (PSF) or imaging kernel is the response of an imaging system to a point-source. It is possible, in principle, to deconvolve the effects of the PSF from the more interesting source image. In the case of scanning superconducting quantum intereference device (SQUID) measurements, the PSF is how an underlying magnetic field $B_z(x, y)$ is converted to the measured flux Φ_S

$$\Phi_S(x, y) = \int g(x' - x, y' - y) B_z(x', y') dx' dy' \tag{3.1}$$

where $g(x, y)$ is the SQUID's point spread function. For simplicity, I have assumed here that the SQUID lies in the x-y plane, and is therefore only sensitive to the z component of the magnetic field. This integral can also be though of as as a convolution of the SQUID's PSF with the z component of the magnetic field. Since our data is discrete, I will represent convolutions and deconvolutions with fast Fourier transforms (FFT) and inverse fast Fourier transforms ($IFFT$) for the rest of this chapter. Eqn. 3.1 written as a discrete convolution for 2D data is

$$\Phi_S = IFFT\Big[FFT[g]FFT[B_z]\Big] \tag{3.2}$$

Knowledge of the SQUID's PSF allows you to (in principle) extract B_z from measured flux images

$$B_z = IFFT\Big[\frac{FFT[\Phi_S]}{FFT[g]}\Big] \tag{3.3}$$

Similarly, if we image a magnetic feature with a known magnetic field profile, we can extract the PSF

$$g = IFFT\Big[\frac{FFT[\Phi_S]}{FFT[B_z]}\Big] \tag{3.4}$$

3.2 Extacting an 'experimental PSF' from superconducting vortex images

One field source with a well known magnetic field is an Abrikosov vortex in a bulk, type-II, 3D superconductor. The field from an Abrikosov vortex can be well-approximated by a monopolar magnetic field a penetration depth (λ) beneath the surface of a bulk superconductor. A vortex's magnetic field, when $z > \lambda$ is approximately

$$\vec{B}_{vortex} = \frac{q_m}{|\vec{r} + \lambda\hat{z}|^3}(\vec{r} - \lambda\hat{z}) \tag{3.5}$$

The negative z direction is defined into the superconductor, so positive z is above the sample. q_m is the magnetic monopole charge, which for a quantized superconducting vortex is a superconducting flux quantum $q_m = \Phi_0 = h/2e$. For a vortex at a position (x_0, y_0), the z component of the field is

$$B_{z,vortex}(x, y, z) = \frac{\Phi_0(z + \lambda)}{\Big[(x - x_0)^2 + (y - y_0)^2 + (z + \lambda)^2\Big]^{3/2}} \tag{3.6}$$

There are two parameters which are effectively free in extracting the point spread function. First, $z + \lambda$ is something we do not know very accurately, mainly because the SQUID's offset height from the sample is determined by the alignment angle, the distance between the SQUID's pickup loop and where the SQUID chip touches the sample, and the scan height above the sample. None of these parameters are in general known to a high enough degree of accuracy to fix this value.

Secondly, filtering of the deconvolution in k-space is necessary to avoid excess noise in the extracted PSF. If the denominator of Eqn. 3.4 goes to zero, any finite noise in the numerator will diverge in amplitude near the zero crossing (e.g. the zero crossing in PSF k-space image in FIG. 3.1. The type of filter and how sharply the data is filtered are both variable and will determine the quality of the extracted PSF. One appropriate filter is called a Hanning filter:

$$H(K) = \begin{cases} 0.5 + 0.5cos(\pi K/K_{max}) & \text{if } K \leq K_{max} \\ 0 & \text{if} K > K_{max} \end{cases} \tag{3.7}$$

where $K \equiv \sqrt{k_x^2 + k_y^2}$.

The experimentally-extracted PSF ,then, is given by

g =

$$g = \frac{1}{dxdy} IFFT\Big[\frac{H(K)FFT[\Phi_S]}{FFT[B_z]}\Big] \tag{3.8}$$

where the factor of $1/dxdy$ normalizes the PSF such that a value of one means that all of the flux in that region is 'captured' by the SQUID. We used a low noise, high resolution image of a superconducting vortex (FIG. 3.1 a, taken by Beena Kalisky) to extract the SQUID's PSF (3.1 b). The filter and height values are chosen somewhat subjectively based on the heuristics presented later.

The lithographically defined size of the circular part of the loop is consistent with the measured PSF (i.e. g is zero outside of the outer radius and close to one inside the inner radius, see FIG. 3.1 b, inset). The 'leads' of the SQUID also capture a finite amount of flux, which results in the tail observed above both the vortex and PSF.

3.2.1 Dependence of PSF on assumed height and filter parameters

Although the generic features of the PSF are robust, the specifics of the shape and amplitude depend on the filter cutoff spatial frequency and height, K_{max} and $z+\lambda$. In particular, both the overall height of the PSF and the presence of negative dips in the PSF at the edges of the pickup loop are sensitive to these parameters. Choosing the 'correct' values is more of an art than a science at this point, and it is not clear that it strongly affects the quality of current inversion images. Quantitative uses of the PSF should take into account how the uncertainties of the PSF outlined here couple into systematic error bars.

I have chosen the parameters in 3.1 b in particular because it represents two features which are favorable: The overall height of the PSF is close to and does not exceed one at the center of the pickup loop and negative dips at the edges of the pickup loop are minimized. In order to better understand the effect of the free parameters in the deconvolution process on these two features, I've varied both $z + \lambda$ and K_{max} and plotted vertical and horizontal line cuts through the maximum of the PSF (FIGS 3.3 and 3.4).

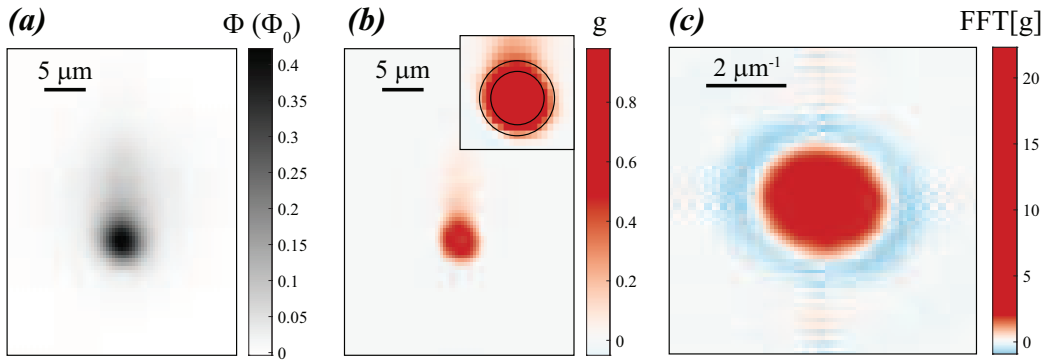

Figure 3.1: **Measured vortex image and an example of an extracted point spread function** (a) A magnetometry image of a vortex taken by Beena Kalisky on a bulk superconductor. (b) The extracted point spread function (g) using a Hanning filter with a cutoff frequency of K_{max} = 5 μm^{-1} and assuming a monopole height of $z + \lambda$ = 1.5 μm. A value of g=1 corresponds to 100% of magnetic flux through a given pixel contributing to the SQUID signal. (Inset) A zoomed in image showing the optically measured inner and outer diameters of a SQUID of the same design ($d_{inner} = 3.73\mu m$ and $d_{outer} = 5.27\mu m$). (c) The real part of the FFT of g, showing a zero crossing at finite k. The real-space PSF was cropped such that its maximum was at the center of the matrix, otherwise other oscillations are present in the FFT.

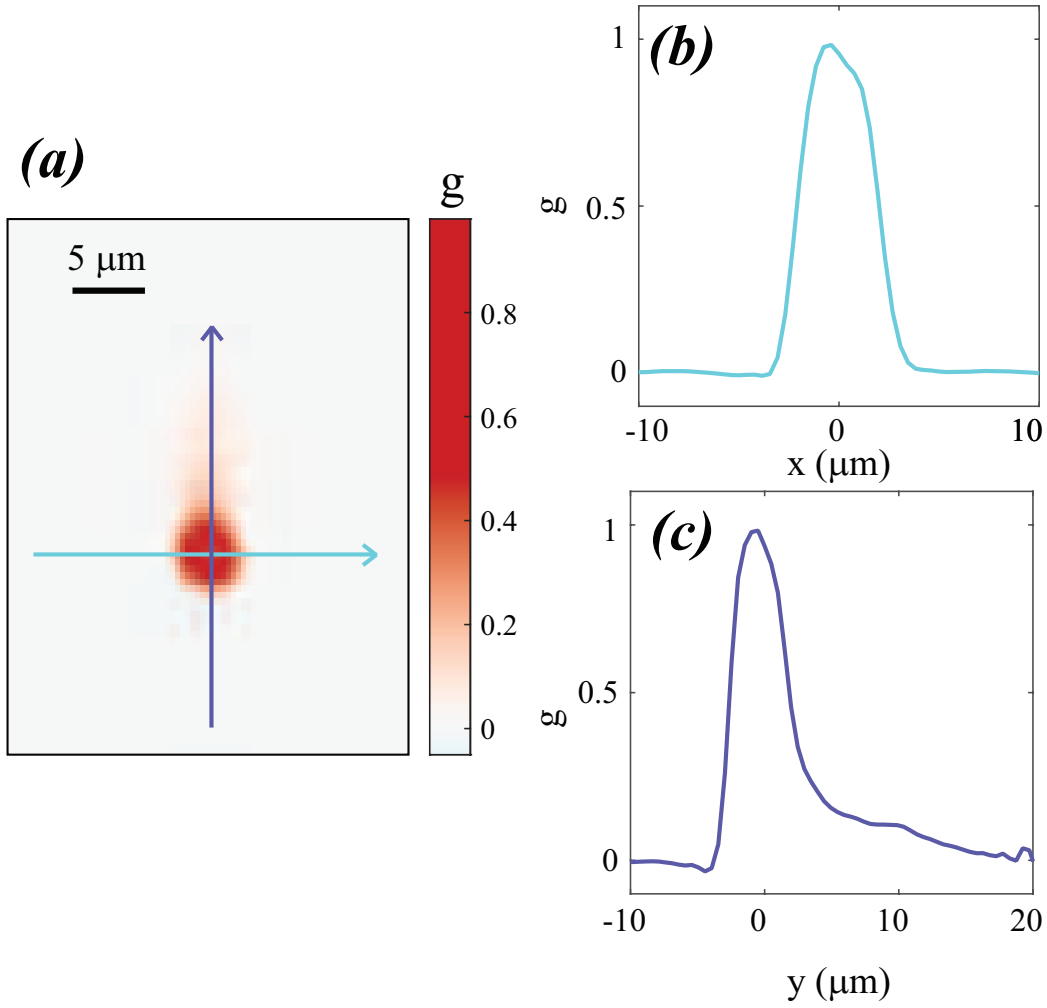

Figure 3.2: **Line cuts through the PSF's maximum** (a) The same image as FIG. 3.1 b, showing where horizontal (purple) and vertical (teal) line cuts were taken. (b,c) Horizontal and vertical line cuts through the PSF's maximum, respectively.

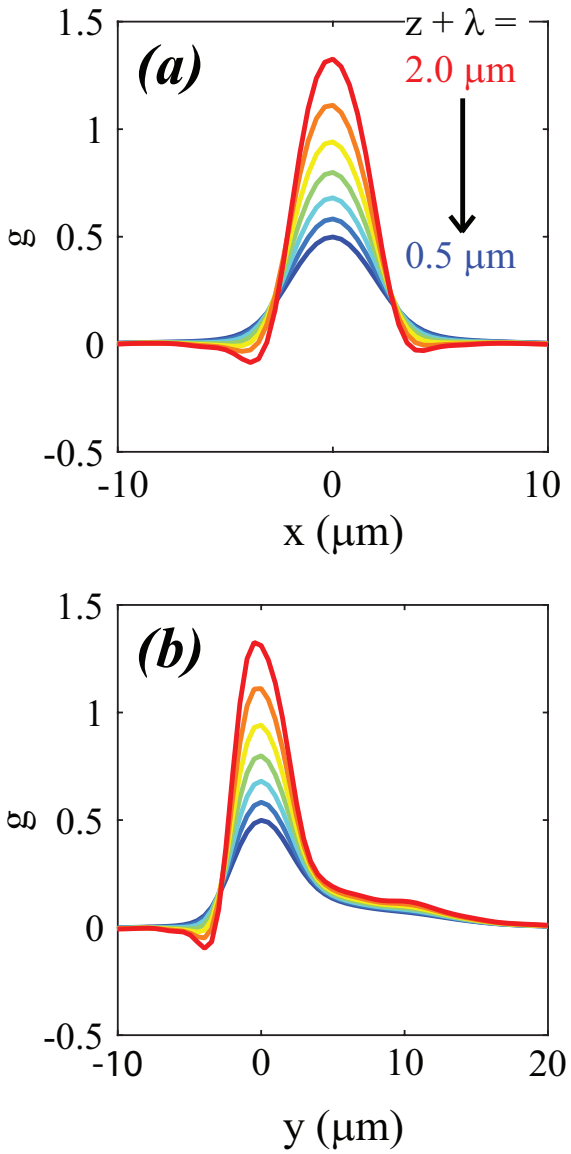

Figure 3.3: **Line cuts of the PSF as a function of the assumed vortex height** (a,b) Horizontal and vertical line cuts through the extracted PSF as a function of the assumed monopole height ($z + \lambda$). K_{max} is fixed at 3 μm^{-1}

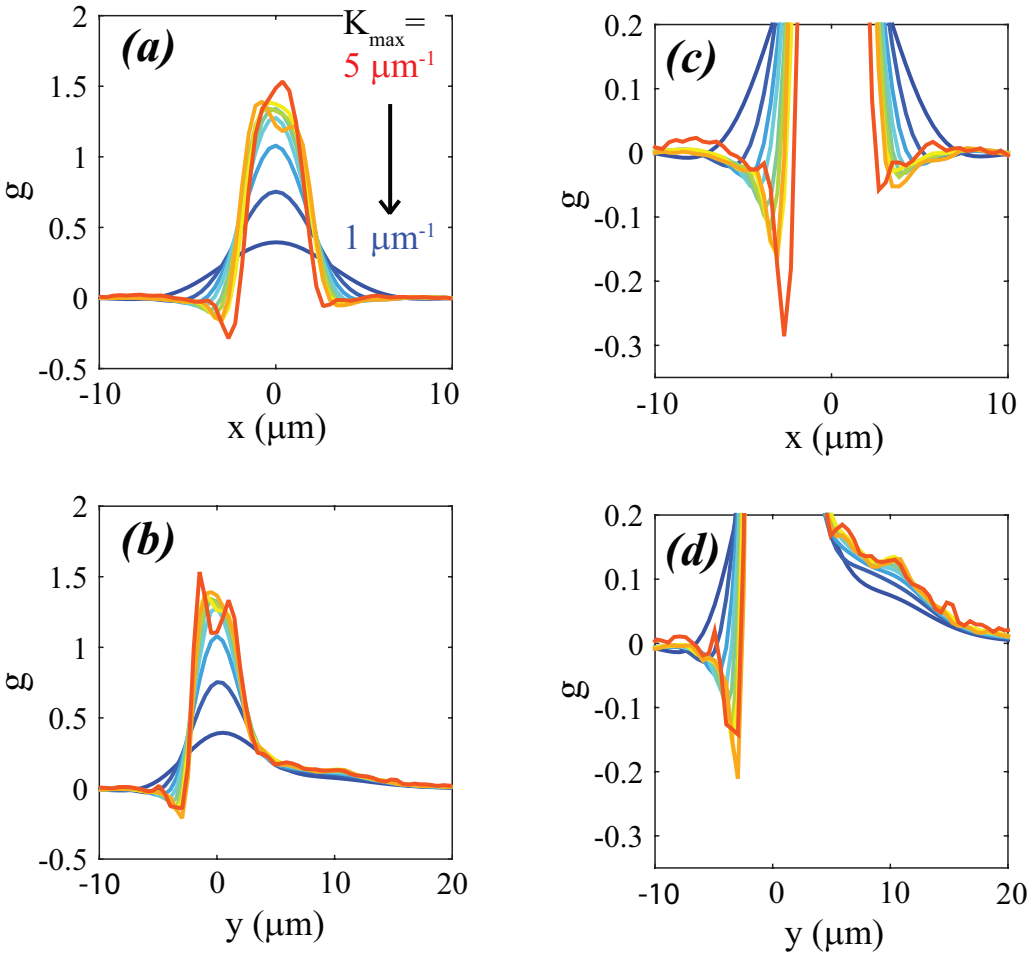

Figure 3.4: **Line cuts of the PSF for different Hanning filter parameters** Horizontal(a,c) and vertical (b,d) line cuts through the extracted PSF as a function of the cutoff frequency of the Hanning filter (K_{max}). The vortex height ($z + \lambda$) was fixed at 2.015 μm

The amplitude of the PSF got larger as the monopole height was increased (FIG. 3.3). As $z + \lambda$ was increased, the amplitude of the magnetic field from a vortex decreased. Therefore, in order for the convolution of g and Bz to produce the correct amplitude in the image, the amplitude of g in the pickup loop increased to compensate.

The amplitude of the PSF also increased as K_{max} was increased (FIG. 3.4) For small K_{max}, the vortex image was smeared out by the filter and therefore the peak in g is artificially broadened and its amplitude drops. As K_{max} was increased, the amplitude of g appears to saturate its value in addition to the becoming noisier. Unfortunately, there is no region which clearly shows both saturation and an acceptable level of noise for this data set. In order to most correctly get the amplitude of g, K_{max} should be set as high as possible without making the PSF too noisy.

Negative dips in the point spread function are the second feature of the PSF which was obviously tuned by both height and K_{max}. As height or K_{max} was increased the amplitude of the negative dips also increased. In the case of a peaked magnetic field with only one sign, such as that of a vortex, a negative dip in the extracted PSF indicates that the measured flux is narrower (in some sense) than the source field. I believe that this is an artifact of taking a height which is too large (and therefore the calculated source field being too broad) rather than a real effect.

Negative values in the point spread function are unlikely to occur in scanning SQUID. A negative value of g indicates that the measured flux is of opposite sign of the corresponding field line at that same location. Flux focusing (screening of the field near the surface of the sample due to the superconducting material of the pickup loop) can move field lines, but the total integrated flux through the scan plane must remain constant. The z component of the vortex's magnetic field is always upwards (positive). This means, that in order for a negative value of the PSF to exist, a field line which initially points upward must be distorted such that it goes down through pickup loop. The hypothetical field line which is bent downwards must go upwards twice outside the pickup loop to conserve total flux, which is unphysical.

Flux focusing does pinch the magnetic fields locally while the SQUID is near the sample, however this effect is different than the images themselves being 'pinched'. Flux focused inwards will increase the measured signal, which increases the overall size of the PSF. If, for some reason, all of the field lines that would penetrate the pickup loop's superconducting lines were focused outwards, this would be well described by a loop which is infinitely thin with the inner radius of the loop. Neither of the extreme cases of flux focusing require negative values in the PSF in order to capture their behavior.

To sum up, the heuristic technique for getting the 'best' PSF (in my opinion) for a given image

is to, at a number of heights maximize K_{max} while keeping the noise in the PSF low. Then, from the optimized PSF at each height, pick the one which gives an amplitude at the center of the pickup loop of ~ 1 and does not have significant negative value. It is not clear at this point, however, that this degree of fine tuning of the extracted PSF is important for the ways in which we currently use it.

3.3 Current inversion

A related problem which makes use of the extracted PSF is the problem of extracting the 2D current density from a scanning SQUID image of flux due to current flowing in a sample. We follow the method outlined in Ref. [90]. The method entails writing down the Biot-Savart law as a convolution and using Fourier techniques to 'deconvolve' the current density. The Biot-Savart law is

$$\vec{B} = \frac{\mu_0}{4\pi} \int \frac{\mathbf{J}(\mathbf{r}') \times (\mathbf{r} - \mathbf{r}')}{|\mathbf{r} - \mathbf{r}'|^3} d^3\mathbf{r}' \tag{3.9}$$

for 2D currents confined to a thickness d, a distance z away from the SQUID, the z component of the field B_z is

$$B_z = \frac{\mu_0 d}{4\pi} \int_{-\infty}^{\infty} dx' \int_{-\infty}^{\infty} dy' \frac{J_x(x', y')(y - y') - J_y(x', y')(x - x')}{[(x - x')^2 + (y - y')^2 + z^2]^{3/2}} \tag{3.10}$$

We can rewrite this as a (somewhat complicated) convolution in k-space where lower case letters indicate a 2D Fourier transform:

$$b_z = g(j_x k_y - j_y k_x) \tag{3.11}$$

$$g \equiv \frac{i\mu_0 d}{2} e^{-Kz} \frac{1}{K} \tag{3.12}$$

where k_x and k_y are the spatial frequencies and I've defined $K \equiv \sqrt{k_x^2 + k_y^2}$.

In order to extract j_x and j_y independently, we must also invoke local current conservation $\nabla \cdot \mathbf{J} = 0$, which in k-space is:

$$-ik_x j_x - ik_y j_y = 0 \tag{3.13}$$

Solving for j_x and j_y we find

$$\begin{aligned} j_x &= b_z \frac{-2ik_y}{\mu_0 e^{-Kz} K} \\ j_y &= b_z \frac{2ik_y}{\mu_0 e^{-Kz} K} \end{aligned} \tag{3.14}$$

In order to extract the current density from 2D images, we then plug in for b_z using actual data (Φ_S) and the extracted PSF (g)

$$\begin{aligned} J_x &= IFFT[\frac{FFT[\Phi_S]H}{FFT[g]} \frac{-2ik_y}{\mu_0 e^{-Kz} K}] \\ J_y &= IFFT[\frac{FFT[\Phi_S]H}{FFT[g]} \frac{2ik_x}{\mu_0 e^{-Kz} K}] \end{aligned} \tag{3.15}$$

The current extraction process is not sensitive to a homogeneous current flowing through the image. For images of patterned devices, I have sometimes have subtracted the average of J_x and J_y far away from the device where no current should be flowing in order zero the images presented in this thesis.

As with extracting the PSF, the filter H and height z influence the details of the image. The filtering requires much smaller frequency cutoffs (K_{max}) than exctracting the PSF. This is because the PSF, which is in the denominator of the expression for current, has a relatively low frequency zero crossing(FIG. 3.1 c). For most of the images presented in this thesis, I've used an asymmetric extension of the Hanning filter

$$H(K) = \begin{cases} 0.5 + 0.5cos(\pi \sqrt{(\frac{k_x}{K^x_{max}})^2 + (\frac{k_y}{K^y_{max}})^2} & \text{if } \sqrt{(\frac{k_x}{K^x_{max}})^2 + (\frac{k_y}{K^y_{max}})^2} \leq 1 \\ 0 & \text{if} \sqrt{(\frac{k_x}{K^x_{max}})^2 + (\frac{k_y}{K^y_{max}})^2} > 1 \end{cases} \tag{3.16}$$

with typical values of $K^x_{max} = 1.5 - 1.8$ and $K^y_{max} = 1.8 - 2.1$.

The maximum values of K_{max} are fixed by a combination of the zero crossing in the k-space PSF and the noise in the flux image. Low values of K_{max} artificially broaden features (FIG. 3.5 left column). Once K_{max} approaches the location in k-space of a zero crossing, the image becomes very noisy. The total integrated current flowing through the image, as determined by summing j_x along a line across the middle of the device, only varies by a couple of percent as a function of K_{max}.

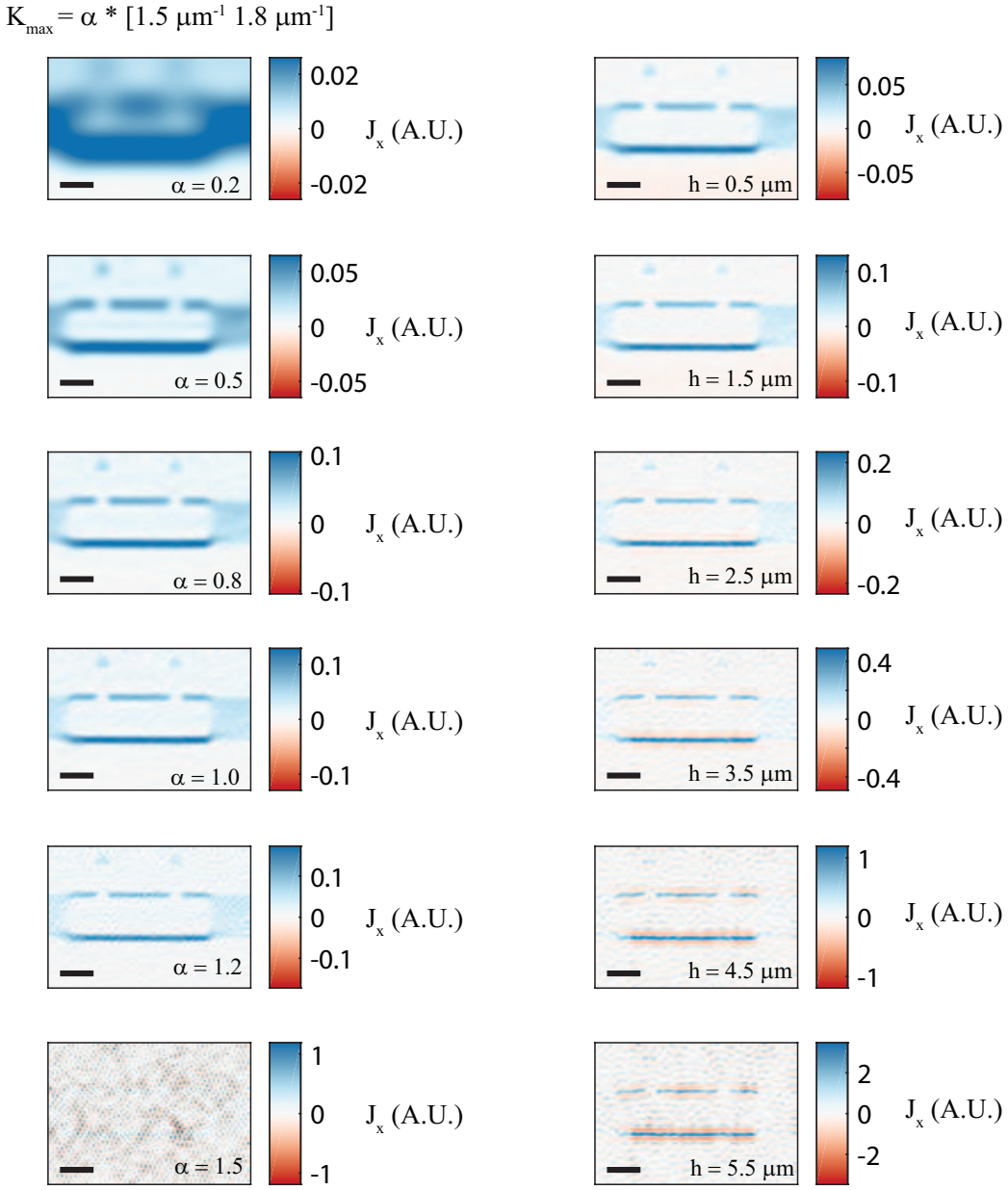

Figure 3.5: **Effect of changing filter parameters and height on current inversion** Resulting images of J_x from current inversion with various K_{max} values (left) and assumed heights, h (right). The left column uses a fixed height $h = 1.5\mu m$ and the right column uses a fixed Hanning cutoff of $K_{max} = [1.5\ 1.8]\mu m^{-1}$. The mean of the bottom five horizontal lines of J_x were subtracted from each image to set zero.

Varying the assumed height h (FIG. 3.5, right column) changes the shape and amplitude of the extracted current density. At low heights, the features in J_x are broadened. At higher heights, ringing and negative values in J_x appear. Similarly to the PSF deconvolution, if the measured features are too narrow to be explained by an infinitely narrow wire at higher assumed heights, the extracted current will compensate. In particular, the current inversion generates counter-propagating currents to artificially generate the narrower magnetic field features. Notice that the ringing present at high heights is not observed for any values of K_{max} when the height is fixed to a smaller value (e.g. $\alpha = 1.2$ in the left column of FIG. 3.5). In contrast with varying K_{max}, the integrated current through the image changes strongly as a function of h.

3.4 Fitting flux from current

For quantitative analysis of current densities in devices, it can be useful to assume a specific form of current flow (e.g. current flowing along the edges of a device) and compare measured profiles of Φ_S to a calculated flux signal. Fitting offers a couple of advantages over current inversion for analysis: It avoids the extra filtering required for current inversion, allows us to extract the amount of current flowing in each channel,it gives a metric (goodness of fit) for determining the height of the scan, and it allows for fitting of heavily averaged lines of Φ_S in order to detect small currents.

We used the Poisson equation to simulate current flow in devices we measured. We used MATLAB's Poisson solver to numerically calculate the expected current distribution, given the dimensions of the device.

For example, in order to simulate current flow in the InAs/GaSb device, we've chosen three possible current flow configurations 3.6 which correspond to current flowing in the top edge, bottom edge, or through the bulk of the material under the top gate. In the ungated part of the device, we assumed that current is allowed to flow throughout the device. We set up the Poisson equation with the boundary conditions that $V = 1$ on the left side and $V = 0$ on the right side of the device, and solved for the local voltage (3.6 a). From the gradient of V(x,y), we then find the current density. We used the simulated current density to generate simulated SQUID images using our experimentally-extracted PSF and used FFT techniques similar to Eqn. 3.14 to quickly calculate the field.

In order to extract how much current flowed in the edges as precisely as possible while keeping the applied currents relatively low, we often scanned the SQUID vertically across the same area of the device many times to obtain 'averaged line cuts' or 'averaged profiles' of the SQUID signal. We fitted these profiles to calculated flux line cuts as described above. For some data sets, the shape

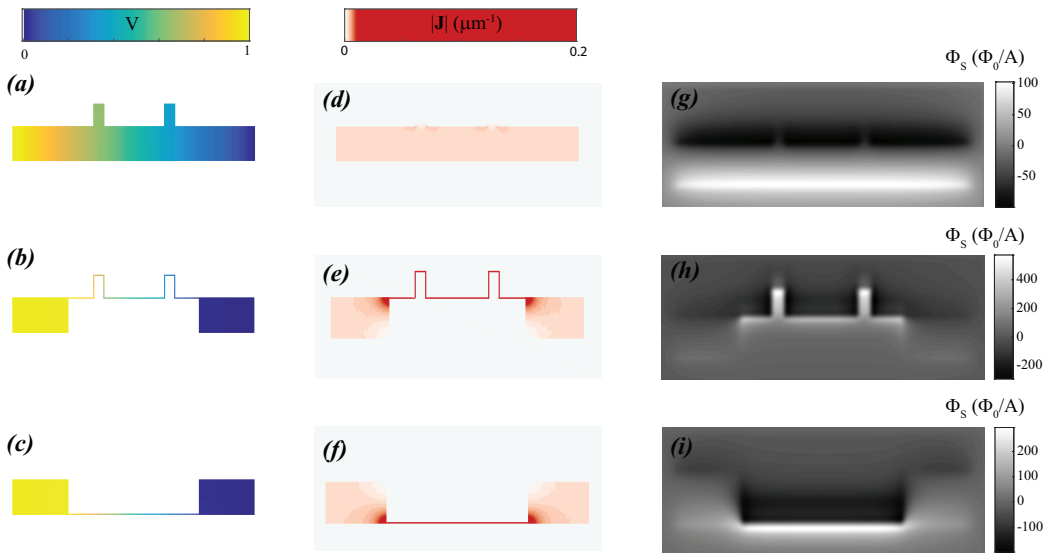

Figure 3.6: **Schematic of Poisson simulation of current flow** Results of Poisson equation simulation for an InAs/GaSb device (see FIG. 6.4). We've devised geometries for current flowing in the bulk (a), along the top edge of the device (b), and along the bottom edge of the device (c). We solved the Poisson equation with boundary conditions of $V = 0$ along the right most edge of the device, and $V = 1$ on the leftmost edge. (d-f) We then calculated $\mathbf{J}$ by taking the gradient of $V(x, y)$. $\mathbf{J}$ was normalized by the sum of the current density along a line through the center of the device. (g-i) We used the extracted current and our experiment PSF to generate the expected flux image for each current pattern. Line cuts through the calculated flux images were used to fit the data (e.g. FIG. 6.6)

of the bulk current flow varied from our simulation, and for those cases we used experimentally extracted profiles at gate voltages where no edge conduction should be present (e.g. at gate voltages where the devices were highly n-doped).

An example of the fits is shown in FIG. 3.7. We fitted flux profiles to the equation:

$$\Phi_S = f_{bulk}\Phi_{bulk} + f_{top}\Phi_{top} + f_{bottom}\Phi_{bottom} \tag{3.17}$$

Where f_i are the fractions of current flowing in each channel, and Φ_i are the difference calculated profiles shown in FIG. 3.7 a. The fits reproduce the shape of the flux profiles well throughout the temperature series. With this particular data set, the tail of the PSF (which was extracted from a SQUID with a different alignment) does not appear to be exactly correct. This can be seen by looking above the device (positive y) and seeing that the fit always undershoots the flux profile above the device, where only the leads of the SQUID are contributing (FIG. 3.7).

3.5 Conclusion

In conclusion, I have outlined the basic steps of extracting a point-spread function for the SQUID and using it to extract the 2D current density from flux images. We also used the PSF to quantify current density in the edge states of devices by fitting.

The considerations for extracting a PSF and current inversion images are usually more aesthetic than an exact technique. In particular, the details of the amplitude of the PSF and presence of negative dips are sensitive to the chosen height and filter. We do not have any direct knowledge of the height, so there is an uncontrolled systematic error in the PSF due to these considerations.

In the case of fitting flux profiles, the fits themselves show the PSF is approximately correct (e.g. the width of the peaks at the bottom edge are well matched to the fit in FIG. 3.7 b). Additionally, the main propagated error in the flux fits from an incorrect PSF would be in overestimating (or underestimating) the amount of current flowing in all channels, while we are primarily interested in their relative amplitudes.

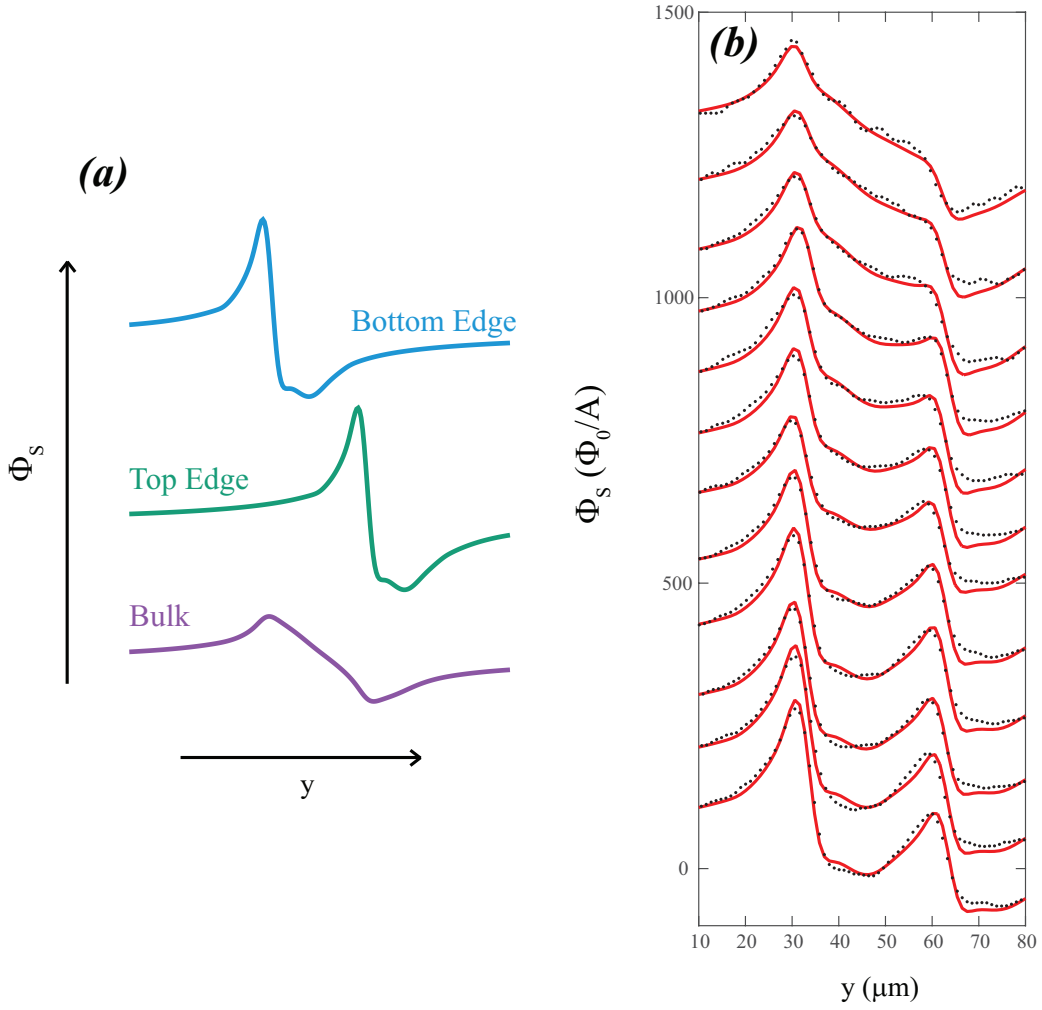

Figure 3.7: **Example of fits to flux profiles using Poisson simulation** (a) Calculated flux profiles for current flowing along the top edge, bottom edge, and through the bulk (corresponding to FIG. 3.6 h,i,g respectively). (b) Fitted profiles (red) and measured flux (black dots) of an InAs/GaSb device at different temperatures (FIG. 6.6). The profiles were fit to Eqn. 3.17 with a scaling factor for the spatial dimension y (which varied due to temperature dependence of the piezoelectric scanners) and a vertical offset. The fitted fractions were normalized to sum to one.

Chapter 4

Local conductivity variation from tetragonal domain structure in $LaAlO_3/SrTiO_3$

This chapter was originally published in:

"Locally enhanced conductivity due to the tetragonal domain structure in $LaAlO_3/SrTiO_3$ heterointerfaces"

Beena Kalisky*, Eric M. Spanton*, Hilary Noad, John R. Kirtley, Katja C. Nowack, Christopher Bell, Hiroki K. Sato, Masayuki Hosoda, Yanwu Xie, Yasuyuki Hikita, Carsten Woltmann, Georg Pfanzelt, Rainer Jany, Christoph Richter, Harold Y. Hwang, Jochen Mannhart, Kathryn A. Moler. *Nature Materials* 12, 1091-1095 (2013)

4.1 Introduction to complex oxides

The complex oxides display many spectacular phenomena, including colossal magnetoresistance and high-temperature superconductivity that result from their special electronic properties. In recent years, dramatic progress in the difficult task of growing oxide heterostructures has enabled the field of "oxide interface engineering" [72], providing opportunities for electronics. LAO and STO are both band insulators, but when four unit cells or more of LAO are grown on a TiO_2-terminated STO $\{001\}$ substrate, the interface conducts [82, 105]. The prevailing explanation of conduction at the interface is electronic reconstruction due to a 'polar catastrophe' in which charge migrates

from the top LAO layer to the interface [105, 17]. Additional physical phenomena in LAO/STO include superconductivity [105, 88, 20, 4, 6, 31, 7] and magnetism [13, 95, 111, 31, 63, 10, 47]. The in-plane angular dependence of magnetoresistance [46], strong trends in spin-orbit coupling with applied back gate voltage obtained from magnetotransport [6, 7, 19], and quantum oscillations [6, 34] all show a diverse set of behaviors in transport studies, but the possibility of correlation between the transport and the local structure is relatively unexplored. Our previous work [10, 47] showed that magnetism and superconductivity in this system can be inhomogeneous. We applied the same local measurement techniques to explore the relationship between structure and normal current flow.

4.2 Results

Here we locally probed how current distributed in seven samples (Supplementary Table S1) using a scanning SQUID with micron-scale spatial resolution[37, 43]. We applied an AC current to each sample and used lock-in techniques to image the AC flux, which is a convolution of the SQUID's point spread function and the z component of the magnetic field due to local currents (FIG. 4.1a, Methods). All images presented are normalized by the applied current. We first present images of sample H1, which is patterned so current flows in a bar with a width that is smaller than that of a single image. In a simulated flux image for current flowing in a sample shaped like sample H1 but with uniform conductivity (Fig. 1b), the measured magnetic flux monotonically changes from positive to negative inside the Hall bar, and decays to zero outside. The actual measured magnetic flux in sample H1 (Fig. 1c) similarly varied overall from positive to negative, but substantially deviated from smooth, monotonic behaviour, demonstrating that the current density varies strongly as a function of position. Although the qualitative conclusion is clear from the raw data, we can better visualize the spatial variations by using an experimentally determined point spread function from a nominally identical SQUID and techniques outlined in Ref. [81] and in Chapter. 3 to extract the 2D current density from flux images. We normalized the 2D current density by the RMS amplitude of the applied current, giving units of μm^{-1}. The component of the 2D current density parallel to the long dimension of the Hall bar shows a large spatial variation in the magnitude of current flow (FIG. 4.1). Line cuts of the current reconstruction reveal that the modulation of the current density is at least a factor of two in sample H1 (FIG. 4.1e). The height of the actual current modulation and corresponding conductivity modulation may be much higher because the observed variations are resolution-limited (see 4.2.2, FIG. 4.7).

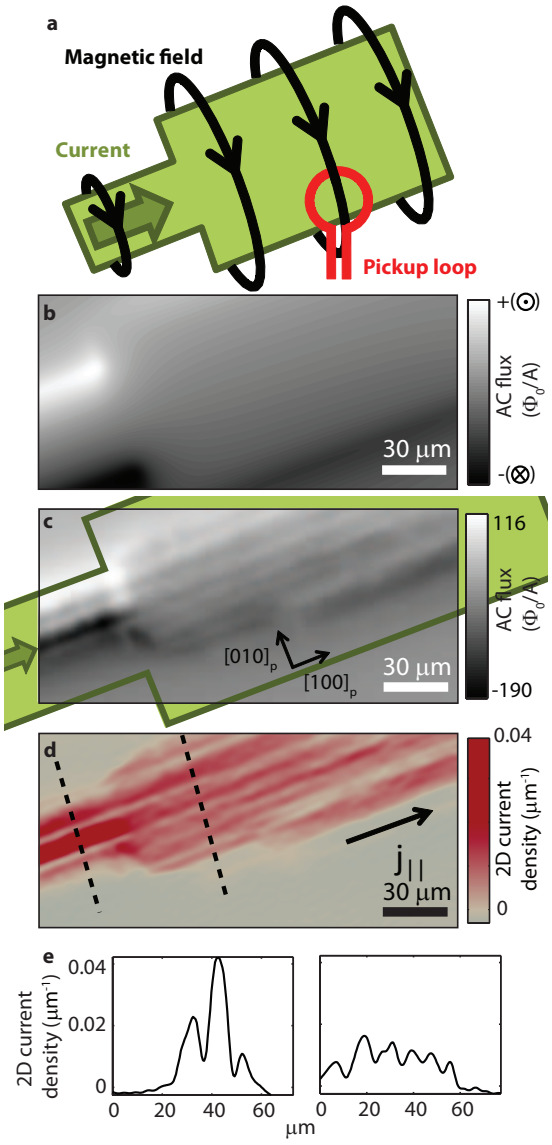

Figure 4.1: **Scanning SQUID measurements of current in LAO/STO heterostructures** a, In our measurement setup, the magnetic flux through the pickup loop (red) from current flowing in the sample is measured as a function of position. b, Simulated flux image for the dimensions of sample H1 with uniform conductivity. In AC flux images, positive flux is flux measured out of the page while negative flux is into the page. c, Magnetic flux image of current in patterned sample H1. Green outline indicates the dimensions of the patterned LAO/STO. d, Reconstructed current densities along the long dimension of the device are obtained from the raw flux image. e, Line cuts through the current densities (dashed lines in d reveal a large modulation of the amplitude of the current density with position. Scale bars are 30 μm.

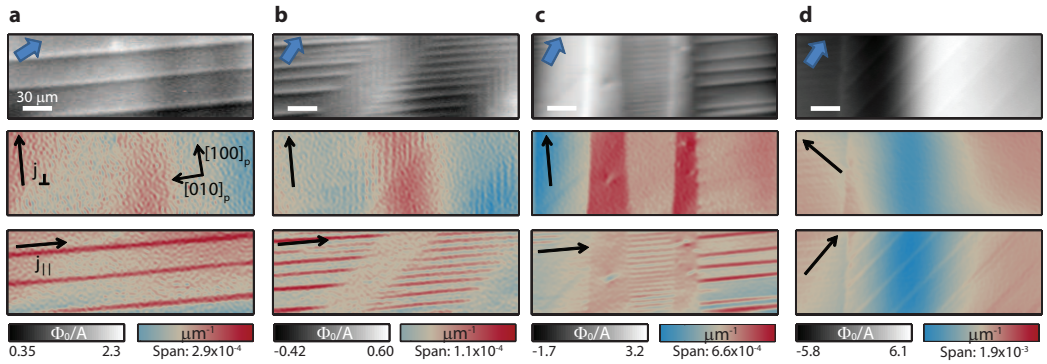

Figure 4.2: **Current in unpatterned LAO/STO flows in narrow paths.** a-d, (Top) Magnetic flux images from current flowing through four 250 μm x 85 μm regions of a 5x5 mm sample. The dark and light lines next to each other correspond to a dipolar feature expected for the z component of a magnetic field from a wire-like current. Blue arrows indicate the expected direction of current flowing in a homogeneous sample, showing that more current is flowing in the narrow paths. (Middle, Bottom) Variation in the 2D current density reconstructed from the AC flux parallel (red) and anti-parallel (blue) to the direction indicated with a black arrow. The background current density cannot be determined from the present data and analysis, so red and blue indicate more and less current flowing with respect to an unknown 2D sheet current. All directions of narrow paths observed in sample M1 are shown: a-c, $[010]_p$, b, $[100]_p$ and d, $[110]_p$. Scale bars are 30 μm.

The current does not flow near the edges of the patterned sample, similar to the behaviour of the superfluid density, which disappears near patterned edges [9]. The paths of higher current density are oriented along the $[100]_p$ STO crystal axis which is also parallel to the edge of the Hall bar (FIG. 4.1c). The p subscript indicates the pseudocubic axes of the STO substrate. The growth direction is labeled $[001]_p$. Atomic force microscopy on sample H1 revealed that the STO miscut terraces are not parallel to the current paths. This finding excludes one-dimensional electron gas at steps in the interface as the origin of our observations [14]. We now present images of an "unpatterned" sample, in which current is able to flow throughout the entire sample, which is much larger than any single image. Flux images of areas of unpatterned sample M1 (FIG. 4.2) further reveal the structure of the spatial variation in current density. The main features are thin, resolution-limited paths of enhanced current flow, oriented along $[100]_p$ (FIG. 4.2b), $[010]_p$ (FIG. 4.2a-c), and $[110]_p$ (FIG. 4.2d). We did not observe similar features along any other direction.

We measured seven samples and similar features were observed in six of them (Table 4.2). We also observed a small number of features that are not resolution-limited, some of which are aligned along the crystallographic axes (FIG. 4.2c).

To confirm whether the current density in the narrow paths is higher or lower than the average

Sample	LAO thickness (u.c.)	Direction of enhanced current flow	Aligned with miscut terraces?
H1	10	$[100]_p$	No
H2	5	$[110]_p$, $[1\bar{1}0]_p$	No
H3	15	$[110]_p$, $[1\bar{1}0]_p$	No
H4	10	None.	-
H5	10	$[100]_p$, $[010]_p$	Yes
M1	5	$[100]_p$, $[010]_p$, $[110]_p$	-
M2	10	$[100]_p$	-

Table 4.1: A list of samples in which current was imaged with scanning SQUID. We found features consistent with locally enhanced conductivity along tetragonal domain boundaries in six of seven sample. The direction(s) of the features and their amplitude varied from sample to sample. The features were not consistently aligned with miscut terraces of the STO substrate, as measured with atomic force microscopy.

current density, we considered the geometry of the sample. For the images in FIG. 4.2, we determined the expected direction of current flow based on the position of the contacts and where the image was taken on the sample (FIG. 4.2). The projection of the current flowing in narrow paths onto the expected current direction is parallel, rather than antiparallel, showing that more current is flowing in the paths. Narrow paths of locally higher current density appear in the middle and bottom panels of Figure 2 as red stripes. Our flux images are dominated by sharp features due to current in narrow paths. Slowly varying fields from a 2D sheet current are more difficult to quantify, so from the present data sets on large samples we cannot accurately determine the fraction of the current that flows in the narrow paths in sample M1.

4.2.1 Thermal cycling to reconfigure domain structure

The configuration of current paths depends on the thermal history of the sample. We thermally cycled sample M1 repeatedly (FIG. 4.3a), and AC flux in the sample area was imaged after each cycle at 4 K (FIG. 4.3b-e). Thermal cycling above a temperature of 105 K, under which the structure of bulk STO transitions from cubic to tetragonal [23], resulted in a new pattern of current paths (compare FIG. 4.3b to c, d to e); thermal cycling to a temperature below 105 K did not result in a similar change (compare FIG. 4.3c and 3d). We therefore relate the configuration of the channels to the configuration of STO tetragonal domains. We imaged sample M1 with polarized light microscopy (Methods), which confirmed the existence of a domain structure that is similar in appearance and behaviour on thermal cycling to current paths observed in these unpatterned samples(FIG. 4.3, Sec.

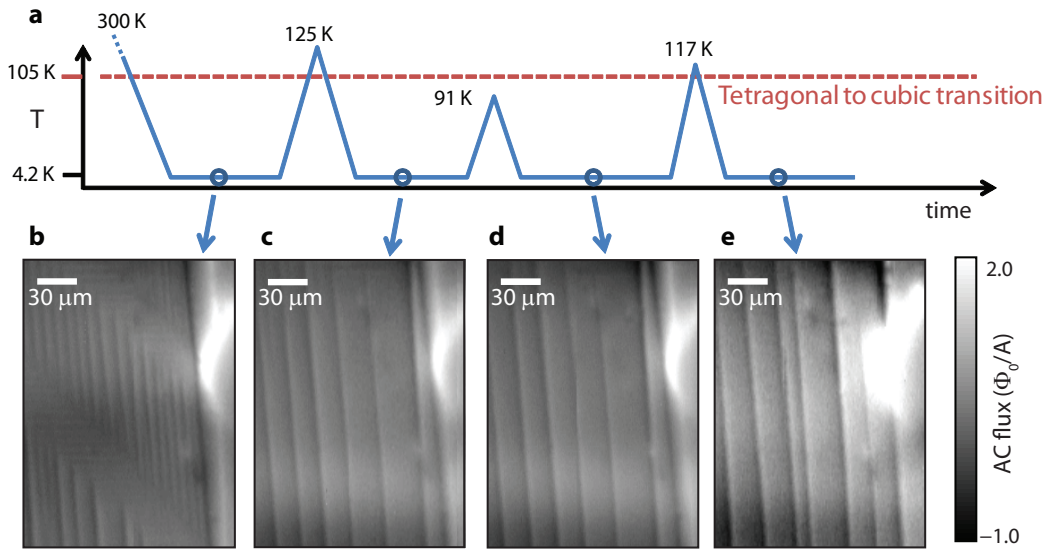

Figure 4.3: **Behaviour of unpatterned LAO/STO on thermal cycling.** a, Thermal history of sample M1 with points indicating when the AC flux was imaged. The same area of sample M1 was scanned after initially cooling down from b, room temperature and after cycling to c, 125 K d, 91 K and e, 117 K. Reconfiguration of the pattern of AC flux due to narrow paths of higher current occurred only when the sample was cycled above the STO transition at 105 K, but not below. Scale bars are 30 μm.

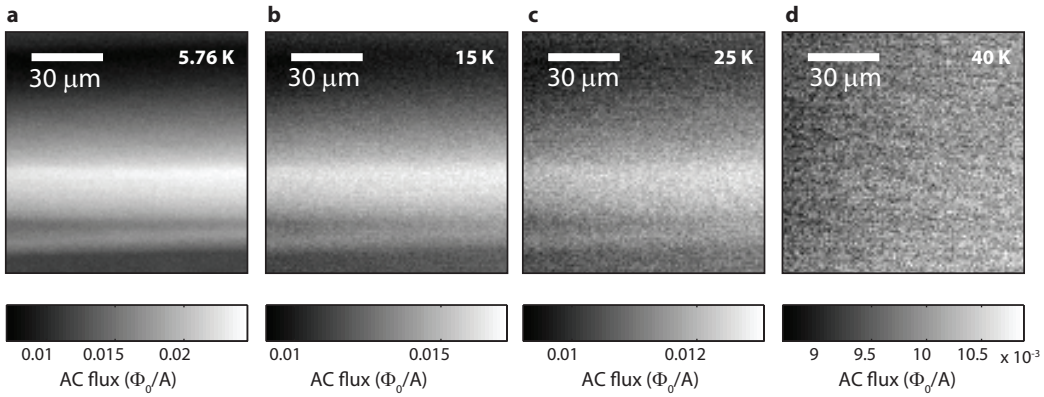

Figure 4.4: **Temperature dependence of LAO/STO features** Scans of AC flux at sample temperatures of a, 5.76 K, b, 15 K, c, 25 K, and d, 40 K. The SQUID was thermally anchored at 4 K while the sample was heated. Scale bars are 30 μm.

4.2.5)

We checked the dependence of the features on both temperature and back gate voltage. In the unpatterned sample M2, we observed structure in the current flow at 5 K similar to the features of the type detected in FIG. 4.1 and 4.2 (FIG. 4.4). The sharp features decayed strongly with temperature, falling beneath the noise level between 40 K and 45 K, indicating that the paths of enhanced conductivity do not exert major influences, if they exist at all, above 40 K. We also investigated normal current flow down to 100 mK in sample H2. Above the superconducting critical temperature, we observed normal current paths oriented along $[110]_p$ and $[1\bar{1}0]_p$. The modulation of the normal current depends on the back gate voltage and disappears below our noise at -100 V in depletion (FIG. 4.5).

It is natural to ask how the spatial patterns in the normal current flow relate to superconductivity. Sample H2 was superconducting with no applied gate voltage at the lowest measured temperature. We measured local diamagnetic susceptibility in sample H2 and detected a small modulation (1% of the total diamagnetic response) with the same orientation and position as the modulations in the normal current flow (See Supplementary Information).

The thermal history dependence of sample M1 (FIG. 4.3) indicated that the observed features are due to the tetragonal structure of STO below 105 K. We expect the domain structure near the interface to be determined predominantly by the STO substrate. The tetragonal transition is driven by the rotation of the TiO6 octahedra about the lengthened axis, labeled as the c-axis [23]. The octahedral rotation angle is 2.1Âř at 4 K, and the sign of the rotation alternates every other octahedron

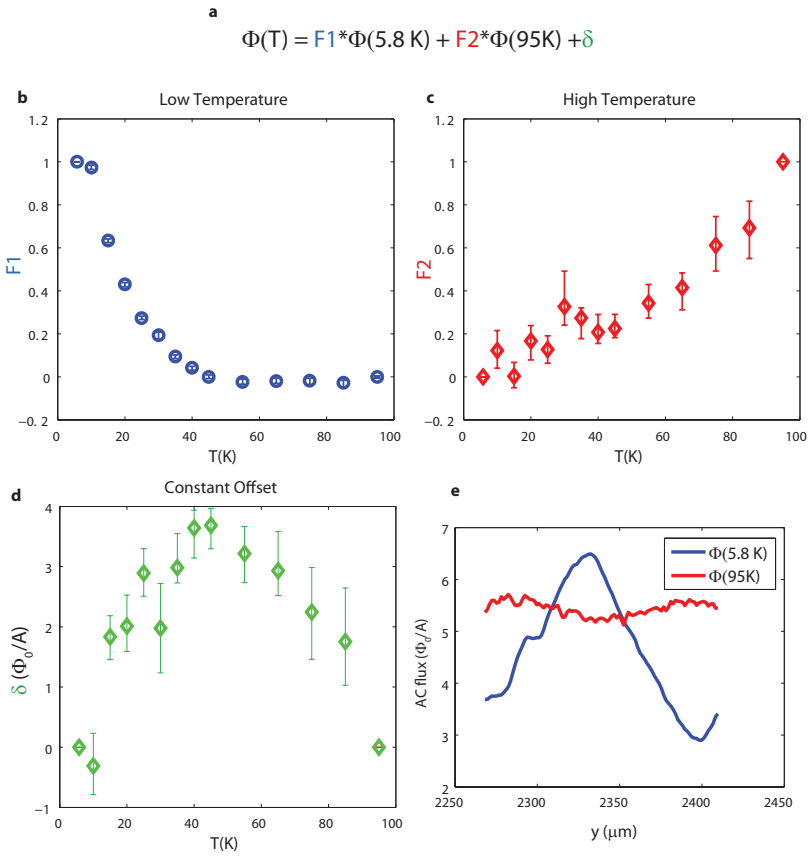

Figure 4.5: **Fitted temperature dependent features of LAO/STO current images** a, Equation used for fitting line cuts of AC Flux images as a function of temperature. b, Low temperature fit parameter (F1) as a function of temperature c, High temperature fit parameter (F2) and d, constant offset (δ) terms of the fit parameters with temperature. e, High and low temperature line cuts used for fitting. Error bars are 95% confidence intervals produced by bootstrapping 1000 times.

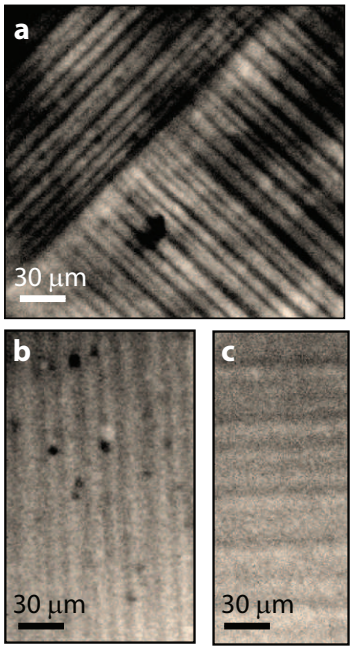

Figure 4.6: **Polarized light microscopy reveals the tetragonal domain structure of LAO/STO.** Polarized light microscopy images of different areas in sample M1 were taken at 20 K a, at near-crossed polarizers and b, c, at near parallel polarizers. We found domains aligned along the crystallographic directions $[100]_p$, $[010]_p$, $[110]_p$, and $[1\bar{1}0]_p$. Scale bars are 30 μm.

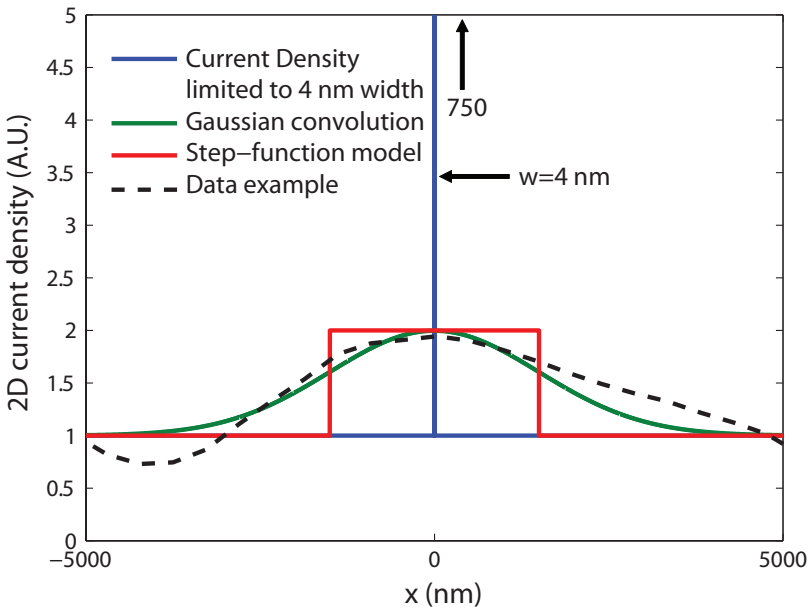

Figure 4.7: **Calculation of current density on narrow features.** The blue line indicates a proposed underlying 2D current density, the effect of the point spread function (example given in black) is roughly replicated by a Gaussian filter with a width of the pickup loop, $3\mu m$ (green). Red data is an approximation of the Gaussian as a step function with the same height and width as the Gaussian distribution, used for the calculation.

in all three directions [107]. Domains with lengthening along all three original cubic axes can form. The four possible twin planes between two tetragonal domains expressed in terms of the original cubic directions are $(110)_p$, $(1\bar{1}0)_p$, $(011)_p$, and $(101)_p$ (FIG. 4.12). Twin boundaries intersect the conducting interface along $[100]_p$, $[010]_p$, $[110]_p$, and $[1\bar{1}0]_p$.

4.2.2 Local conductivity and spatial resolution

The SQUID can determine the total amount of current flowing through a feature, but for resolution-limited features knowledge of the width is need to determine the enhancement in current density and local conductivity. For simplicity in this calculation, we approximate the effect of the SQUID's pickup loop as a Gaussian filter of the initial current density, which gives a broadened current density and roughly reproduces the observed features in FIG. 4.1. We further approximate the effect of the SQUID as a step function with a width of w_{SQUID} ($\approx 3\mu m$) and the same height as the convoluted current density.

Given an observed enhancement of current density on a feature of $j_{observed}$, a background 2D

sheet current of j_{2D}, and the physical width of the feature and SQUID (w_{path} and w_{SQUID}), we find the relationship between the conductivity of the 2D sheet and the conductivity of the narrow path is:

$$\frac{\sigma_{path}}{\sigma_{2D}} \approx \frac{w_{SQUID}}{w_{path}}\left(\frac{j_{observed}}{j_{2D}} - 1\right) \tag{4.1}$$

when $w_{SQUID} \gg w_{path}$. If the features observed in Fig. 4.1 (where we can accurately determine the background 2D current density) are due to single twin boundaries with a width of 4 nm, the enhancement of conductivity on the twin boundary would be roughly 750 times that of the 2D sheet conductivity of the device away from the boundary. A domain with a width of 1 micron would correspond to a local enhancement of conductivity of a factor of 3.

4.2.3 Temperature dependence of current flow

We imaged features similar to those observed in different cooldowns as a function of temperature, and found that the domain-structure-like current density disappeared around 40 K. Four selected scans at different temperatures are shown in FIG. 4.4. The feature mentioned in the main text is strongest at the lowest measured temperature, 5.76 K, and became weaker with temperature until it dissappeared below the noise at 40 K. In order to clearly represent the supression of the domain structure-like feature with temperature, we fit vertical line cuts of all 14 flux images. We fitted the line cuts to a linear combination of a constant offset, the lowest temperature linecut and the highest temperature linecut (FIG. 4.5). The low temperature component (FIG. 4.5 a), which is similar in structure to other features we observed due to tetragonal structure, was strongly suppressed with temperature. The more slowly spatially varying high temperature component (FIG. 4.5b), which we attribute to inhomogeneity in the sample, rises with temperature. The offset(FIG. 4.5 c) is zero at both the low and high temperature points by definition.

4.2.4 Measurements of low-temperature superconductivity and backgate dependence

Sample H2 was imaged using a scanning SQUID in a dilution refrigerator with a nominal base temperature of 20 mK[37] to investigate the superconducting properties of the sample and their relation to the normal current behavior. The sample was superconducting at base temperature with zero applied back gate voltage. The relation between variations in the normal current flow and superconductivity were examined by measuring the diamagnetic susceptibility at base temperature and AC Flux from normal current flow at 300 mK (above the superconducting critical temperature)

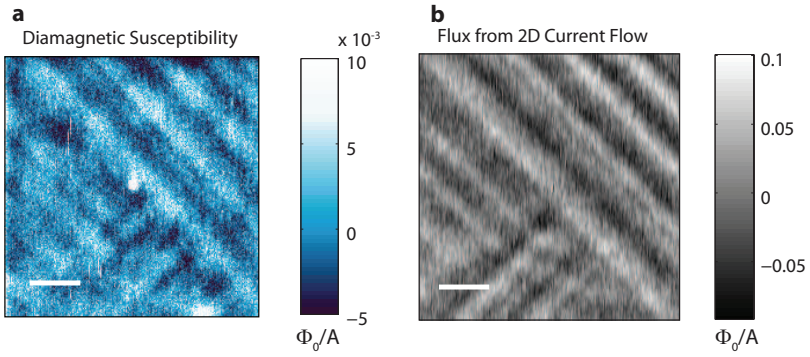

Figure 4.8: **Successive scans of diamagnetic response and normal current.** Scans of a, diamagnetic susceptibility at base temperature and b, normal current flow at 300 mK. A slowly varying background is subtracted from both images to accentuate details. The entire area imaged in a is superconducting. Positive values of diamagnetic response indicate less superconducting regions. Scale bars are 30 μm. 6

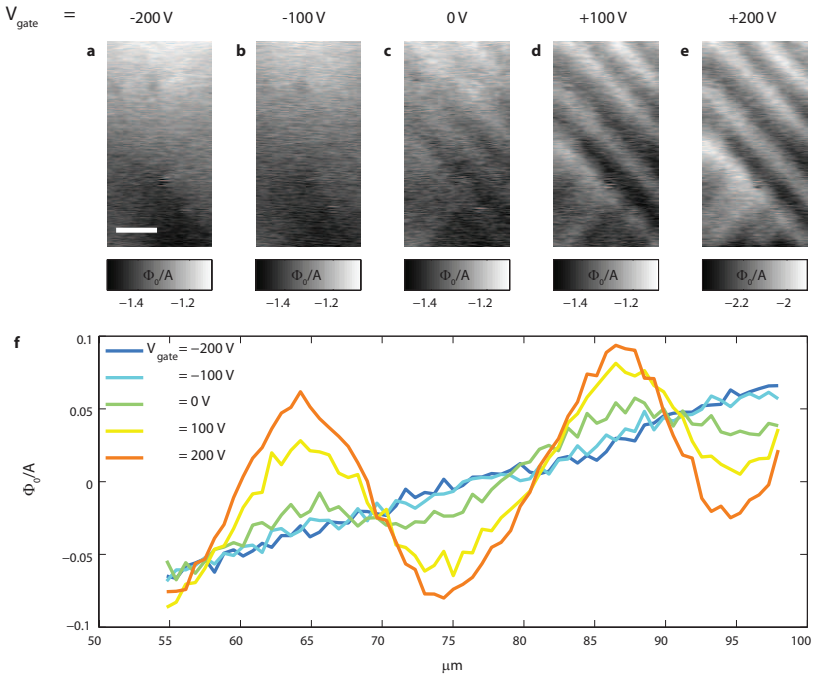

Figure 4.9: **Normal current flowing in paths decreases with decreasing gate voltage.** AC flux images of normal current at V_{BG} = a, -200 V, b, -100 V, c, 0 V, d, 100V. e, Averaged line cuts along the direction of the current paths with an offset subtracted. Scale bars are 30 μm.

in succession (FIG. 4.8). The pattern in diamagnetic susceptibility is recognizably similar to that observed in normal current flow. The magnitude of the variation in diamagnetic susceptibility is of order 1% compared to the total local diamagnetic response of the sample. The strength of this effect in terms of the superfluid density or penetration depth depends on the width of the feature and the SQUID geometry, as in Ref.[56].

The diamagnetic response increased with more positive gate voltage, consistent with what was observed in Ref. [9]. At the lowest gate voltage measured, -200 V, there is no longer detectable superconductivity. Images taken of normal current flow at four different gate voltages of the same area are shown in FIG. 4.9 a-d, and averaged profiles of a section of the images are shown in FIG. 4.9e. The general trend is that of reduced amount of current flowing in paths as the back gate voltage is decreased.

More thorough investigation of the superconductivity's relation to structure near T_c would certainly be warranted given the recent discovery of locally enhanced T_c due to STO's tetragonal domain structure [79]. We have, as of yet, not observed movement of the features in current flow with back gate voltage.

4.2.5 Polarized light microscopy

We investigated the domain structure of sample M1 and H1 using polarized light microscopy. Linearly polarized light is incident on the sample, and a second polarizing filter (analyzer) is used to analyze the reflected light. Polarized light microscopy has been used to investigate domain structure, specifically twin boundaries. We used polarized light microscopy to confirm the orientation and spacing of tetragonal domains in LAO/STO. Domains oriented along $[100]_p$ and $[010]_p$ were observed when the polarizer and analyzer were nearly parallel, and $[110]_p$ and $[1\bar{1}0]_p$ when they were nearly crossed. Their measured widths were comparable to the observed spacing between current paths (FIG. 4.10). The domains disappeared at about 105 K and reappeared with a different configuration after cooling the sample again through the structural transition and imaging the same location in the sample (FIG. 4.11). This finding is consistent with the observed behavior of the narrow paths of enhanced current on thermal cycling (FIG. 4.3).

4.3 Discussion

The directions of the narrow paths are consistent with local conductivity enhanced by twin boundaries. Higher conductivity on narrow domains with lengthening along either $[100]_p$ or $[010]_p$, but

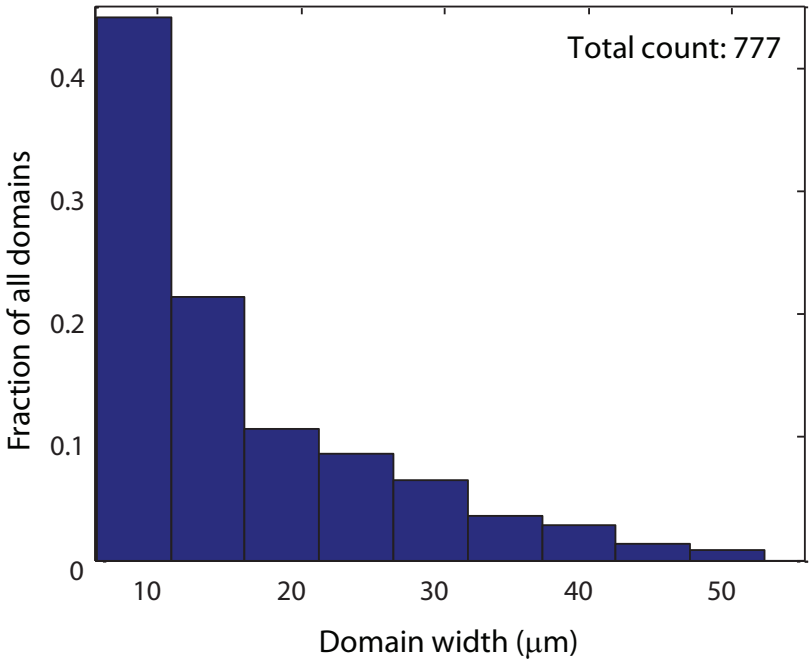

Figure 4.10: **The width of the tetragonal domains observed by polarized light microscopy.** Histogram of the domain widths observed on a 1.5 mm x 1.2 mm region in sample M1. The widths range from 50 Îijm to below our spatial resolution.

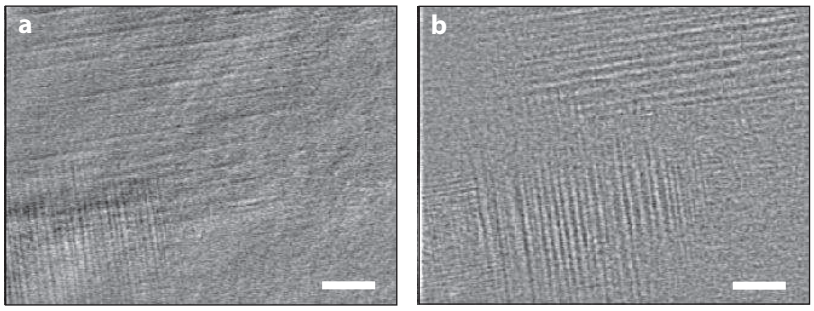

Figure 4.11: **The configuration of tetragonal domains changes after cycling through the structural transition.** Polarized light microscopy images taken at 4.7 K showing $[110]_p$ and $[110]_p$ domains a, before and b, after cycling the temperature to 120 K, above bulk STO's structural transition. Scale bars are 50 μm.

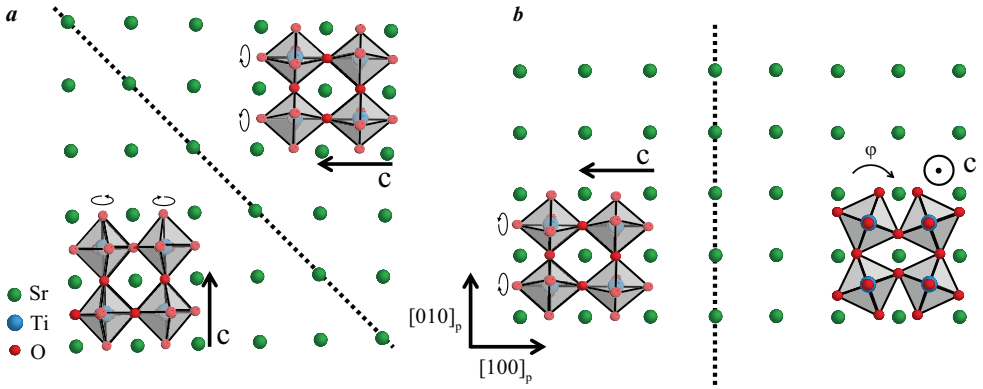

Figure 4.12: **Schematic of twin boundaries in the low-temperature tetragonal phase of STO.** A view of STO domain structure looking along the growth direction, $[001]_p$. The twin planes a, $(110)_p$ and b, $(101)_p$ result in four possible geometries (the two shown here and their rotations by $90\mathrm{deg}$). The twin boundary extends in the growth direction in a while the boundary shown in b extends at approximately 45° to the growth axis. TiO_6 octahedral rotations (circular arrows) along the lengthened c-axis (black arrows) are exaggerated, and the exact structure of TiO_6 octahedra close to the twin boundary and interface will be more complicated.

not both, are also possible scenarios. Higher spatial resolution measurements could distinguish micron-sized domains from domain boundaries. Antiphase boundaries only occur parallel to the primary crystal axes [18] so cannot by themselves explain our observations. A combination of enhanced conduction on boundaries and domains mentioned above may lead to a pattern similar to the one observed. The presence of LAO will most likely affect the tetragonal domain structure near the interface. Because the LAO layer is extremely thin, we do not expect domain structure of the LAO itself to be on a micron-sized length scale. The lattice constant of bulk LAO is slightly smaller than that of STO, so the LAO lattice constant is shortened in the growth direction. In addition, more subtle distortions to both the LAO and STO layers have been observed, including lengthening of the TiO6 octahedra in the first layer of STO[92], buckling between the cations and oxygen in the LAO layers,[83] and octahedral distortion and rotation induced by the LAO in the STO layer[45]. The structural distortion, and therefore polarization of both the LAO and STO are directly linked to the properties of the interfacial conduction [100]. All of these effects may be important to the structure of twin boundaries and tetragonal domains near the interface, and therefore useful for understanding the physical interpretation of our results. We now turn to a discussion of possible origins of the enhanced conductivity. Walls between ferroelectric domains are conducting in other perovskite

systems that are known to be ferroelectric [94, 40], but there is no clear evidence for ferroelectricity in LAO/STO, so we consider different mechanisms. Enhanced domain wall mobility, with similar temperature dependence to the observed features (FIG. 4.4), was attributed to increased polarity of walls at low temperatures[93]. Domain walls in STO are also predicted to be polar with an enhancement of the polarization in the presence of free carriers [73]. For a polarization parallel to the wall and perpendicular to the interface, we would expect an accumulation of charges which could lead to a change in conductivity along the wall which depends on the polarization. We, however, have not observed narrow paths of decreased conductivity which we would naively expect for domain walls with a range of polarization directions. Higher conduction due to tetragonal domain structure indicates a local increase in either mobility or carrier density. The mobility of La-doped SrTiO3 has been shown to be strongly enhanced by strain [44], and the strain due to twin boundaries or tetragonal distortion of the interface may similarly decrease the effective mass. We are unaware of any mechanism by which scattering could decrease by a large amount at a twin boundary or in certain domains. The low-energy twin boundaries in STO are not expected to be charged [18], although an increase in carrier density could come from either increased oxygen vacancy density near the boundary or a change in the twin structure near the interface. Detailed theoretical studies of the change of the domain structure near the interface and the electronic details arising from this change are needed to clarify the origin of the locally enhanced conductivity observed. Factors important for domain formation, such as strain and cooling rate, will also influence the local conductivity, which may manifest itself in transport studies at low temperatures. Anisotropic conductivity and dependence of transport on other direction-dependent tuning parameters, such as an externally applied magnetic field, may also be affected by the presence of enhanced conductivity due to tetragonal domain structure. In addition, the extraction of global physical parameters from transport assuming uniform conduction may have to be modified for samples with a high density of paths of enhanced conduction (e.g. FIG. 4.1). The interplay of interfacial conduction and domain structure adds another level of intricacy to the physical phenomena observed in complex oxide heterostructures. This work emphasizes the ability of small structural changes in the perovskite crystal structure to strongly influence the electronic properties of heterostructures. We have shown that the intersection of domain structure and interfaces can exert effects on the physical properties of the materials system, effects that may not be limited to conductivity in other materials. Accounting for and controlling domain structure may enable the engineering of novel and interesting physical systems.

4.4 Methods

Sample H1 was patterned using an AlOx hard mask. The sample was prepared in a similar manner to Ref.[4]. Atomic force microscope images of the patterned sample H1 showed terraces with an average width of 200 nm, indicating a miscut angle of 0.1 degrees. The sample had a 2 K sheet resistance of 2.45 kΩ, low-field (1 Tesla) Hall sheet carrier density of $3.56x10^{13}cm^{-2}$, and a Hall mobility of 71.5 $cm^2/(Vs)$. Gold contacts were patterned onto samples M1 and M2 using ion etching and filled by sputtering with $\sim$50 nm of Ti and then $\sim$150 nm of Au. LAO was deposited in partial oxygen pressure using pulsed-laser deposition and were post-annealed in a partial pressure of oxygen. Typical mobility and carrier concentrations for samples grown under these conditions are presented in Ref. [4]. Resistance vs. temperature measurements of sample M1 show typical behavior as well as a two-point resistance of 340 ohms at 4.2 K during the SQUID measurement. AFM images of the substrate of sample M1 show terrace widths of on average 200 nm and a miscut angle of 0.1 degrees. Transport data for samples H1 and M1 are provided in supplementary information. We used a scanning SQUID to image magnetic fields from the samples by recording the magnetic flux through a 3-μm pickup loop (FIG. 4.1a) as a function of position[37, 43]. The measured flux is given by $\Phi = \int_S g(x,y)\vec{B}\cdot\vec{da}$ where the integral is taken over the plane of the SQUID, g(x,y) is the point spread function of the pickup loop, and B is the magnetic field produced by the sample. We applied an AC current to the sample and used lock-in techniques to image the flux due to local currents in the sample. Thus, each flux image is a convolution of the SQUID pickup loop and the z component of the magnetic field produced by a current. A current-carrying wire appears as a white stripe next to a dark stripe. To provide more intuitive images, we deconvolved the pickup loop's point spread function from the raw data and inverted the resulting magnetic field to produce a current image, as described elsewhere [81]. The RMS amplitude of the applied current is 15.8 μA in FIG. 4.1c, 147 μA in FIG. 4.2a and 2d, 294 μA in FIG. 4.2b, 2c, and 3. Features typical of those presented in the main text were imaged at several different applied currents, and the features in un-normalized flux images scaled linearly. The frequency of the AC current varied between 600 Hz and 5 kHz. We also imaged local magnetic susceptibility using a field coil on the SQUID chip that is concentric with the pickup loop [43] . Measurements on samples H1, M1, and M2 were made using scanning SQUIDs with a base temperature of 4.2 K. Measurements of superconductivity and normal current in sample H2 were made using a scanning SQUID in a dilution refrigerator [37, 43]. We used a constant flow cryostat with optical access and polarization preserving components for polarized light microscopy. Light was first linearly polarized and was then reflected off the surface

of the sample. The reflected light was analyzed using a second polarizing filter. The contrast in an image was due to spatially dependent rotation of the light's polarization reflected off the sample.

Chapter 5

Images of edge current in HgTe quantum wells

This chapter is in part based on work which was also published in:

"Imaging currents in HgTe quantum wells in the quantum spin Hall regime"

Katja C. Nowack, Eric M. Spanton, Matthias Baenninger, Markus König, John R .Kirtley, Beena Kalisky, Christopher Ames, Philipp Leubner, Christoph Brüne, Hartmut Buhmann, Laurens W. Molenkamp, David Goldhaber-Gordon, Kathryn A. Moler. *Nature Materials* 12, 787-791 (2013)

5.1 Introduction to topological materials

Most phases of matter we discuss in condensed matter physics are defined by which symmetries they break: crystals break translational symmetry, superconductors break U(1) gauge symmetry, etc.. Topological phases exist outside of this paradigm, and are defined by a topological invariant (or invariants), rather than what symmetry they break.

The quantum Hall effect, a strikingly precise quantization of the Hall conductivity of a 2D electron gas in a field, was first observed experimentally by von Klitzing and collaborators [52]. In hindsight, this was the first experimental identification of a topological phase, characterized by a topological invariant (the TKNN invariant or Chern number) which can take any integer value [106, 2]. The Hall conductivity, it turns out, is directly related to the topological invariant which characterizes the state, allowing for unambiguous identification of the value of the Chern number at a given magnetic field and density.

Two important general features of topological invariants are that they can only take on certain

discrete values and that they are well defined only when the system is gapped. Therefore, small (adiabatic) changes to the Hamiltonian cannot change the topological invariant, as long as the system remains gapped. Conversely, any transition which changes the topological invariant of a system must be accompanied by a gap closing.

A topological invariant, ν, which is distinct from the quantum Hall invariant can be written down for time-reversal symmetric, gapped Hamiltonians. This can either take the value of $\nu = 0$ ('trivial') or $\nu = 1$ ('topological') and is sometimes referred to as the $\mathcal{Z}_2$ topological invariant [50]. In an inversion-symmetric system, ν is set by the product of the parity eigenvalues of the occupied bands [42]

$$(-1)^{\nu} = \prod_{a} \xi(\Lambda_a) \tag{5.1}$$

where Λ_a label high symmetry points in k-space for all occupied bands and ξ is the parity operator. The vacuum ordering of bands gives ν = 0 and is labeled as topologically trivial. Using Eqn. 5.1, we can see that one theoretical exercise for generating new possible topological insulators is to find a system which is known to be trivial, and then find a way to 'invert' the order of two of the bands with different parity, which will change ν.

For example, if a p-orbital band with odd parity is initially occupied in the trivial case, and is tuned to switch order with an s-orbital band (even parity) such that the s-band lies below the p-band, ν must change from 0 to 1 if no other bands cross during the process. The concept of 'band inversion' is very commonly used to describe topological transitions of this nature. Later, I will specifically address two different materials where band inversion is predicted, HgTe quantum wells and InAs/GaSb quantum wells.

5.1.1 Experimental observables in 2D topological insulators

The physical manifestation of the topological invariant is less direct in time-reversal protected topological insulators than in the quantum Hall effect, where the invariant is directly measurable via the Hall conductivity. In 2D, it was initially proposed that the spin Hall conductivity would similarly be directly related to the Z2 topological invariant, hence the alternate name "quantum spin Hall effect" (QSHE) for this class of 2D TIs, in analogy to the quantum Hall effect.

Practically, the main driver of band inversion in possibly topological materials is the spin-orbit coupling. The precise quantization of spin Hall conductivity relies on spin being a good quantum number, which is not true in a system with spin-orbit coupling [50]. Therefore, one expects a finite,

but non-quantized spin Hall effect in the QSHE in any real material where spin-orbit coupling is present. Finite spin Hall conductivities exist for a number of non-topological systems, making its observation at best an indirect measure of the topological invariant.

Similar to the quantum Hall effect, the QSHE should exhibit protected edge states with special properties. An intuitive way to understand the presence of edge states is to recall that topological invariants can only change when a system is ungapped. A sample of finite size must have a boundary (an edge in 2D) where it meets either a non-topological insulator or the vacuum. As a function of space, the topological invariant must go from $\nu = 1$ inside the QSHI to $\nu = 0$ in the vacuum, and therefore there must exist a gapless region at the edge of the sample.

The properties of the QSH edge states are equivalent to two copies of the chiral edge states in the quantum Hall effect, one right-moving mode with 'spin'-up and one left-moving mode with 'spin-down. These edge modes are often called 'helical' edge states, because their 'spin' and direction of motion are linked. The edge states can be approximated as linearly-dispersing and live in the band gap (FIG. 5.1)

Although spin is not actually a good quantum number in the edge states, I will refer to their spin-polarization and spin-properties for simplicity.

The edge states are 'protected' in the sense that their existence is guaranteed by the band structure of the material. Their experimental signatures are much more weakly protected. If the edge states are ballistically conducting, their conductivity should be quantized in units of e^2/h per edge, where the resistance is due to quantum contact resistant. Non-local transport should also produce similarly quantized values as predicted by Landauer-Buttiker formalism [15].

Ballistic conduction of QSH edges is only possible in the absence of backscattering. Conduction along the edge is protected against single-particle elastic backscattering, but not from other sources of backscattering [86]. The spin-structure of the edge means that any resistance-producing scattering must be accompanied by a spin flip. Such scattering cannot occur for single-particle elastic processes when time-reversal symmetry is not broken. If only such processes are present, the edge states should be ballistically conducting.

However, inelastic, multi-particle, and magnetic scattering can all destroy ballistic conduction in QSH edge states. I will discuss these scenarios in detail in the context of our results on InAs/GaSb quantum wells.

The most easily accessible experimental signature of the QSHE are transport through the edge channels. The conductivity of the edges, however, is not directly linked to the topological invariant and can be modified by scattering. In the absence of any number of allowed scattering processes, the

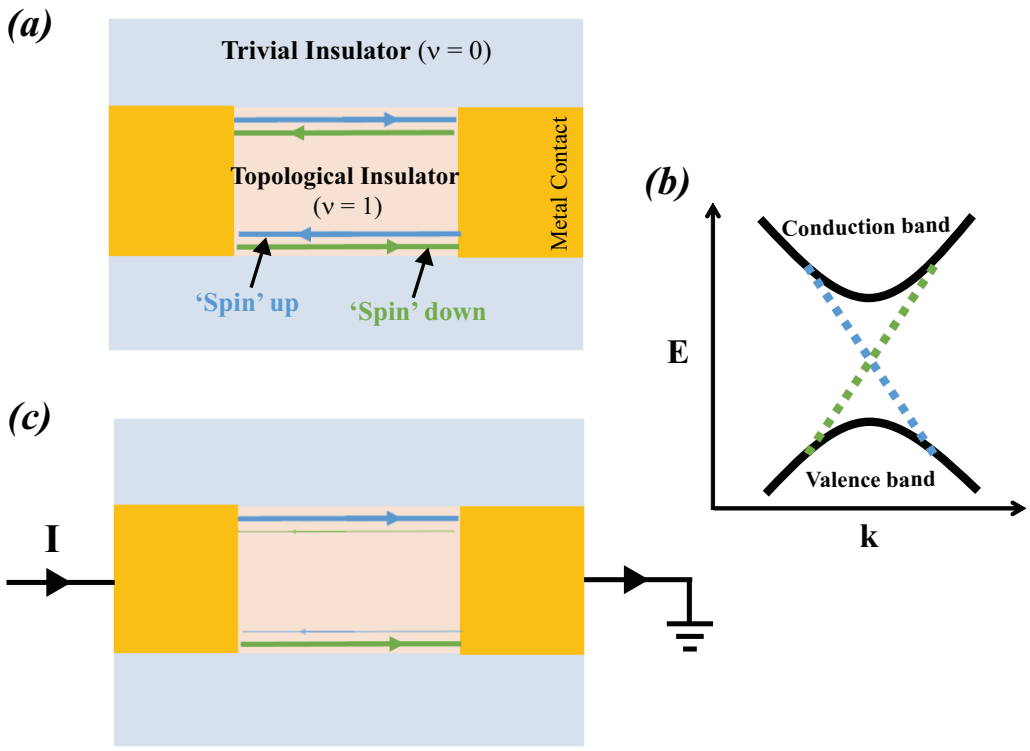

Figure 5.1: **Schematic of edge states in a 2D time-reversal protected topological insulator** (a) A schematic of a quantum spin Hall insulator device. The change in the topological invariant (ν) across the edge of the sample leads to gapless edge states. The 'helical' edge states have a 'spin'-up right moving mode and a spin-'down' left moving mode on the top edge. (b) A schematic band structure for a QSHI. The edge states can be approximated as linearly dispersing, and the +k and -k modes at a given energy have opposite 'spin'. (c) A simple schematic for experimental detection of the edge states through charge transport. A charge current leads to a net 'spin' polarization on the edge of the sample, which would lead to a quantized spin Hall conductance in the absence of spin-orbit coupling.

edge states should produce characteristically quantized non-local transport signatures and exhibit a finite spin Hall conductivity. The quantization of longitudinal and non-local conductivity of the edge states is *only* guaranteed by mesoscopic physics, rather than any fundamental link to topological invariants, as in the Hall conductivity in the quantum Hall effect.

5.2 Theoretical prediction of QSHE in HgTe quantum wells

The quantum spin Hall effect was first predicted to occur in graphene [49], however the predicted band gap was to be too small to observe experimentally.

The first experimentally viable prediction of the quantum spin Hall effect was in HgTe/CdTe quantum wells [8]. HgTe quantum wells consist of a small thickness (d) of HgTe sandwiched between barrier layers (semiconductors with a sizeable gap) which are either $CdTe$ or $Hg_{1-x}Cd_xTe$.

Bulk HgTe has strong intrinsic spin-orbit coupling which leads to an inversion of the Γ_6 (s-type) and Γ_8 (p-type) bands from the normal ordering (e.g. the ordering in CdTe). Bulk HgTe is actually a semimetal in the bulk, but when it is strained by the barrier material, an energy gap is opened.

The 2D band structure (subband structure) of the quantum well can be intuited by inspecting the band edge diagram (FIG. 5.2a). The bulk band edges can be thought of as potential wells, and the subbands as the ground state energy in those wells. If the bulk band structure is unchanged, tuning the thickness changes the confining potential and can shift the relative energies of subbands up or down, depending on whether they are electron or hole-like.

For a thin quantum well, the lowest occupied s-type subband lies above the lowest occupied p-type subband (FIG. 5.2a). The confinement energy of the quantum well has restored the normal ordering of bands ('non-inverted') and therefore the quantum well should be a trivial insulator sans QSH edge states (FIG. 5.2b).

For thicker HgTe quantum wells, the p-type and s-type subbands swap order and the quantum well's subband structure becomes 'inverted' (FIG. 5.2c). In an inverted quantum well, linearly-dispersing QSH edge states should exist in the energy gap (FIG. 5.2d).

Luckily, group II-IV semiconductors were already a subject of some research due to their applications in infrared detection, and first experimental results on HgTe quantum wells followed shortly after their theoretical prediction [59].

I will postpone discussion of transport work done by our collaborators until section 5.6, where I will discuss it in combination with our work and its implications on the topological nature of edge states in HgTe quantum wells.

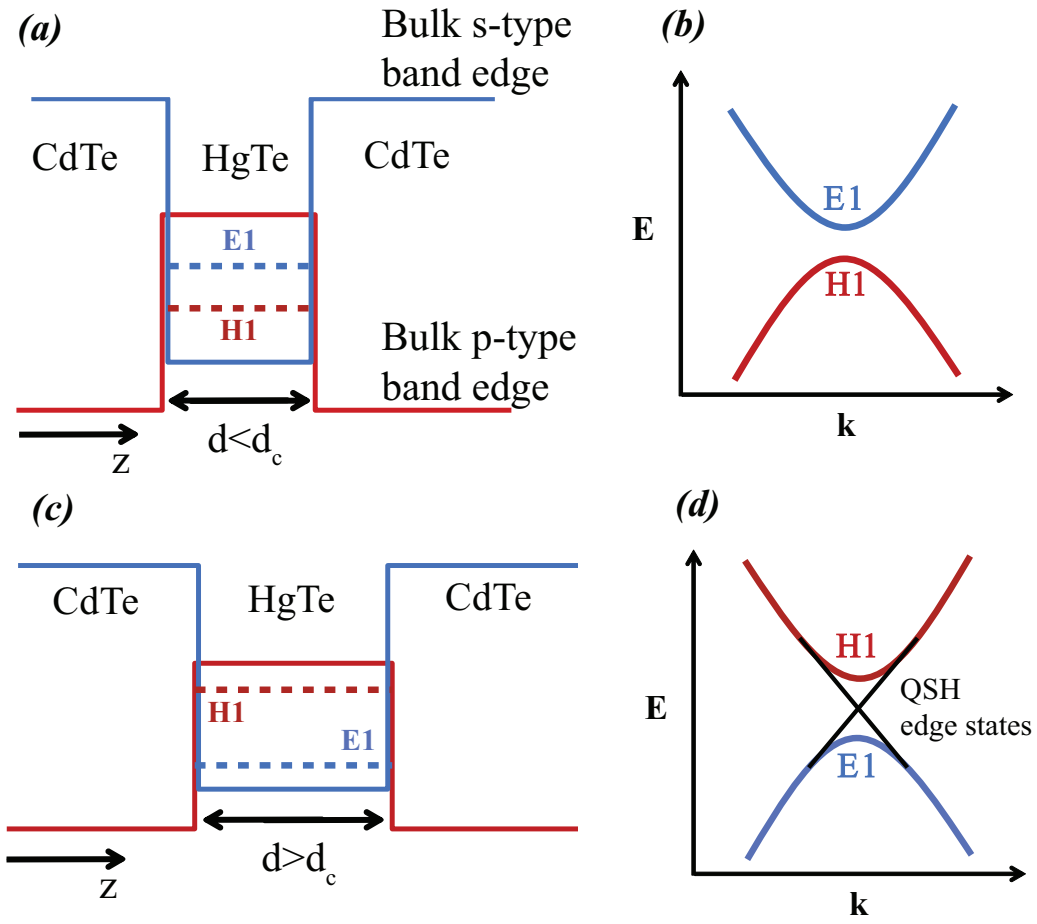

Figure 5.2: **Schematic of band diagram for HgTe quantum wells** (a) A band edge diagram for non-inverted HgTe. The bulk band edges of HgTe and CdTe are shown in solid lines. Spin-orbit coupling causes an inversion of the bulk bands with respect to the trivial insulator CdTe. In a narrow quantum well (thickness less than the critical thickness d_c, the 2D subbands (represented by dashed lines) restore the trivial ordering of bands because of confinement. (b) Schematic of the low-energy band structure of a non-inverted HgTe quantum well. The band ordering is trivial, so there are no QSH edge states in the gap. (c) Band diagram for a quantum well with thickness larger than the critical thickness. Confinement is a small enough effect that the inverted order of subbands (dashed lines) is present. (d)Schematic of the low-energy band structure of an inverted HgTe quantum well. QSH edge states are predicted to exist for this type of device (black lines).

5.3 Scanning SQUID of Inverted HgTe quantum wells

Using scanning SQUID microscopy, we imaged 2D current in multi-terminal devices fabricated from HgTe quantum wells. We utilized techniques described in chapter 3. to obtain the 2D current density from individual flux images.

We measured two inverted quantum wells ($d > 6.3nm$) and one non-inverted quantum well ($d < 6.3$ nm). The nominal thicknesses, and layer orders are shown in Fig. 5.3. The lattice constant of the barrier layers, which is tuned by the relative concentration of Hg and Cd should shift the critical thickness for band inversion. Additionally, the type of doping (or whether there is doping) in the surrounding layers will affect the disorder landscape. Layer orders are presented in FIG. 5.3

A schematic of the devices we measured are shown in 5.4. We tuned the Fermi energy (E_F) of the device using a voltage applied to a metal top gate (V_{TG}) which covered a portion of the device (FIG. 5.4), which allowed us to the device from n-type conduction (in the conduction band) through the energy gap, where QSH edge states should live, and then to the p-type conduction regime (E_F in the valence band).

In order to leave enough room for the SQUID to image, we only wire-bonded to the top contacts of the device, allowing only for two-terminal resistance measurements (FIG. 5.4). Additionally, the devices (and specifically the length of the edges of the device) are larger than the device size normally probed by transport measurements [59] in order to accommodate the SQUID's spatial resolution. The device sizes are given in FIG. 5.4.

As a function of gate voltage, we found a peak in the two-terminal resistance for both inverted devices (FIG. 5.4 and 5.8. The peaked resistance trace indicates that we are tuning through the energy gap, and because the peak occured at negative V_{TG} the devices must be slightly electron-doped in the absence of an applied V_{TG}.

The height of the resistance peak is much higher than is expected for ballistic transport through edge states in this configuration. We used Landauer-Buttiker formalism [15] to calculate the expected ballistic two-terminal resistance and assumed the contacts act as a phase-randomizing scatterers. We found that the expected resistance in this two-terminal configuration should be $5/6h/e^2$ (21.5 $k\Omega$). The height of the resistance peak (≈ 200 $k\Omega$ for devices H2 and H3) indicates that, if the transport is through quantum spin Hall edges, backscattering is destroying ballistic transport. In the limit where scatterers backscatter an electron with 50% probability, this corresponds to a scattering length (l_ϕ) of a couple of μm.

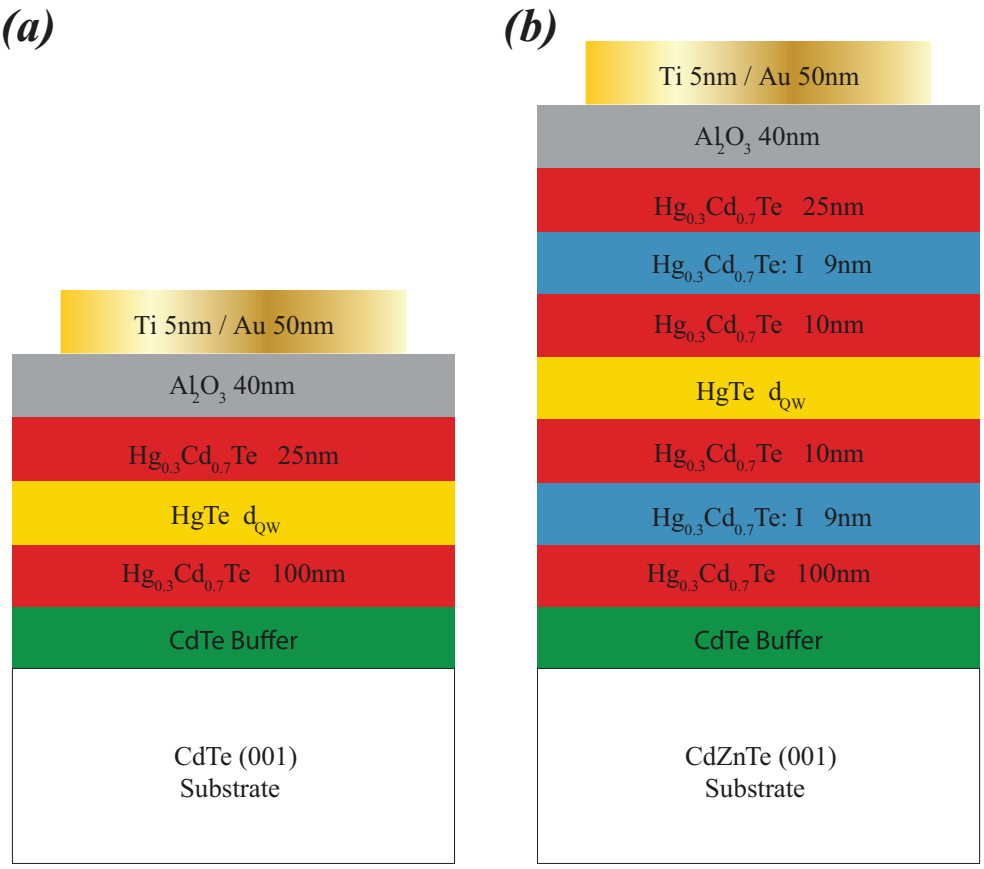

Figure 5.3: **Layer order for measured HgTe devices. (Adapted from REF. [81])** (a) Layer order for H2 and H3, the second inverted device (FIG. 5.8) and the non-inverted device (FIG. 5.12). Their quantum well thicknesses are d_{QW} = 8.5 nm and 5 nm, respectively.(a) he first inverted device (FIG. 5.6). d_{QW} for the first device is 6.6 nm.

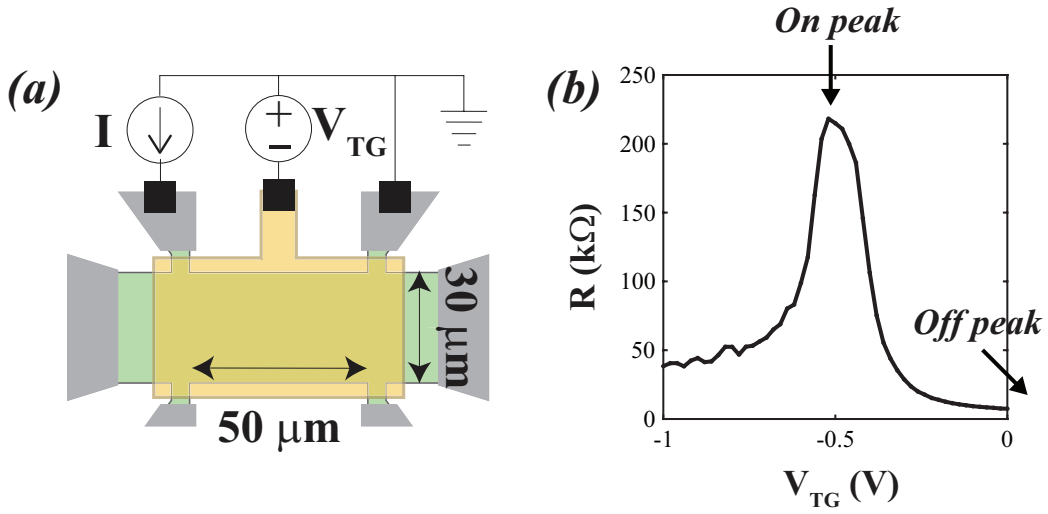

Figure 5.4: **Schematic of the measured HgTe device and two-terminal resistance in the inverted regime.** (a) A schematic of the lithographically defined device design measured in this chapter. The mesa was etched through the quantum well except in the device region (green). A dielectric and metal top gate (gold) were then added to the device in order to tune the Fermi level (E_F). The two 'top' metal contacts (gray) were used to measure two-terminal resistance (R) and flow current for imaging. (b) The two-terminal resistance of sample H1 as a function of applied top gate voltage (V_{TG}). The resistance peak at $V_{TG} \sim -0.5V$ indicates that the devices is being tuned through it's energy gap

5.4 Current density images of inverted devices

We imaged current in both of the inverted devices and found that current flowed primarily along the edges of the device when V_{TG} was tuned to the resistance peak, and homogeneously through the bulk of the device when V_{TG} was tuned far away from the peak (deep in the hole or electron-like conduction regimes).

The flux data of device H1 (sans any image processing) already shows edge conduction in the energy gap (FIG. 5.5). In the n-type regime, the flux image varies smoothly across the bulk of the device, and looks more or less like a homogeneous strip of current (FIG. 5.5 a).

When the device was tuned to it's resistance peak, the qualitative features of flux image changed significantly. Two positive/negative pairs of lines appear which trace out the edges of the device 5.5 b). These features are consistent with wires of current flowing along the edges of the sample, rather than homogeneous current flow through the bulk.

The reconstructed current density images match the qualitative features gleaned from the flux images(FIG. 5.6). In the n-type and p-type regimes, the current flows from the top contacts and spreads out relatively homogeneously through the width of the device (FIG. 5.6a). On the resistance peak, the current flows primarily along the top edge of the device, where it is much more spatially confined than images in less-resistive regimes (FIG. 5.6b). In addition to the top edge, a small amount of current flows along the bottom edge.

There are two features of note in the current flowing along the bottom edge of the device. First, the current flow pattern traces the small voltage probes of the device, showing that the current is really hugging the edges of the device. The current continues flowing along the edge of the device until it reaches the contacts, where is can cross over to the other edge of the device (FIG. 5.6b).

Secondly, the amount of current flowing along the bottom edge of the device is much smaller in magnitude than the top edge (a schemtic of the explanation of the current density is presented in 5.6d). The longer path length and higher number of metallic contacts interrupting the bottom edge should both explain the lower amount of current along the bottom edge.

All of the features observed in device H1 were reproduced in a second device (H2) at T$= 4$ K (FIG. 5.8). The edges are not straight due to piezoelectric bender distortion.

5.4.1 Gate and temperature dependence of edge conduction in HgTe

We measured the dependence of the current density images on gate voltage and temperature and found that the edge states persist for a wide range of gate voltages and up to a temperature of 20

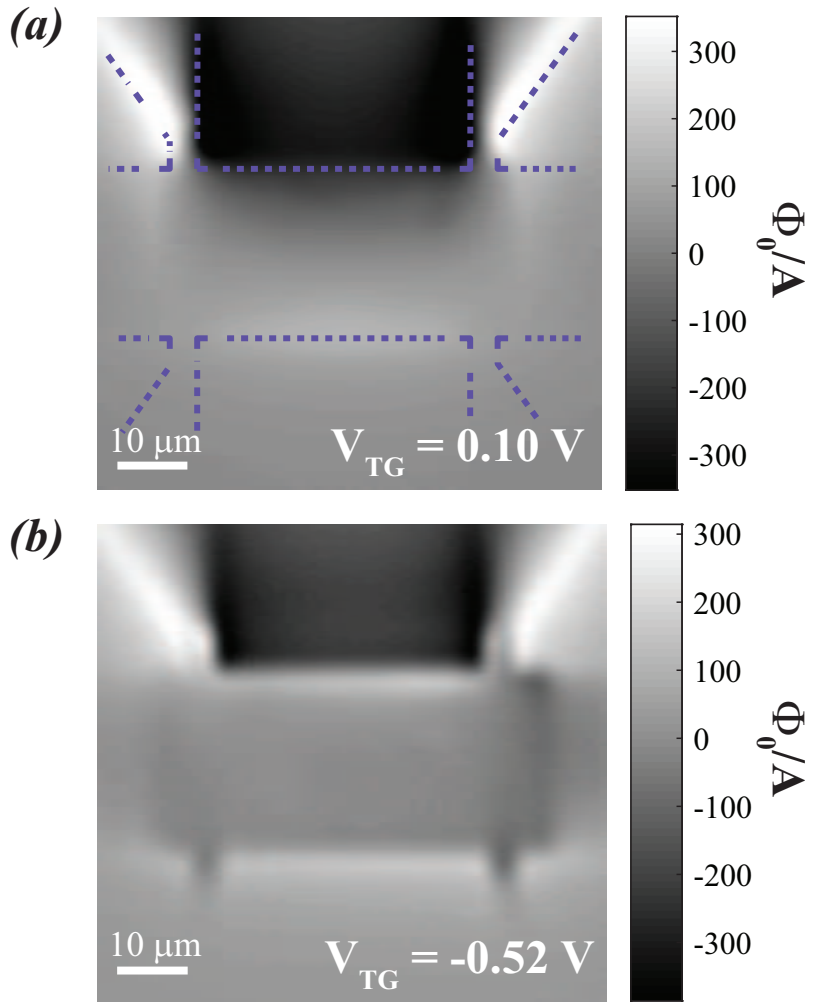

Figure 5.5: **Images of flux due to an applied current in an inverted HgTe quantum well (H1)** (a) Flux through the SQUID's pickup loop far away from the resistance peak. The approximate location and size of the device are indicated by the purple dashed lines. Current is applied from the top left contact to the top right contact. (b) Flux image taken at V_{TG} where the device's resistance was maximized. This image was taken at T $\sim 3K$.

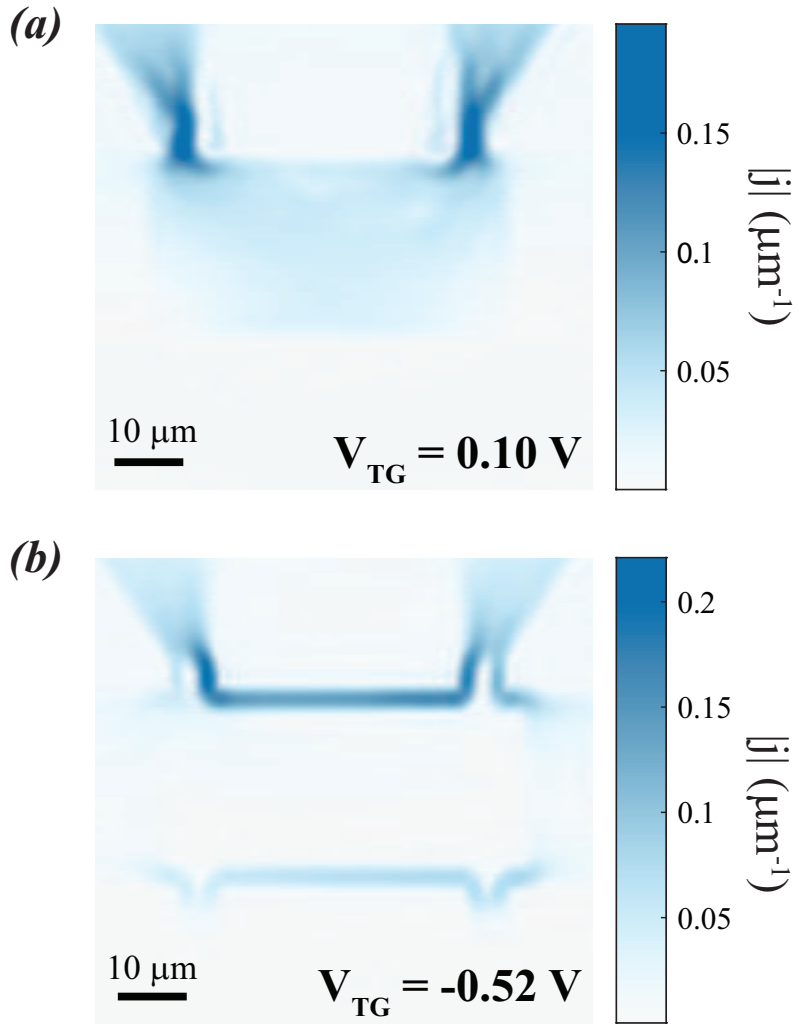

Figure 5.6: **Images of current density in an inverted HgTe quantum well.** Images of current density extracted directly from the data in FIG. 5.5 taken on device H1. (a) Image of the magnitude of the 2D current density ($|j|$) far from the resistance peak. The current spreads out from the top leads and flows homogeneously through the bulk of the device. (b) Current density image at the resistance peak, showing current flows primarily along the top edge (and to a lesser extent the bottom edge) of the device.

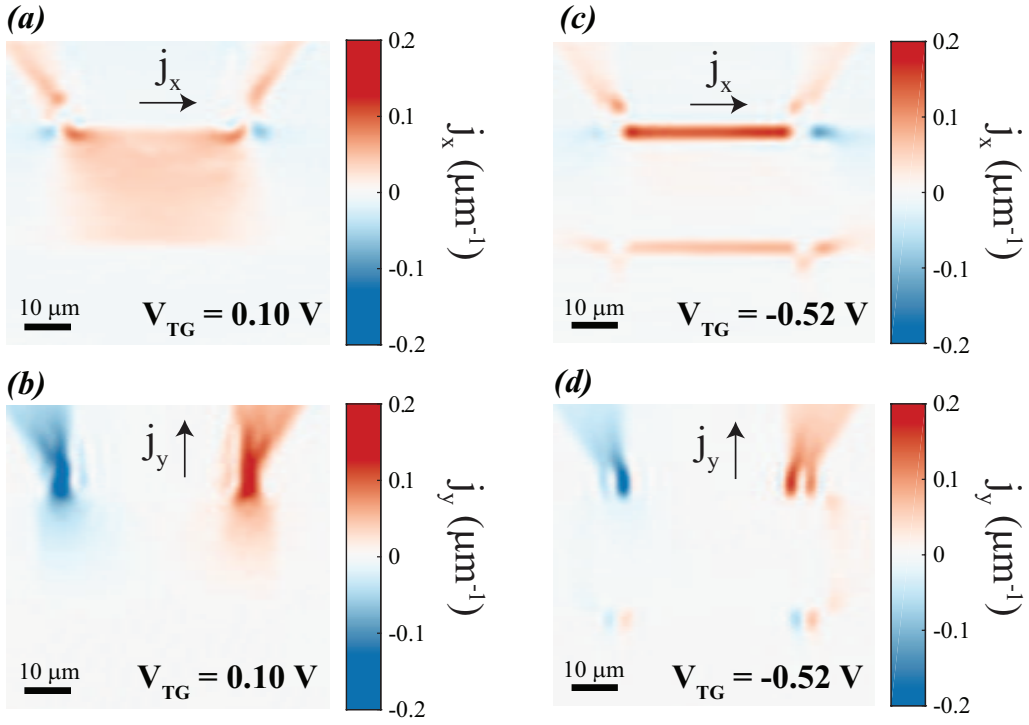

Figure 5.7: **Images of j_x and j_y in an inverted HgTe quantum well** We also obtain directional information from current inversions, I have chosen to omit this information for simplicity. Current is always conserved locally in the extracted current density. (a,b) Extracted current density along the horizontal and vertical directions of the device far from the resistance peak. (c,d) Extracted current density along the horizontal and vertical directions of the device on the resistance peak.

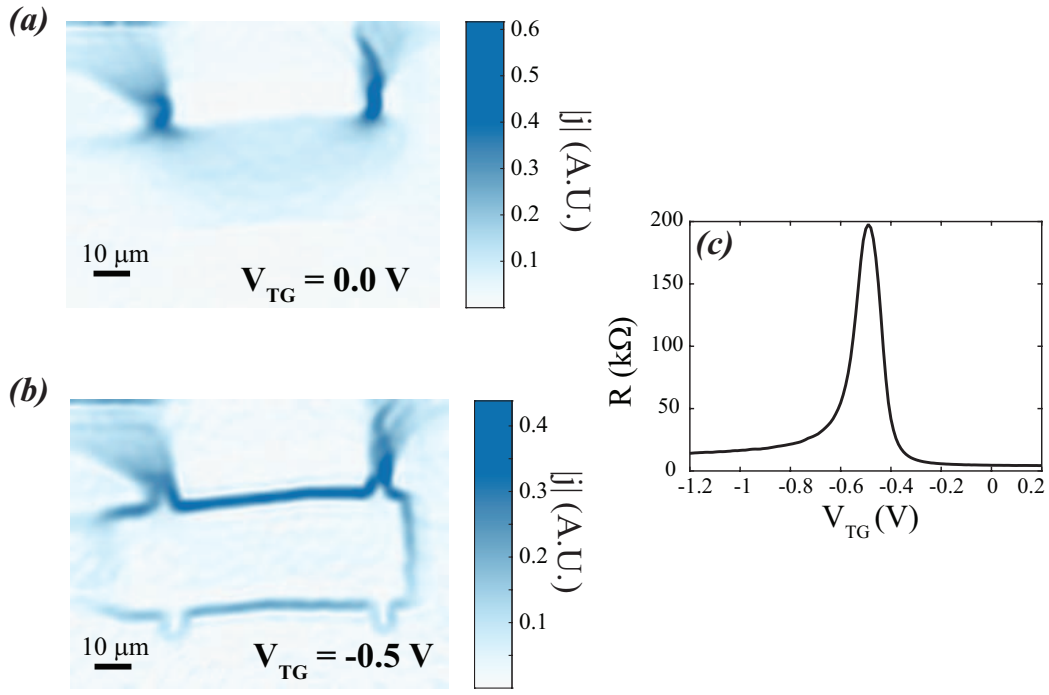

Figure 5.8: **Images of current density in a second inverted HgTe quantum well** Images of current density extracted directly from raw flux data taken on device H2, a second inverted HgTe quantum well. The images are distorted due to an unknown issue with our piezo positioners in this particular experiment. Images were taken at liquid Helium temperatures ($\sim$ 4 K). (a) Image of the magnitude of the 2D current density ($|j|$) far from the resistance peak. The current spreads out from the top leads and flows homogeneously through the bulk of the device. (b) Current density image at the resistance peak, showing current flows primarily along the top edge and bottom edges of the device. (c) Two-terminal resistance as a function of V_{TG}, showing very similar behavior to the first sample (H1).

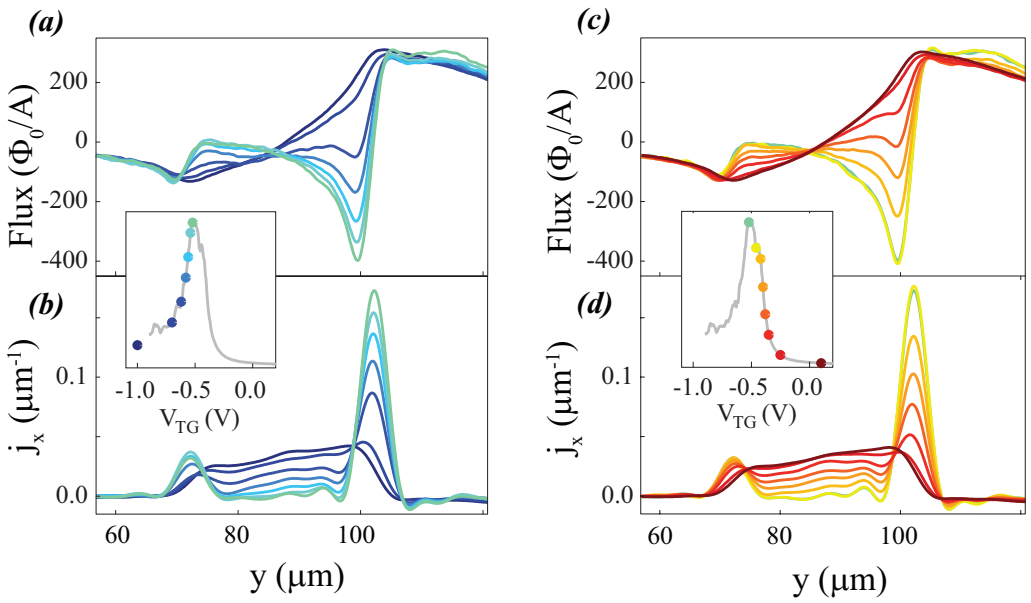

Figure 5.9: **Flux and current density profiles as a function of gate voltage** (a) Measured vertical flux profiles across the center of device H1 as a function of V_{TG} on the left (a) and right (c) sides of the resistance peak.). (b) The measured resistance of the sample as a function of temperature. The gate voltage was fixed as the temperature w

K. The effective resistance of the edges (extracted from a combination of fitting current line cuts and transport measurements) remains constant for a large range of gate voltages and at all measured temperatures.

We imaged current in device H1 as a function of applied top gate voltage (V_{TG}). Vertical profiles of flux and current density show a continuous evolution between bulk-dominated current at low resistances and edge-dominated current near the resistance peak 5.9. This can be seen most easily in j_x (FIG. 5.9 b,d), where near the resistance peak, the current is dominated by two peaks, one high amplitude peak on the top edge and one smaller peak on the bottom edge. As the gate voltage was tuned away from the resistance peak, the height of the peaks fall and j_x in the middle of the device rises, indicating that some current was being carried by bulk states.

We more quantitatively analyzed the current as a function of V_{TG} by fitting j_x profiles (FIG. 5.10). For this data set, we used experimentally obtained j_x at the resistance peak to define what edge-dominated transport looked like and j_x far from the resistance peak to define the expected j_x profile for bulk-dominated transport (FIG. 5.10 b). In order to separate the top and bottom edge, we truncated the edge profile halfway in the middle of the sample to isolate the top edge, and set the

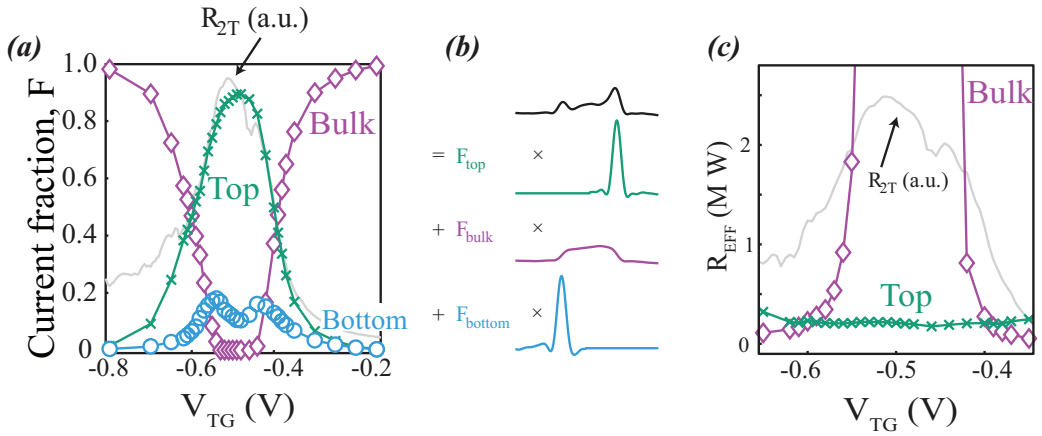

Figure 5.10: **Flux and current density profiles as a function of gate voltage** (a) Measured vertical flux profiles across the center of device H1 as a function of V_{TG} on the left (a) and right (c) sides of the resistance peak.). (b) The measured resistance of the sample as a function of temperature. The gate voltage was fixed as the temperature was swept.

rest of the profile to zero. In order to generate the bottom edge fitting profile, the top edge profile was translated vertically to be centered at the bottom edge.

The results of fitting to the top edge, bottom edge, and bulk j_x profiles (normalized correctly) to the experimental curve gives the fraction of current (F) flowing in each channel.

$$j_x^{experimental}(y) = F_{top} * j_{top}(y) + F_{bottom} * j_{bottom}(y) + F_{bulk} * j_{bulk}(y) \tag{5.2}$$

where $F_{top} + F_{bottom} + F_{bulk} = 1$. At the resistance peak, $/sim90\%$ of current was flowing in the top edge while the remaining current flowed in the bottom edge. As the sample became less resistive, the amount of current flowing in the top edge decreased while the bulk current increased.

F_{bottom} has two maxima away from the resistance peak (FIG. 5.10 a), which can be explained by more closely examining the path that current takes before entering the bottom edge. The sample is contacted from the top, so in order for current to flow to the bottom edge in the absence of bulk conductivity it must flow along a length of edge outside of the contacts, cross into the n-type contacts and then re-enter the bottom edge. When the bulk becomes more conducting, the current can bypass the outside length of edge at the top of the sample by shorting through the bulk to the bottom edge. It is possible that this path allowed more current to flow in the bottom edge at intermediate gate voltages.

We modeled the device as three parallel resistors (top edge, bottom edge, and bulk) and used

the extracted current fraction and the measured resistance of the sample to extract the effective resistance (R_{EFF}) of each channel, given by $R_{EFF} = R_{2T}/F$. The results of this analysis are plotted for the top edge in FIG.5.10 c. We omitted the bottom edge, as R_{EFF} extracted takes into account the entire path that current flows, which changes significantly as a function of gate voltage for the bottom edge. Therefore, the extracted R_{EFF} of the bottom edge probes a combination of the bulk and bottom edge's resistance, the proportion of which changes as a function of V_{TG}.

R_{EFF} was constant as a function of V_{TG} for a wide range of bulk conductivities. The absence of a gate voltage dependence of the edge's resistance indicates that the edge's properties may be decoupled from the presence of either conducting electrons or holes.

In device H2, we performed similar analysis of the current fraction and R_{EFF} as a function of temperature while staying on the resistance peak (FIG. 5.11). We measured flux profiles over the center of device H2 and averaged them heavily, in order to overcome temperature induced noise in the SQUID (5.11). We fitted the raw flux profiles since we did not have full flux images to reconstruct the current.

At low temperatures (blue solid line in 5.11 a), the flux exhibited two peaks positioned at the edges, indicating current was flowing in two wires along the top and bottom edges. The flux profile is comparable to what was observed at the resistance peak in device H1 (see FIG. 5.9 a), except with a higher amplitude feature (more current flowing) at the bottom edge.

As the temperature was increased, the peaks decreased in size and the flux profile becomes more broad, indicated that more current was homogeneously flowing through the bulk. However, the high temperature flux profile (red curve in FIG. 5.11) never fully resembles the 'off peak' flux profiles observed as a function of gate voltage(FIG. 5.9 a) which indicates that current was still flowing along the edges of the device at 20 K.

The current fractions (F) obtained by fits to flux profiles (described in Ch 3) replicate the qualitative assessment made from flux profiles (FIG. 5.11 c). At $T = 4.5$ K, the bottom and top edges both carried $\sim 40\%$ of the total current, while the bulk carried $\sim 10\%$. This differs from the current fractions obtained on device H1 at $T = 3$ K, where the top edge carried the majority of the current and the bulk was fully insulating. The difference in bulk current may be attributed to the difference in temperature in addition to the difference of substrates between device H1 and H2 (FIG. 5.3), which may tune the band gap of the quantum well. The difference in the top and bottom edges can partially be explained by the bulk shorting some length of the bottom edge's path, as mentioned previously, but a difference in the disorder along one of the edges is probably also necessary to account for the discrepancy.

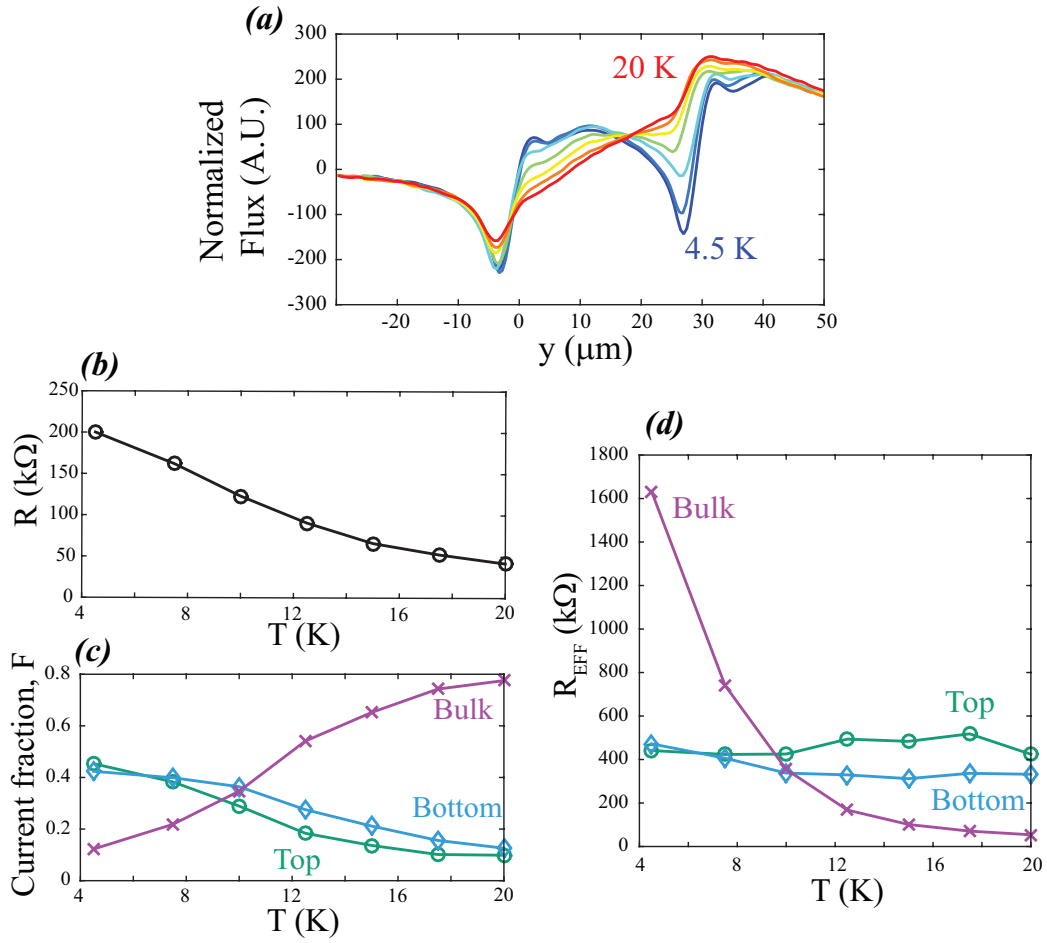

Figure 5.11: **Flux profiles and effective resistance (R_{EFF}) as a function of temperature** (a) Measured vertical flux profiles across the center of device H2 as a function of temperature from 4.5 K (blue) to 20 K (red). (b) The measured resistance of the sample as a function of temperature. The gate voltage was fixed as the temperature was ramped. Separate measurements sweeping the gate voltage at each temperature showed that the resistance peak did not shift significantly as a function of gate voltage. (c) The fitted. fraction of current (f) flowing in the top edge, bottom edge, and through the bulk, as a function of temperature. (d) The effective resistance (R_{EFF}, see text) of the top and bottom edges, and the bulk of the sample. The effective resistance of the bulk drops strongly with temperature as T gets the same size as the energy gap, while the effective resistance of the edge states is relatively temperature independent.

As the temperature was raised, the fraction of current flowing along the edges decreased monotonically while the bulk rose to carry $\sim 80\%$ of the current by 20 K. We used the current fraction (FIG. 5.3 c) and the measured two-terminal resistance (FIG. 5.3 b) to extract R_{EFF} of each channel as a function of temperature. We found that the effective resistance of the top and bottom edges both depended only weakly on temperature, while R_{EFF} of the bulk fell sharply with temperature, as expected for a narrow band gap semiconductor.

5.5 Current images of non-inverted HgTe quantum wells

We also imaged current in a thin quantum well (device H3) which is predicted to be a trivial insulator. At 4 K, the sample went completely insulating (R $> 10^9\Omega$) at negative applied V_{TG} (FIG. 5.12 a).

We were unable to flow current through an actual insulator, but we did investigate the regions in which we were able to flow a current. We imaged current on the sides of the resitance peak and we found no clear evidence of edge states which were as conducting as those imaged in inverted devices (FIG. 5.12 b-e). In replotting this data as current density instead of flux (as it was presented in [81]) for my thesis, I've noticed what might look like very weak edge conduction in FIG. 5.12 d, but it is hard to distinguish from possible effects from the positioning of the contacts and the apparent height difference between the images in (b,c) and (d,e), and possible Fourier effects from the current inversion process.

From these images, we can put a rough limit of $< 10\%$ current flowing along the edge of the device, which puts a limit of $R_{edge} > 5M\Omega$ for edge states in this non-inverted sample. More strict limits on edge conduction in non-inverted samples could be obtained by performing measurements of averaged line cuts (such as those performed for FIG. 5.11), better calibration of the height above the sample, and a strip-like geometry which allows for more uniform injection of current into the device. I believe improved data would be useful in putting bounds on trivial conducting edge states in HgTe quantum wells near band edges. From the insulating behavior of the sample, it is already clear that far in the gap no conducting edge states exist.

5.5.1 Possibility of n-type high-resistance edge states in non-inverted devices

The measurements presented in FIG. 5.12 rules out edge conduction which is similar in conductivity to the observed edge channels in inverted samples. We, however, did not look carefully for much more resistive edge channels. In re-analyzing images of non-inverted HgTe for my thesis, there are

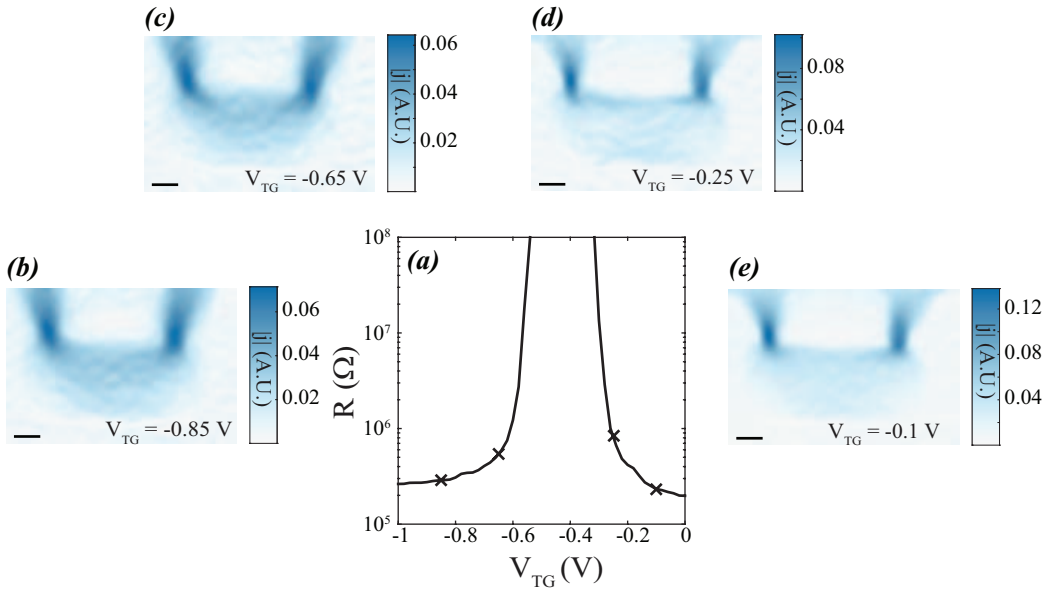

Figure 5.12: **Current images of a non-inverted HgTe quantum well.** Images of current density extracted directly from raw flux data taken on device H3, a non-inverted HgTe quantum well. Images were taken at liquid helium temperatures ($\sim$ 4 K). (a) Two-terminal resistance as a function of V_{TG}, showing strongly insulating behavior ($R > G\Omega$) at the resistance peak. We could not flow current in the insulating regime, so we imaged along the flanks of the resistance peak to check for trivial edge conduction. (b-e) Images of the magnitude of the 2D current density ($|j|$) on the sides of the resistance peak at the indicated V_{TG}. All images show primarily bulk-like current flow, putting approximate lower limits on the resistance of trivial edge states near the band edge (see text).

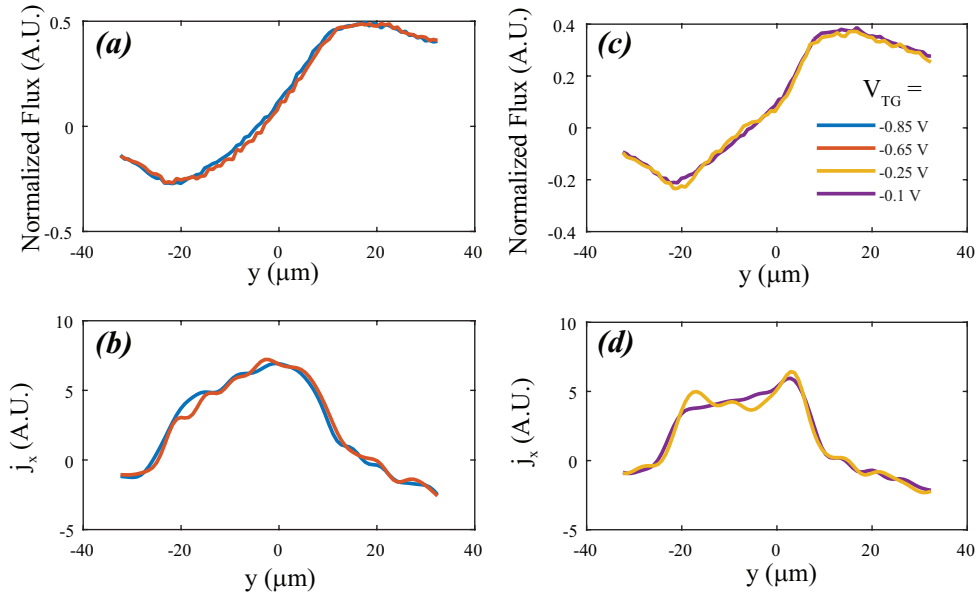

Figure 5.13: **Line cuts of flux and j_x in a non-inverted HgTe device.** Line cuts of flux (a,c) and current density (b,d) taken vertically across the center of device H3, a non-inverted HgTe quantum well. (a,b) Flux and current line cuts showing on the p-doped side of the resistance peak. No indications of enhanced current along the edges are observed in line cuts (c,d) Flux and current line cuts showing on the n-doped side of the resistance peak. At $V_{TG} = -0.25$ V in yellow, slightly enhanced conduction may be present along the edges of the device. If the subtle effect is real, the edge states' resistance would be $\sim 10M\Omega$, much more resistive that the edge states observed in inverted devices of the same size.

some indications of a slight enhancement of current along the edges of the device on the n-side of the resistance peak (FIG. 5.13).

The resistance of the sample at $V_{TG} = -0.25$ V , where a slight enhancement of current on the edges was possibly present , was $\sim M\Omega$. Because the enhancement is so weak, the resistance of these possible n-type trivial edge channels should be at least an order of magnitude higher than the sample's overall resistance. This data is not good enough to firmly establish the existence of n-type trivial edge channels for sure, but my hope in including this data is to encourage further study of the effect.

I believe that similar features may have also been observed in microwave impedance microscopy (MIMS) of non-inverted HgTe devices [70]. In particular, MIMS images near the insulating region on the n-doped side look edge-like, while the p-side images do not (FIG. 2e from REF. [70]).

Both scanning SQUID and MIMS have seen (what I think could be) subtle features which are possible observations of high-resistance n-type edge trivial edge states. If these edge states

do indeed exist, they cannot by themselves explain the observed edge conduction in the inverted regime, due to their very different conduction properties. However, their existence could provide additional scattering mechanisms to the edge states observed in the inverted regime.

5.6 Are the edge states in HgTe topological?

5.6.1 Overview of previous transport works

Here I will briefly review other works on HgTe quantum wells, including previous transport works by our collaborators as well as other scanning probe experiments performed at Stanford.

Transport experiments rely on the expected protection from elastic backscattering in order to observe a quantized conductivity per uninterrupted edge of e^2/h. Additionally, large metallic contacts should act as phase randomizers, which leads to a transmission probability of 0.5 through a contact. Therefore, the conductivity of a ballistic mode with a single contact in interrupting the edge should have a conductivity of $e^2/2h$. Using these rules, one can construct the expected ('quantized') 4-terminal resistances of a device based only on the positions of the contacts and not on the length of the edges.

Electrical transport measurements were performed very shortly after the theoretical prediction of the quantum spin Hall state, investigating the measured 4-terminal resistances in standard Hall Bar devices and so-called 'h-bar' devices meant to probe the non-local resistances [59, 89].

In samples with lateral dimensions of a couple microns, close to quantized resistance of $h/2e^2$ (fluctuating by $\sim 4k\Omega$) was observed in inverted quantum wells. In larger inverted devices, more resistive transport was observed, and in non-inverted devices true insulating behavior was observed [59].

In slightly different multi-terminal geometries, close to quantized 'non-local' four-terminal resistances were also observed [89]. The presence of sizable non-local resistances is clear evidence of edge transport and an insulating bulk.

The alternative scenario to quantum spin Hall edges are trivial edge states, whose conduction properties accidentally give conductivity close to the expected quantized value. This is possible if there are N trivial edge modes which have $\sim 1/N$ transmission. Is the current experimental evidence inconsistent with trivial edge states which produce accidental quantization in small samples? I believe the answer is that current experimental results do not decisively rule out this possibility.

The specific alternative scenario is that there are edge states with a resistance per unit length (ρ) which is close to $\frac{h/e^2}{l_{edge}}$ where l_{edge} is the length of the edge in a device. Because ρ could in principle

depend on disorder in the wafer or other growth or patterning conditions, it could vary from sample to sample. Additionally, the edges could in principle have resistance which scales non-linearly with length.

First transport works on 'local' resistances show that samples with lateral dimensions of 1 μm display close to quantized resistance ($\sim h/2e^2$), and samples with a lateral dimension of 10 μm show a non-quantized resistance ($\sim 10h/3e^2$) [59]. These two results are consistent with an edge with a resistance per unit length of h/e^2 per 1 μm.

The non-local results are also not wildly inconsistent with trivial edge states, although they are better fit by the quantum spin Hall picture. The length of edges of the devices measured are similar enough that the expected non-local resistances for trivial edge states can roughly match the measured values (FIG. 3 from Ref. [89]) within $\sim 20\%$ if the resistance per unit length is somewhat fine-tuned to h/e^2 per 2 μm. Additional contact resistance in the two-terminal measurements would make the trivial edge state scenario look more like the experimental data.

A more comprehensive study of different contact configurations and devices with very different lengths would more clearly differentiate the transport between trivial and topological edges. Specifically, different permutations of topologically equivalent measurements (e.g. $R_{13,54} to R_{24,65}$) should give the same answer in the QSH case, while the answer should differ in the trivial case. This data is not presented in Ref. [89].

More in depth transport work could go a long way to more firmly establishing quantization. A series of devices from the same wafer with different edge lengths showing that the quantization survives for different device sizes would go a long way to establishing the quantization on more solid ground. If the edge states are trivial, the resistance of such devices should be able to pass through the quantized value for small enough devices.

Shorting through the bulk, for example, could obscure such results. If the quantization is destroyed at slightly smaller sizes by bulk conductivity, and at slightly larger sizes by scattering in the edges, the experimental situation is unfortunately just as well explained by trivial edge states which can take values both below and above the quantized values. Given the imperfect quantization, such studies should be considered necessary to firmly establish the quantum spin Hall state (in the absence of other evidence).

5.6.2 Scanning SQUID discussion

Our scanning SQUID work establishes three experimental observations which were not necessarily apparent from transport measurements.

1. In two inverted devices, the edge states conducted throughout the energy gap, even when bulk carriers were thermally excited. In the more extensively measured device, the edge states' resistance was weakly varying for a large range of gate voltages. (FIG. 5.10).

2. In an inverted device, the temperature dependence of the resistance of the edges was weak (FIG. 5.11).

3. In a non-inverted device, there were no conducting edge states near the band edge with a resistance similar to those observed in inverted devices (FIG. 5.12).

Items 1 rules out some class of trivial edge states which arise from band bending. A large asymmetry in the edge states' resistance between the n-doped and p-doped regimes, if it existed, could have indicated that the edge states were due to a large amount of band-bending originating near the conduction or valence bands. Because the resistance is fairly constant, this means that if the edge states are due to trivial band bending, the amount of band bending must exceed the size of the energy gap.

Additionally, the non-observation of highly conducting channels on the sides of the truly insulating gap in a non-inverted sample constrains possible band bending scenarios (Item 3). Specifically, it shows that if band bending originating from either of the band edges exists in both samples, their conduction must be strongly tuned by the width of the quantum well.

The temperature dependence of the edge state current (Item 2), however, is not obviously consistent with quantum spin Hall edges. The high resistance of the edge modes indicates that backscattering mechanisms occur in the edge state. A wide variety of backscattering mechanism which are not single-particle elastic mechanisms are allowed, but generically they lead to strong temperature dependences, which we do not observe (e.g. Refs. [101, 91, 62, 24]) (for a more detailed discussion, see the next chapter on InAs/GaSb 6). Generally speaking, temperature-independent scattering mechanisms tend to be elastic and therefore not allowed in quantum spin Hall edges [86]. Scattering due to disorder-formed charge puddles with an odd number of electrons leads to a weak temperature dependence which is consistent with our results[109, 108].

5.6.3 Other scanning probe results

Two other relevant scanning probe experiments were performed at Stanford around the same time as our scanning SQUID experiment which I'd like to briefly highlight [57, 70].

Scanning gate microscopy studied the effect of a locally applied electric field to the edge of an inverted HgTe quantum well [57]. A tip-induced local electric field is shown to induce increased

resistance when the tip is some distance away from localized regions along the edge, indicating localized scattering centers along the edge which can be tuned by an electric field. The charge puddle picture, one explanation for weak temperature dependence of the resistance of the edge states, could produce such a signature in scanning gate microscopy [109, 108].

In one of the scanning gate images, the conductance of the edge is completely suppressed. This is surprising, because the maximum decrease for a quantum spin Hall edge would naively be a reduction by a factor of two (the case where the scanning gate induces a large metallic n-type region along the edge). Although a full suppression of edge conduction is not allowed for QSH edge states, it is perfectly allowed for trivial edge states, in which band bending could be undone by a local potential. This behavior was only observed in one region of one sample, so further study is certainly warranted to fully understand and characterize full suppression of edge conductivity.

The scanning gate results point out the utility of local gating in establishing the robustness of the edge states. In principle, transport measurements involving local gating (either scanning gate tip, finger gates, or a side gate along the whole edge) would all provide relevant evidence to discriminate between QSH edge states and trivial edge states, which should have different responses to locally applied electric fields.

Another scanning technique, microwave impedance microscopy (MIMS) probes the local conductivity of a sample using a tip as a waveguide for microwaves. They also observe edge conductivity consistent with SQUID measurements, but they also are able to measure in high magnetic fields [70]. They find that edge conduction is present to high magnetic fields, far above where quantum spin Hall edge states should exist. The presence of edge states at high fields, if they are indeed connected to the low field edge states, hints at the possibility of a trivial edge state explanation.

In conclusion, experimental evidence from transport and other scanning techniques paint a complicated picture of edge conduction in HgTe quantum wells. The presented transport evidence [59, 89] is, in my opinion, not strictly inconsistent with trivial edge states.. Scanning gate [57] and MIM [70] measurements are consistent with scanning SQUID and transport at low fields, however each measurement has details which are not consistent with a simple QSH picture. Scanning SQUID studies of edge conduction in one non-inverted device and two inverted devices as a function of gate show that if band bending is at play, the properties of band bending edge states must be tuned strongly by thickness. Additionally, the weak temperature dependence of the edge states up to temperatures of order the energy gap favors either the charge puddle explanation for scattering in a QSH edge, or elastic scattering if the edges are trivial.

5.7 Persistent Currents in HgTe antidots

Measuring persistent currents in HgTe antidots could elucidate the properties of the edge channels in inverted HgTe in a non-transport measurement. A hole (more precisely, an antidot, because the hole does not completely pierce the substrate) drilled through a 2D topological insulator should host helical edge states on the edge of the hole (FIG. 5.14a). The edge's wavefunction must remain single-valued, so the wavenumber can only take values such that the wave function fits an integer number of periods around the ring. The momentum spacing between adjacent states for a ring of circumference L will be $\Delta k = 2\pi/L$ (FIG. 5.14 b). For linearly-dispersing edge states, the spacing in energy would then be $\Delta E = hv_F/L$.

Rings of metal which are small enough can exhibit persistent currents, currents which flow without an applied voltage, even without the presence of superconductivity [16]. A similar effect should occur in the geometry outlined here, a finite current should flow around the ring for a magnetic flux applied through a QSH antidot. The cartoon picture is that left moving and right moving states move up and down in energy with an applied flux (FIG. 5.14).

Although the edge states are in equilibrium, the expectation value is for a finite current to flow around the ring. The maximum current flowing around a single QSH edge is that of a single electron at the Fermi velocity, v_F. Therefore the amplitude of the persistent current could be as high as $I_{max} = ev_F/L$ which is 16 nA for a HgTe antidot with a circumference of 5 μm. The current can be reduced by scattering which disrupts phase coherence and will be periodic in the non-superconducting flux quantum ($\Phi = h/e$).

Scanning SQUID is a uniquely suited tool for this measurement, as has been demonstrated by our group's past measurement of diffusive persistent currents in gold rings [11]. The size of the signal in those measurements was at least an order of magnitude smaller than the predicted signal size for ballistic persistent currents in HgTe antidots.

Persistent currents represent a measure of the phase coherence of electrons around the edge of the antidot, and could help in determining the true nature of edge states in HgTe. We have not been successful in observing a persistent current in HgTe antidots, but I will describe the progress we have made in hopes of informing future measurements.

5.7.1 Experimental considerations

The size of antidot which we can measure is limited on both the small and large sizes. For small antidots, although the current flowing around the ring is enhanced as the circumference is decreased

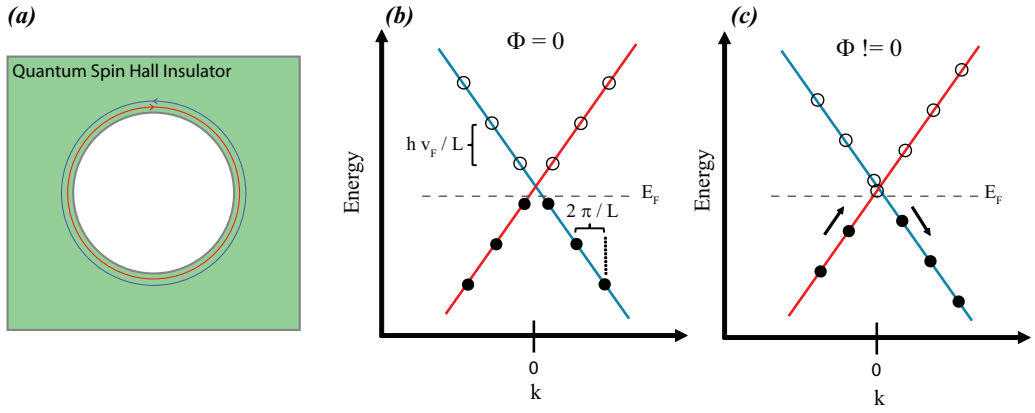

Figure 5.14: **Schematic of persistent current measurement in HgTe antidots** (a) A hole (or 'antidot') in a QSHI will host a helical edge channel on its edge which forms a closed loop. (b) When the edge channels are confined to a ring around the edge of the antidot, the energy levels become discrete with a spacing of $k = 2\pi/L$ where L is the circumference of the antidot. For linearly dispersing edge channels, the energy spacing between levels is hv_F/L. (c) When a magnetic flux is threaded through the ring, right moving modes (red) shift in one direction while left moving modes (blue) shift in the opposite direction.

($I_{max} = ev_F/L$), the overall measurable magnetic signal decreases with size, $M \sim I_{PC}L^2 \propto L$. On the larger side, the persistent current will be reduced by scattering in the edge state, which occurs on a length scale of a couple microns [59]. Additionally, the SQUID's pickup loop and field coil need to be well matched to the antidot size in order to effectively apply magnetic flux through the loop to observe multiple periods of the persistent current and to get good signal to noise. Antidots which would safely put the edges in the ballistic regime $L \sim 1\mu m$ are hard to fabricate and would require very small SQUIDs to effectively measure.

These considerations led us to attempt to measure persistent currents with next generation IBM SQUIDs with smaller features, although they are still not optimally matched to the ideal antidot size. The noise of the IBM SQUID's is comparable to previous generations, but non-linear (and non-static in time) backgrounds with an applied field coil current ultimately make this measurement somewhat beyond our grasp for the time being.

A second consideration is how to find the antidots in a SQUID measurements. Superconducting markers or current carrying wires can be used as coarse navigation, but centering over the antidot is difficult using features which are a distance away from the antidot. In measurements of persistent currents in Au rings, unexpected paramagnetism in the Au lead to a measurable signal which allowed for centering of the SQUID's pickup loop over the ring [11].

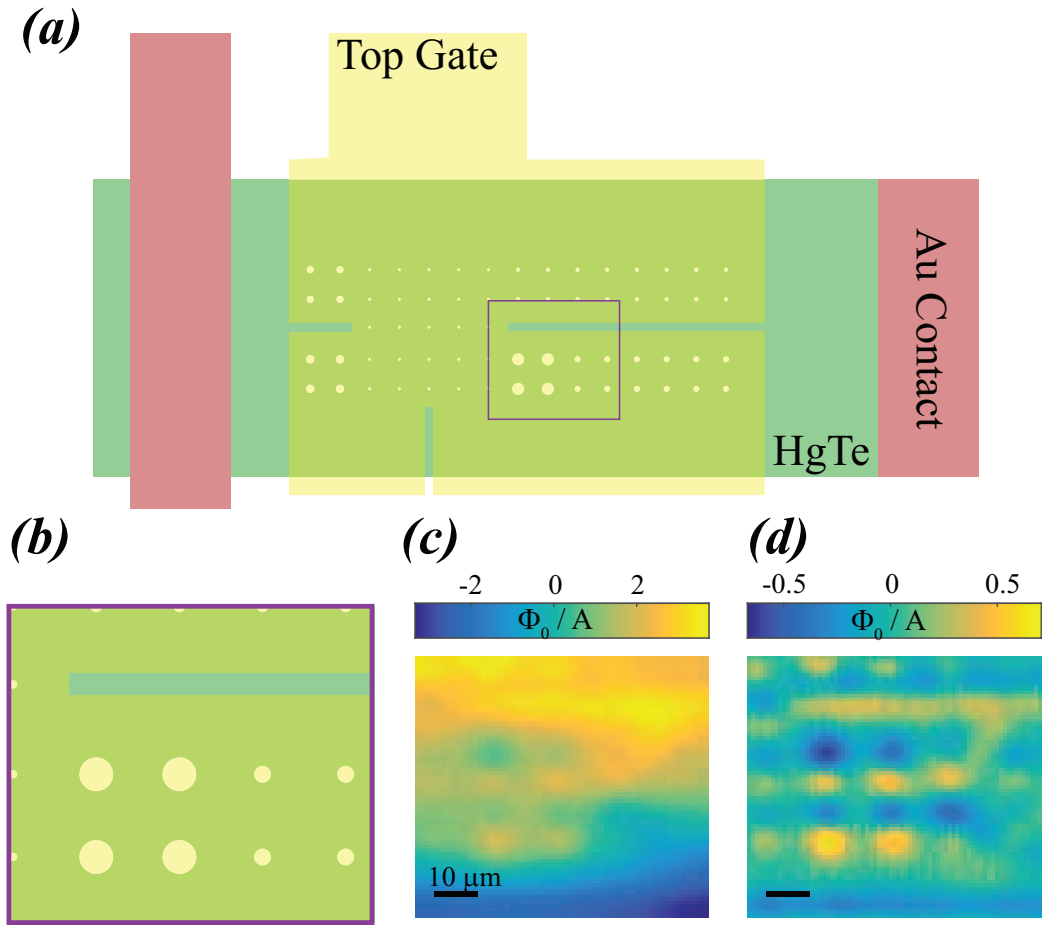

Figure 5.15: **Schematic of sample design and navigation by current imaging** (a) A schematic of the sample design, which is a large HgTe Hall bar with arrays of antidots with various widths patterned into it. A top gate and ohmic contacts allow us to tune the Fermi energy into the gap as well as monitor the overall resistance of the sample. (b) Zoomed in version, showing features in the top gate for navigation as well as approximate antidot configuration. (c) A raw flux image of current flowing between the Au contacts at $V_{TG} = 0$ V. Dipole-like features indicate a hole in the current flow pattern. $5\mu A$ r.m.s. was flowed to produce this image. (d) Flux data from (c) with a Gaussian filtered image subtracted to accentuate the features due to antidots.

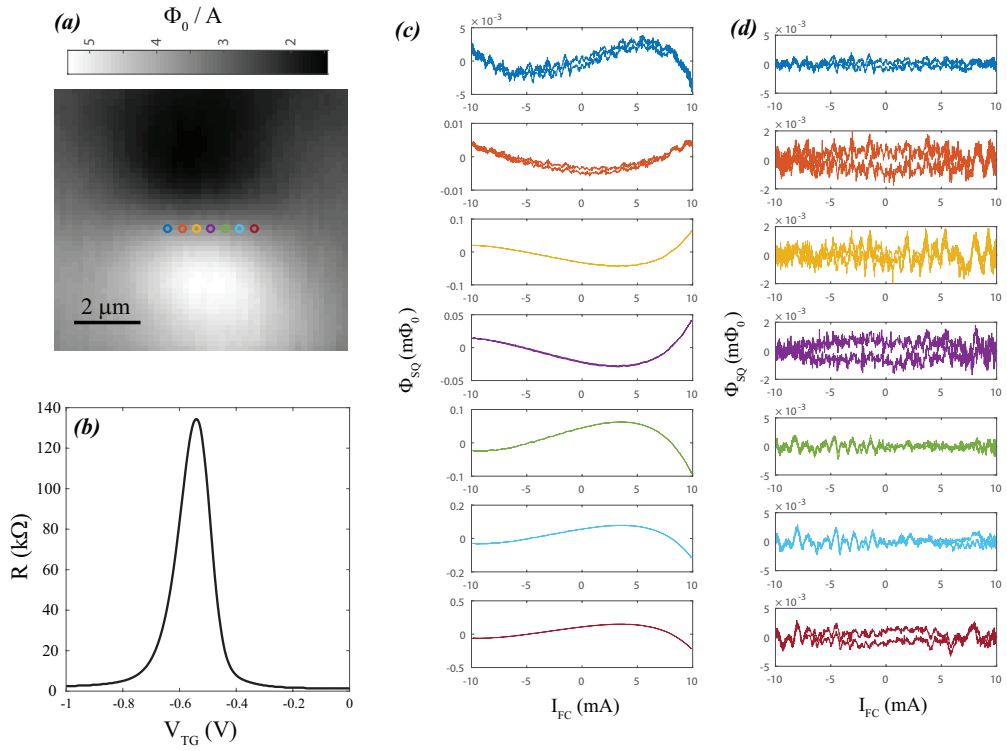

Figure 5.16: **Attempted persistent current measurement on a 2 μm diameter antidot** (a) A zoomed in flux image showing flux from current at $V_{TG} = 0V$. Colored open circles indicate the position that Φ_{SQ} vs. I_{FC} curves were recorded. (b) Measured two-terminal resistance of the device vs. V_{TG} (c,d) Φ_{SQ} vs. I_{FC} curves at different positions and V_{TG} = -0.53 V with an experimental background subtracted. Additionally a linear (c) or 6th order polynomial (d) was subtracted subtracted. Approximately two periods of the persistent current should appear for this range of I_{FC} and antidot size

The sample design which allows for consistent positioning over antidots is shown in FIG. 5.15. A large bar-like device was contacted with ohmic Au contacts and had a top gate to tune the Fermi energy. Arrays of antidots of various sizes in the center of the device were patterned using e-beam lithography. In the n-type conduction regime ($V_{TG} = 0$ V), current flowed everywhere except where the antidots were, which showed up in flux images as dipoles (FIG. 5.15 c,d). The amplitude of the 'current dipoles' roughly scaled in amplitude with the size of the antidot, as expected. In order to resolve the signal due to antidots, I flowed a relatively high (up to couple tens of μAs), but not ridiculous, amount of current.

This method of navigation allows for identification of individual antidots and additionally gives a natural feature which is centered on the antidot, unlike other methods of navigation. We used

these features to attempt to measure persistent currents in a number of antidots (FIG. 5.16).

We measured the flux through the SQUID's pickup loop (Φ_{SQ} as a function of current through the field coil (I_{FC}). We positioned the SQUID at many positions near the center of the 'current dipole' feature of an antidot with a designed diamter of 2 μm (FIG. 5.16 a). We then swept the gate voltage to the resistance peak, so the Fermi energy was tuned into gap and edge states should be circulating the antidot (FIG. 5.16 b).

We measured Φ_{SQ} vs. I_{FC} at a number of positions near the center of the 'current dipole' at the resistance peak. An experimental background taken far away from the antidot before the measurement was subtracted from all presented curves. Linear background subtraction of the data (FIG. 5.16 c) reveals a large non-linear component which is not intrinsic to the antidot and is not necessarily repeatable. This non-linear component is most striking at large applied field coil currents, which are necessary to thread multiple flux quanta through the small antidot.

The non-linear background is much larger than the expected persistent current signal (at most tens of $\mu\Phi_0$), thus we need to subtract it. However, only a couple periods of the persistent current will be captured by at this field coil amplitude, and any polynomial which removes the non-linear background will also remove or significantly distort a real persistent current signal.

In addition to the slowly-varying non-linear background, a more quickly varying non-linear background is also present, and can be seen in the same data with a 6th order polynomial subtracted (FIG. 5.16 d). The non-linear background, shown here as a function of position, changes in amplitude and character over time as well. A similar non-linear background was observed in last generation 'Huber' SQUID, however it was stable over the time scale of days and therefore easy to subtract.

Both types of non-linear backgrounds made definitive measurement of the persistent current signal using this new generation SQUID difficult. It is not known at this point if this behavior is universal to new generation SQUIDs, or if this SQUID in particular was bad. Additionally, the smallest antidot which were well defined after etching were 1 μm in diameter, which have an edge length of 3 μm, of order the observed scattering length in the best HgTe samples. The size of antidots required to possible have ballistic conduction along the edges require very high field coil currents to get multiple periods, where non-linear effects will be most likely to occur.

Chapter 6

Images of edge currents in InAs/GaSb heterostructures

This chapter is based on work which is also published in:

"Images of Edge Current in InAs/GaSb Quantum Wells"

Eric M. Spanton, Katja C. Nowack, Lingjie Du, Gerard Sullivan, Rui-Rui Du, and Kathryn A. Moler. *Phys. Rev. Lett.* 113, 026804 (2014)

"Edge Transport in the Trivial Phase of InAs/GaSb"

Fabrizio Nichele, Henri J. Suominen, Morten Kjaergaard, Charles M. Marcus, Ebrahim Sajadi, Joshua A. Folk, Fanming Qu, Arjan J.A. Beukman, Folkert K. de Vries, Jasper van Veen, Stevan Nadj-Perge, Leo P. Kouwenhoven, Binh-Minh Nguyen, Andrey A. Kiselev, Wei Yi, Marko Sokolich, Michael J. Manfra, **Eric M. Spanton**, Kathryn A. Moler. *arXiv preprint* arXiv:1511.01728

6.1 Introduction to InAs/GaSb

Searching for new prospective quantum spin Hall insulators (QSHIs) is a worthy endeavor for many reasons. HgTe quantum wells have many properties which are less than ideal. One reason for the small (but growing) amount of investigations of HgTe is that it is hard to grow. Growth of II-VI group semiconductors is not very widespread, so for broader study it would be ideal to have a QSHI which is comprised of more commonly grown semiconductors. Second, the lithography of HgTe is challenging in part because diffusion of the quantum well begins to become relevant at very low temperatures ($80^{\circ}C$) [26], which makes fully baking resists used in standard lithographic techniques difficult. Additionally, find a material with longer apparent scattering length scales and

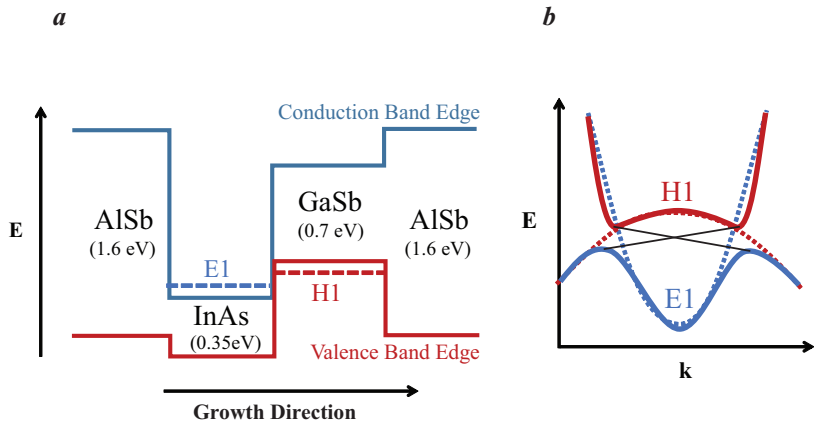

Figure 6.1: **Band edge diagram and cartoon band structure of InAs/GaSb** (a) A band edge diagram of InAs/GaSb/AlSb quantum wells. Solid lines indicate the band edges of the bulk materials, while the dashed lines indicate the lowest subbands for a well in the QSH regime (b) A schematic of the low-energy band structure near the Γ point of an inverted quantum well. Dashed lines indicate the band structure before hybridization of the hole and electron subbands

larger band gaps would make systematic investigation of the quantization of edge modes easier.

InAs/GaSb asymmetric quantum wells, predicted to exhibit the QSHE soon after HgTe[66], offer an alternative materials system to search for and investigate the QSHE. InAs/GaSb differs in a number of important ways from HgTe. InAs/GaSb is comprised of III-V semiconductors, meaning its growth can in principle be performed by many groups. Another difference is that holes and electrons are spatially separated in the GaSb and InAs layers, respectively. This leads to a number of novel effects, most important of which is the ability to tune band inversion using an electric field.

The QSHE effect was predicted to occur specifically in AlSb/InAs/GaSb/AlSb heterostructures where the AlSb layers act as confining barriers. InAs/GaSb is called a 'broken band gap quantum well' because, in the bulk, InAs's conduction band edge lies below the valence band edge of GaSb, as, illustrated in FIG. 6.1a). The reversed ordering of band energies drives the band inversion in InAs/GaSb, rather than intrinsic spin-orbit coupling in the case of HgTe.

The confinement energy of a quantum well results in 2D subbands. For certain thicknesses of the InAs and GaSb layers, the lowest populated electron subband in InAs remains below the hole subband localized in GaSb (dashed lines in 6.1a). In the absence of tunneling, the bands cross and the quantum well is gapless for any chemical potential (dashed lines in FIG. 6.1b). Taking into account tunneling between the hole (GaSb) and electron (InAs) layers, mixing of hole and electron states can occur which turns the band crossing at finite k into an anticrossing (solid lines in

FIG. 6.1a), leading to a gap which is termed the 'hybridization gap'.

In the inverted regime, quantum spin Hall edge modes appear in tight binding calculations as expected (schematically indicated as black lines in FIG. 6.1b) [66]. The weirdly-shaped band structure arising from hybridization results in much shallower slope of the edge modes in the band diagram compared to HgTe, which has a similarly sized energy gap. This slope is proportional to the Fermi velocity, which is therefore much slower in InAs/GaSb ($\sim 3e4m/s$ [55]) than in HgTe quantum wells ($\sim 5 \times 10^5 m/s$ [58]). This means that electron-electron interaction should be much more relevant in InAs/GaSb that in HgTe. This is reflected in the Luttinger parameter of the different heterostructures, $K_{HgTe} \sim 0.5 - 1$ and $K_{InAs/GaSb} \sim 0.2$, where a value of one indicates vanishingly weak interactions and lower numbers are more interacting [71]. This will become relevant later in evaluating candidate scattering mechanisms.

6.2 'Undoped' InAs/GaSb quantum wells

Tunneling between electron and hole layers can be disrupted by scattering and disorder at the interface betwen InAs and GaSb. Because the gap itself is established by hybridization, the aforementioned scattering leads to a finite density of states in the hybridization gap [75, 53]. In the absence of localization effects, the conductivity is predicted to be independent of temperature and disorder (as long as it is finite) [75]. Using a dual-gated device, this behavior was confirmed and the scaling of the measured conductivity with gap size approximately matched the expected dependence [54].

Finite conductivity (or 'residual bulk conduction') in the hybridization gap makes the observation of possible quantum spin Hall edge states difficult. Knez et al. investigated the presence of edge channels by studying samples of different sizes with the same aspect ratio [55]. In a homogeneous bulk conductor, the resistance should be independent of size as long as the aspect ratio is held constant. The presence of edge modes leads to a size dependence of the resistance for devices with the same aspect ratio. Their results are consistent with edges whose resistance scales with length and the extracted resistance of the edge approaches the correct quantized value as the size of the device goes to zero [55].

We used scanning SQUID to image current in a device made from a wafer which was 'undoped'[1] Our main result on undoped InAs/GaSb is the observation of enhanced current flow along the edges of the samples when the device was tuned to its resistance peak (FIG 6.2). We were unable to image the full device due to topography, the area we were able to image is shown in FIG 6.2a. The area

[1]Meaning that there were no intentional dopants added during growth to any of the heterostructure's layers.

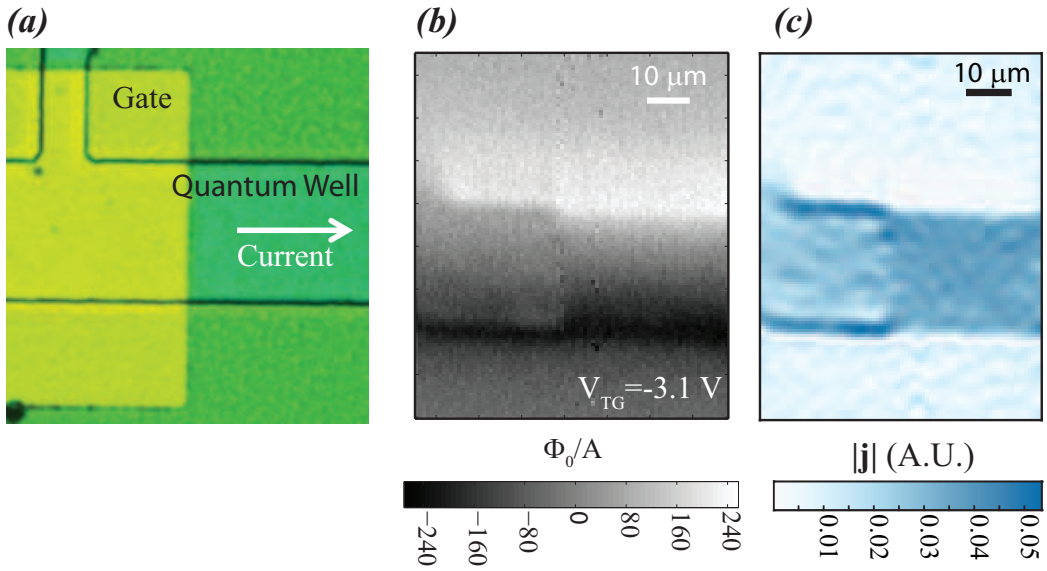

Figure 6.2: **Current flow in an undoped InAs/GaSb heterostructure.** (a) An optical image of the sample, showing the geometry of the sample as well as the region which is top gated. (b) Flux image due to an applied AC current in the device when the device has been tuned to its most resistive state using a top gate. (c) 2D current density along x, showing that more current flows on the edge of the sample under the top gate, but flows uniformly in the ungated region.

under the gold top gate was tuned to the highest resistance, which was observed at a top gate voltage of $V_{TG} = -3.1V$. The raw flux image (FIG 6.2b) shows qualitatively different behavior between region under and the region far away from the top gate. Current inversion along the horizontal (x) direction (FIG 6.2c) shows homogeneous current flowing far away from the gate, where the quantum well was n-doped and acts as a homogeneous conductor. Under the gate, there was a higher current density along the edges than in the bulk. There was, however, still current still flowing in the middle of the device. This observation is consistent with conducting edge states coexisting with residual bulk conduction.

We further analyzed the current as a function of gate voltage by fitting line cuts perpendicular to current flow under the gate (See 3 for fitting details). The two-terminal resistance (which contains a significant contact resistance due to the sample design) as a function of V_{TG} (FIG 6.3a) shows a peak , indicating we were able to tune the device through the hybridization gap. The conduction at more positive gate voltages was electron-like, and at very negative V_{TG} was hole-like. In these regions, fitting showed very little extra current flowing along the top and bottom edges (FIG 6.3b). However, a finite peak in the current flowing along the edges (about 10% in each edge) coincides

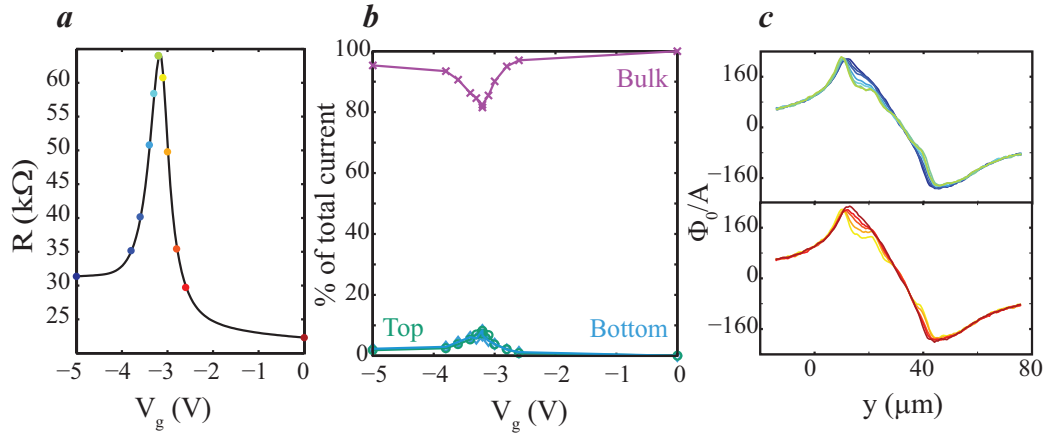

Figure 6.3: **Percentage of current flowing in the edges as a function of V_{TG} in the undoped device.** (a) Resistance vs. V_{TG} for the undoped device, colored dots indicate the respective flux profiles in (b), which were taken over the gated portion of the sample. (c) The percentage of current flowing in the top edge (green), bottom edge (blue) and bulk (purple) as a function of gate voltage obtained from fitting flux profiles.

with the peak in resistance. This is consistent with edge states which exist in the hybridization gap of the heterostructure, as expected for the QSHE. The flux profiles, which we fitted, (FIG 6.3c) showed similar shape near the resistance peak to those observed at elevated temperatures in HgTe, again confirming that undoped InAs/GaSb devices exhibit a coexistence of bulk and edge conduction.

6.3 Si-doped InAs/GaSb quantum wells

6.3.1 Images of edge current and gate voltage dependence

The problem of residual bulk conductivity in InAs/GaSb quantum wells has been alleviated by the addition of increased disorder and/or doping, presumably due to localization of the residual carriers. Silicon doping at the interface [32], Beryllium doping in the barrier layer [102], and use of a Gallium source with charge-neutral impurities [22] all lead to quantum wells with significantly higher resistances in the hybridization gap. In the case of Silicon and Beryllium doping, close to quantized resistance was observed in small devices [102, 32].

We investigated a device made from a wafer (FIG. 6.4a) with $\sim 10^{11}\ cm^{-2}$ Si dopants at the InAs/GaSb interface and layer thicknesses that are predicted to result in an inverted band structure exhibiting the QSHE [66]. Observation of dissipative non-local transport at high fields in InAs/GaSb suggests inversion of the lowest Landau levels, which is consistent with the inverted band structure

necessary for the QSHE [76]. The growth of the Si-doped wafer is described in Ref. [32]. FIG. 6.4b shows a schematic of the device. The lengths of the edges of our device ($> 50\ \mu m$) are much larger than the extracted phase coherence length observed in similar samples (4.2 μm) [32]. Such edges exhibit backscattering and their resistance scales with length [32].

To determine the 4-terminal resistance ($R_{14,23}$) of the sample, we applied current from contacts 1 to 4, and measured the voltage between contacts 2 and 3. Each reported resistance was either measured at a root mean square (rms) current of 10 nA at quasi DC frequencies (< 5 Hz) or extracted from fitting full current-voltage (I-V) characteristics (< 10 nA). $R_{14,23}$ at zero applied front gate voltage ($V_{TG} = 0V$) is $10\ k\Omega$. Using the front gate, we depleted n-type carriers by applying a negative gate voltage. FIG. 6.4c shows $R_{14,23}$ as a function V_{TG}. We observed a maximum in $R_{14,23}$ at $V_{TG} = -2.35V$, indicating that we tuned the chemical potential into the deviceâĂŹs insulating gap. The maximum value of $R_{14,23} >> h/(4e^2)$, the expected quantized value, indicates that (if the edge states are from the QSHE) backscattering occurs along the edges. At more negative voltages, $R_{14,23}$ decreases again, indicating that the chemical potential lies in the valence band and that the majority of carriers are hole-like.

As is sometimes the case in gated devices, $R_{14,23}$ depends on the gate voltage history. The device was consistently more resistive on downward sweeps of the gate. Such history dependence implies that repeated sweeps, as well as temporal drift, likely give different realizations of the disorder potential and tune either scattering in the edge and/or tune the bulk conductivity.

To image current, we applied an AC current with a nominal rms amplitude of 150 nA and used lock-in techniques to measure the resulting flux through the SQUID's 3-μm-diameter pickup loop (shown schematically in FIG. 6.4b). We corrected the images and profile for phase shifts and attenuation from unintentional RC filtering due to capacitance in our wiring.

FIG. 6.4 shows two images of magnetic flux produced by current in the InAs/GaSb device, contrasting the cases where the chemical potential was tuned into the conduction band (V_{TG} = 0 V) and into the gap (V_{TG} = -2.35 V). At V_{TG} = 0 V, the magnetic flux varied smoothly and monotonically across the device (FIG. 6.4e), indicating that current flowed uniformly inside the sample. When the device was tuned near its resistance peak (V_{TG} = -2.35 V), the flux had sharp features centered on the edges of the device, signifying that current flowed along the edges of the sample (FIG. 6.4d).

To better visualize the current, we used Fourier techniques (described in Ch. 3) [90, 81] to extract the 2D current density from each flux image. The resulting current images confirm that in the conduction band, the current distributed uniformly throughout the device (FIG. 6.4g,i). In the

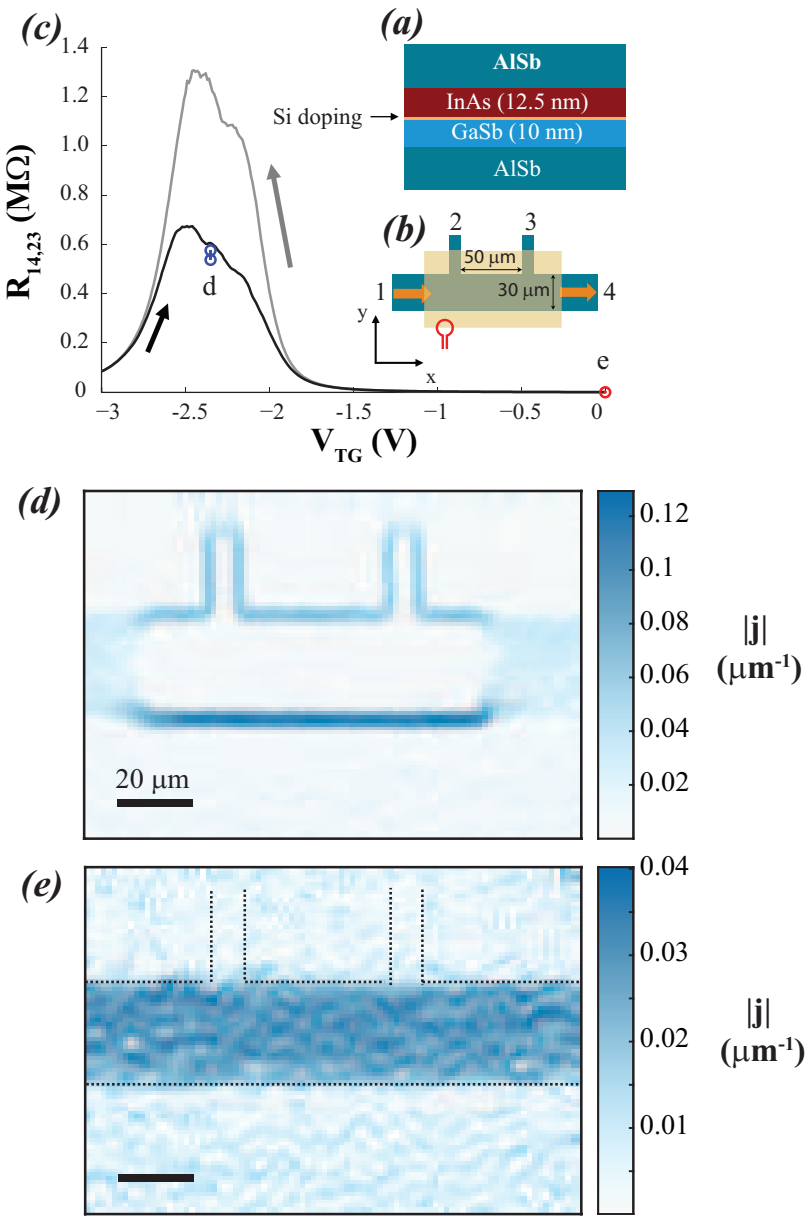

Figure 6.4: **Flux and current maps of a device made from a Si-doped InAs/GaSb quantum well.** (a) Schematic of the Si-doped InAs/GaSb heterostructure. Si doping suppresses residual bulk conductance in the gap. (b) Schematic of the measurement. Alternating current (orange arrows) flows from left to right. A voltage (V_{TG}) applied to the front gate tunes the Fermi level. The SQUIDâĂŹs pickup loop (red circle) scans across the sample surface, with lock-in detection of the flux through the pickup loop from the out of plane magnetic field produced by the applied current. (c) Four-terminal resistance $R_{14,23} = V_{23}/I_{14}$ as a function of V_{TG}, showing both the upwards (black) and downwards (gray) gate sweeps. The resistance peaks when the Fermi level is tuned into the gap. (d,e) Flux images for the sample tuned into (d) the bulk gap, V_{TG} = -2.35 V, and (e) the n-type regime, V_{TG} = 0 V. (f-i) Reconstructed horizontal (j_x) and vertical (j_y) 2D current densities, showing that the current flows on the edges in the bulk gap and uniformly otherwise.

gap, however, the current flowed almost entirely along the edges under the front gate (FIG. 6.4 f,h), a signature of the QSHE. Edge currents are particularly illustrated in the vertical leads (FIG. 6.4h), in which current flowed along the lead until it reached an un-gated part, where the current crossed and returned along the opposite edge of the lead. The qualitative features of the images did not depend on gate voltage history.

Observation of ballistic conduction in $1\mu m$ wide devices [32] sets an upper limit of $\sim 500nm$ on the possible width of the edges, below our spatial resolution. The geometry of the SQUID's $3\mu m$-diameter-pickup loop, the height above the sample ($\sim 1.5\mu m$), and the current inversion all limited our spatial resolution and determined the apparent width of the edge conduction.

To understand the evolution of current with gate, we imaged current at a series of gate voltages (FIG. 6.5). The gate was swept downward and the resistance was recorded before and after each scan FIG 6.5b. In FIG. 6.5a we present selected profiles of the x-component of the current density as a function of gate voltage. The area over which the profiles were averaged is indicated in FIG. 6.4g. We fit flux profiles, as described in Ch. 3, to quantify the amount of current flowing in the top edge, in the bottom edge, and homogeneously through the bulk (FIG. 6.5c). More current flowed along the edges as the sample was tuned with V_{TG} to be more resistive.

6.3.2 Temperature Dependence and Backscattering

Next, we studied how the current distributed as a function of temperature while fixing V_{TG} at -2.35 V. The resistance peak remained at the same gate voltage value over the range of temperatures measured. We measured flux profiles along y at the center of the device between 4.5 K and 32.5 K. We extracted a 2D current density from each flux profile (FIG. 6.6a). The total resistance dropped with increasing temperature (Fig. 6.6b) as more current flowed in the bulk of the sample, indicating that the bulk's conductivity increased relative to the edges. We fitted the flux profiles as a function of temperature in the same manner as the gate series (FIG. 6.6c).

To further analyze the temperature dependence, we modeled the bulk and edges as parallel resistors, and define an effective resistance of the edges and bulk as $R_{eff} = R_{14,23}/F$, where F is the fraction of current flowing in each channel. R_{eff} in our 4-terminal geometry does not depend on the contact resistance and is directly proportional to the actual resistance of the edges.

R_{eff} vs. temperature is presented in FIG. 6.8. As a function of temperature, the bulk R_{eff} decreases strongly with temperature, consistent with thermally activated carriers [32]. The top edge's current was more strongly influenced than the bottom edge's current by temperature-induced bulk

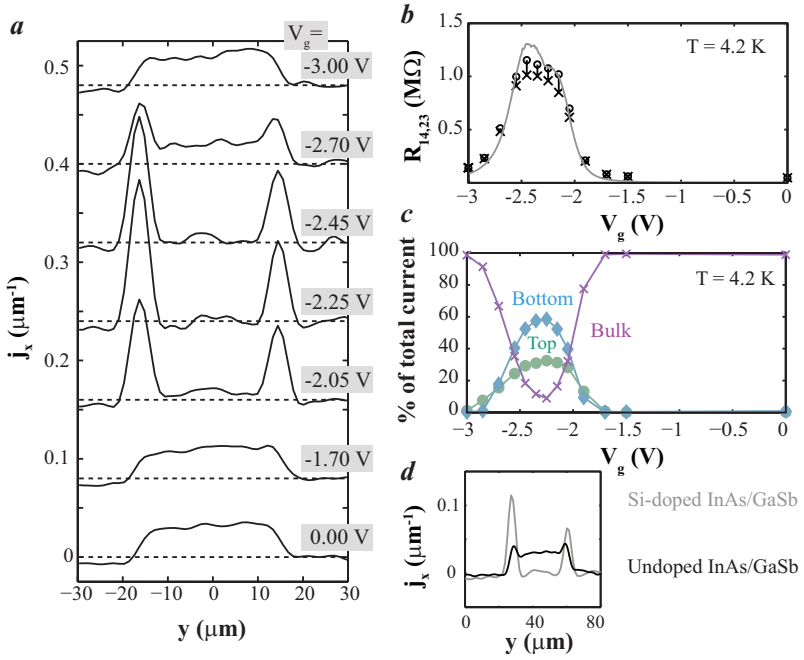

Figure 6.5: **Percentage of current flowing in the edges as a function of V_{TG} in the Si-doped device.** (a) Selected profiles of the x-component of the current density show the evolution between bulk-dominated and edge-dominated transport, and offset for clarity. The zero of each profile is indicated by the dashed line. Profiles were averaged over the region between the contacts, as shown by the black bracket in Fig. 1g. (b) Resistance vs. V_{TG} in a downward gate voltage sweep before imaging the current (gray), and immediately before (o) and after (x) each image in a subsequent sweep. (c) The percentage of current flowing in the top edge (green), bottom edge (blue) and bulk (purple) as a function of gate voltage obtained from fitting flux profiles. (d) A comparison linecuts of j_x in undoped (gray) and Si-doped (black) InAs/GaSb devices taken at their respective resistance peaks. In the Si-doped device, the bulk conduction present in undoped devices is supressed.

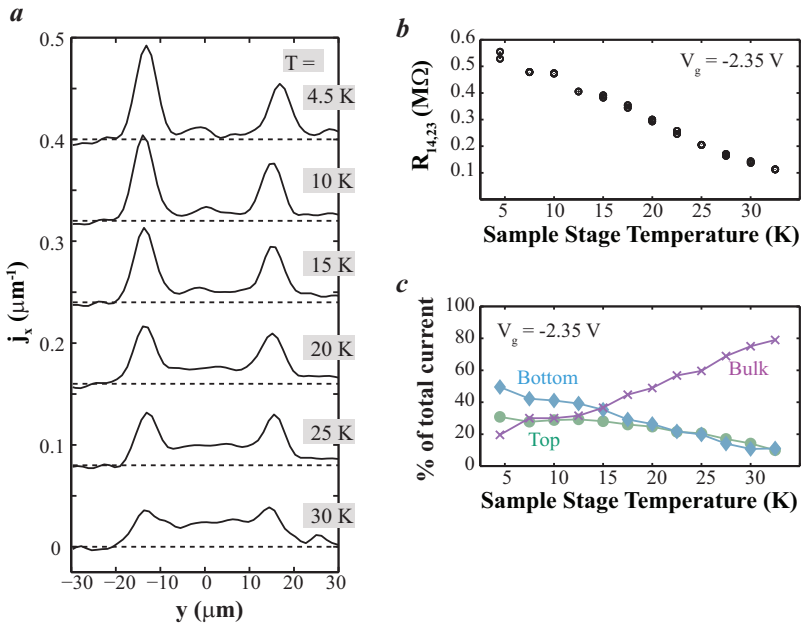

Figure 6.6: **Temperature dependence of the edge and bulk currents in Si-doped InAs/GaSb.** All measurements are performed at a constant gate voltage of V_{TG}=-2.35 V (a) $R_{14,23}$ of the Si-doped device as a function of sample stage temperature. (b) Profiles of the x-component of the current density at selected temperatures, showing more bulk conductivity at higher temperatures, and the presence of edge states up to 30 K. The profiles are offset for clarity and zero of each profile is indicated by a dashed line. (c) Percentage of current flowing in the top (green), bottom (blue), and bulk (purple), obtained from fitting flux profiles (see main text).

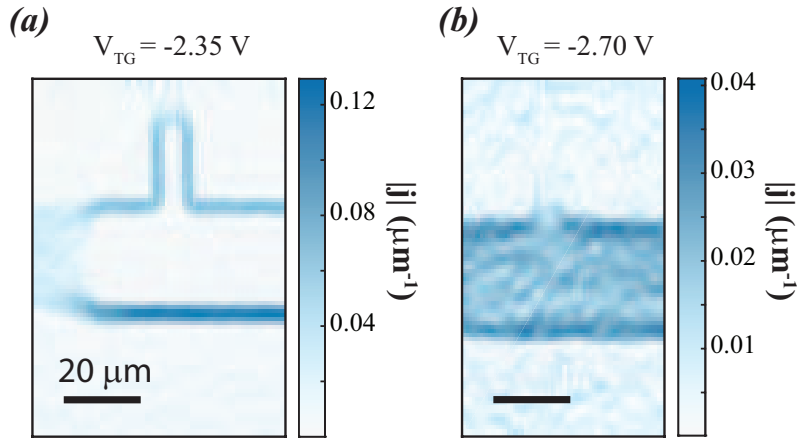

Figure 6.7: **Comparison of edge current flow with and without bulk conduction in Si-doped InAs/GaSb** (a,b) The x component of the current density shows enhanced current flow along the in the main body of the device both with (a) and without (b) significant bulk conduction. (c,d) The y component of the current density shows that current flows up the entirety of the gated contact when there is little bulk conduction (c), but when there is bulk conduction current does not flow up the narrow contacts (d), showing that the edges along the narrow contact are effectively âĂIJshortedâĂİ by the conducting bulk.

conduction, because the bulk provided an alternative path across the top leads, effectively decreasing the length of the current path along the top edge. An example of this behavior is demonstrated in FIG. 6.7 for a similar situation, when the bulk was tuned to be conducting as a function of V_{TG}. When the bulk is at its most insulating, the majority of current flowed up the entire length of the gated portion of the contacts (FIG. 6.7a,c). However, when the gate voltage is tuned away from the measured resistance peak, current had an alternative path which is much shorter across the small width of the voltage leads (FIG. 6.7b,d. In our naive model of three parallel resistors, the corresponds to the top edge's R_{EFF} decreasing, although the resistance of the 'actual' edge mode may be unchanged.

The top edge's R_{eff} decreased by a factor of two over the measured temperature range, consistent with a constant resistance per length of the edge, but with the length along the vertical leads (compare FIG. 6.4f) getting shorted by the bulk. This behavior is confirmed, as discussed above, by images at gate voltages with moderate bulk conduction. The bottom edge was not susceptible to this effect, because there were no 'extra' leads interrupting the edge. Correspondingly, R_{eff} of the bottom edge remained constant within the sensitivity of our analysis from 4.5 K to 32.5 K.

We have shown that the resistances of long (high resistance) edges are unchanged up to high

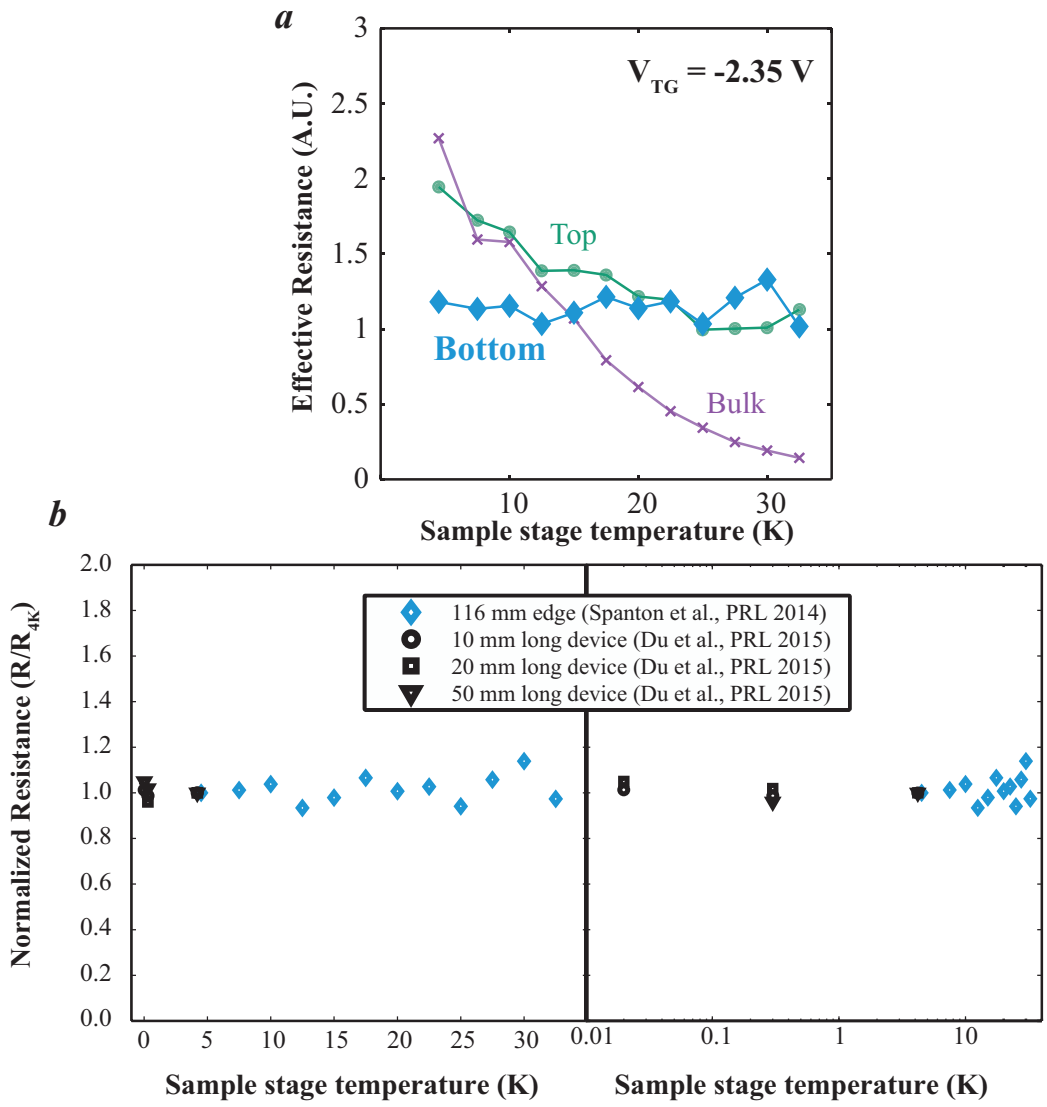

Figure 6.8: **Effective resistance of the quantum spin Hall edges vs. temperature in Si-doped InAs/GaSb** We extracted the effective resistance of the edges and bulk using a parallel resistor model. (a) The effective resistance of the bulk varies strongly with temperature. The effective resistance of the top edge is reduced by a factor of two, consistent with shorting of the top contacts by the bulk, rather than a change in the resistance per unit length (see text). The effective resistance of the bottom edge remains constant with temperature, which known scattering theories do not predict. (b) We normalized our effective resistance of the bottom edge and the resistances measured by Du, et al. to their 4 K values, and plotted them together to emphasize the lack of temperature dependence on a linear (left) and semilog (right) scale. The resistance of the edges appear to be constant with temperature between dilution refrigerator temperatures up to temperatures of order the insulating gap.

temperatures where the rate of possible inelastic backscattering mechanisms should naively be varying the most. Additionally, transport measurements have shown that the resistances of long devices remain constant from 20 mK to 4 K [32], as illustrated in FIG 6.8b. With these two results, the resistance per unit length of the edge states of InAs/GaSb does not vary strongly in any measured temperature regime.

6.3.3 Possible edge state scattering mechanisms

In contrast to this experimental result, inelastic scattering mechanisms universally predict temperature dependence of QSH edges. Generic inelastic scattering centers lead to a T^4 or stronger temperature dependent reduction of the conductivity [101, 91, 62, 24], which our data and Ref [32] firmly rule out experimentally for InAs/GaSb. Charge puddles formed by disorder can couple via tunneling [109] or directly to the edge states [89] and both can induce backscattering. The effect of the coupling on conductivity as a function of temperature depends on the hierarchy of thermal, puddle and edge energies and the number of electrons in the puddle [109, 108]. For odd-electron puddles formed by electric potential disorder, the Kondo effect may lead to sub-power-law temperature dependence above the Kondo temperature [71, 104, 1, 108]. Even in this limit, the resistivity scales as $ln^2(T)$, which is inconsistent with our observations [108]. If the temperature is larger than the charging energy of a puddle, the temperature dependence may saturate [108]. However, the size of charge puddles required to explain temperature-independence of the resistance down to 20 mK is of order the sample size which is unphysical. Coupling of the electron and nuclear spins leads to non-linear IV, temperature dependence, and a predicted scattering length in InAs/GaSb [28] that are inconsistent with our observations. Weaker temperature dependence may be possible in unexplored models; however, it is difficult to understand how any inelastic scattering mechanism would lead to temperature-independent conductivity over three orders of magnitude.

Recently, low-temperature and very low bias voltage measurements of InAs/GaSb show a power law dependence of the resistance of the edge states, which was interpreted as evidence of helical Luttinger liquid behavior [64]. While the edge state can be somewhat localized at very low temperatures and biases due to electron-electron interactions, this mechanism does not explain why the edge states have a non-quantized and temperature independent resistance we observed at higher temperatures [64].

Elastic processes may seem like the natural way to obtain temperature-independent conductivity, but the puzzle remains unless time-reversal symmetry is spontaneously broken (e.g. [84]). However, the predicted critical temperature of the scattering mechanism (($\sim 10K$), in Ref. [84] is below

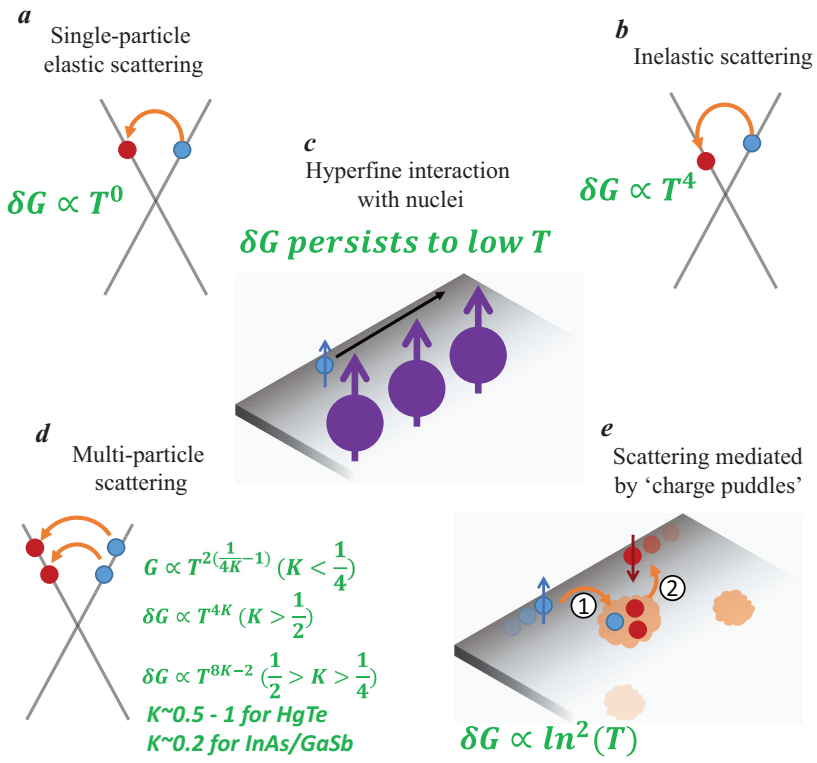

Figure 6.9: **A schematic of the different candidate scattering mechanisms in QSH edge states** The temperature dependence of the change in conductivity ($\delta G = G_0 - G(T)$) for different scattering mechanisms (a) Single-particle elastic scattering, scattering from a right-moving spin up electron to a left-moving spin down electron with the same energy, is suppressed by time reversal symmetry [113]. (b-e) Other candidate mechanisms are theoretically allowed, however their resulting characteristics do not match the experimental evidence for InAs/GaSb (See main text).

the highest temperature measured here. Multi-particle scattering processes may also contribute, but are not generically temperature independent [62]. Trivial edge states, however, do not have protection against elastic backscattering and could explain the weak temperature dependence of the edge conduction. In the next section, we investigated dual-gated InAs/GaSb and observed edge states in the trivial regime, showing that trivial edge states may exist in the QSH regime and could have an effect on the observed transport.

6.3.4 Non-linearity

Our measurements of the Si-doped device were not made in the linear regime, i.e. the amount of current applied to take images ($150nA_{rms}$ in the case of images of the Si-doped device) is outside the range where the voltage drop across the sample scales linearly with the applied current. V-I characteristics of the device near the resistance maximum taken in the same gate sweep as FIG. 6.4 c,e,g are shown in Fig. 6.10. At $150\sqrt{2}$ nA applied current amplitude (red-highlighted data), the V-I characteristic already noticeably deviates from the resistance determined by fitting low-current behavior (black dashed line).

To discover the effect of non-linearity on our images, we applied higher currents ($500nA_{rms}$) to a Si-doped device. This device is a 2nd Si-doped device which was prepared identically to the one presented earlier. The device was tuned to the resistance peak, using the top gate (V_{TG}) which was defined with respect to ground, and an applied current was sent from the left most contact to the rightmost contact which was grounded (FIG. 6.11). Closest to ground, the sample showed behavior close to what was expected on the resistance maximum, with the majority of the current along the edges. Farther away from ground, the current appears to flow more along the bulk (FIG. 6.11 b,c). We attribute this non-linearity to the AC potential which deviates farthest from zero on parts of the sample âĂŸfurthestâĂŹ away from ground. This interpretation is confirmed by switching which contact is grounded, and observing that the trend in the images also flips (FIG. 6.11 d-f). The lock-in measured images are the amplitude of the first harmonic of the applied current, which will be determined primarily by the high-current behavior. We do not see a systematic gradient in the images taken at 150 nA, and therefore conclude that the main features of the images are not affected by the non-linearity. A strongly gate-voltage dependent scatterer, such as those observed in [59] could be affected by such non-linearity and may be masked by this effect.

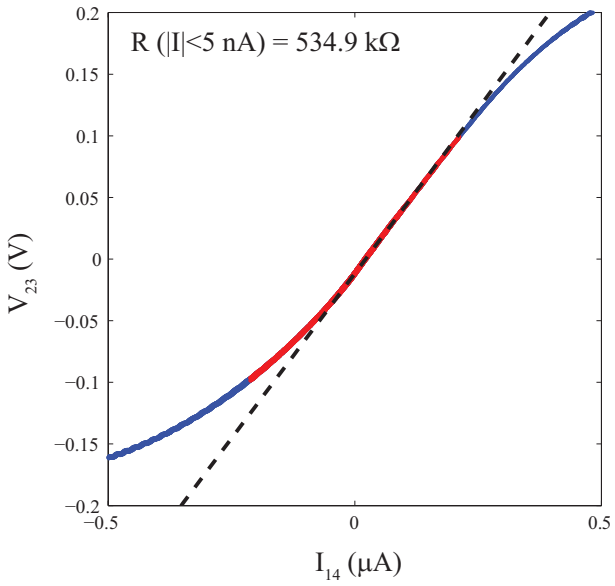

Figure 6.10: **V-I Characteristics of Si-doped InAs/GaSb when it is tuned into the gap.** ($V_{TG} = -2.35V$). The range of the applied current for the images shown ($150nA_{rms}$) is indicated by the red portion of the curve. A linear fit to the low current resistance between âĂŞ5 nA and +5 nA is indicated by the dashed black line.

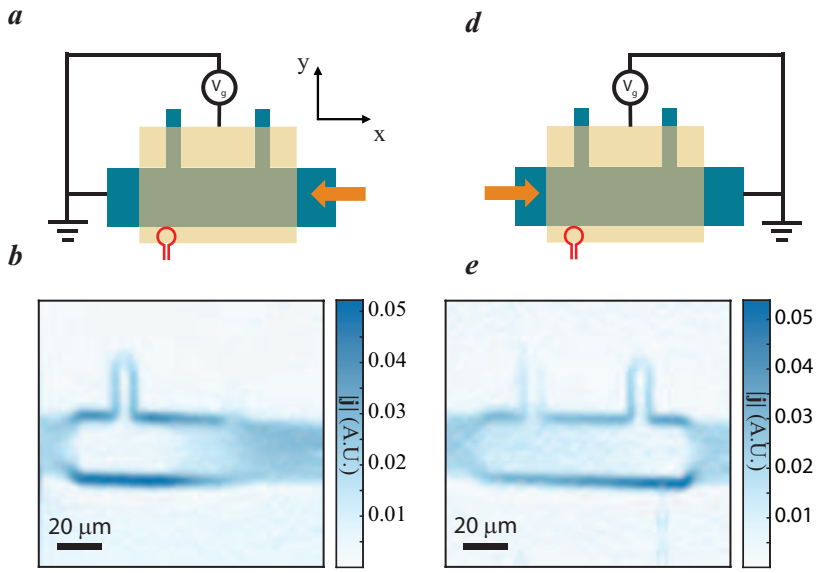

Figure 6.11: **Images of Si-doped InAs/GaSb at high applied currents** $500nA_{rms}$ was applied to the device, which is tuned to the resistance peak. The top gate voltage is applied with respect to a ground that is shared with side of the sample, while an AC excitation is applied to the other side. (a-c) When the left contact is grounded, as shown schematically in (a), the behavior closest to ground is that of a device tuned into the gap, showing strong edge conduction with very little current flowing in the bulk. However, the right side of the image is much more bulk like indicating that the potential of the interface with respect to the gate become important (b,c). When the right side is grounded and the excitation applied to the left, the non-linear behavior flips as well (d-f).

6.3.5 Expected Signal from Spin Polarization

In the quantum spin Hall state, each edge state is doubly-degenerate and the two states are time-reversed pairs (Kramer's pairs), meaning they have opposite spin and crystal momentum. In the presence of an applied charge current, there is also an associated net spin polarization due to the non-equilibrium occupation of the edge states. We estimated the associated magnetic signal from the excess spins and find that they are well below our experimental resolution in this geometry.

The spin-polarization of the edge current can be estimated from the applied current and properties of the quantum well in question. We naively calculate the net linear magnetic moment density induced by edge current as $\lambda_s = g\mu_B I/(ev_F)$ where g is the g-factor, $\mu_B = e\hbar/(2m_e)$ is the Bohr magneton, I is the applied current, e is the electron charge, and v_F is the Fermi velocity of the edge states. For an InAs/GaSb quantum well, we use $g = 10$ and $v_F = 4x10^4 m/s$ with our experimentally applied current of 150 nA. For comparison we also investigate the expected spin polarization for HgTe, using the values $g = 18$ and $v_F = 5x10^5 m/s$. We have estimated values for the bulk g factors from the literature [115, 78], however it is unclear that these values are necessarily correct for typical quantum wells or that the g-factor of edge electrons would be the same.

Our scanning SQUID magnetometer measures the magnetic flux penetrating the SQUID's pickup loop $\int g(x,y)\vec{B}\cdot\vec{da} \sim \int g(x,y)B_z(x,y,h)da$, where the integral is taken over the plane of the SQUID, g(x,y) is the point spread function, $\vec{B}$ is the magnetic field produced by the sample and B_z is the out of plane component of that field at a scan height, h. Here we present B_z for simplicity, however we have separately confirmed all of the conclusions using a calculated flux signal with an experimentally determined point spread function, as described in Ch. 3.

We assumed a semi-infinite strip of quantum spin Hall insulator with a 20 μm width and currents running along the edges of the strip. We calculated $B_z(y)$, where y points along the width of the strip. Each edge carries half of the applied current, and the top and bottom edges have opposite spin polarization (FIG. 6.12a). We used a height of $1\mu m$ in our calculation, a typical scan height for our SQUIDs. We calculated the expected magnetic field for both HgTe quantum wells (FIG. 6.12 b and c) and InAs/GaSb quantum wells (FIG. 6.12 d and e). We found in both cases that the expected field from the edge current is much larger than the spin-polarization signal. In InAs/GaSb, the estimated field is a factor of 40 smaller than the signal from the current. The signal from spins in HgTe is an order of magnitude smaller owing to its much faster Fermi velocity.

The residuals of our fits to flux linecuts, which probably come primarily from errors in our SQUID's point spread function, are much larger than the expected signal from spin polarization (FIG 6.13). Even if our knowledge of the point spread function was exact, it is unclear that we

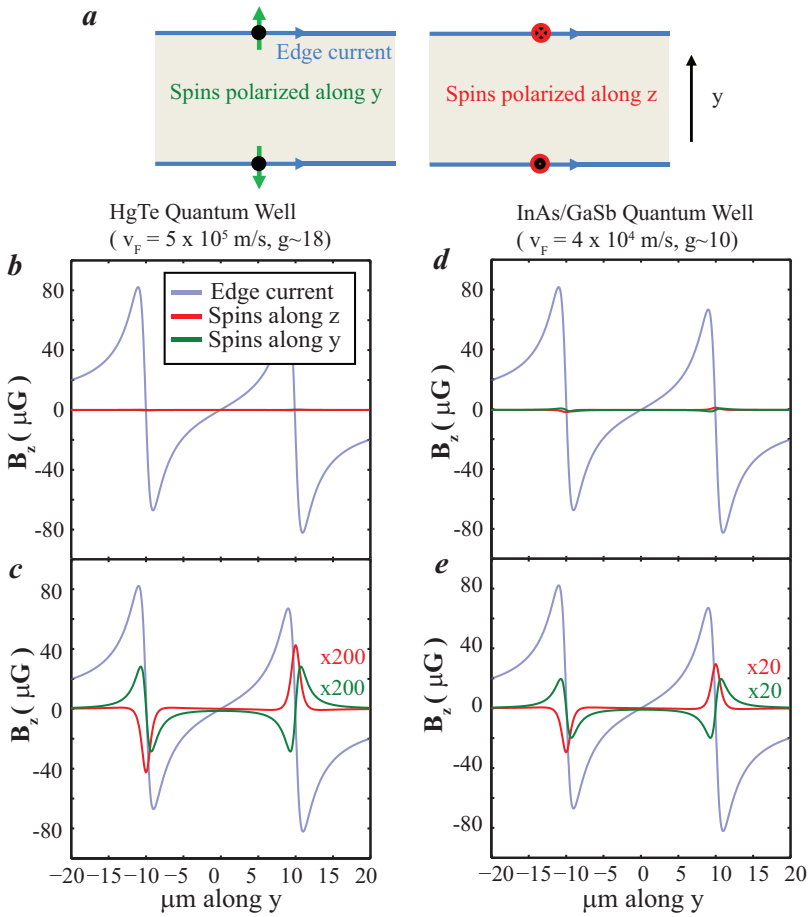

Figure 6.12: **The expected spin polarization signal is much smaller than the magnetic fields from current flow** Calculation of the z-compononent of the magnetic fields from edge currents and resulting spin-polarization. Our SQUID measures the sum of the fields from the current and spin polarization. (a) A schematic of the geometry used to calculate the expected magnetic fields for in-plane (green) and out-of-plane (red) spins as well as the applied edge current (green). The fields were calculated at a height of 1 μm. We used approximate numbers for the electron g-factor and Fermi velocity to calculate the expected spin polarization in (b,c) HgTe quantum wells and InAs/GaSb quantum wells (d,e). Signal were calculated using an applied current of 150 nA, however all signals are expected to scale linearly with current. The magnetic field from spin polarization is a factor of $\sim 40 (\sim 400)$ than the magnetic field from current flow in InAs/GaSb (HgTe).

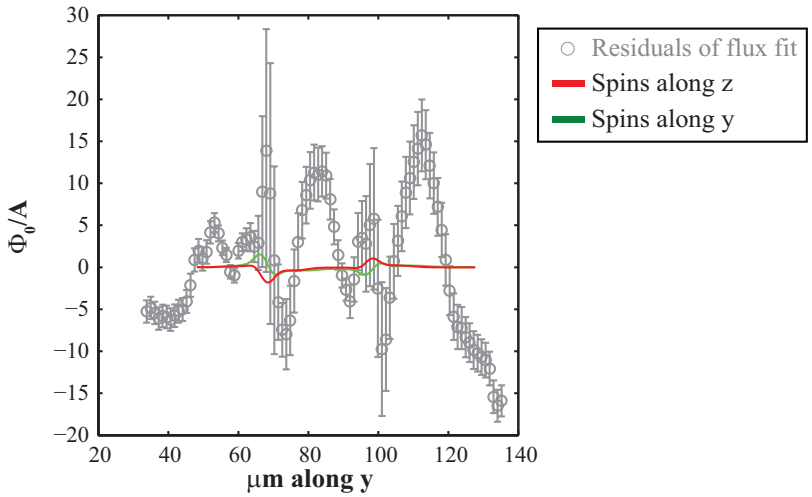

Figure 6.13: **The residuals of our fits of flux from current flow are much larger than the expected spin polarization signal** We calculated flux profiles from spin polarization of the edge states for InAs/GaSb (red and green curves indicate out of plane and in plane spin polarization, respectively). The residuals of our fits to flux from current along the edges (gray circles) are much larger than the expected signal size, therefore we are unable to observe the spin polarization of the edges. The residuals shown are the result of bootstrapping data on the resistance peak 100 times, the error bars indicate 100% confidence intervals from our bootstrapped fit.

would be able to discriminate a spin polarization signal from slight differences in how current flowed along the top and bottom edges. Therefore, in this geometry detection of the spin polarization is not practical.

6.4 Dual-gated devices

InAs/GaSb's unique layer structure results in the ability tune both the Fermi level and the band structure using only electric fields. In a dual-gate geometry (both a top and back gate) both of these are independently controllable, and with large enough applied voltages one can tune between non-inverted ('trivial') band structure and an inverted band structure which should exhibit the QSHE.

Our transport measurements at $T = 400mK$ show behavior consistent with an electric field induced inverted to non-inverted transition, which is corroborated by more in-depth transport characterization on the same wafer [87] and different wafers [77]. The right side (positive V_{BG}) of the 2D plot of R_{xx} shows a relatively high-resistance region where we believe the Fermi level lies in a non-inverted band gap (FIG. 6.14 a).

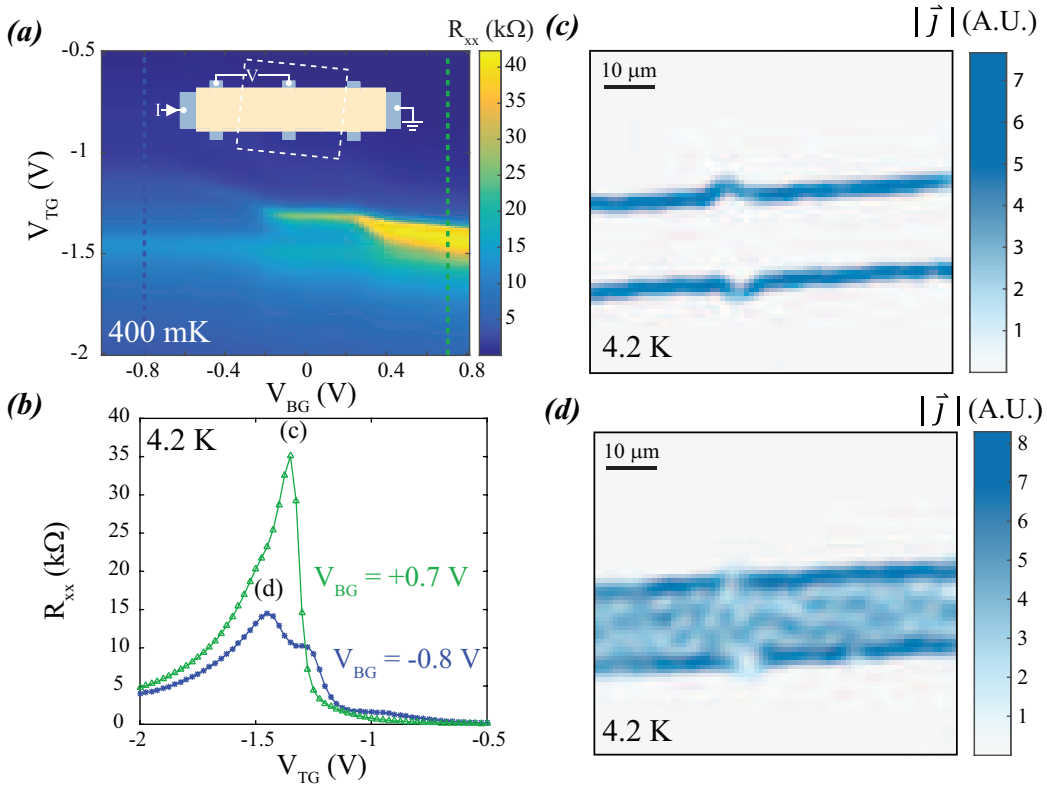

Figure 6.14: **Current density imaging of dual-gated InAs/GaSb reveals conducting edge states in the non-inverted regime.** (a) Transport vs. top gate (V_{TG}) and back gate (V_{BG}) in dual-gated an InAs/GaSb device. We have assigned the most resistive region at positive V_{BG} as the non-inverted gap. A subtler resistance peak, and secondary peaks appear at negative V_{BG}, which is consistent with the inverted regime with residual bulk conductivity. (Inset) Schematic of the device with the contacts used to measure R_{xx} and the approximate region of the device which was imaged. (b) Line cuts of R_{xx} of the same device measured at 4.2 K. (c,d) Current density images (extracted from a raw flux image) taken in the non-inverted (trivial) regime (c) and the inverted regime (d).

At negative V_{BG} we observed a lower resistance peaked structure, which exhibited two clear peak-like features. In other transport measurements on the same wafer, two side peaks associated with the onset of electron-hole hybridization were observed, in addition to a central peak which was associated with the hybridization (inverted) band gap. In our data, there is a third very diffuse bump at more positive V_{TG}, indicating that the larger of the two more prominent peaks is the onset of electron-hole hybridization, while the smaller peak is the middle of the hybridization gap (FIG. 6.14 b). In our dual-gated device, no effort was taken to suppress residual bulk conductivity, as was done in the Si-doped devices, and therefore the maximum resistance in the inverted regime is quite low.

We imaged flux from current at the resistance peak in the non-inverted (trivial) regime and found that the vast majority of the current was carried along the edges. We extracted the current density in the non-inverted regime by imaging flux in the indicated area on the device (6.14 a, inset). In the non-inverted regime, where the resistance peak is high, but not fully insulating ($\sim 40k\Omega$), we observed that close to zero current flowed in the middle of the device. Instead, the current in the non-inverted, gapped regime was carried completely by, presumably trivial, conducting paths along the edge of the device.

We also imaged current in the inverted regime at positive V_{BG}. We imaged current at the resistance peak at fixed $V_{BG} = -0.8V$, which places the Fermi level closer to the valence band than in the middle of the hybridization gap. We found enhanced current along the edges of the device, which is coexistent with a bulk which remained conducting, albeit less conducting than the edges. This is consistent with what we observed previously in single-gate, un-doped InAs/GaSb devices.

Images of current density far from the peaks in resistance yielded no evidence for edge conduction.

We observed edge conduction in both the inverted and non-inverted regimes, and now wish to more thoroughly study their evolution across the phase diagram in order to learn more about the relationship of the trivial edge states to the observed edge conduction in the inverted regime.

We measured averaged flux line cuts vertically across the sample ,away from the voltage probes, at the maximum resistance observed at many fixed V_{BG}. We then extracted j_x line cuts from measured flux using current inversion techniques (6.15 a). The gate voltage positions of the line cuts, along with R_{xx} taken at 4.2 K, is presented in 6.15 b. We observed that the edges carry all of the current at large positive V_{BG}, far in the non-inverted regime. As V_{BG} was tuned to more negative values, the amount of current flowing in the middle of the device grew. Enhanced edge conduction was observed in every j_x line cut as a function of V_{BG} .

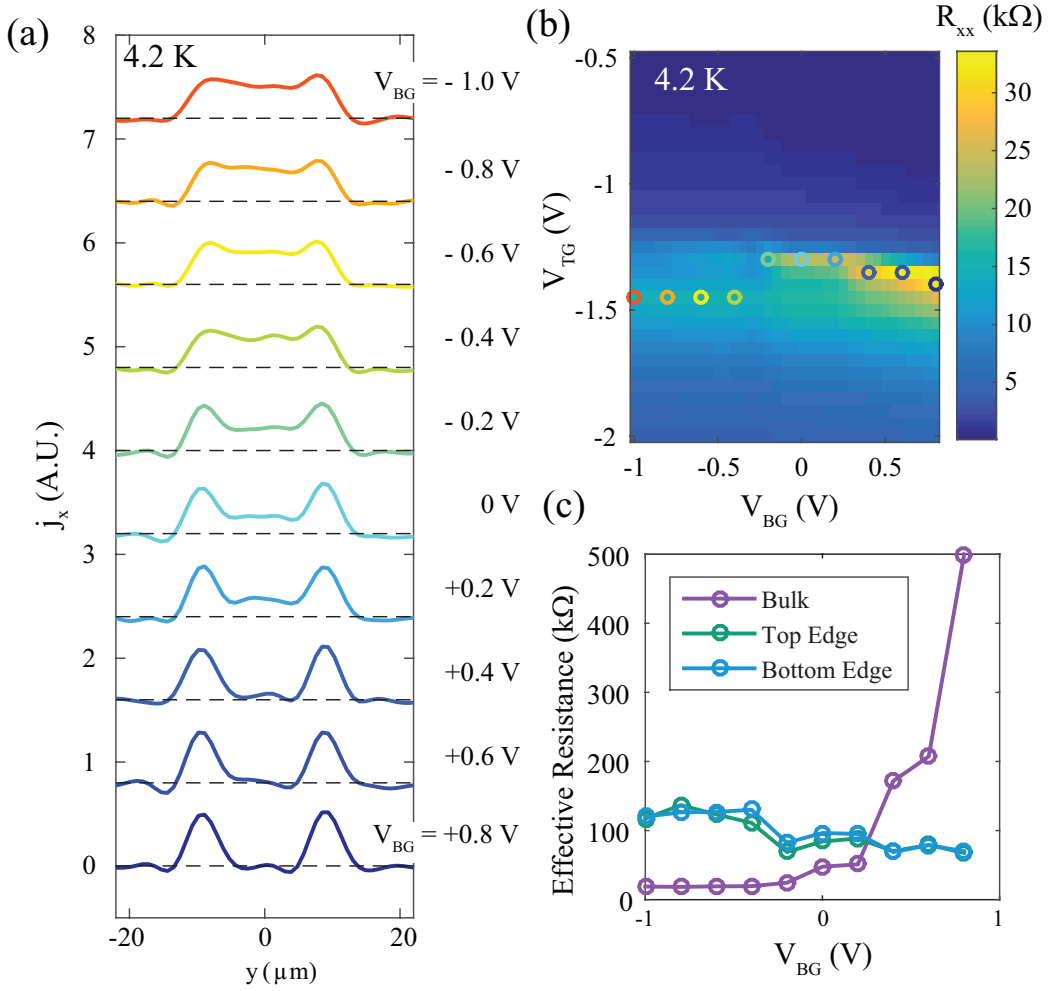

Figure 6.15: **Edge state conduction was observed across the inverted to non-inverted phase diagram** (a) Line cuts of current density along the horizontal direction (j_x) on the resistance peaks at various fixed back gate voltages (V_{BG}) (b) Four-terminal resistance (R_{xx}) taken at 4.2 K. The gate voltages at which each line cut was taken are indicated by open circles. (d) The extracted effective resistance (R_{EFF}) from fitted flux profiles and R_{xx}.

It is important to note, that in other wafers, the non-inverted resistance peak is almost completely absent [77]. The smaller than expected non-inverted gap and the difficulty of characterizing the inverted gap in the presence of residual bulk conductivity are the next hurdles in fully characterizing this material. Seeing gapped behavior in both regimes, by the addition of Si dopants as in Ref. [32] and measurements in a Corbino geometry as in [76] would enable a full characterization of the topological-trivial transition in the bulk and rule out any doubt about the identification of inverted and non-inverted regions.

We performed effective resistance (R_{EFF}) analysis described earlier by fitting line cuts. We found that R_{EFF} of the bulk strongly increases at positive V_{BG}, which corresponds with an energy gap which is getting bigger with higher V_{BG}, consistent with a non-inverted gap. We do not observe a similar increase in the bulk's R_{EFF} at negative V_{BG}. If there is an opening of the non-inverted gap, it will be obscured by residual bulk conductivity in this device [75]. Residual bulk carriers from imperfect hybridization should lead to a constant dependence of the bulk's resistance on gate voltage even as the gap grows [54]. This is consistent with what we observe. Similarly, we do not observe any clear signatures in the bulk's R_{EFF} of the gap closing, however this could also be obscured by residual bulk conductivity.

The effective resistance of the edges changed by less than a factor of two between the inverted and non-inverted regimes. Their is a jump in the R_{EFF} of the edges between V_{BG} = -0.2 V and -0.4 V. This is approximately where the transition between the inverted and non-inverted regions occurs. It also corresponds to the resistance maximum (used in this case to choose what gate voltages were selected to take line cuts) jumping from the middle of the gap at more positive V_{BG} to the valence band edge at more negative V_{BG} (6.15 b). Either or both of these effects could be driving the change in the edge's resistance, and therefore more detailed gate dependence measurements are necessary to further understand this effect.

Our observations do not indicate that the states responsible for edge conduction in the non-inverted regime become localized or irrelevant in the inverted regime. Specifically, we do not observe a peak in the resistance of the edge states near the transition from inverted to non-inverted, which would be an indication that the edge states on either side are of distinct origin.

6.5 Discussion of trivial edge states in InAs/GaSb

We have observed edge conduction across the electrically-tuned phase diagram of InAs/GaSb, which is naively very surprising. First, I will discuss the phase diagram in more detail in order

to elucidate what is going on as a function of gate voltage. Secondly, I will outline a basic picture of band bending which could explain the observations, and what the presence of band bending edge states would mean for quantum spin Hall edge states. Thirdly, I will speculate briefly about the implications of our work on previous works claiming the observation of the quantum spin Hall effect in InAs/GaSb.

6.5.1 InAs/GaSb phase diagram

InAs/GaSb's double quantum well structure enables electric field tuning of the band structure [66]. The dual-gate geometry allows one to tune the Fermi level and band gap independently, and therefore tune from an inverted to non-inverted band structure in a single device with large enough electric fields.

The identification of the non-inverted and inverted regimes, done very schematically above, is integral to the conclusions drawn from our work (and associated transport work). The evidence is very suggestive that these assignments are correct, but I do think there is room for more definitive evidence. Therefore, I will outline the experimental evidence below and identify areas where I believe further investigation is warranted.

The experimental evidence for tuning from inverted to non-inverted band structure is mainly gained from magnetotransport measurements [77, 87]. All of the available evidence points towards the electric-field induced topological transition in the bulk. In particular, there are two high-resistance regimes (high resistance relative to the heavily electron and hole doped regions) that exist on the gate phase diagram [87].

The more resistive regime occurs at positive back gate voltage, which is where non-inverted band structure should occur for the layer order of InAs/GaSb studied [87, 77]. From Hall and quantum oscillations measurements, the carriers at all Fermi energies outside the gap are either all electron or all holes, consistent with bands which are not hybridized. The longitudinal resistance's dependence not change significantly with an applied in-plane magnetic field [87]. This fact was used to support the assertion that the bulk band structure did not change significantly with field. However, we now know that transport currents in this region are carried by edge states, and therefore longitudinal resistance is not a sensitive probe of what the bulk is doing.

The most convincing evidence of the non-inverted nature of this region, in my opinion, is that the bulk band gap gets larger with more positive back gate voltages. This is observed by measuring the bulk conductivity versus temperature in a Corbino disk geometry at various gate voltages. The resistance shows Arrhenius behavior and a bulk insulating gap can be extracted. The extracted

energy gap gets larger as more positive gate voltages are applied. Independent of what is going on at negative gate voltages, an inverted gap should open with higher back gate voltage and a non-inverted gap should close (This behavior is reversed if the layer order of InAs and GaSb are switched). The size of the bulk gap, however, is much smaller than is expected [77], which is one observation that is not yet fully understood.

In the second 'high' resistance regime, the magnetotransport behavior is qualitatively different that the previous region, and consistent with an inverted band gap with residual bulk conduction. The Hall and quantum oscillations measurements in this region show both hole and electron carriers near the band edges[87]. The in-plane field longitudinal resistance shows dispersion with field, which was taken as evidence of magnetic field induced changes to the hybridization gap [87].

The overall resistance of this region is much lower, which is consistent with residual bulk conductivity, as we(or the addition of more conductive edge states, which our measurements rule out). The presence of residual bulk conductivity is a unique feature of InAs/GaSb with inverted band structure [75]. Therefore, we can fairly confidently state that the band structure is inverted in this region.

6.5.2 Band bending edge states

We observed conducting trivial edge states in InAs/GaSb, but have yet to speculate on their origin. The obvious candidate is band bending near the lithographically defined edges of the device. A schematic picture of band bending is presented in FIG. 6.16. In the absence of any other states or charge in the system, the conduction and valence band positions remain constant as a function of distance from the edge. However if there is some density of states on the edge of the sample, either due to surface states or adsorption of molecules, the bands can bend [116].

For concreteness, let's add some (non-conducting) states to the edge of the sample, which have their own Fermi energy, and therefore some of them are occupied or unoccupied (FIG. 6.16a). In equilibrium, the Fermi energy must be constant for the whole system. In order to reconcile the difference in Fermi energies, charge is transferred from the non-conducting edge states to the material (FIG. 6.16 b). In other words, the bands of the bulk materials 'bend' near the edges to allow for more electrons (or holes) in order to equilibrate with the non-conducting surface states.

Band bending in InAs has been studied on atomically flat surfaces (e.g. Ref. [5, 85]). Depending on which atomic plane is exposed, how clean it is, whether the surface is passivated, etc., the band bending can be negligible [85] or up to a couple hundred of meV [5, 85]. In these studies, cleaved surfaces of InAs were studied in vacuum, while in our work the surfaces are lithographically

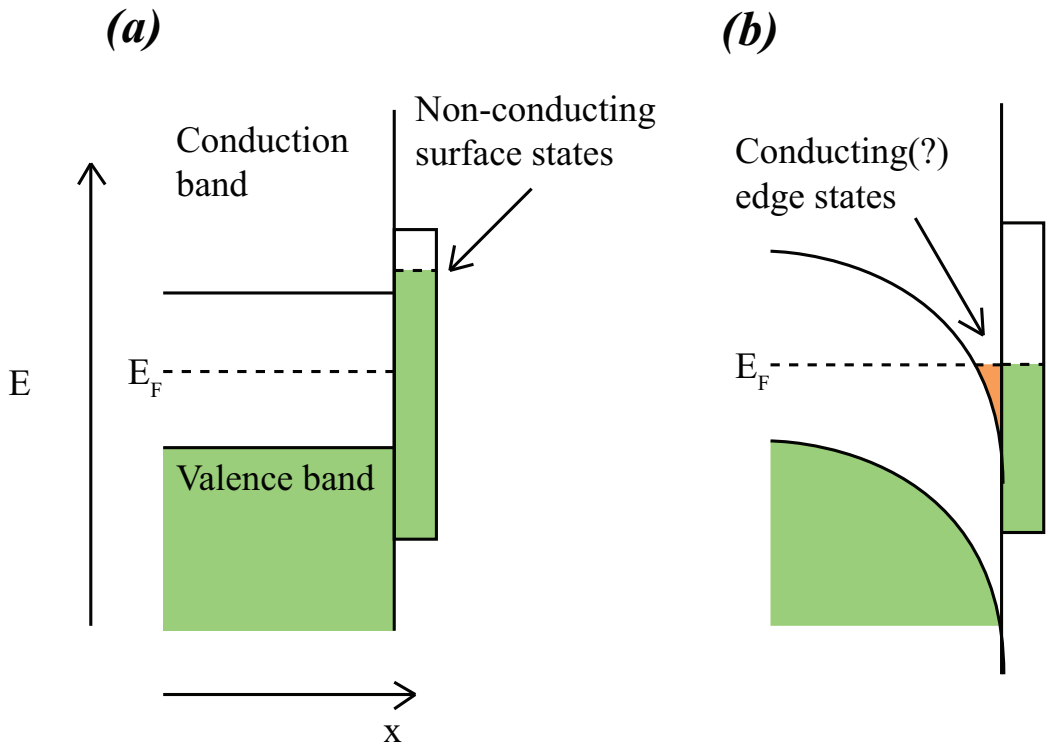

Figure 6.16: **Schematic of band bending in a small band gap system.** Figure inspired by [116]. (a) A schematic band edge diagram of an intrinsically-doped semiconductor with some surface states at a patterned edge which do not contribute directly to transport. This picture is out of equilibrium. (b) In order to equilibrate, charge is transferred from the surface states to the semiconductor. In this case, the bands bend downward to accommodate extra electrons near the edge of the device. In a small band gap system, such as InAs/GaSb or HgTe, the band bending scale can surpass the gap and create edge states which are present throughout the gap and can in principle be conducting.

defined edges, which are presumably extremely disordered in comparison to cleaved surfaces. The very different crystal and chemical properties of lithographic edges and the presence of different materials in the heterostructures makes an estimation of the expected band bending in this material fraught.

However, given the relatively small band gaps (at most a couple of meV) of prospective quantum spin Hall insulators, it certainly seems possible that band bending of order the energy gap could arise from states at lithographically defined edges. Discovering the true origin of trivial edge states on lithographically defined edges will require quite a bit of experimental legwork.

6.5.3 Implications on other InAs/GaSb work

Without measuring dual-gated structures from other groups, it is hard to definitively assign trivial edge states as the culprit for observed quantization [32, 102]. However, in transport work on dual-gated materials in the trivial regime, accidental quantization of non-local resistances was observed on similarly sized samples to those studied in previous works [77]. Additionally, the measured temperature dependence of the edge states in the trivial regime was shown to be temperature independent at high temperatures [77], very similar to the behavior observed in our scanning SQUID measurements and in transport in the nominally inverted regime [99, 32].

Similar lithographic processes were used for all published InAs/GaSb work, so it would be surprising if trivial edge states were not present to some extent in all devices made using similar methods. Detailed length dependence measurements of the quantization for small lengths, (like those performed on trivial edge states in Ref. [77]) would definitively settle whether the quantization of InAs/GaSb conductivity in the inverted regime is accidental or not. Extending dual-gated measurements to Si-doped samples would allow for direct comparison of the behavior of edge states in both regimes and would further elucidate the role of trivial edge states in the inverted regime.

6.6 Conclusion

We've extensively studied the edge states of InAs/GaSb under a variety of conditions. We found that edge states in single-gated, nominally inverted structures exist in both undoped and Si-doped samples, and that the bulk is localized in the Si-doped case. The edges were long and exhibited backscattering, and the backscattering was temperature independent. Temperature independent backscattering is surprising if the edge states are helical, as the only origin we know of for T-independent scattering is single particle elastic backscattering, which is explicitly disallowed in

helical edge states. In dual-gated structures without doping, we observed edge states continuously across a continuously tuned transition from inverted to non-inverted band structure. The presence of conducting edge states in the trivial regime points out the need for much more experimental work to determine the role of trivial edge states in the topological regime in addition to their interaction with possible quantum spin Hall edge states.

Chapter 7

Electric coupling effect in current imaging of ferromagnets

This chapter was previously posted to a preprint server as:

"Electric coupling in scanning SQUID measurements" Eric M. Spanton, Aaron J. Rosenberg, Yihua H. Wang, John Kirtley, Ferhat Katmis, Pablo Jarillo-Herrero, Jagadeesh S. Moodera, Kathryn A. Moler. *arXiv preprint* arXiv:1512.03373 (2015).

7.1 Executive Summary

In Ref.[112], written by several of us, scanning superconducting quantum interference devices (SQUID) were used to investigate the magnetic domain structure and current flow in EuS/Bi_2Se_3 bilayers. A back gate voltage was used to tune the chemical potential of the Bi_2Se_3. At negative gate voltages, images of flux from current applied to the sample ($d\Phi/dI$) showed features which were interpreted as signatures of domain wall currents associated with the quantum anomalous Hall effect (QAHE). The signal in $d\Phi/dI$ (from written magnetic domain structure) scaled with the local voltage of the sample, rather than the current, which was interpreted as evidence of the current's chiral nature.

In the section 7.2, **Sample-SQUID electric coupling model**, we derive a model for electric coupling between the SQUID and sample, which leads to an artifact in $d\Phi/dI$ and $d\Phi/dV$ imaging when the sample is back-gated and magnetic. The charge of the back-gated Bi_2Se_3 device is modulated when a voltage is applied to the sample. The charge of the sample couples electrically to the grounded metal on the SQUID itself. The electric coupling causes the height of the SQUID's

pickup loop above the sample to oscillate when an oscillating voltage or current is applied to the sample. In the presence of magnetic fields from the sample, the gradient of the local magnetic field is coupled into the $d\Phi/dI$ and $d\Phi/dV$ images by the oscillation of the SQUID. We simulated $d\Phi/dI$ images from both chiral currents and the electric coupling artifact, which is proportional to the height derivative of the magnetic image ($d\Phi/dz$). The images from chiral currents and the electric coupling artifact are qualitatively very similar, although the electric coupling artifact is noticeably sharper.

In section 7.3, **Experimental signatures of electric coupling in** EuS/Bi_2Se_3, we compare the theoretical predictions of the electric coupling artifacts to new measurements of the field, frequency, and back gate voltage dependencies of magnetic images of EuS/Bi_2Se_3 bilayers. We found that current and voltage images ($d\Phi/dI$ and $d\Phi/dV$) match the expected features of the electric coupling artifact. Specifically, we imaged $d\Phi/dV$ and found that the sign of the signal reverses sign as a function of frequency and back gate voltage, and the signal disappears when the SQUID is in contact with the sample. These features are not consistent with a signal from chiral currents along domain walls.

Based on these measurements, we've reevaluated the $d\Phi/dI$ images in Ref. [112] in **Implications for Ref. [112]** (section 7.4). We show that the detailed spatial dependence of $d\Phi/dI$ images taken by Wang et al. along the edge of a device (Fig. 2 in Ref. [112]) very closely matches the height derivative of the magnetic image ($d\Phi/dz$), as expected for electric coupling. We also show previously unpublished data taken by Wang et al., showing that the $d\Phi/dI$ features observed in Fig. 2 disappear halfway through a scan, suggesting that the SQUID is in contact. Additionally, sign reversal of $d\Phi/dI$ features as a function of back gate are shown for a written domain.

The results of the new measurements and the presence of strong evidence for the electric coupling artifact in measurements performed for Ref. [112] lead to the conclusion that the results of Ref. [112] are primarily, if not completely due to electric coupling, rather than chiral currents.

Finally, in **Electric coupling in other current imaging experiments** (section 7.5) we briefly comment on other works where scanning SQUID was used to image current, and describe why the electric coupling artifact present in EuS/Bi_2Se_3 SQUID measurements are not responsible for the features observed in those works [81, 48, 99].

7.2 Sample - SQUID electric coupling model

7.2.1 Model of electric coupling

Scanning SQUID is a sensitive local flux to voltage converter. The SQUID's pickup loop is brought very close to a sample and scanned in order to image magnetic fields. Our SQUIDs also have a field coil which is concentric with the pickup loop, and can be used to apply a local field. Our SQUID devices are fabricated on silicon chips, which are polished close to the pickup loop in order to bring it very close to the sample (typically within a few microns).

Our scanning SQUID chip is typically mounted on a copper cantilever (FIG.7.1 a) for scanning. We detect a deflection of this cantilever capacitively when the SQUID chip touches the sample, which gives us topographic imaging of the sample. We can either scan with the SQUID "in contact" with the tip of the polished SQUID chip touching the sample, or "out of contact" which means that the SQUID's tip scans above the sample.

When the SQUID is out of contact it is free to vibrate or deflect if a force is applied to it. We modeled the coupling between grounded metal on the SQUID and the charge on a gated sample (FIG. 7.1 b). The tip of the scanning SQUID (FIG. 7.1 c) has a pickup loop with superconducting shielding (green) and a field coil which also has shielding (purple). Both loops and their shielding are grounded during normal operation of the SQUID. A charge on the sample will exert a force on a grounded metallic SQUID. The Coulomb force will lead to a deflection of the SQUID which depends on the charge accumulated on the sample.

The following model is very similar to how charge is measured in electric force microscopy, however the amount of charge on the sample itself is also modulated by a voltage.

A generic electric equation for the force on the grounded SQUID due to a gated semiconducting sample with a voltage applied to the sample is:

$$F_z = a_1\sigma^2 + a_2(V - V_{CPD})^2 = a_1^*(V_{BG} - V)^2 + a_2(V - V_{CPD})^2 \tag{7.1}$$

where a_1,a_2, and a_1^* are parameters with the appropriate units which depend on the SQUID and sample geometry, σ is the 2D charge density induced in the semiconductor by a back gate, V is the voltage applied to the sample, V_{BG} is the voltage applied to the back gate, and V_{CPD} is the contact potential difference.

The first term is the force between the charged sample and a grounded metallic object, and this is the term which is relevant for this paper. This force will be proportional to the square of the

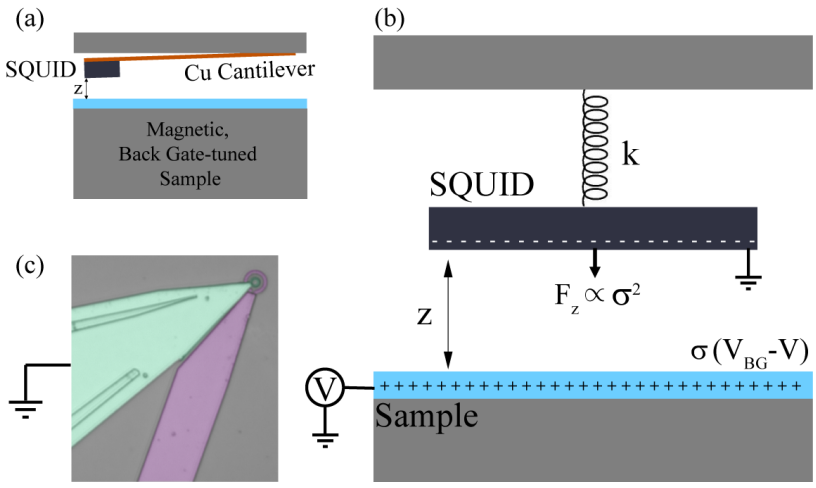

Figure 7.1: **Overview of scanning SQUID measurements and a simple model of electric coupling.** (a) A schematic side view of a scanning SQUID measurement. The SQUID is attached to a copper cantilever, the deflection of which is used to determine when the SQUID is touching the sample. The height of the SQUID above the sample (z) is adjusted with piezo-based scanners (not shown). (b) A schematic of parameters relevant for the electric coupling model. The scanning SQUID's pickup loop, and often times the field coil as well, are electrically at ground during measurements. When measuring current (or in the case of a directly applied voltage) the sample is locally at some voltage, V. The SQUID is attached to a Cu cantilever which has a spring constant, k.The charge density on the sample is fixed by the sample's properties and the applied electric fields. In the case of a gated sample the net charge of the sample can be non-zero. The electric force between the grounded SQUID and the charge on the sample leads to a coupling between height and voltage of the sample (see text). (c) A false color image of a typical SQUID used for scanning, showing the SQUID's pickup loop and shielding (green) and the field coil and it associated shielding (purple).

induced charge on the sample. A second term, which is present due to the applied voltage difference between the sample and SQUID, leads to a term which goes as V^2. The contact potential difference (is a term which is important for Kelvin Probe Force microscopy [80], for example) is typically less than 1 V in magnitude.

The back gate acts as a parallel plate capacitor with the sample and back gate as the plates. Therefore, the induced charge density on the sample will be proportional to $V - V_{BG}$, leading to the second equality in Eqn. 1. For a lock-in measurement, we are only concerned with terms linear in V when we are measuring the 1st harmonic. If V_{CPD} is small, the second term goes primarily as V^2 and will only show up in 2nd and higher harmonics. For the purposes of this discussion we will ignore this term, but it can in principle also lead to other artifacts.

We can now balance the electric force with the restoring force of the cantilever

$$F_z = a_1^*(V_{BG} - V)^2 = k(z - z_0) \tag{7.2}$$

Where k is the spring constant of the cantilever and z_0 is its equilibrium position. Solving for $z - z_0$, we find:

$$\Delta z \equiv z - z_0 = \frac{a_1^*}{k}(V_{BG}^2 + V^2 - 2V_{BG}V) \tag{7.3}$$

Again, since we only are concerned with terms linear in V for lock-in measurements, we can drop the first two terms and find the first harmonic of the response to a sinusoidal excitation:

$$\Delta z = -\frac{2a_1^*}{k}V_{BG}Vsin(\omega t) \tag{7.4}$$

We have now established, for a back-gated sample with an induced charge and a grounded SQUID, that the application of a sinusoidal voltage excitation to the sample can lead to a sinusoidal height variation of the SQUID. This height variation directly couples the gradient of any DC magnetic fields in the sample into a lockin measurement of the SQUID's response.

By applying a voltage to the sample and measuring the SQUID's response, we are measuring the constant component of $\frac{d\Phi}{dV}$. The full measured $\frac{d\Phi}{dV}$, taking into account the above height variation is:

$$\frac{d\Phi}{dV} = \frac{\partial\Phi}{\partial V} + \frac{\partial\Phi}{\partial z}\frac{dz}{dV} = \frac{\partial\Phi}{\partial V} - \frac{2a_1^*}{k}V_{BG}\frac{\partial\Phi}{\partial z} \tag{7.5}$$

The first term is the true change in the flux from the sample due to the applied voltage, for

example from a chiral current which is modulated by gate voltage or from voltage-induced domain wall motion. The second term is the 'electric coupling artifact' term due to linear coupling of the height of the SQUID to the applied voltage, which is the main result of this section.

Similarly, if we want to measure $\frac{d\Phi}{dI}$, there is an electric coupling term. Flowing a current in a resistive sample leads to a voltage drop across the sample. The local voltage of the sample near the SQUID will induce a coupling to the height of the SQUID. The strength of the electric coupling ($\frac{dz}{dI}$) however, will vary as a function of position along the sample and the sample's resistance. In our model, the electric coupling at a fixed position will be proportional to R, ($\frac{dz}{dI} \propto RV_{BG}$).

The electrostatic model established here is simplistic. We have not included a realistic model of the actual form of the electric coupling, a_1^* or the frequency dependence of the response of the cantilever. The electric coupling a_1^*, depends on the geometry and distance between the SQUID and sample and the screening from the sample itself. As the sample becomes more conducting, the screening of the back gate induced charge will decrease the electric coupling coefficient, which in the case of EuS/Bi_2Se_3 means that the electric coupling artifact will be diminished at positive gate voltages, where the sample is more conducting. Additionally, the resonance of the cantilever will also lead to a mechanical resonance-like response in the strength and sign of the electric coupling artifact.

In conclusion, the robust predictions of the electric coupling model presented here are that the electric coupling signal will be proportional to $d\Phi/dz$, it will change sign as a function of back gate voltage, and it will also be proportional to the mechanical response (and any resonances) of the cantilever.

7.2.2 Signals due to chiral currents and electric coupling are qualitatively similar

In the quantum anomalous Hall state, chiral currents flow along the edges of devices and at domain walls [110]. The magnetic fields (specifically the out of plane component, B_z) from chiral currents should be spatially resolvable by scanning SQUID microscopy. We simulated the expected $d\Phi/dI$ images due to currents along the edge of a device and at the wall of a written magnetic domain, and then compared them to the simulated image due to the electric coupling artifact derived above. We find that they are qualitatively similar, and therefore great caution must be exercised in attempting to measure chiral currents in samples with magnetic structure using scanning SQUID.

We simulated images of the expected signals at the edge of a sample with a uniform out-of-plane polarization (FIG. 7.2) and around a written domain (FIG. 7.2). The expected signal from current flowing along the edge of the sample (7.2 c) is qualitatively reproduced by the electric coupling

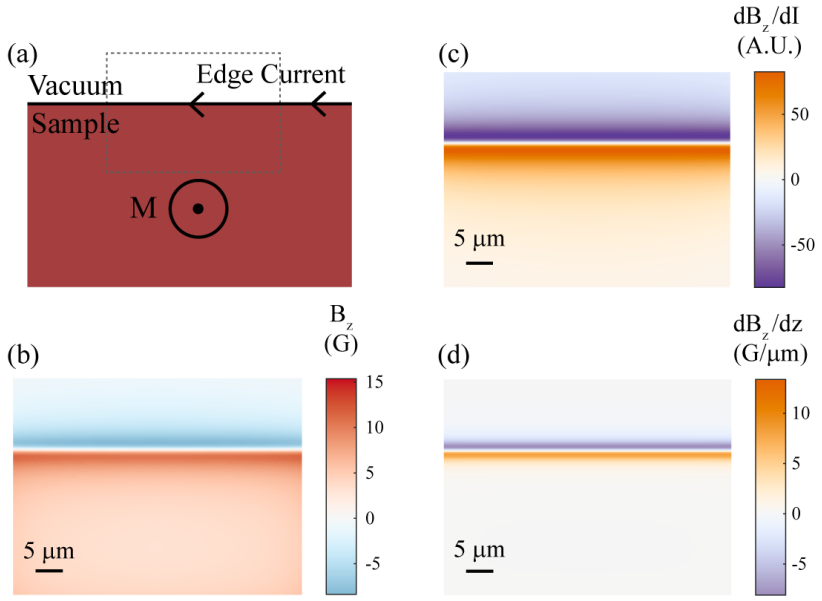

Figure 7.2: **Simulated B_z, $\frac{dB_z}{dI}$, $\frac{dB_z}{dz}$ images at the edge of a polarized out-of-plane ferromagnet** (a) Simulated sample. (b) Simulated B_z image at h=1.5μm. (c) Simulated out of plane field (B_z) from a chiral current along the edge of the sample. (d) Simulated signal from the electric coupling artifact ($\frac{dB_z}{dz}$)

artifact, dB_z/dz (FIG. 7.2 d). Similarly, the current flowing along the domain wall of a written domain (FIG. 7.3 c) looks qualitatively similar to the electric coupling artifact, dB_z/dz (FIG. 7.3 d).

The spatial dependence of the chiral current images and the electric coupling images are different in the details. The chiral current and magnetic field images for out of plane domains, however, are identical up to an overall scaling factor for the geometries we've simulated (FIG. 7.3 b and c). Therefore, comparing images of $d\Phi/dI$ to both Φ and $d\Phi/dz$ gives us another way of discriminating between real chiral current signals and electric coupling artifacts.

In the following section, we will use the SQUID-sample coupling model to show that electric coupling is dominant in new measurements we've performed on EuS/Bi_2Se_3.

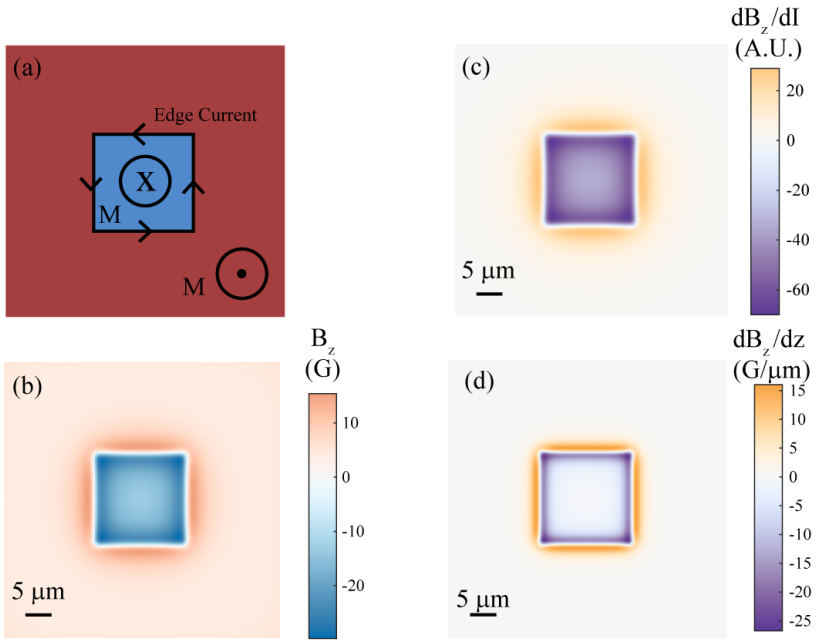

Figure 7.3: **Simulated B_z, $\frac{dB_z}{dI}$, $\frac{dB_z}{dz}$ images of a written square magnetic domain** (a) Simulated square up domain written in a film which is polarized down everywhere else. (b) Simulated B_z image at h=1.5μm. (c) Simulated out of plane field (B_z) from a chiral currents along the domain wall. (d) Simulated signal from the electric coupling artifact ($\frac{dB_z}{dz}$)

7.3 Experimental signatures of electric coupling in EuS/Bi_2Se_3

Here we will give four pieces of evidence that strongly indicate that the electric coupling term is dominant in our new measurement of EuS/Bi_2Se_3 bilayers. We argue that all of the signals observed in this measurement of $d\Phi/dV$ and $d\Phi/dI$ are due to electric coupling. The four pieces of evidence are:

1. Close mapping between $\frac{d\Phi}{dV}$ and $\frac{d\Phi}{dz}$ (FIG. 7.5).
2. Disappearance of the $\frac{d\Phi}{dV}$ and $\frac{d\Phi}{dI}$ signals when the SQUID chip is in contact (FIG. 7.6, also 1 and 2)
3. Characteristic gate voltage dependence of $\frac{d\Phi}{dV}$ and $\frac{d\Phi}{dz}$ (FIG. 7.7) and a sign flip of the signals observed in $\frac{d\Phi}{dV}$ (FIG. 7.7 and 7.8).
4. Mechanical resonance in the frequency dependence of the $\frac{d\Phi}{dV}$ signal (FIG. 7.9)

All of these effects are easily understandable in the model presented above, and hard to reconcile with a signal that arises due to chiral currents along magnetic domain walls and edges.

Typical DC magnetometry (Φ) and $\frac{d\Phi}{dV}$ images are presented in FIG. 7.4. We measured the sample as-cooled, with no external field applied at any point during the cooling process. We focused on a 30 μm x 30 μm area of the device. We found ferromagnetic domain structure in DC magnetometry, the size of which is mostly limited by the SQUID's spatial resolution (FIG. 7.4 a). At large negative V_{BG} ($-200V$), we observe a large signal in $d\Phi/dV$. The spatial pattern of $d\Phi/dV$ is very similar to the domain structure observed in the Φ image (FIG. 7.4 b).

To investigate the signal in a different way, we measured the dependence of Φ and $d\Phi/dV$ on height above the sample (FIG. 7.5 a & b). At a fixed gate voltage and temperature ($V_{BG} = -200V$ & $4.2K$) we measured $\Phi(z)$ and $d\Phi/dV(z)$ and changed the applied out-of-plane field (B_z). $\Phi(z)$ (FIG. 7.5 a) is tuned by the field by changes in the domain structure and the paramagnetic response of the sample. We found that $d\Phi/dV(z)$ appears to be much more sharply varying than $\Phi(z)$ and that $d\Phi/dV$ goes to zero when the SQUID is in contact with the sample.

The electric coupling term in Eqn. 5 is directly proportional to $\partial\Phi/\partial z$, so we took the numerical derivative of Φ with respect to height in order to compare the two. We applied a smoothing filter (over z$\sim 0.1\mu m$) to Φ before taking a numerical derivative, in order to more clearly see the qualitative features. We found that the shape and dependence on field of $d\Phi/dz(z)$ qualitatively

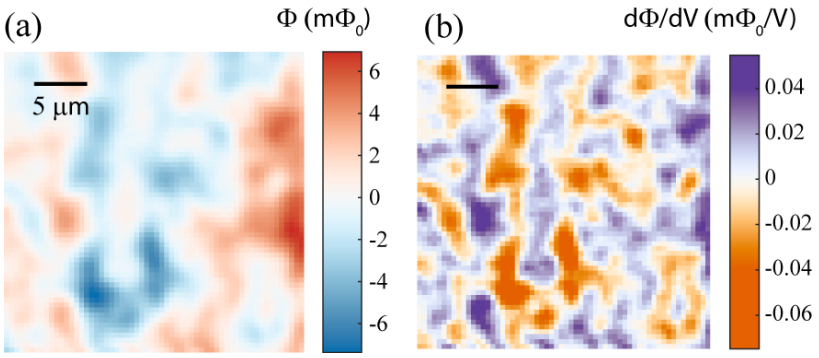

Figure 7.4: **Scanning SQUID DC flux and $d\Phi/dV$ images of a EuS/Bi_2Se_3 bilayer device at V_{BG} = -200 V.** (a) A DC flux images (Φ) of as cooled domain structure in a EuS/Bi_2Se_3 bilayer. (b)$d\Phi/dV$ image taken simultaneously with the Φ image. This image is, as we argue in the text, due to electric coupling between the SQUID and sample in the presence of DC magnetic fields. We applied a voltage directly to one terminal of the device with all of the other terminals floating. This scan was taken at V_{AC}^{pk} = 10 V, f = 685 Hz, with the SQUID's chip out of contact with the sample.

matches that of $d\Phi/dV(z)$ (Fig. 7.5 c & d). Specifically, both are significantly sharper than Φ and are strongly reduced while in contact with the sample.

The sharp height dependence of $d\Phi/dV(z)$ and its similarity to corresponding $d\Phi/dz(z)$ curves are suggestive that electric coupling is responsible for the observed signal. The disappearance of $d\Phi/dV$ when the SQUID is in contact with the sample is, we believe, a strong piece of evidence that the $d\Phi/dV$ signal is indeed the electric coupling artifact. To further investigate this, we imaged of $d\Phi/dI$ in and out of contact (FIG. 7.6).

When the SQUID's chip is in contact with the sample, we expect the electrically-induced vibration of the SQUID to be strongly damped due to the restoring force of the sample itself. We imaged Φ both in contact and out of contact (FIG. 7.6 a & b). The only difference between in contact and out of contact Φ is the sharpness of images, which is because magnetic field lines spread as distance from the sample increases. The $d\Phi/dI$ images both in contact and out of contact (FIG. 7.6 c & d) are qualitatively different. Out of contact, (FIG. 7.6 d), we primarily observed a similar structure to what is observed in $d\Phi/dV$ (FIG. 7.4 b). However, when we imaged $d\Phi/dI$ in contact (FIG. 7.6 c) the magnetic domain-like features completely disappear. We were left only with a plane-like spatial dependence, consistent with homogeneous current flow in the device.

The stark difference in the measured $d\Phi/dI$ in and out of contact makes sense if the magnetic-domain like signals in $d\Phi/dI$ are due to electric coupling. In $d\Phi/dV$ the magnetic domain-like feature disappear in contact as well (as we showed in height dependence, FIG. 7.5). Additionally,

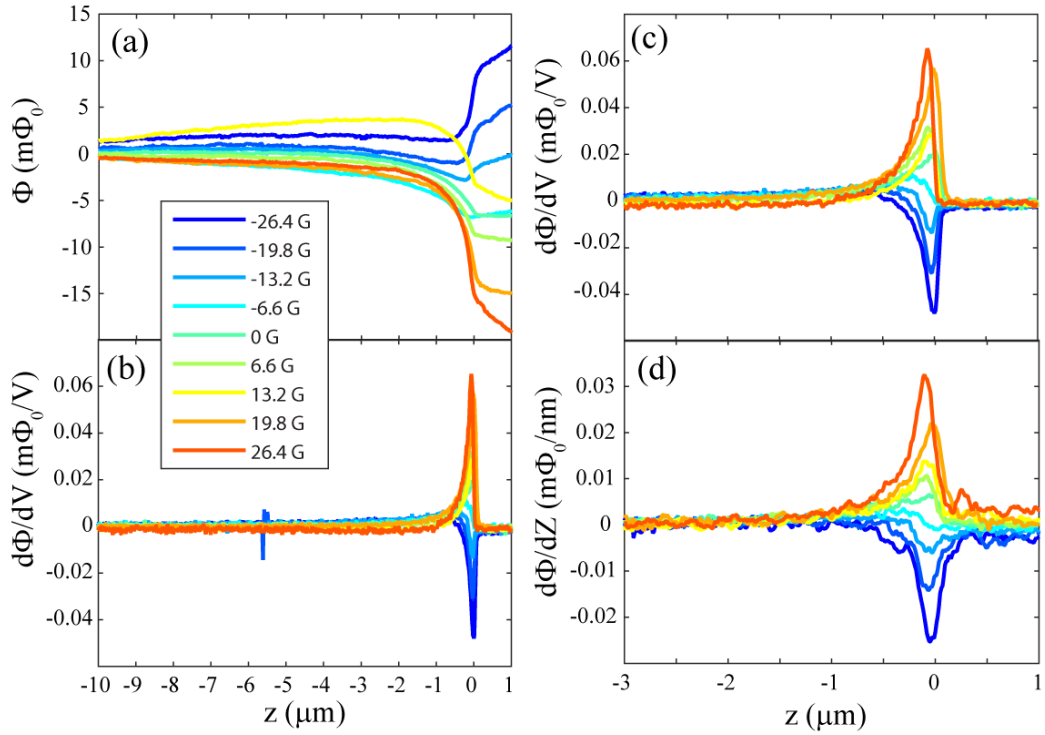

Figure 7.5: Φ, $d\Phi/dV$, **and numerically determined** $d\Phi/dz$ **height dependencies as a function of applied out of plane magnetic field.** (a) Φ vs. height of the SQUID above the sample. Negative heights indicate the distance above the sample, while positive distances indicate that the SQUID's chip is touching the sample, and does not actually reflect the true height above the sample. $\Phi(z)$ changes significantly as a function of an applied field out of plane field, which occurs due to a combination of the paramagnetic response of the sample and changing domain structure. (b) $d\Phi/dV$ as a function of height. We find that similar to $\Phi(z)$, $d\Phi/dV$ (z) changes strongly with applied field. (c) A zoomed in plot of (b). (d) Numerically determined $d\Phi/dz$ curves obtained from the $\Phi(z)$ curves (see main text). We find that the dependence of $d\Phi/dV(z)$ and $d\Phi/dz(z)$ are qualitatively very similar, as expected from electric coupling. Specifically, the magnetic field at which the touchdown curves change sign, the relative heights of the curves, and the strong reduction of the signals when the SQUID chip is in contact with the sample all point toward the electric coupling explanation.

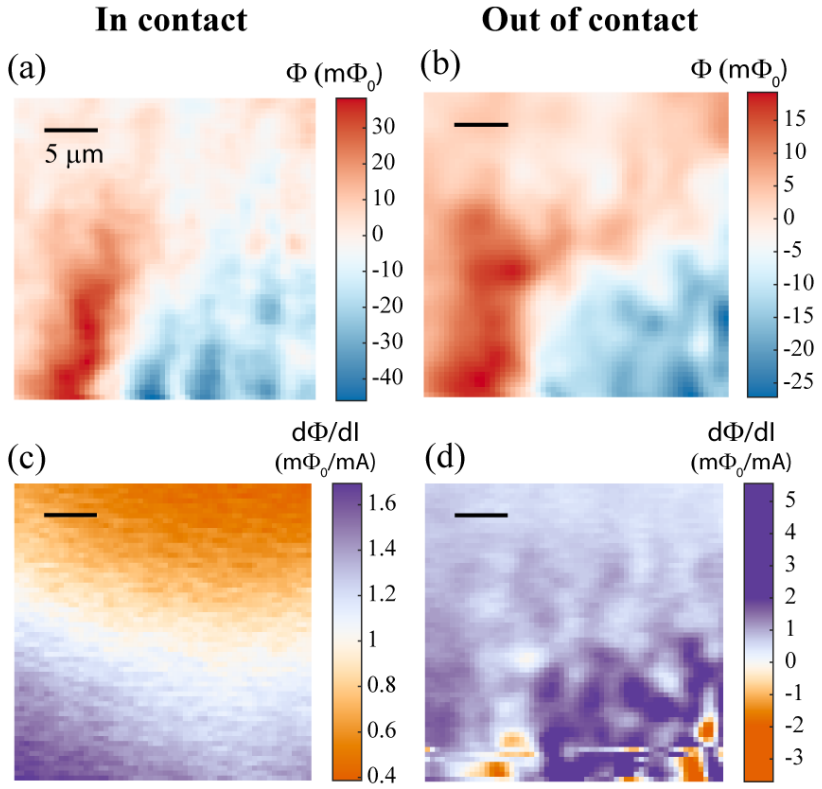

Figure 7.6: Φ **and** $d\Phi/dI$ **images with the SQUID's chip in and out of contact with the sample.** (a,b) Φ images in contact and out of contact, respectively. In contact (a), the ferromagnetic domain structure was more strongly resolved due to reduced spread of the magnetic fields originating from the sample. (c,d). $d\Phi/dI$ images in and out of contact, respectively. In contact (c), we found that the current flow image was smoothly varying and did not match the domain pattern, consistent with bulk current flowing in the sample. Out of contact (d), the magnetic domain like features appear in $d\Phi/dI$ image, washing out the bulk current signal. The stark difference between $d\Phi/dI$ (and also $d\Phi/dV$) images taken in and out of contact are only easily understandable if the features are due to electric coupling.

the apparent lack of any domain-like signal while the SQUID is in contact shows that there is no measurable signal from chiral currents in this particular image.

Another explanation for the in contact behavior could be that the voltage applied to the sample is shorted to the SQUID. We checked this possibility by putting the SQUID in contact with the sample while applying a DC voltage and measuring leakage. We did not observe any leakage current from the sample to ground, indicating that shorting was not an issue in this measurement. The presence of an insulating layer on top of the sample (AlO_x) makes shorting unlikely. In previous experiments on top-gated samples, we have observed shorting of a couple of volts to the SQUID, and in these cases we were unable to successfully take SQUID images due to the shorting. These problems were not present in EuS/Bi_2Se_3 measurements, indicating that shorting was most likely not occurring while imaging.

We compared $d\Phi/dV(z)$ and $d\Phi/dz(z)$ as a function of V_{BG} to further corroborate the electric coupling explanation. In order to maximize the observed signal, we applied an out of plane field B_z = -26.4 G. Looking back at Eqn. 5, we expect the electrically-induced vibration, and therefore the electric coupling term in $d\Phi/dV$ to change sign with V_{BG}. We measured $d\Phi/dV$ and $d\Phi/dz$ as a function of V_{BG} (FIG. 7.7) and found that while $d\Phi/dV$ varied strongly and ultimately flipped sign at positive V_{BG}, $d\Phi/dz(z)$ varied considerably less. The relative sign between $d\Phi/dz(z)$ and $d\Phi/dV(z)$ changed between V_{BG} = 0 and -25 V., which is consistent with what we predicted in Eqn. 5. The fact the sign of $d\Phi/dV(z)$ changes at a non-zero V_{BG} indicates that the heterostructure's flat band voltage is non-zero, which is plausible.

The sign change of $d\Phi/dV$ is predicted by electric coupling, but inconsistent with a chiral current explanation. We further showed this by taking images at many V_{BG} around zero voltage in zero applied field (FIG. 7.8). We found that the DC magnetic features remained constant (FIG. 7.8 a-e), while the relative sign of the features in $d\Phi/dV$ flipped between V_{BG} = 0 and -25 V. As grown Bi_2Se_3 is strongly n-doped, so the presence of any chiral current features near V_{BG} = 0 V is highly unlikely, but the sign flip of the features is inconsistent with a signal from chiral currents.

Finally, we also observed that the features in $d\Phi/dV$ flipped sign as a function of the frequency of the voltage excitation (FIG. 7.9). The features in $d\Phi/dV$ images (FIG. 7.9 a-d) match the domain structure observed in Φ (FIG. 7.9 e), however the features in $d\Phi/dV$ flipped sign around f=600 Hz. To further show the frequency dependence, we plotted the $d\Phi/dV$ value in the bottom left corner of this area at many frequencies (FIG. 7.9 f). We found $d\Phi/dV$ signal's sign flipped and its magnitude peaked at f$\sim$ 600 Hz.

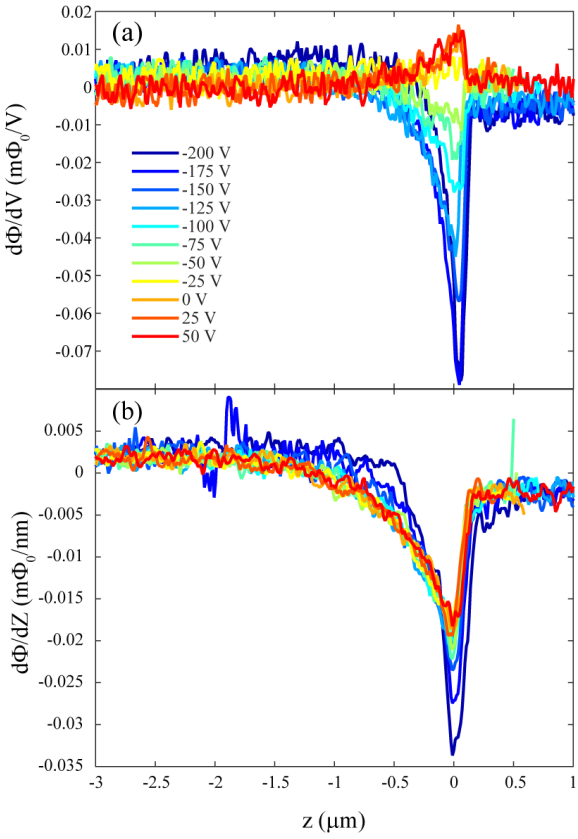

Figure 7.7: $d\Phi/dV$ **and** $d\Phi/dz$ **as a function of back gate voltage.** This data was taken in an applied field of B_z = -26.4 G, V_{AC}^{pk} = 10 V, f_{AC} = 271.06 Hz. (a) $d\Phi/dV(z)$ as a function of back gate voltage. We find that $d\Phi/dV(z)$ changes sign at approximately $V_{BG} - 25V$, consistent with a sign flip around zero volts from our basic model of the electric coupling. We have subtracted a constant offset from the data far away from the sample, which became nonzero at positive gate voltages. (b) $d\Phi/dz(z)$ curves as a function of gate voltage. We took the numerical derivative of $\Phi(z)$ and found that the sign does not switch when the sign of $d\Phi/dV(z)$ changes. This means that dz/dV must change sign if the $d\Phi/dV$ signal is from electric coupling, which is predicted by our electric coupling model.

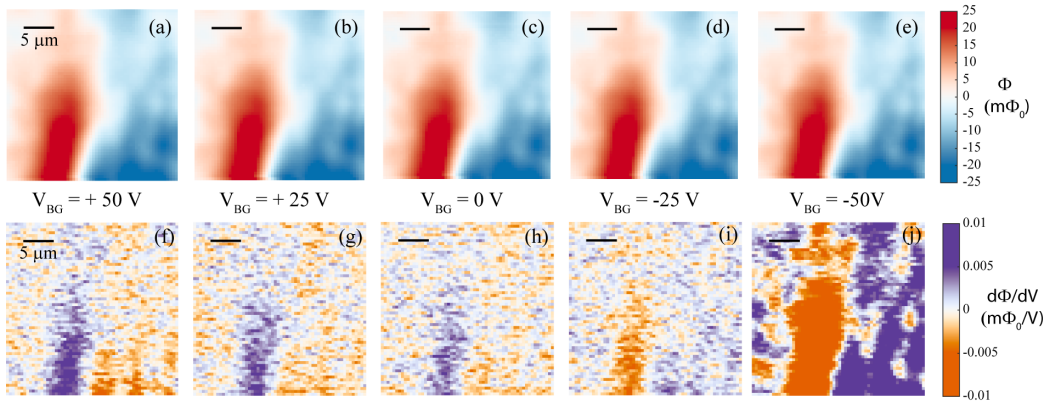

Figure 7.8: Φ **and** $d\Phi/dV$ **images as a function of gate voltage show a sign flip of the features observed in** $d\Phi/dV$ **between VBG = 0 and -25 V.** Images were taken at f=612.4 Hz, V_{AC}^{pk} = 10 V, B_z= 0 G. (a)-(e) Φ images of ferromagnetic domains as a function of back gate voltage, showing little dependence. (f)-(j) $d\Phi/dV$ images as a function of gate voltage, showing that the relative sign of features in $d\Phi/dV$ change sign as a function of gate voltage.

The frequency dependence of $d\Phi/dV$ strongly indicates a mechanical resonance of the SQUID's cantilever. In our derivation of the electric coupling we assumed static forces, and therefore did not take any mechanical resonance of the cantilever into account. A resonance leads to a frequency dependence which would also affect the magnitude and sign of dz/dV and therefore the electric coupling term in $d\Phi/dV$. We roughly estimated the resonance of our Cu cantilever using Copper's room temperature values for the Young's modulus (E = 130 GPa) and density ($\rho = 9g/cm^3$), and approximate size of the cantilever's thickness and length ($T = 100\mu m$ & L = 10 mm). We calculated $f_0 \sim$ 600 Hz, close to the measured resonance.

We have performed careful height, field, frequency, and V_{BG} dependencies of $d\Phi/dV$ and $d\Phi/dI$ and compared them to predictions for the derived trivial electric coupling term. The disappearance of the magnetic-domain like signal in $d\Phi/dV$ and $d\Phi/dI$ in contact, and the sign flips of the observed signals as a function of frequency and V_{BG} are all easy to explain by electric coupling and extremely hard to reconcile with a signal from chiral currents along domain walls.

7.4 Implications for Ref. [112]

We have demonstrated in the previous section that electric coupling is completely responsible for the observed $d\Phi/dV$ and $d\Phi/dI$ images in a new measurement on EuS/Bi_2Se_3 bilayers. We will now analyze the images obtained in the studies that led to Ref. [112] and argue that they are also

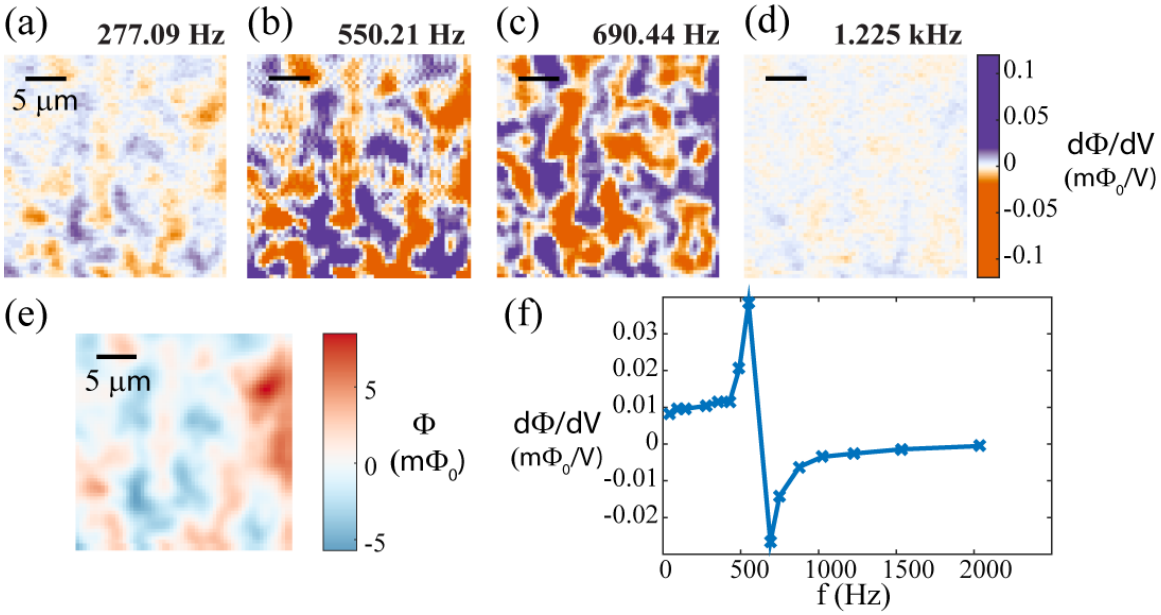

Figure 7.9: **Frequency dependence of $d\Phi/dV$ images shows a mechanical resonance.** (a)-(d) $d\Phi/dV$ images as a function frequency show that both the amplitude and sign of the features in the images change with frequency. The sign change happens around 600 Hz, consistent with the calculated resonance expected for the Cu cantilever on which the SQUID sits. (e) Φ image of the same area for reference, it does not change with frequency of the applied voltage. (f). The measured in phase $d\Phi/dV$ signal at a fixed point on the scans (bottom left corner) as a function of frequency. The sign change and amplitude dependence with frequency closely matches that of a mechanical resonance.

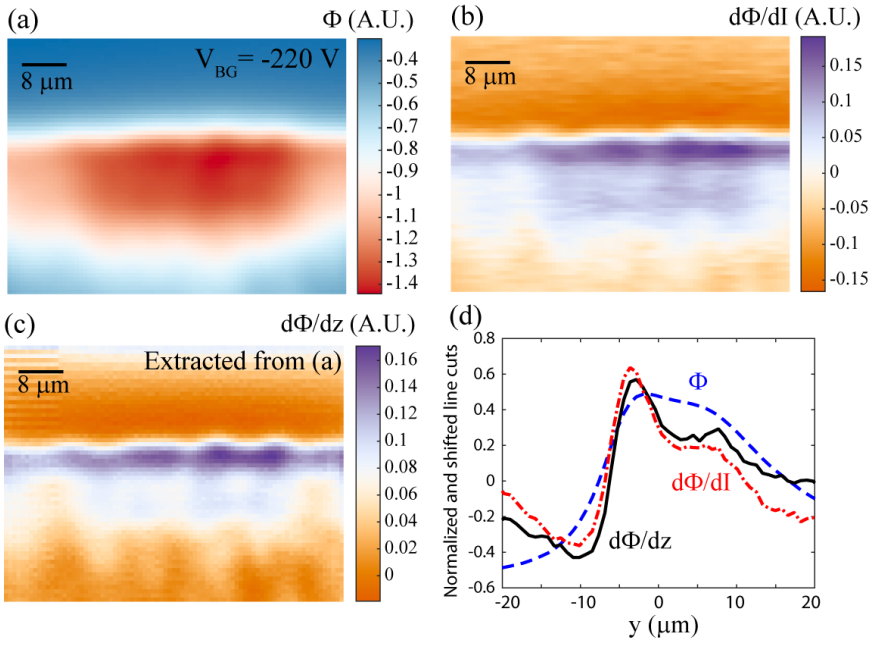

Figure 7.10: $d\Phi/dI$ **edge image from Ref [112] closely match extracted** $d\Phi/dz$ **images.** (a) (same as FIG. 2B from [112]). Magnetic flux image (Φ) of the edge of a sample which has been cooled in an out of plane field. (b) (same as FIG. 2E from [112]) Measured magnetic response from current ($d\Phi/dI$) taken simultaneously, showing what qualitatively matches the expected signal from edge currents. (c) Extracted $d\Phi/dz$ from height propagation of (a), see the main text for details. $d\Phi/dz$ reproduces the features observed in (b). (d) Normalized and shifted vertical line cuts of (a-c), showing the shape of $d\Phi/dI$ (red dot dashed line) more closely matches $d\Phi/dz$ (black solid line) than Φ (blue dashed line).

caused by electric coupling, rather than chiral currents.

We will first show that the $d\Phi/dI$ images from Ref. [112] match very closely the spatial dependence expected for the electric coupling artifact ($d\Phi/dz$) by propagating the Φ images in height. Specifically, we have reproduced Fig. 2 B & E from Ref. [112] in FIG. 7.10 a & b.

In order to extract $d\Phi/dz$ from a single magnetometry image, we utilized Fourier techniques to propagate the magnetic image up in height:

$$\Phi(z = h + dh) = IFFT[e^{-kdh} FFT[\Phi(z = h)]] \tag{7.6}$$

Where FFT and IFFT are the 2D fast Fourier transform and its inverse, k is the magnitude of the spatial frequency $\sqrt{k_x^2 + k_y^2}$, h is the height of the SQUID above the sample, and dh is the height we have propagated the magnetic image [90].

In order to get $d\Phi/dz(h)$, we then subtract the two images:

$$\frac{d\Phi}{dz}(h) \approx \frac{\Phi(h) - \Phi(h + dh)}{dh} \tag{7.7}$$

We found that the extracted $d\Phi/dz$ image (FIG. 7.10 c) is nearly identical to the spatial structure in the measured $d\Phi/dI$ image (FIG. 7.10 b). This is strongly suggestive evidence that the observed signal in Ref. [112] is due to electric coupling.

From simulations (see FIG. 7.2 & 7.3), we found that the spatial dependence of a chiral current signal more closely matches the spatial dependence of the magnetic fields from an out of plane domain, rather than its height derivative. Specifically, for out-of-plane domains, the magnetic fields from a fully polarized domain are equivalent to a current flowing along the edge of the domain. This is a generalization of $\mu = Ia$, where μ is the magnetic dipole moment of a small dipole, and I is the current flowing in a loop of area a.

The spatial dependence of the $d\Phi/dI$ image presented in Ref. [112] is nearly identical to what we expect for electric coupling ($d\Phi/dz$), and is sharper than the magnetic fields we naively expect for chiral currents along the edge of an out of plane polarized domain structure. Line cuts of the images (FIG. 7.10 d) further show the similarity between the simulated $d\Phi/dz$ and $d\Phi/dI$.

Next, we will look at unpublished data that was taken in the same cooldowns as the results presented in Ref. [112]. We show that two of the main pieces of evidence for electric coupling in the new measurements are also present in those data sets. Specifically, the $d\Phi/dI$ images observed in Ref. [112] also disappear while the SQUID is in contact, and signals of reversed sign are observed at large positive back gate voltages for written domains.

Taken in sequence with the other gate voltage images shown in Fig. 2 of [112], an image was taken at V_{BG} = -280 V, where $d\Phi/dI$ goes to zero for a large portion of the scan (FIG. 7.11). This disappearance of $d\Phi/dI$ during the scan was previously interpreted as an inhomogeneous back gate voltage distribution in the sample before an equilibrium of charge distribution was reached. However, a more likely explanation for this effect is that the signal disappears in contact, and that the SQUID is touching the sample for the right half of the image.

The right side of FIG. 7.11 b shows that while the SQUID is contact, there is no observable signal indicating an edge current. This indicates that not only is the electric coupling artifact present in these measurements, but that it accounts for all of the signal observed in the left half of the scan.

In combination with the effects described in previous section, we have also observed in multiple cooldowns that the voltage applied to the piezo-positioner which is required to touch the sample with the SQUID varies as a function of V_{BG}. We found that the SQUID seems to 'snap to' the

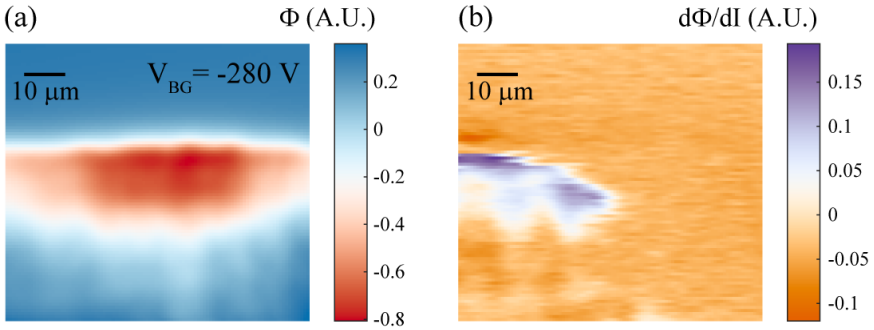

Figure 7.11: $d\Phi/dI$ **edge image taken in the same gate series presented in Ref [112] shows the signal disappearing in contact.** (a) Magnetic flux image (Φ) of the edge of a sample which has been cooled in an out of plane field. Both images were taken at V_{BG}= -280 V. (b) Measured magnetic response from current ($d\Phi/dI$) taken simultaneously, showing what looks like edge currents disappearing in the right half of the image. This is most likely because the SQUID is touching the sample for the right half of the image due to a scan plane error, and the signal disappears in contact. The lack of any signal in the right half of the image puts strong limits on the real chiral current signal present at this gate voltage. It is less than 5% of the signal observed when the SQUID was out of contact.

sample at large negative gate voltages. In other words, a DC electric force leads to height variation for images taken with nominally the same parameters. We believe that this effect, in combination with the disappearance of the signal when the SQUID is in contact, can explain the lack of a signal observed at $V_{BG} = -350V$. Images of the same sample, in the same cooldown, show strong signals in $d\Phi/dI$ at a similar back gate voltage ($V_{BG} = -357V$), showing that it is likely that Fig.2F from Ref. [112] was taken in contact with the sample.

A sign reversal of the $d\Phi/dI$ signal was observed between large negative and positive gate voltages in unpublished measurements by Wang, et al. on domain structure written with the field coil (FIG. 7.12). Domain structure was written by applying an inhomogeneous DC magnetic field with the field coil, similar to what was done for Fig. 4 in Ref. [112]. The sign of the $d\Phi/dI$ signal switched between large negative and positive back gate voltages (FIG. 7.12 c & d). This is inconsistent with a signal from chiral currents, and can be explained by the electric coupling artifact.

The $d\Phi/dI$ signal at large positive V_{BG} was significantly weaker than at large negative V_{BG}, roughly a factor of 20 for bias voltages applied to the same end of the sample. The asymmetry in signal size is not predicted by our simple model. Multiple factors can in principle contribute to the asymmetry, including height differences between the scans, differences in the actual applied local voltage due to contact resistance, differences in the screening length, and the contribution of

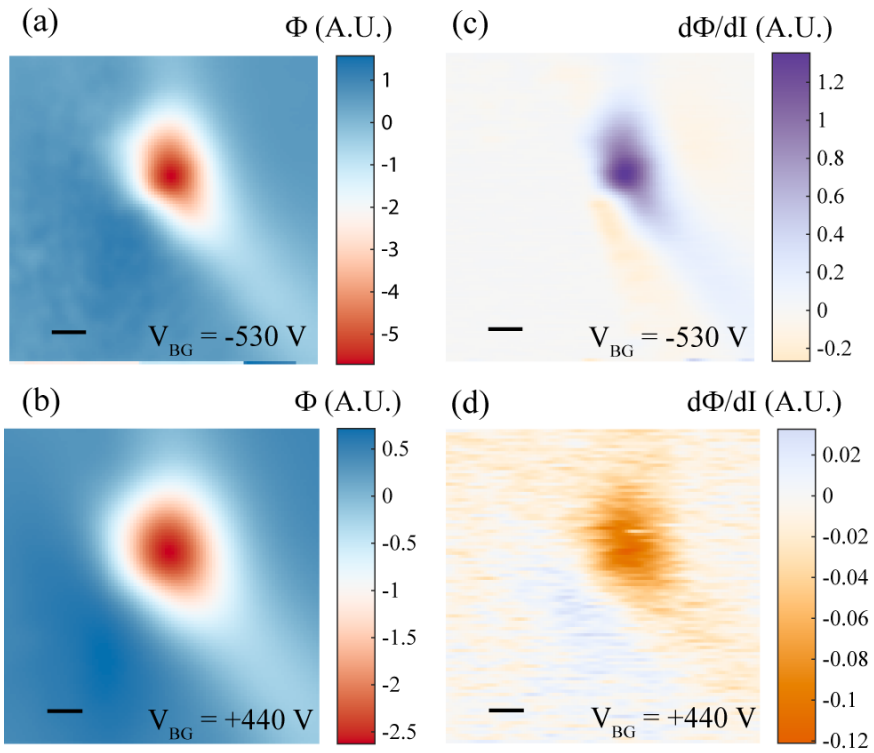

Figure 7.12: $d\Phi/dI$ **images taken over domain structure written by the field coil (similar to Fig. 4 from Ref. [112]) show a sign reversal between large positive and negative gate voltages** (a,b) Magnetic flux images (Φ) of field coil written domain structure at V_{BG} = -530 V and +440V, respectively. The sample appears to be farther away in (b). (c,d) Measured magnetic response from current ($d\Phi/dI$) taken simultaneously with (a,b), respectively. The sign of the main feature changes from positive to negative as the sign of the gate voltage is changed. This is consistent with the electric coupling explanation, specifically the prediction of a sign flip of the electric coupling artifact in Eqn. 5. Here we have presented images taken with the voltage applied to different ends of the sample. The magnitude of the signals with the applied voltage to the same side of the sample are approximately a factor of 20 weaker at positive gate voltages than at negative gate voltages. We attribute the difference in the size of the $d\Phi/dI$ mainly to the effects of screening at positive gate voltages and V_{BG} dependent scan height (see text).

a true chiral current signal at negative gate voltages. The asymmetry is also observed at lower gate voltages in the new measurements, where we have ruled out the presence observable chiral current signals by scanning in contact. Therefore we believe the asymmetry does not require the presence of chiral currents. The large difference in signal size can be accounted for by taking into account screening and height.

For Fig. 7.12, we estimate that the difference in size of $d\Phi/dz$ due to V_{BG} induced height differences between negative and positive gate voltages is $\sim$3 by the looking at calculated $d\Phi/dz$ images. In Fig. 7.8, we observed a factor of 5 difference between positive and negative gate voltages. At low voltages, we do not observe a large height shift in Φ images (FIG. 7.8 a-e), so we attribute this factor of 5 mainly to screening effects. Therefore, height and screening effects contribute a lower bound of a factor of $\sim$15 to the asymmetry between positive and negative gate voltage $d\Phi/dI$ images, which is close to the observed factor of $\sim$20.

We have shown that the signal observed in Ref. [112] is consistent with a signal that is due to electric coupling between the SQUID and the EuS/Bi_2Se_3 device. The measured current image $d\Phi/dI$ at the edge of the sample very closely matches the extracted $d\Phi/dz$ image, and is naively 'too sharp' to match the expected spatial variation expected for chiral currents. We also found evidence that the signal in unpublished measurements done in the same experiments as Ref. [112] disappeared when the SQUID was in contact, and flipped sign between negative and positive back gate voltages.

Taken together with the electric coupling model developed in this paper and the new measurements performed on EuS/Bi_2Se_3, we have shown that the signals reported in Ref. [112] are dominated by electric coupling and show no clear evidence of chiral currents.

7.5 Electric coupling in other current imaging experiments

Scanning SQUID has been utilized to measure $d\Phi/dI$ and reconstruct current densities in $LaAlO_3/SrTiO_3$, HgTe quantum wells, and InAs/GaSb quantum wells ([81, 48, 99]). In HgTe and InAs/GaSb, we observed current along the edges of the devices for certain top gate voltages. In $LaAlO_3/SrTiO_3$, we observed that the more current flowed along features due to the tetragonal domain structure of STO. The electric coupling effect described above cannot explain the main observations of those papers for a number of reasons.

Most important, there were no features in Φ which match the observed current features in any of the previous scanning SQUID results. The electric coupling artifact produces features in $d\Phi/dV$ or

$d\Phi/dI$ which qualitatively match the signal observed in Φ. If the samples are non-magnetic (Φ = 0, and therefore $d\Phi/dz$ = 0), then the electric coupling term in Eqn. 5 also goes to zero. In both HgTe and InAs/GaSb, there were no observed features in Φ. In $LaAlO_3/SrTiO_3$, some of the observed samples were magnetic, as discussed in [10], however this magnetism occurred in resolution-limited magnetic dipoles, which does not match the quasi 1D features observed in $d\Phi/dI$.

Additionally, in both HgTe and InAs/GaSb the gates are top gates rather than back gates, which significantly changes the electric field environment. Both top and back gates modulate the charge on the device itself, but the metallic top gate is between the grounded SQUID and the sample, which will strongly screen the charge on the sample from the SQUID, resulting in an extreme reduction electric coupling.

7.6 Conclusion

In conclusion, electric coupling between the SQUID and sample can lead to an electric coupling artifact in a specific type of measurement and sample. Specifically, $d\Phi/dI$ and $d\Phi/dV$ measurements of back-gated semiconducting samples with magnetic features. Any SQUID measurements of this type should be very strongly scrutinized. The electric coupling effect is present and the dominant signal in our new measurements of EuS/Bi_2Se_3, and can also explain all of the observations of Ref. [112].

If the sample is non-magnetic or top-gated, or the measurements are not $d\Phi/dI$ or $d\Phi/dV$, the electric coupling effect described here will not be relevant.

Chapter 8

Current-phase relations in few-mode InAs nanowire Josephson junctions

This content of this chapter is also part of a publication which is in progress

"Current-phase relations in few-mode InAs nanowire Josephson junctions"

Eric M. Spanton, Mingtang Deng, Peter Krogstrup, Jesper Nygård, Charles M. Marcus, Kathryn A. Moler

8.1 Introduction

Proximitized superconductivity in high-spin orbit or topological systems is of great interest due to the prediction of Majorana quasiparticles with non-Abelian statistics. Semiconductor nanowires have so far shown the most promise in realizing the sought after quasiparticle [74, 25, 29]. Additionally, clean, gate-tunable nanowires are of interest for superconducting qubits [61, 27]. Recently, the growth of epitaxial aluminum on InAs nanowires has shown a large reduction of in-gap states [60, 21], which is of interest for both Majorana and nanowire-based qubit proposals.

The current-phase relation (CPR) of a Josephson junction is the relationship between the current flowing through the junction and the phase difference between the superconducting leads. Near the superconducting critical temperature (T_c), the current-phase relation is generically sinusoidal with an amplitude which is the junction's critical current (I_c). At low temperatures, however, the behavior of the CPR can deviate from sinusoidal behavior in a variety of ways depending on the properties of the junction. Current-phase relations are a unique, non-contact method for measuring the properties of junctions made of novel materials.

The shape of a CPR can reveal a lot of information about the properties of novel Josephson junctions[38]. For example, an arbitrary phase shift in the CPR can arise due to spin-orbit coupling or in topological junctions in so-called 'ϕ_0' junctions [103]. A doubling of the normal periodicity (4-π periodicity or fractional Josephson effect) and telegraph noise associated with switching between different 4-π periodic branches is an expected signature of topological and Majorana junctions [35]. A backward-skewed shape can occur due to pair breaking processes in the superconducting contacts [38]. Lastly, a forward-skewed shape of the CPR can occur in high transmission superconductor-normal-superconductor (SNS) junctions.

8.2 Methods

Direct measurements of the current-phase relation have been performed on a number of materials systems, but are not a widespread experimental technique. One method of measuring the CPR is by using an on-chip inductive readout to measure the signal from a single-junction ring, either using a SQUID or RC tank circuit (e.g. [33]). In order to read out the current, the single-junction structures can require very high self-inductances, limiting their applicability to high critical current junctions and leading to artifacts in the shape of the CPR. Another method requires measuring an asymmetric SQUID with a large critical current junction with a known CPR. These types of measurements have been very successful in observing phase shifts of the CPR, most recently finding ϕ_0-junction behavior [103]. Extracting the shape of the CPR from such measurements requires very precise knowledge of the CPR of the reference junction, which is not always possible.

Recently, our group has inductively measured CPRs in 3D topological insulator Josephson junctions [97, 98]. Here, we extend this measurement technique to low temperatures, junctions with a small number of conducting modes, gate-tunable junctions, and more precise determination of the shape of the CPR.

We measured Josephson junctions in a single-junction ring geometry (FIG. 8.1 a), where the phase drop across the junction (ϕ) was tuned by an applied flux (Φ_A) through the ring, and the current in the ring (I_{ring}) was measured inductively. We used scanning superconducting quantum interference device (SQUID) microscopy, which allows us to measure many single-junction rings on a single chip. The SQUID's pickup loop was used to inductively detect the current flowing in a ring while the SQUID's field coil was used to apply a local field to thread flux through the ring. (FIG. 8.1 a). The size of the rings was selected to optimize pickup loop - ring and field coil - ring mutual inductances. Our SQUID devices are gradiometric, so the flux through the pickup loop due

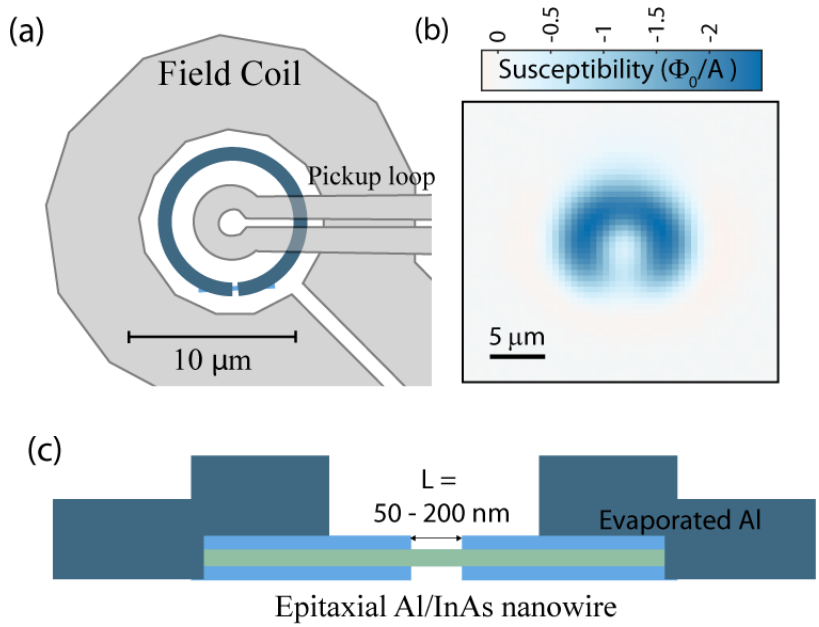

Figure 8.1: **Schematic of current-phase relation measurments of Al/InAs nanowire/Al Josephson junctions.** (a) Schematic of a scanning SQUID CPR measurement of an Al ring with a single InAs nanowire junction. A sketch of the field coil / pickup loop pair (gray) shows the relative size of the SQUID components to the junction and ring (blue). The field coil carries a current that threads a flux through the Al loop and hence a phase across the InAs nanowire junction. The pickup loop measures the change in flux. (b) A typical local susceptibility image of a ring, which shows the diamagnetic response of the evaporated Al ring. Susceptibility images were used to center the SQUID's pickup loop and field coil over the ring for CPR measurements. (c) A side view schematic of the junction. The InAs nanowires have a thin layer of epitaxial Al, a variable length (L) of which was etched away to create the normal junction. The evaporated Al (which directly contacts the epitaxial Al) forms the ring.

to the applied field was largely canceled [43].

In addition to the signal from currents circulating the ring, the SQUID is also able to image the local diamagnetic susceptibility of the Al ring itself (FIG. 8.1 b). We used the diamagnetic response of the Al to position the SQUID over the center of the ring. We also observed a reduction in the diamagnetic screening at the position of the junction in the ring FIG. 8.1 b).

The junctions we studied are InAs nanowires (radius $\approx 50 - 60nm$) which were coated on all sides ('fully-coated') with epitaxial Al (thickness $\approx$ 20-25 nm), whose growth is described in Ref. [60]. The Al of the fully coated nanowires was then etched to reveal a variable length (50-200 nm) of bare InAs nanowire (L). This unetched length forms the normal part of the SNS junction. The ends of the nanowire which are still coated in epitaxial Al were then connected into a ring geometry using evaporated Al (thickness $\approx$ 120 nm) FIG. 8.1 c).

We measured three different samples (sample A,B,C) each of which contained many single-junction rings. The first sample (sample A) had a relatively low yield of measurable CPRs. Many of the rings in sample A had critical currents beneath our detection threshold ($I_c <\sim$ 5 nA) or were hysteretic ($I_c >> 1\ \mu A$). We speculate that the hysteretic junctions which were shorted by Al due to imperfect etching, as their properties were similar to control rings without any etching. In sample B, we pre-screened junctions for possible shorts and the number of hysteretic junctions was correspondingly much lower. For rings which had non-hysteretic behavior, I_c's ranged from 10 nA to a couple of μA. The critical currents of sample B were much more in line with reported values for similar junctions than the rather high critical currents observed in sample A [60].

We attempted backgating in samples A and B, but the gates either leaked or did not tune the critical current. In the sample C, nanowires were placed on Au bottom gates with an AlOx dielectric (thickness $\approx$ 40 nm), and for one of the rings the bottom gate tuned the critical current between 0 and $\approx$ 100 nA. The rest of the rings on sample C were hysteretic.

8.3 Characterizing the current-phase relation

In order to obtain the CPR of an individual junction, we centered the pickup loop over the ring and the field coil current was swept sinusoidally (I_{FC}) while the flux through the pickup loop (Φ_{PU}) was recorded. The signal was averaged many times to obtain a single CPR. An experimental background was obtained in a similar manner, by either measuring far away from the sample or in contact with a ring with no observable critical current. The experimental background subtraction removes a non-linear background which was relatively static in time as well as a linear background due to imperfect

counter-balancing of the pickup loop, field coil mutual inductance.

An additional linear background due to the diamagnetic response of the ring (FIG. 8.1 b) was subtracted. A finite phase shift was required to fit the linear diamagnetic background, indicating that small phase shift occur in either the applied field coil current or in the measured flux through the pickup loop (Φ_{PU}).

The processing up to this point gives Φ_{PU} vs. I_{FC} for only the currents flowing around the ring and therefore through the junction. In order to extract the current-phase relation (CPR), we need to know three inductances: the field coil-ring mutual inductance ($M_{FC,R}$), the pickup loop-ring mutual inductance ($M_{PU,R}$) and the ring's self-inductance (L_S). We used techniques outlined in Ref. [12] to model the mutual inductances as a function of height of the SQUID above the ring, and also the self-inductance of the single-junction ring. The calculated value of L_S for the design of all of the rings studied here is 13.9 pH. Experimentally, we obtained $M_{FC,R}$ by fitting the periodicity of the response of the ring and assuming 2-π periodic behavior. We then used the modeled $M_{FC,R}$ height dependence to obtain the SQUID's height above the ring and get the calculated ($M_{PU,R}$) for the same height. This method of acquiring $M_{PU,R}$ will result in systematic errors of order $\sim 10\%$ in the extracted I_{RING} if the center of the pickup loop and ring are misaligned by a couple microns.

The current in the ring (I_{ring}) and the phase drop across the junction (ϕ) are respectively given by

$$I_{ring} = \frac{\Phi_{PU}}{M_{PU,R}} \tag{8.1}$$

$$\phi = \frac{2\pi}{\Phi_0}(M_{FC,R}I_{FC} + L_s I_{ring}) + \phi_{BG} \tag{8.2}$$

ϕ_{BG} is a phase which occurs due to the existence of static background magnetic fields from imperfect magnetic shielding of our experiment. We do not know ϕ_{BG} independently, but it should be fairly consistent from ring to ring.

Examples of two measured CPRs from sample C are shown in (FIG. 8.2 a,d). The shape of the CPR is in both examples are clearly non sinusoidal, the first maximum after ϕ = 0 is at $\phi > \pi/2$, 'forward' of what is expected for a pure sine wave. This is true of the majority of the CPRs we measured. Generically, forward-skewness in SNS junction's CPRs indicates highly transmitting junctions at low temperatures.

In the absence of time reversal symmetry breaking, the CPR can be decomposed into a sine

Fourier series [38]. We confirmed this behavior by taking fast Fourier transforms of the current-phase relation (FIG. 8.2). The FFTs show peaks at integer multiples of the fundamental frequency of the CPR with alternating signs. We observed peaks in the FFT up to the 6th and 8th harmonics, indicating that a sine Fourier series is an appropriate functional form for the CPR. For sample C, we fitted to a sine Fourier series, with two phase shifts which allow for overall shifts of the CPR on forward and backward sweeps:

$$I(\phi) = \begin{cases} \sum_{n=1}^{N} A_n sin(n(\phi + \phi_{FW})) & \text{if } d\phi/dt > 0 \\ \sum_{n=1}^{N} A_n sin(n(\phi + \phi_{BW})) & \text{if } d\phi/dt < 0 \end{cases} \tag{8.3}$$

8.3.1 Anomalous phase shifts

In measurements of samples A and B, phase shifts between harmonics significantly improved the residuals of fits of the CPRs. The phase shifts occured due to unintentional filtering due to our SQUID feedback box. The phase shifts lead to noticeable distortion of the CPR's shape which depends on the sweep direction. In order to analyze these CPRs, we included a free phase between the harmonics:

$$I(\phi) = \begin{cases} \sum_{n=1}^{N} A_n sin(n(\phi + \phi_n^{FW})) & \text{if } d\phi/dt > 0 \\ \sum_{n=1}^{N} A_n sin(n(\phi + \phi_n^{BW})) & \text{if } d\phi/dt < 0 \end{cases} \tag{8.4}$$

For a 7 harmonic fit, there were then 21 free parameters: 7 amplitudes, 7 forwards phase shifts and 7 backwards phase shifts. These fits more correctly captures the shape of the CPRs in samples A and B (FIG. 8.3). The phase shift between harmonics is in part due to the SQUID feedback loop. More information on the SQUID's PID loop can be found in Appendix A. Due to the phase issue in measurements on samples A and B, which is especially important for higher harmonics, we will restrict any quantitative discussion to the first couple of harmonics for measurements on samples A and B.

8.3.2 Harmonic fits reproduce the CPR shape

We fitted the measured CPRs to Eqn. 8.4 with N=7 for sample A and N=5 for sample B and to Eqn. 8.3 with N=7 for sample C.

We performed harmonic analysis on many measured CPRs, in FIG.3 we present the results of the fits for CPRs from sample B (8.3 c) and sample C (a more restrictive fit to short junction theory is

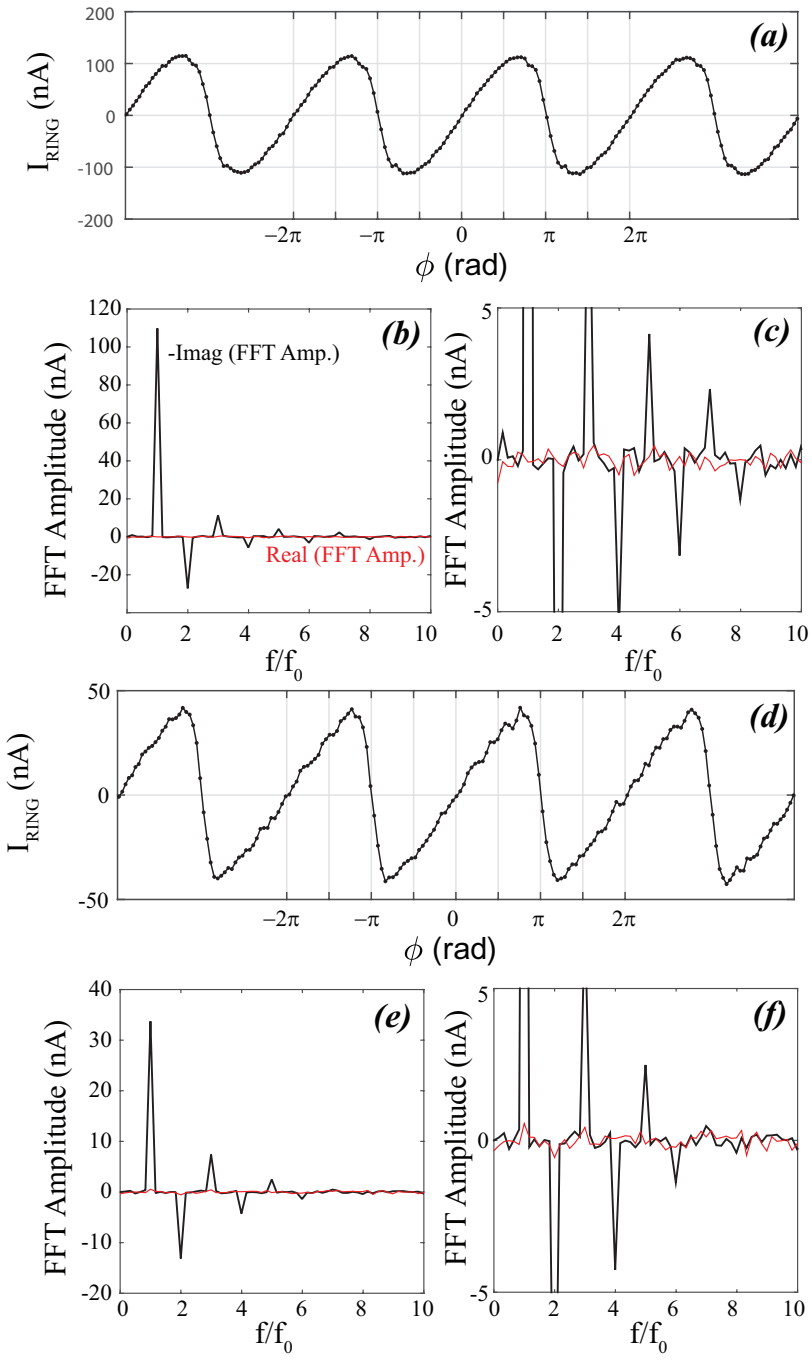

Figure 8.2: **Fast Fourier transform of selected CPRs.** Current phase relations measured on sample C at V_{BG} = -2.35 V (a) and 3.45 V (d) at base temperature ($\approx$ 30 mK). A small phase shift of ϕ_{BG} = 40 mrad was applied to the CPR such that zero current was flowing at zero phase. Full range and zoomed in plots of the imaginary (black) and real (red) components of the FFT for the first (b,c) and second (e,f) CPR. FFTs are plotted vs. f/f_0 the normalized frequency of the CPR.

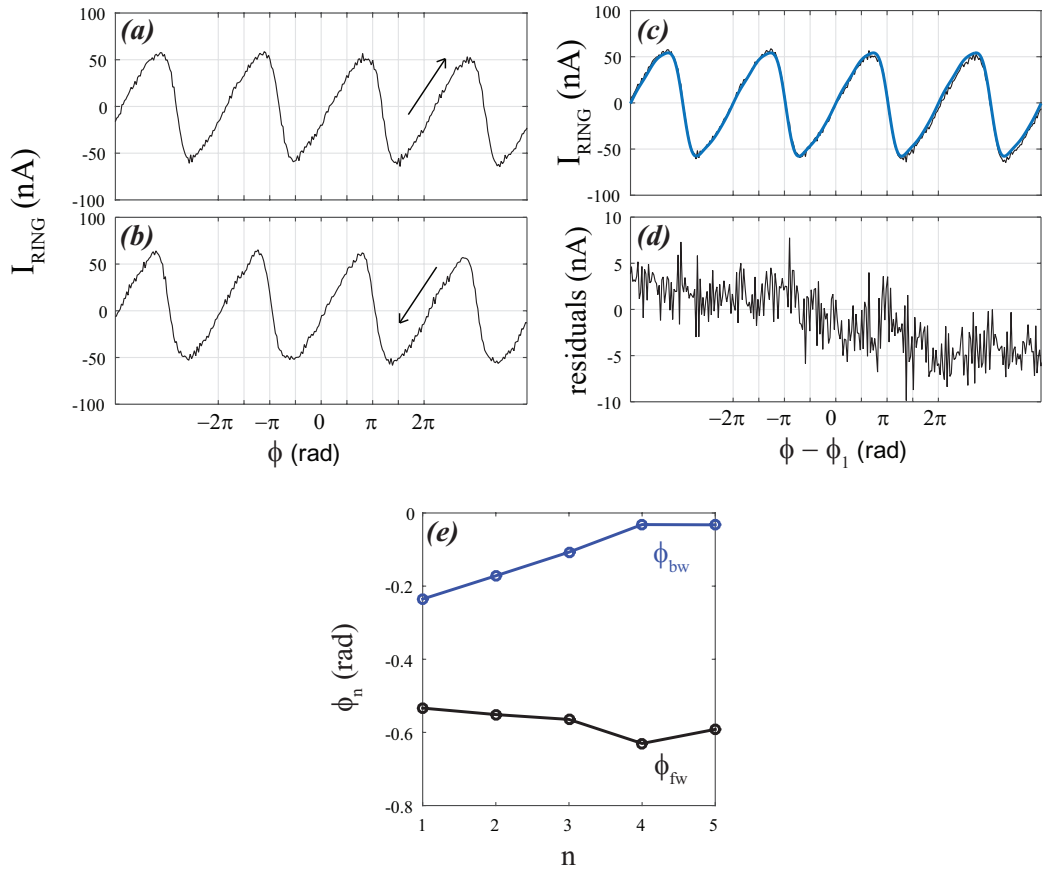

Figure 8.3: **Different phases between harmonics are required to correctly fit some CPRs** (a,b) Forward and backwards sweep of the same CPR from an L=50 nm ring on sample B. The positive and negative peaks have different shapes, and the shape depends on sweep direction, indicating phase shifts which are different depending on the sweep direction. (c,d) Example of a free phase fit (Eq. 8.4, blue line) to the forward sweep and the residuals. (e) The fitted phases of the harmonics vs. harmonic number n.

shown in FIG. 8.14 c,d). The quality of the fits are high, as can be observed by the lack of structure in the residuals (FIG. 8.3 d and FIG. 8.14 d). The highest critical current (non-hysteretic) CPRs exhibit systematic structure in the residuals of order a couple percent which only occurs for fitting more than two periods.

We obtained statistical error bars on fitted parameters by bootstrapping 100-1000 times and taking the 90% confidence intervals.

8.3.3 Intuition about fitting parameters

The harmonic amplitudes A_n are the main parameters which determine the shape of the CPR, (the phase shifts are due to instrumental effects). For comparing many CPRs, it is convenient to plot the fitted parameters instead of showing CPRs directly. The amplitudes of A_n are sensitive to errors in positioning of the SQUID over the center of the single-junction ring, and for an error of a couple microns this will result in a systematic error in all of the A_n of $\sim 10\%$. A_1, in particular, is approximately the critical current of the junction and will incur these systematics.

It is useful to separate the overall amplitude A_1 from the functional form or shape of the CPR. By pulling A_1 out front of the harmonic series, the rest of the parameters A_n/A_1 are made insensitive to systematic errors in positioning and directly determine the shape of the CPR:

$$I(\phi) = A_1 \sum_{n=1}^{N} A_n/A_1 sin(n\phi) \tag{8.5}$$

We define the shape parameters, a_n:

$$a_n \equiv (-1)^{n+1} A_n/A_1 \tag{8.6}$$

The negative sign term ensures that, for forward-skewed CPRs (which comprise most of the measured CPRs) a_n is positive for all n. a_2 is directly proportional to how far from $\pi/2$ the first maximum of the CPR is. Higher order shape parameters are important for determining the overall shape of more forward-skewed CPRs and comparing to theory.

Now, we will show the dependence of the harmonic amplitudes (A_n) and shape parameters (a_n) on length of the etched region for many different junctions, back gate voltages, and with temperature. Then, we will compare the results to theories of Andreev bound states in SNS junctions to gain insight about the nature of superconductivity in InAs nanowire Josephson junctions.

In the short junction limit, for a single mode junction, more forward-skewed CPRs indicate

higher transmission through the junction. This intuition is useful to keep in mind for parsing the following experimental results. I will address more in depth the validity of this heuristic in later sections.

8.4 Length dependence

In sample B, we measured many junctions with an assortment of etched lengths (L) of 50 to 250 nm. The CPRs of many different junctions 30-50 mK are shown in FIG. 8.4 a. The CPRs with measurable critical currents (all of which are forward skewed) show large junction to junction variation in shape and amplitude, and more forward-skewed shape does not correlate with higher critical current. The fitted harmonic components (A_n) and shape components (a_n) show this (FIG. 8.4 b,c).

There is no correlation between the amplitude of the 1st harmonic , A_1, and nominal length of the junction (FIG. 8.4 b). There is a weak dependence of a_2 on length (FIG. 8.4 c), with a lot of scatter for nominally identical junctions, indicating that the transmission (and therefore the forward-skewness) of the junctions decreased as the length of the etched region was increased. The variation in shape and lack of correlation between length and critical current indicates that the position of the Fermi level and the importance of disorder varies from junction to junction. Investigation of a gated nanowire more concretely explores the role of disorder and Fermi energy in these nanowire junctions.

8.5 Shape fluctuations in a gated InAs nanowire junction

In sample C, we measured nanowires with bottom gates which allowed us *in principle) to tune the electron density in the nanowire. CPRs of a L=50 nm nanowire junction at base temperature of our dilution refrigerator ($\approx 30mK$) showed strong fluctuations in both their amplitude and in the shape of the CPR, which is especially apparent in the CPRs at low densities (FIG. 8.5). In particular, in this narrow range of gate voltages we observed both the most forward-skewed CPR we measured as well as a backwards-skewed CPR, which has its first maximum before $\pi/2$.

Fits show that both the amplitude and shape of the CPR of a single junction fluctuate (behave non-monotonically) over the full gate voltage range probed (FIG. 8.6). The amplitude of all of the harmonics fit show fluctuations (FIG. 8.6 b). A_n of different n do not fluctuate proportionally.Iin other words, their relative amplitude A_n/A_1 also fluctuates with gate voltage. These fluctuations are exactly the 'shape' fluctuations we observed in raw CPR traces.

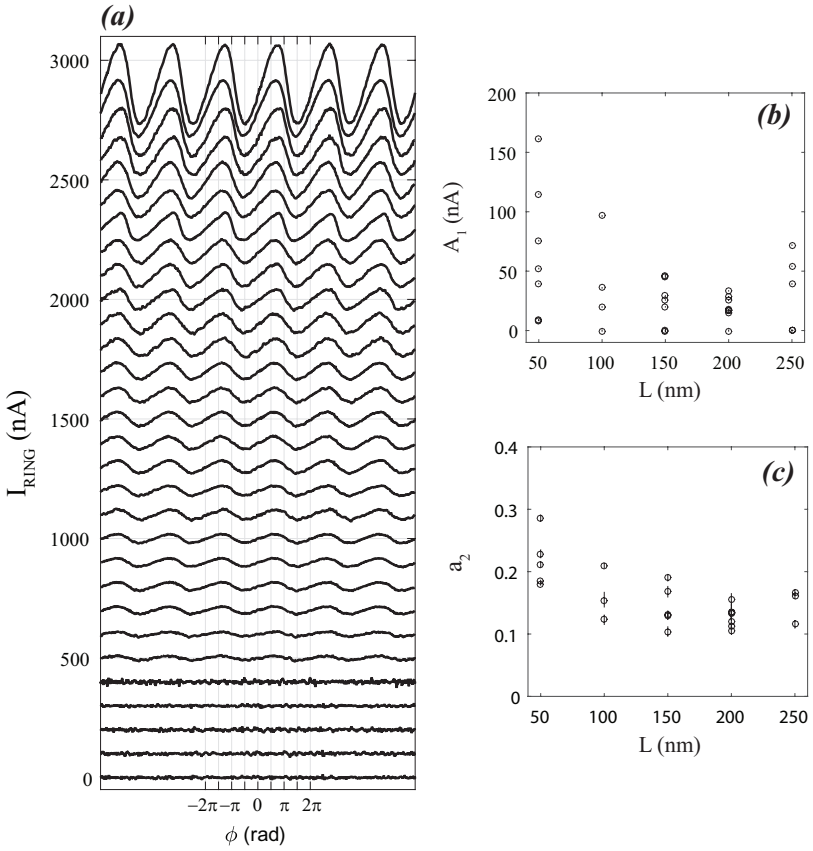

Figure 8.4: **CPRs of many nanowire Josephson junctions of various lengths** (a) CPRs of 31 different rings of various etched lengths (L = 50 - 250 nm) on sample B. Measurements were performed between T=30-50 mK. The CPRs are ordered from smallest to largest fitted A_1, with offsets for clarity. (b) Fitted harmonic amplitude A_1 vs. junction length (L). (c) Fitted shape parameter $a_2 = -A_2/A_1$ vs. L. Only junctions with $A_1 > 10$ nA were plotted. Error bars are 90% confidence from bootstrapped fits to Eq. 8.4.

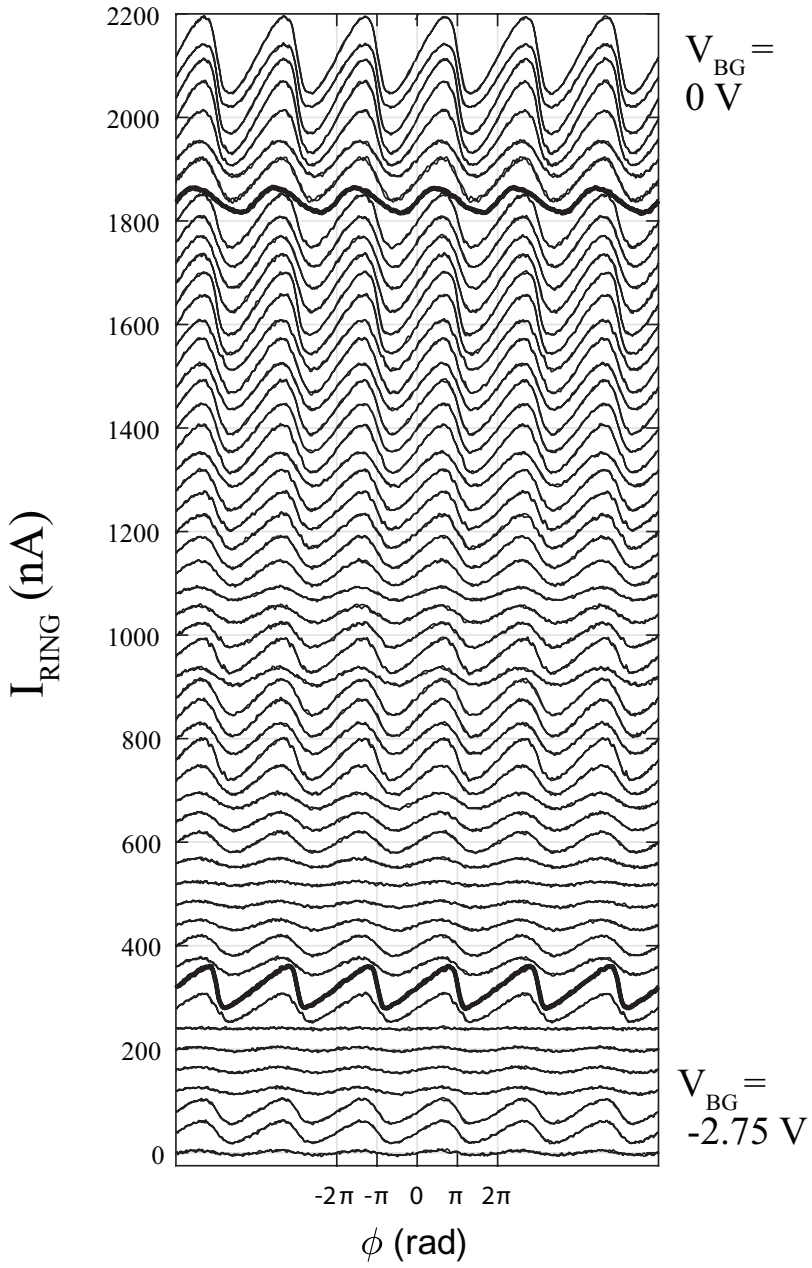

Figure 8.5: **CPRs at low gate voltages** Plot of the CPR for the same junction as a function of bottom gate voltage V_{BG}. V_{BG} =-2.75 V is very close to full depletion of the nanowire. CPRs are offset for clarity.

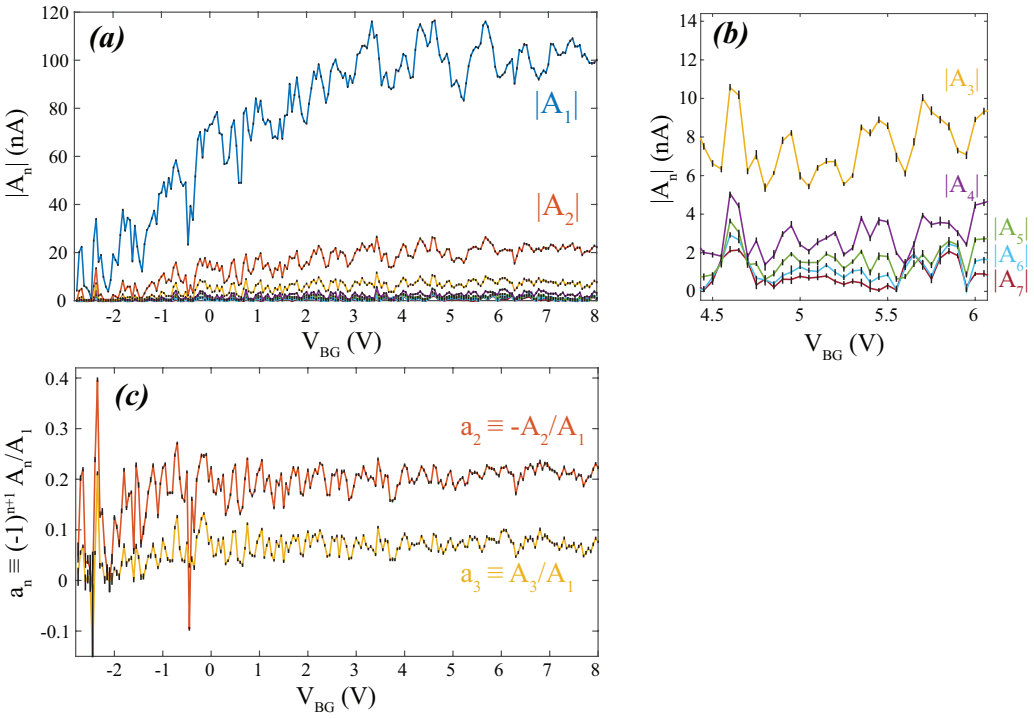

Figure 8.6: **Fitted amplitude and shape of the CPR vs. gate voltage** Results of fitting > 200 measured CPRs at various gate voltages.(a) Harmonic amplitudes ($|A_n|$) plotted vs. applied bottom gate voltage (V_{BG}). The critical current ($\sim A_1$) varied from 0 nA at low gate voltages to 100-120 nA at high V_{BG}. (b) The fluctuations of higher harmonics (up to the 7th) are apparent at high gate voltages. (c) The shape, as determined by the normalized harmonic components or shape parameter (a_n) also fluctuate as a function of V_{BG}.

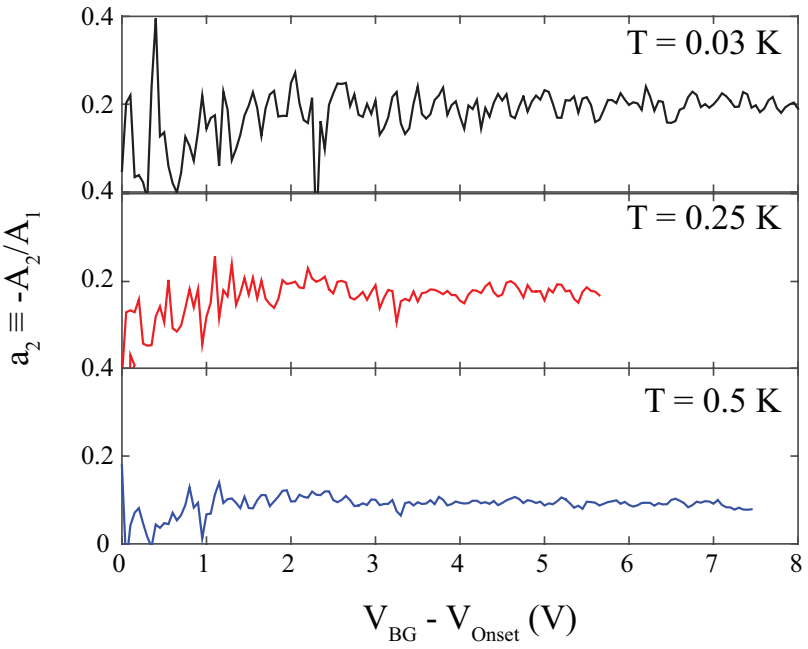

Figure 8.7: **Gate voltage dependencies of the forward-skewness at elevated temperatures.** The shape of the CPR (as captured by a_2) vs. V_{BG} - V_{Onset}. V_{Onset} is the gate voltage at which the first non-zero CPR was observed. V_{Onset} = -2.75 V, -1.8 V, and -1.9 V for 30 mK, 250 mK, and 500 mK respectively.

The fluctuations in shape (a_n) occur most wildly at low V_{BG}, and appear to reduce in amplitude as the electron density in the nanowire was tuned higher (FIG. 8.6 c).

We measured gate voltage sweeps at higher temperatures and found that the scale of the fluctuations decreased with increasing temperature for similar gate voltages (FIG. 8.7). The average value of the shape parameter at high gate voltages also decreases, indicating that the temperature dependence of the CPR (i.e. the fact that higher harmonics have a more dramatic temperature dependence, see FIG.8.10) itself plays a major role in suppressing shape fluctuations.

At the lowest V_{BG} near the onset of a finite critical current, the shape fluctuated the most. We remeasured this region with smaller gate voltage steps, and found peak-like behavior in the amplitude and shape parameters of the CPR (FIG. 8.8). The largest peak, which was observed to have A_1 = 34 nA and a_2 = 0.394 on the initial, coarser gate sweep, was found to have reduced amplitude and forward skewness after sweeping the gate (A_1 = 29.4 nA and a_2 = 0.332, FIG. 8.8). The peaks are asymmetric and cusp-like in the shape parameter.

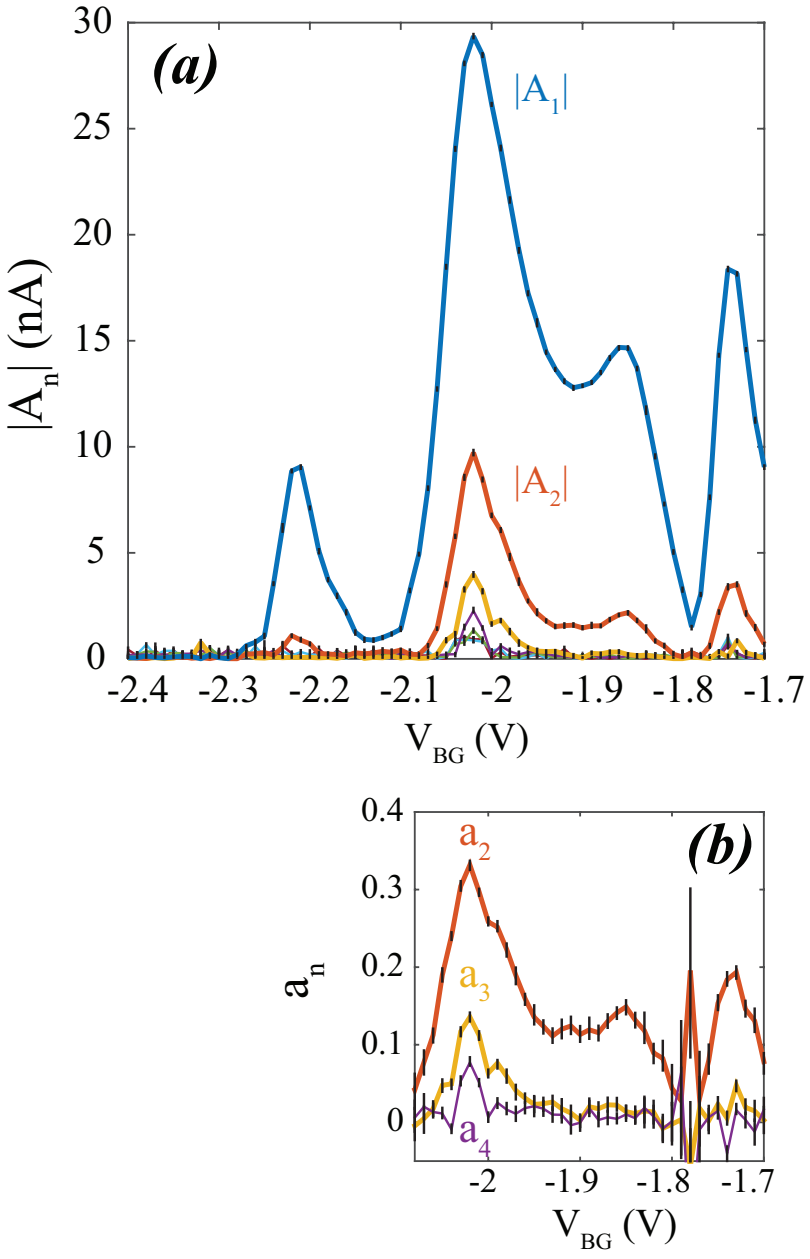

Figure 8.8: **Low gate voltage harmonic amplitudes and shape parameters.** A_n (a) and a_n (b) vs. V_{BG} near the onset of superconductivity. This data was taken after sweeping the full gate voltage series presented in FIG. 8.6.

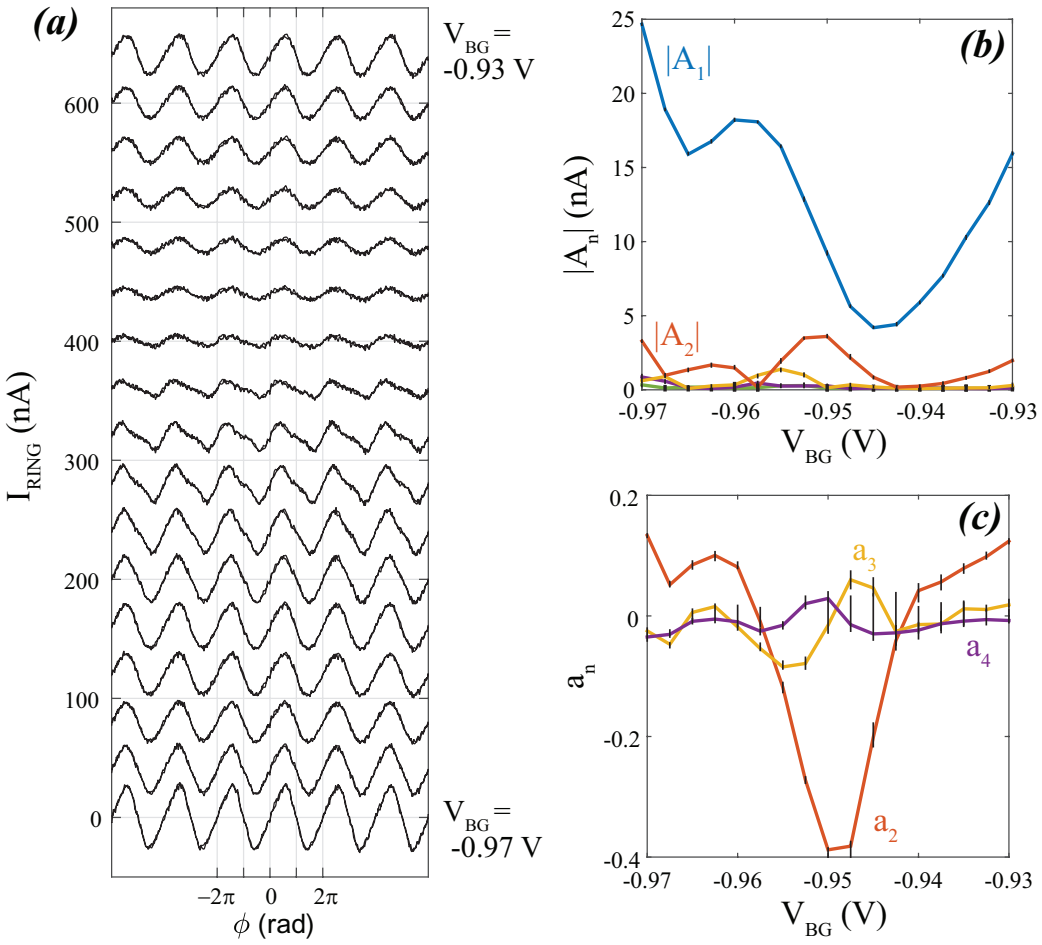

Figure 8.9: **CPRs and fits near the backwards-skewed CPR** (a) CPRs taken between V_{BG} = -0.97 and -0.93 V at 30 mK. (b,c) $|A_n|$ and a_n obtained by fitting the presented CPRs. (c) A negative a_2 indicates that the sign of A_1 and A_2 are the same, which is not the case for forward-skewed CPRs. The full range of V_{BG} explored here is smaller than the spacing between CPRs in FIG. 8.6.

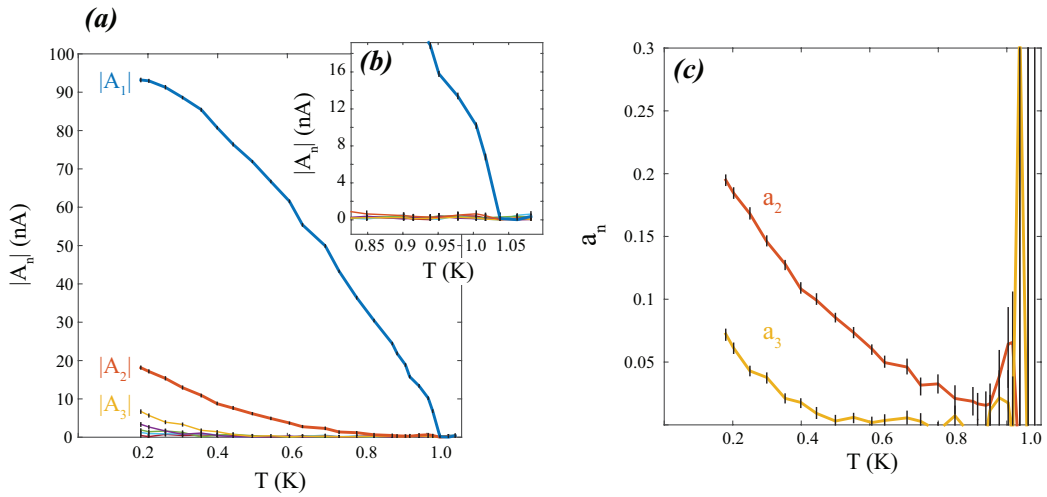

Figure 8.10: **Temperature dependence of CPR at fixed** V_{BG} (a,b) A_n and (c) a_n vs. temperature at fixed $V_{BG} = 5.55V$. Error bars are 90% confidence intervals obtained by bootstrapping 100 times.

A second region of interest is around the backwards-skewed CPR. We confirmed the reprehensibility of this feature by finding the backwards-skewed feature again after sweeping V_{BG} and measured the region around the backwards-skewed CPR in finer V_{BG} steps (FIG. 8.9). The backwards-skewed CPR appears only in a very narrow range of gate voltages (less than 0.02 V, FIG. 8.9 c) and is almost, but not completely coincident with a minimum in the overall critical current (FIG. 8.9 b).

8.6 Temperature dependence

We measured the CPR of the gated nanowire junction at fixed V_{BG} $(5.55V)$ as a function of temperature (FIG. 8.10). We observe that the CPR's amplitude goes to zero between T= 1.02 K and 1.04 K (FIG. 8.10 b). This is the same T_c which was observed for the evaporated Al of the ring by imaging diamagnetism (not shown). At temperatures close to T_c, the CPR was sinusoidal, and higher harmonics only began to contribute to the CPR's shape at lower temperatures (FIG. 8.10 a,c).

We measured the temperature dependencies of the CPRs in all three samples. Although we only measured to high enough temperatures to observe T_C in sample C, we observed strong temperature dependence of higher harmonic components in all three samples on many nanowires.

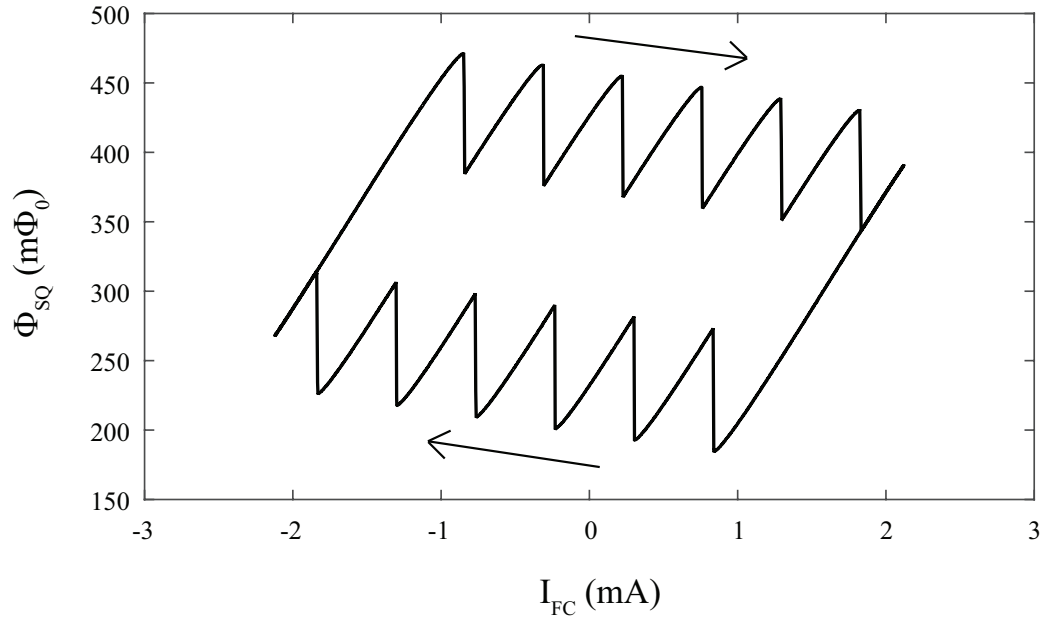

Figure 8.11: **Example of a hysteretic ring** A typical measurement of Φ_{SQ} vs. I_{FC} on a hysteretic ring on sample C. Arrows indicate the sweep direction of the field coil current.

8.7 Aside: Hysteretic rings

We measured many rings which had a high critical current which prevented direct measurement of the current phase relation. In the case where $\beta \equiv 2\pi L_S I_c/\Phi_0 > 1$, the Josephson energy has multiple local energy minima for a given applied flux through the ring. This results in an open shape of the measured response of the ring which depends on sweep direction (FIG. 8.11). The height of the individual jumps (in current) is given by $\Phi_0/2L_S$, while total maximum current is just given by the critical current I_C (subtracting any linear backgrounds). The height of the jumps was similar for many rings and consistent with the calculated self inductance of 13.9 pH. The overall height of the hysteretic pattern varied from ring to ring.

8.8 Aside: High I_{FC} CPRs

We measured many periods of the CPR by using higher field coil currents. In the sample A, we observed a beating pattern in the CPR (FIG. 8.12 a). The first minimum in the amplitude modulation depended strongly on height (it was closest to $I_{FC} = 0$ when the SQUID was pressed into the ring). The periodicity of the beating is too fast to be explained by Fraunhofer effects, as the fields

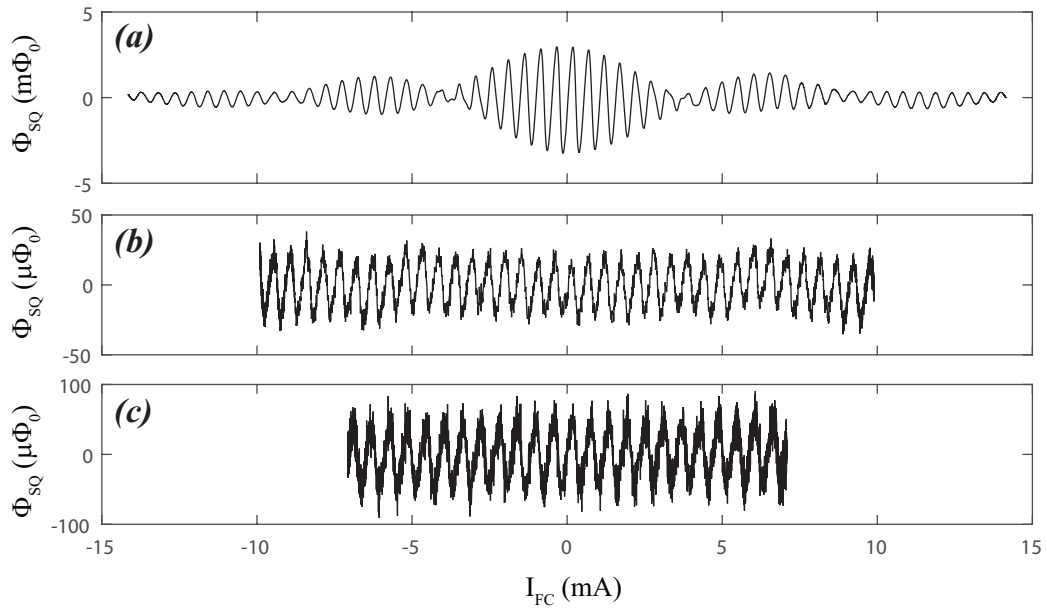

Figure 8.12: **High field coil current measurements of the CPR** (a) In sample A, we found amplitude modulation or 'beating' of the CPR at higher field coil currents. (b) In sample B and C we found no evidence of this effect. For sample A and B, we've subtracted a polynomial to get rid of non-linear backgrounds which occurred at high applied I_{FC}.

required to thread a flux quantum through the junction area are much higher than what we can apply with the field coil. We performed superconducting simulations to see if effects due to the width of the annulus of the ring could cause amplitude modulation due to different paths around the ring enclosing different flux. We found a somewhat similar pattern, but the calculated amplitude modulation was much slower than the observed beating.

In samples B and C, we did not find modulation of the amplitude of the CPR at high field coil currents (FIG. 8.12 b,c). The only difference in design between the two samples is the length of epitaxial Al/InAs nanowire which was not covered by evaporated Al. In samples B and C, the distance between the end of the etched region and the start of the evaporated Al was minimized, while in the sample A the total length of nanowire not under evaporated Al was up to 1 μm while the etched region was only 250 nm at most.

8.9 Discussion

8.9.1 Comparison to SNS short junction theory

The properties of SNS Josephson junctions and which theoretical expressions are applicable depends on a number of length scales of the junction [38]. Specifically, the superconducting coherence length (ξ_0), the normal phase coherence length of the junction (l_{phi}), the mean free path (l_{mfp}), and the physical dimensions of the junction (L,W) all strongly affect the properties of the induced superconductivity. One set of limits of SNS theory are the short junction (often written as $\xi_0 << \mathrm{L}$) and long junction ($\xi_0 >> \mathrm{L}$) limits. In the short junction limit, only Andreev bound states (ABS) contribute to the CPR , while in the long junction limit continuum states also contribute to the supercurrent [3].

Beenakker's formulation of short junction SNS theory [3] is useful because it makes clear the connection between Andreev bound states and the normal state conducting modes. Specifically, in the short junction limit, the CPR is completely determined by transmission coefficients (τ_p) of the normal conducting modes of the junction and the bulk superconducting gap (Δ_0)

$$I(\phi) = \frac{e\Delta_0(T)}{2\hbar} \sum_{p=1}^{N} \frac{\tau_p sin(\phi)}{[1 - \tau_p sin^2(\phi/2)]^{1/2}} tanh(\frac{\Delta_0(T)}{2k_B T}[1 - \tau_p sin^2(\phi/2)]^{1/2}) \qquad (8.7)$$

where the sum is over N modes in the junction, τ_p is the transmission probability of the pth mode, which can be anywhere between 0 and 1, T is the temperature, and ϕ is the phase drop across the junction.

We plotted the CPRs for various τ for a single-mode junction (FIG. 8.13). The CPR's forward skewness, as mentioned earlier, is monotonically related to the the transmission of the normal mode. A perfect transmission mode will have, in addition to a very forward-skewed shape, a quantized critical current of $e\Delta_0(T)/2\hbar$. Fits of the CPR show that the harmonic amplitudes alternate sign and their magnitude decreases for higher harmonics. Higher harmonics are increasingly sensitive to deviations from perfect transmission, which can be seen in the shape parameter (FIG. 8.13 c).

In contrast to normal transport, the short-junction CPR depends non-linearly on each modes transmission probability [3]. Therefore, the shape of the CPR contains separable information about the number of modes in the junction and the distribution of transmission probabilities which is not typically true of two-terminal transport measurements.

Eqn. 8.7 is only applicable in the short-junction limit, and additionally relies on a couple of approximations[3]. The theory assumes that the normal state scattering matrix of the junction is

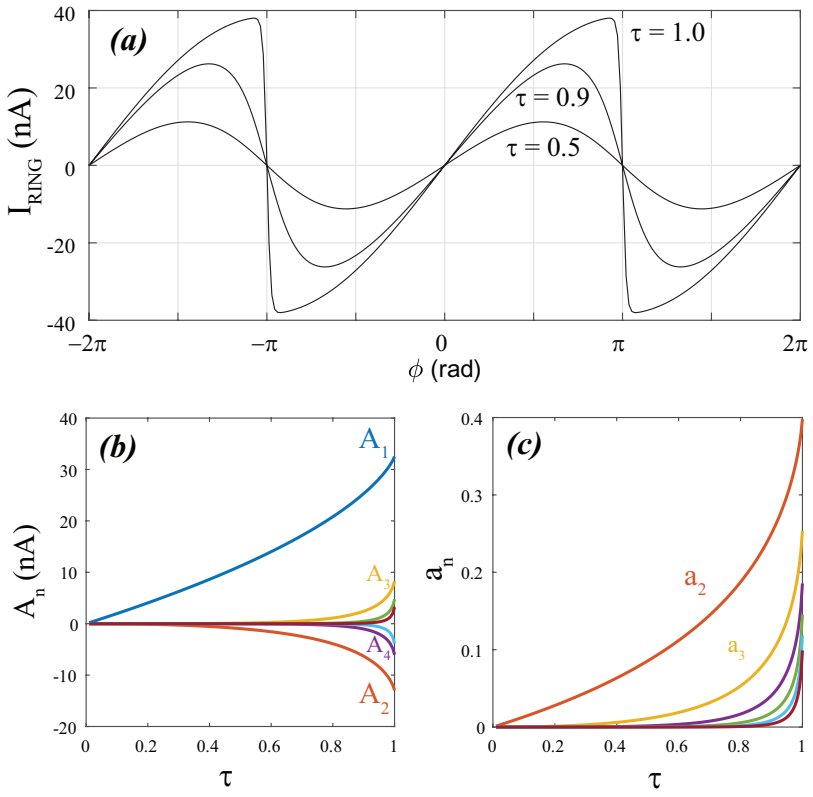

Figure 8.13: **Predicted CPR behavior vs. transmission coefficient for a single mode junction** (a) Selected predicted CPR for a single-mode short SNS junction with the indicated transmission coefficient (τ), T=0.03 K and T_c=1.04 K, calculated using Eqn. 8.7. (b,c) Fitted harmonic amplitudes A_n and shape parameters for short junction CPRs vs. τ.

constant as a function of energy anywhere near the superconducting gap. The typical energy scale of variation of the S-matrix is given by the correlation energy (a.k.a Thouless energy), $E_C \sim \frac{\hbar}{\tau_\phi} = \frac{\hbar v_F}{l_\phi}$, where τ_ϕ and l_ϕ are the phase coherence time and length, respectively, and v_F is the Fermi velocity of the junction material. Therefore, the short junction limit is satisfied when $E_C >> \Delta_0$ [3]. Our junctions are in the coherent transport regime and therefore the phase coherence length should be the length of the junction itself, L.

Another assumption for Eqn. 8.7 is the Andreev approximation, $E_F >> \Delta_0$. Both requirements are violated near the onset of a subband, and therefore a gate voltage dependence of the CPR in the low-mode limit will necessarily include regions where the short junction limit is violated. Based on tight-binding simulation using Kwant [39], we estimate the spacing between subbands to be tens of meV for an InAs nanowire of a radius of 50 nm. The Andreev approximation will, therefore, only be violated for energies within $\sim 150\mu eV$ of the band onset. The short junction approximation, rearranged to solve for the Fermi energy is $E_F > \Delta^2 L^2 m^*/(2\hbar^2)$, which is only $10\mu eV$ for an L = 50 nm InAs junction. Therefore, for most positions of the chemical potential in the low-mode limit, the short junction and Andreev approximation for SNS junctions remain valid for all subbands.

8.9.2 Fitting to short-junction limit at low gate voltages

We start by fitting the most forward-skewed CPR we observed to Eqn. 8.7 for a single mode (FIG. 8.14). We also allow an overall phase shift to account for background fields and other phase-shifting effect. The best fit, for temperature fixed at the measured mixing chamber temperature of 30 mK, is given by a perfect transmission ($\tau = 1.0$) mode. The fit (FIG. 8.14 a,b) slightly underestimates the amplitude of the CPR and gives a shape which is too forward skewed.

We introduced two more free parameters, the temperature T_{fit} and a scaling of the theoretical CPR's amplitude $1 + \epsilon$. A free temperature is justified because, although the mixing chamber's thermometer reads 30 mK, it is possible the temperature of the electrons in the ring is higher. An electron temperature of $\sim$ 100 mK was observed in similar types of ring measurements in the same dilution refrigerator [11]. Temperature and transmission enter Eqn 8.7 in different ways, which allows us to fit both at the same time (at least for very forward-skewed, single-mode CPRs). The overall amplitude adjustment is justified due to imperfect positioning of the SQUID, which will lead us to over estimate the mutual inductance between the SQUID's pickup loop and the ring.

We found that the best fit yields fitted parameters of $\tau = 1.0$ (perfect transmission), T_{fit} = 130 mK, and an adjustment to the mutual inductance of $1 + \epsilon$ = 1.08, well within our estimated systematic error due to positioning errors. The fit does not lead to any observable structure in the

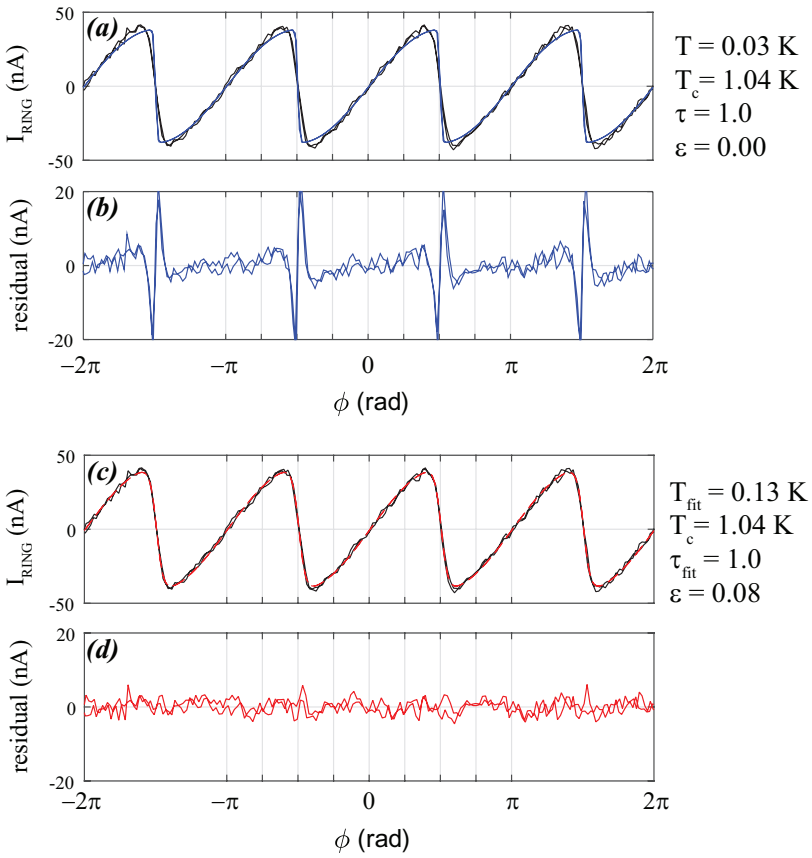

Figure 8.14: **Fits of the most forward skewed mode to short junction theory** (a) Fit (blue) of the most forward-skewed CPR (data in black) to single-mode short junction theory with two free parameters, τ and an overall phase shift δ. (b) Residuals of fit in (a). (c) Fit (red) with four free parameters, τ, δ, the electron temperature which we allowed to vary (T_{fit}), and ϵ an overall adjustment to the mutual inductance which multiplies the fitted CPR by (1+ϵ). (d) Residuals of the four parameter fit. The perfect transmission extracted from fitting is robust to how many fit parameters we allow to vary, including temperature and an overall scaling factor.

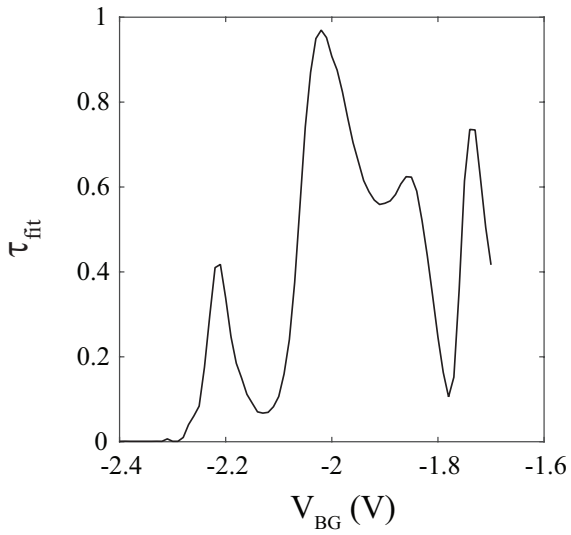

Figure 8.15: **Low gate voltage behavior is well fit by a single mode with fluctuating transmission** The transmission τ extracted from a fit to the single mode short-junction formula for the data presented in FIG. 8.8. The root mean square error of the fits with fixed scaling factor ($\epsilon = 0$) and temperature ($T = 0.13K$) resulted in residuals which only deviated from the full harmonic fits by at most $\approx 10\%$

residuals (FIG. 8.14 d). We, therefore, conclude that we have directly measured the current-phase relation of a single Andreev bound state with very close to perfect transmission.

The shape of the CPR allows us to discriminate between a single-mode with transmission τ and two modes with transmission $\tau/2$, for example. We found that the low gate voltage behavior is well fit by a single mode with fluctuating transmission (FIG. 8.15). The shape of the transmission fluctuations are peak-like, indicating that supercurrent due to resonant tunneling may be the correct way to understand superconductivity in this nanowire Josephson junction.

8.9.3 Resonant tunneling

In the presence of finite tunnel barriers at the SN interface, SNS junctions will cross over into SINIS behavior. Similarly to SNS junctions, there is a short-junction limit where Eqn 8.7 is valid, which is that the tunneling rate through both tunnel barriers are $\Gamma > \Delta$. The transmission of a resonant mode is given by the Breit-Wigner formula[3]:

$$T_{BW} = \frac{\Gamma_1 \Gamma_2}{(E_{res} - E_F)^2 + 1/4(\Gamma_1 + \Gamma_2)^2} \tag{8.8}$$

Γ_1 and Γ_2 must be equal for perfect transmission to occur. Additionally, the width of the resonance is determined by the sum of both tunnel rates. In the short-junction limit ($\Gamma > \Delta$), the height of a perfect transmission peak is determined, then, by the superconducting gap. In the opposite limit ($\Gamma < \Delta$), the height of the peak is less, and proportional to Γ [3].

We attribute the observed close to perfect transmission mode to resonant tunneling. In otherwise perfect SNS junctions, resonant states can form due to mismatch between the Fermi velocities of the superconductor and normal materials [36]. These resonant states are Fabry-Perot resonances which tune both the normal conductivity and the CPR of the junction. In epitaxial Al/InAs nanowires, the Fermi velocity mismatch may occur either at the interface between the Al and InAs, or between the etched portion of the InAs nanowire which is gated and the fully coated portion of the nanowire which has a relatively fixed density.

We performed simulations very close to what was performed in Ref. [36] in order to gain insight into the role of Fabry-Perot like oscillations in an otherwise ballistic junction. The simulated geometry is an InAs 2DEG with similar dimensions to that of our actual nanowire. This simulation should correctly reproduce the periodicity of Fabry-Perot oscillations, but it does not capture the correct subband spacing and degeneracy. Simulations with a more realistic cylindrical geometry are in progress. We have included a Fermi energy dependent transparency for each subband based on the Fermi velocity mismatch:

$$Z = \sqrt{Z_0^2 + (1-r)^2/(4r)}; \tag{8.9}$$

where $r = v_{F1}/v_{F2}$ the ratio of the Fermi velocities of the lead and junction, and $Z_0 = V/\hbar^2 v_F$ is the contribution to the transparency due to an added delta function potential with magnitude V (in units of eVm) at the interface. We have taken into account the subband and Fermi Energy dependence of Z, and plotted the results vs. 1D electron density (which is proportional to V_{BG} in the absence of quantum capacitance) rather than E_F.

For our simulation, we took $m* = 0.023m_e$, $v_{F,lead} = 1.5x10^6 m/s$, $V = 0$, $T = 50$ mK, and $T_c = 1$ K.

For a single subband, we find peak like behavior in A_n and a_n parameters which qualitatively match our data vs. V_{BG} (FIG. 8.16 a,b). Specifically, the shapes of the peaks in a_n are asymmetric and the width of the first peak is narrower than the width of the second in both. On a more basic level, close to perfect transmission requires that the tunnel rates at either contact are within a couple percent of each other, and that is more easily explained by a robust and equal tunnel barriers due to Fermi velocity mismatch than accidental quantum dot behavior.

We also theoretically investigated the many subband case and find that overlapping resonant

structure from different subbands leads to fluctuations in the shape of the CPR (FIG. 8.16 c,d). Because the subband spacing and Fabry-Perot spacing are of similar energy scales, multiple subbands lead to fluctuations rather than peak-like structure when multiple modes are occupied. It is important to note that the wildly fluctuating forward-skewness at low gate voltages is simulated for an otherwise perfectly ballistic junction with no added potential barrier at the contact.

The scale of the fluctuations in shape of calculated CPRs decrease with increasing density, which is also what we observed for higher gate voltages in the gated junction we measured(FIG. 8.16 d and FIG. 8.6 c

The gate voltage scale of shape fluctuations we observed can probably not be solely explained by regularly spaced Fabry-Perot resonances. The relatively simple behavior of the transmission at low gate voltages leads us to believe, however, that a small amount of disorder (e.g. a few charge traps) could lead to the more complicated resonant structure we observe. The backwards skewed CPR is not explained by the SNS or SINIS junction theories we've presented and may give clues to what sort of disorder leads to 'extra' fluctuations.

8.9.4 Backwards-skewed CPR

Backwards-skewed CPRs are generally due to pair-breaking in the superconducting leads, and can occur in SIS or SNS junctions [38]. The very narrow range of V_{BG} for which a backwards-skewed CPR was observed, and because the leads themselves should not be influenced strongly by gate voltage, leads us to believe that the origin is not pair-breaking in the Al shell. We speculate that SNINS behavior may lead to pair-breaking in the proximitized superconducting region in the InAs, in analogy to the SIS case where for a weak tunnel barrier pair-breaking occurs due to suppression of superconductivity near the tunnel barrier. A tunnel barrier in the middle of the junction may lead to such behavior.

Backwards-skewed behavior was attributed to noise rounding in Ref. [33]. Their junctions were very close to $LI_c/\Phi_0 \quad 1$ limit, or in other words very close to they hysteretic regime. Our junctions are in the $LI_c/\Phi_0 \ll 1$ limit, and therefore noise rounding cannot explain the observed backward-skewed CPR.

A study of SNINS junction behavior in the relevant limits has not been performed theoretically, to our knowledge. The extreme shape and V_{BG} dependence of the backwards skewed CPR gives some strong experimental observations to compare to possible theories.

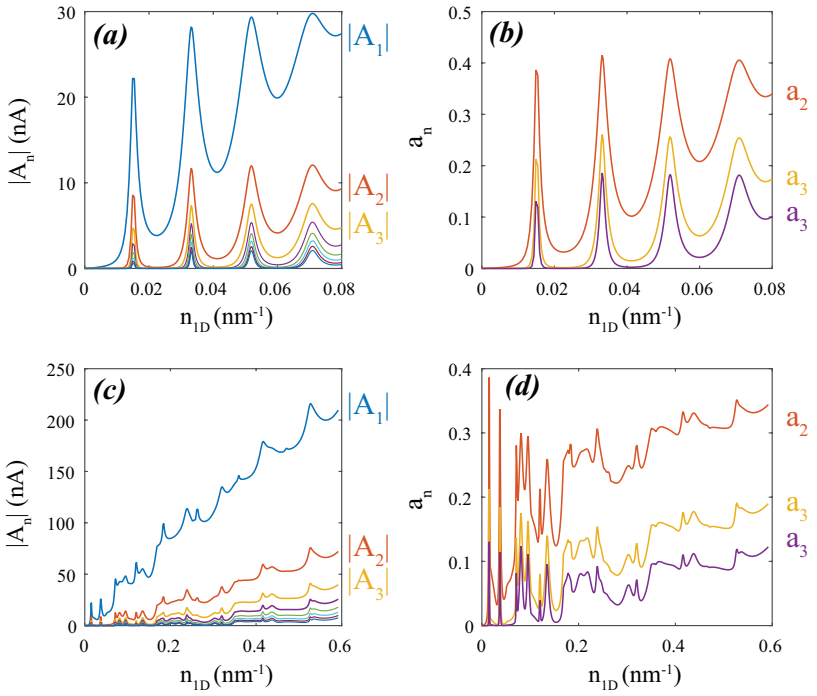

Figure 8.16: **Simulation of CPRs show Fabry-Perot resonant states.** CPRs were calculated as described in the text. Fitted harmonic amplitudes (a) and shape parameters (b) for a single subband show the properties of Fabry-Perot resonances in the CPR. When multiple subbands are included in the calculation (c,d) a more complicated structure of fluctuations in the amplitude and shape

8.9.5 InAs NW conclusions

We measured the CPR of InAs nanowire junctions of various lengths and as a function of gate voltage and temperature. We found that the shape and amplitude of the CPR fluctuate strongly with gate voltage and from junction to junction. The fluctuations at low densities are qualitatively very similar in shape and amplitude to single-mode Fabry-Perot resonances, which we expect contributed at least in part to the fluctuations at higher gate voltages. In the low gate voltage regime, we observed a CPR which is consistent with that of a single, perfect transmission mode. Additionally, we observe a very narrow gate voltage range where the CPR is backwards-skewed which requires more theoretical investigation.

We are still working through the broader implications and context of this work. Briefly, the current phase relation is of importance for reconstruction of current density profiles extracted from measurements of Fraunhofer patterns (e.g. [41]), and non-sinusoidal current-phase relations are pertinent for determining the operation of nanowire-based Josephson junction qubits [61, 27].

Our measurements vs. gate voltage are obviously a very sensitive probe of disorder and structure in the junction. We have argued that Fabry-Perot like oscillations due to a Fermi velocity mismatch will lead to similar low density behavior. In principle, good enough measurements may allow us to reconstruct or at least estimate the scale of other disorder necessary to explain our data. We hope to use effective tight-binding models [39] to estimate what sort of disorder is necessary to reproduce our data in order to learn more about the disorder.

Appendix A

SQUID feedback box frequency dependence

A.1 Introduction

The SQUID's feedback boxes (designed by John Martinis) have been somewhat of a black box for us. In this appendix, I will briefly derive the behavior of the feedback box, and show that its experimental behavior is easily captured by the theory of PI controllers. More importantly, I will show that the 'gain knob' of the feedback box has big effects on the frequency response of the SQUID at high frequencies. These effects were relevant for understanding shape distortion of current-phase relations in ch. 8.

A.2 Feedback circuit

The feedback box is designed for high speed SQUID feedback. Although the specific op amp and components are probably important for it's high speed operation, it is conceptually just a PI (proportional - integral) feedback loop with a differential input (FIG. A.1).

The signal which the feedback box 'locks' onto is the output of the SQUID (V_{SQUID}) which is periodic in voltage applied to the modulation coil (V_{mod}, FIG. A.2 a). V_mod is the output of the feedback box and also the signal we measure. The response of the feedback box is determined by the proportional gain (G_P) and the RC time constant of the 'I Stage' (τ_{RC}).

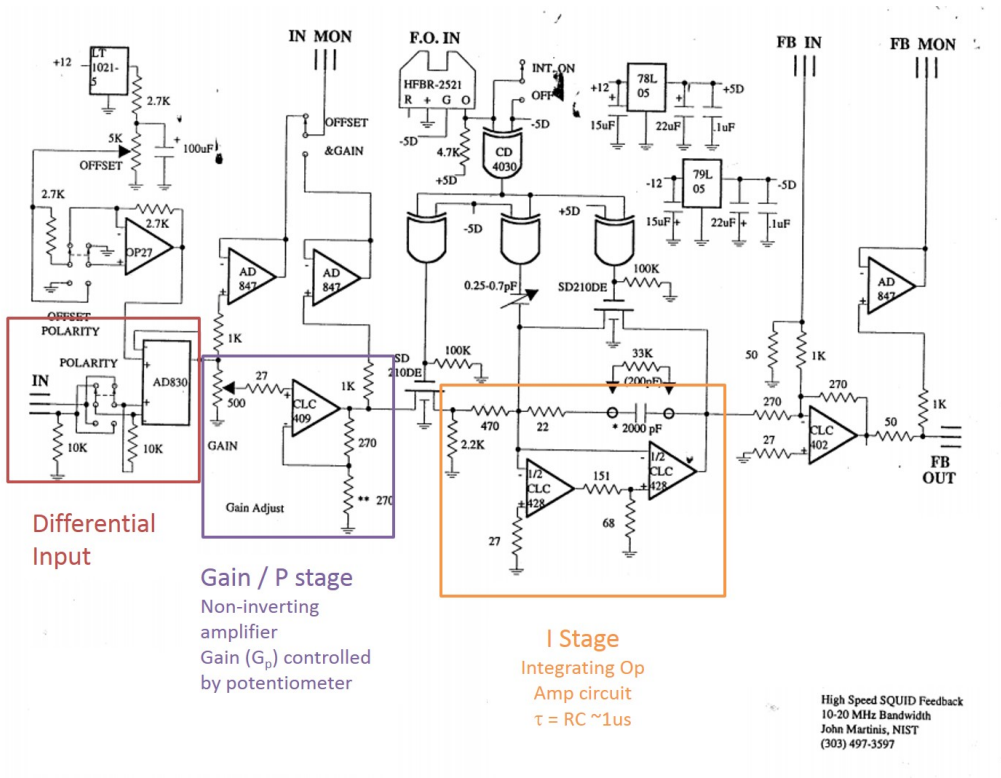

Figure A.1: **Feedback box circuit diagram** Full circuit diagram for the scanning SQUID feedback boxes. The highlighted regions are the only conceptually important regions for understanding the feedback and are fairly straight-forward op-amp circuits. The potentiometer in the Gain/P stage is the pot which can be tuned from the front of the feedback box, and is the main thing we regularly change about the feedback boxes properties.

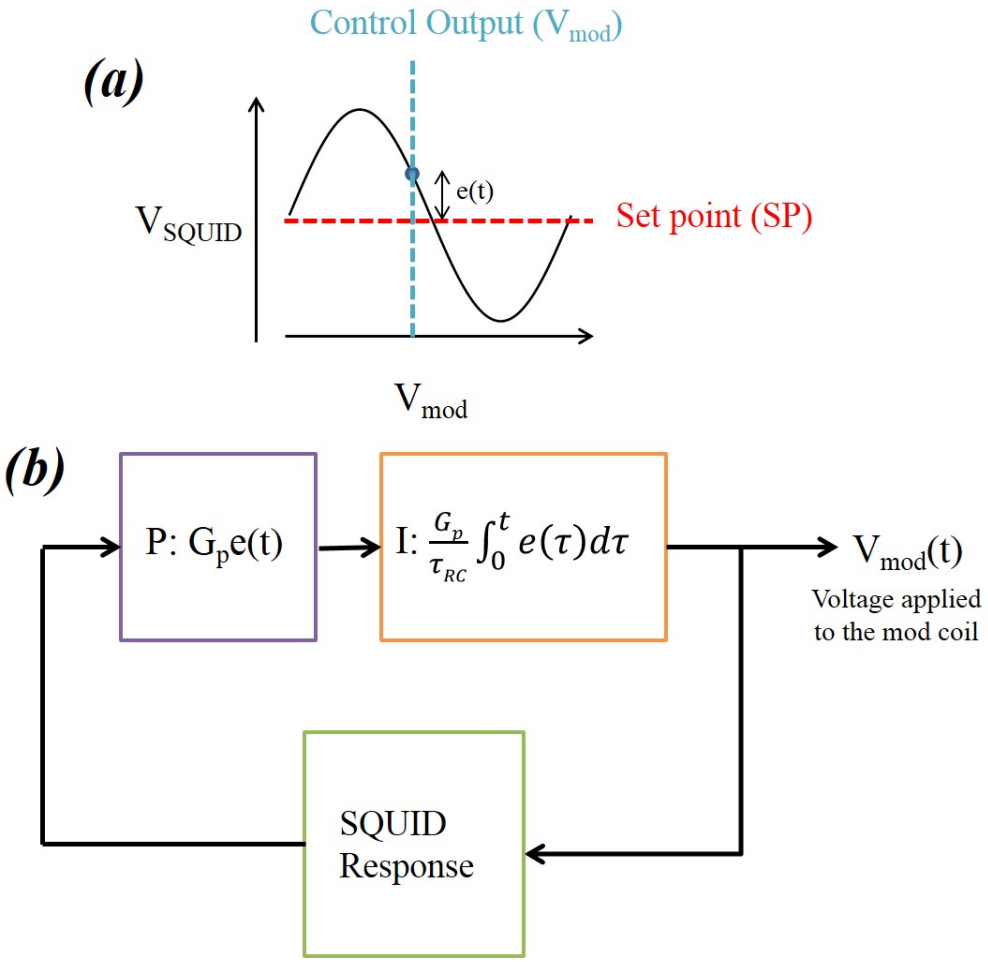

Figure A.2: **PI feedback schematic** (a) Schematic of the periodic output of the SQUID (V_{SQUID}) vs. applied modulation coil voltage (V_{mod}), which is the output of the feedback box. The feedback attempts to maintain V_{SQUID} at a set voltage or 'set point' and the output of the feedback box is determined by difference between the set point and the actual output of the SQUID, $e(t)$. (b) Block diagram of the feedback, showing the functional form of the output of the P and I blocks as a function of the error, $e(t)$.

A.3 Theoretical PI behavior

The error for a sinusoidal V_{SQUID} vs. V_{mod} is given by:

$$e(t) = V_M sin(2\pi \frac{\Phi_{PU}(t) + V_{mod}(t)M/R_{mod}}{\Phi_0} \tag{A.1}$$

Where V_M of the amplitude of the SQUID's modulation, Φ_{PU} is the flux through the pickup loop, M is the mutual inductance between the SQUID and modulation coil, and R_{mod} is the bias resistor which converts the output V_{mod} to a current through the mod coil. If the error is small, we can approximate the error as linearly depending on V_mod:

$$e(t) \approx 2\pi V_M \frac{\Phi_{PU}(t) + V_{mod}(t)M/R_{mod}}{\Phi_0} \tag{A.2}$$

The full response of the feedback box in the time and frequency domains are, respectively:

$$V_{mod}(t) = G_P e(t) + G_P/\tau_{RC} \int_0^t e(\tau)d\tau \tag{A.3}$$

$$V_{mod}(\omega) = G_P e(\omega) - \frac{G_P}{i\omega\tau_{RC}} e(\omega) \tag{A.4}$$

Therefore, for a sinusoidal SQUID signal at a given frequency ω, the measured response of the SQUID is given by:

$$\frac{\Phi_{meas}(\omega)}{\Phi_{actual}(\omega)} = \frac{G(1 - (i\omega\tau_{RC})^{-1})}{1 - G(1 - (i\omega\tau_{RC})^{-1})} \tag{A.5}$$

where $G \equiv (G_P V_M M)/(\Phi_0 R_{mod})$, Φ_{meas} is the measured SQUID signal, and Φ_{actual} is the actual SQUID signal. It is important that the frequency response of the feedback box depends not only on the feedback box itself, but the modulation depth of the SQUID, and other external factors, and can therefore change over time.

A.4 Feedback box response vs. frequency

We checked the response of the feedback box by varying the frequency of a sinusoidal signal applied to the field coil. We found that the qualitative behavior of the feedback box, in the amplitude and phase of the measured signal, matched well with simulated behavior using Eqn. A.5 (FIG. A.3).

Significant attenuation and phase drops can occur at relatively low frequencies (as low as 1 kHz)

depending on the tuning of the feedback box and the modulation depth of the SQUID. Therefore, it is very important to check the frequency dependence of the SQUID response experimentally before attempting measurements which require fast time response of the SQUID. Additionally, the frequency dependence of the feedback box must be taken into account when quoting and measuring noise figures at high frequencies.

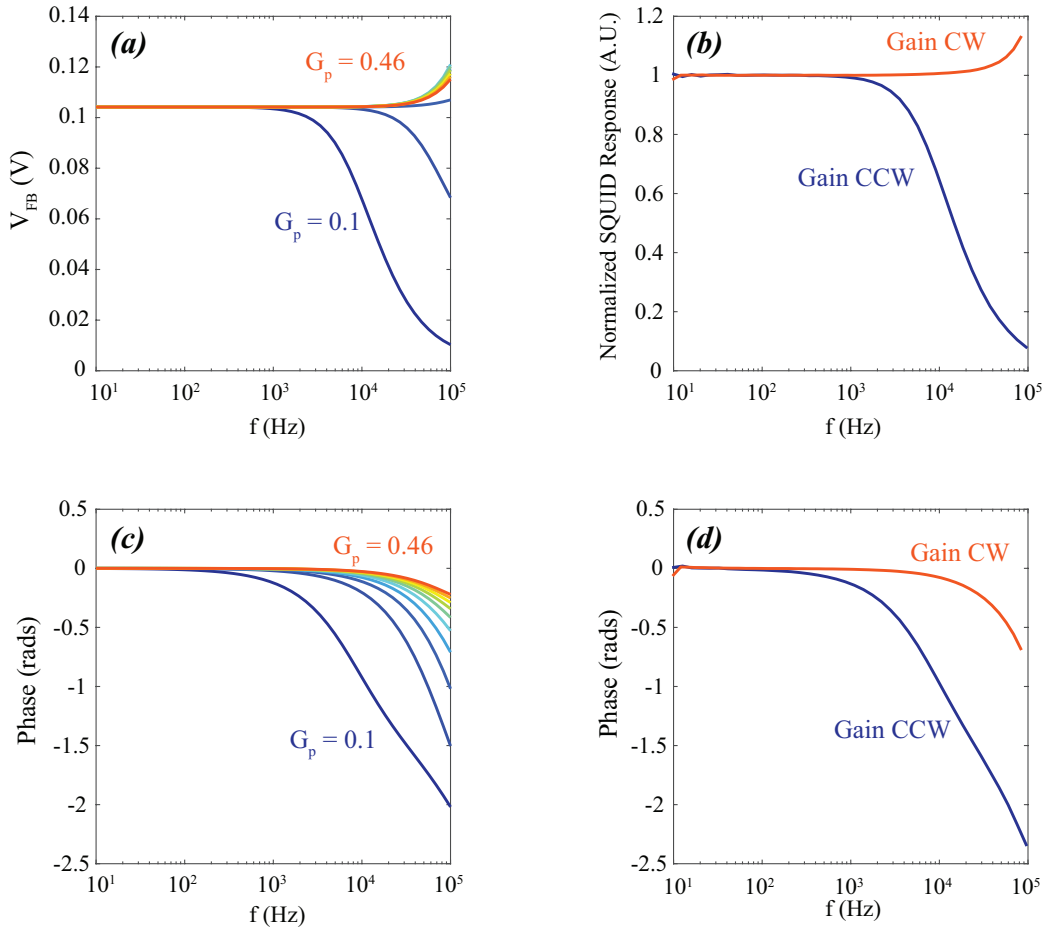

Figure A.3: **PI feedback comparison to theory** (a) Theoretical prediction for amplitude of V_mod vs. frequency for a sinusoidal signal applied to the SQUID. The proportional gain (G_P) was varied from 0.1 to 0.46. The parameters used for the simulation were: R_{mod} = 1 $k\Omega$, M = 9600 Φ_0/A, V_M = 50 mV, τ_{RC} = 0.94 μs (b) The experimentally measured amplitude response of the SQUID to a sinusoidal signal applied to the field coil. The blue curve is the gain knob turned counter clock wise, while the orange curve is the gain knob tuned in the opposite direction. (c,d) Simulation and experimental results for the phase of the measured signal with respect to the applied SQUID signal.

Bibliography

[1] B. L. Altshuler, I. L. Aleiner, and V. I. Yudson. Localization at the edge of a 2D topological insulator by Kondo impurities with random anisotropies. *Phys. Rev. Lett.*, 111:086401, Aug 2013.

[2] Joseph E Avron, Daniel Osadchy, and Ruedi Seiler. A topological look at the quantum Hall effect. *Physics Today*, 56(8):38–42, 2003.

[3] CWJ Beenakker. Three "universal" mesoscopic Josephson effects. In *Transport Phenomena in Mesoscopic Systems*, pages 235–253. Springer, 1992.

[4] C Bell, S Harashima, Y Kozuka, M Kim, BG Kim, Y Hikita, and HY Hwang. Dominant mobility modulation by the electric field effect at the $LaAlO_3/SrTiO_3$ interface. *Physical review letters*, 103(22):226802, 2009.

[5] G. R. Bell, C. F. McConville, and T. S. Jones. Plasmon excitations and accumulation layers in heavily doped InAs(001). *Phys. Rev. B*, 54:2654–2661, Jul 1996.

[6] M. Ben Shalom, A. Ron, A. Palevski, and Y. Dagan. Shubnikov de haas oscillations in $SrTiO_3/LaAlO_3$ interface. *Phys. Rev. Lett.*, 105:206401, 2010.

[7] M. Ben Shalom, M. Sachs, D. Rakhmilevitch, A. Palevski, and Y. Dagan. Tuning spin-orbit coupling and superconductivity at the srtio3/laalo3 interface: A magnetotransport study. *Phys. Rev. Lett.*, 104:126802, 2010.

[8] B. Andrei Bernevig, Taylor L. Hughes, and Shou-Cheng Zhang. Quantum spin hall effect and topological phase transition in HgTe quantum wells. *Science*, 314(5806):1757–1761, 2006.

[9] J. A. Bert. Gate-tuned superfluid density at the superconducting $LaAlO_3/SrTiO_3$ interface. *Phys. Rev. B*, 86:060503, 2012.

[10] Julie A Bert, Beena Kalisky, Christopher Bell, Minu Kim, Yasuyuki Hikita, Harold Y Hwang, and Kathryn A Moler. Direct imaging of the coexistence of ferromagnetism and superconductivity at the $LaAlO_3/SrTiO_3$ interface. *Nature physics*, 7(10):767–771, 2011.

[11] Hendrik Bluhm, Nicholas C Koshnick, Julie A Bert, Martin E Huber, and Kathryn A Moler. Persistent currents in normal metal rings. *Physical review letters*, 102(13):136802, 2009.

[12] Ernst Helmut Brandt. Thin superconductors and SQUIDs in perpendicular magnetic field. *Physical Review B*, 72(2):024529, 2005.

[13] Alexander Brinkman, M Huijben, M Van Zalk, J Huijben, U Zeitler, JC Maan, WG Van der Wiel, G Rijnders, DHA Blank, and H Hilgenkamp. Magnetic effects at the interface between non-magnetic oxides. *Nature materials*, 6(7):493–496, 2007.

[14] N. C. Bristowe, T. Fix, M. G. Blamire, P. B. Littlewood, and E. Artacho. Proposal of a one-dimensional electron gas in the steps at the $LaAlO_3$-$SrTiO_3$ interface. *Phys. Rev. Lett.*, 108:166802, 2012.

[15] M. Büttiker. Four-terminal phase-coherent conductance. *Phys. Rev. Lett.*, 57(14):1761–1764, 1986.

[16] M Büttiker, Yoseph Imry, and Rolf Landauer. Josephson behavior in small normal one-dimensional rings. *Physics letters a*, 96(7):365–367, 1983.

[17] Claudia Cancellieri, Denis Fontaine, Stefano Gariglio, Nicolas Reyren, AD Caviglia, Alexandre Fete, SJ Leake, SA Pauli, PR Willmott, M Stengel, et al. Electrostriction at the $LaAlO_3/SrTiO_3$ interface. *Physical review letters*, 107(5):056102, 2011.

[18] W. Cao and G. R. Barsch. Landau-ginzburg model of interphase boundaries in improper ferroelastic perovskites of D_4h18 symmetry. *Phys. Rev. B*, 41:4334–4348, 1990.

[19] AD Caviglia, M Gabay, Stefano Gariglio, Nicolas Reyren, Claudia Cancellieri, and J-M Triscone. Tunable rashba spin-orbit interaction at oxide interfaces. *Physical review letters*, 104(12):126803, 2010.

[20] AD Caviglia, Stefano Gariglio, Nicolas Reyren, Didier Jaccard, T Schneider, M Gabay, S Thiel, G Hammerl, Jochen Mannhart, and J-M Triscone. Electric field control of the $LaAlO_3/SrTiO_3$ interface ground state. *Nature*, 456(7222):624–627, 2008.

[21] W Chang, SM Albrecht, TS Jespersen, Ferdinand Kuemmeth, P Krogstrup, J Nygård, and CM Marcus. Hard gap in epitaxial semiconductor–superconductor nanowires. *Nature nanotechnology*, 10(3):232–236, 2015.

[22] Christophe Charpentier, Stefan Fält, Christian Reichl, Fabrizio Nichele, Atindra Nath Pal, Patrick Pietsch, Klaus Ensslin, and Werner Wegscheider. Suppression of bulk conductivity in InAs/GaSb broken gap composite quantum wells. *arxiv:1308.3375*, 2013.

[23] R. A. Cowley. Lattice dynamics and phase transitions of strontium titanate. *Phys. Rev.*, 134:A981–A997, 1964.

[24] François Crépin, Jan Carl Budich, Fabrizio Dolcini, Patrik Recher, and Björn Trauzettel. Renormalization group approach for the scattering off a single Rashba impurity in a helical liquid. *Phys. Rev. B*, 86(12):121106, 2012.

[25] Anindya Das, Yuval Ronen, Yonatan Most, Yuval Oreg, Moty Heiblum, and Hadas Shtrikman. Zero-bias peaks and splitting in an al-inas nanowire topological superconductor as a signature of majorana fermions. *Nature Physics*, 8(12):887–895, 2012.

[26] V. Daumer, I. Golombek, M. Gbordzoe, E. G. Novik, V. Hock, C. R. Becker, H. Buhmann, and L. W. Molenkamp. Quasiballistic transport in HgTe quantum-well nanostructures. *Applied Physics Letters*, 83(7), 2003.

[27] G. de Lange, B. van Heck, A. Bruno, D. J. van Woerkom, A. Geresdi, S. R. Plissard, E. P. A. M. Bakkers, A. R. Akhmerov, and L. DiCarlo. Realization of microwave quantum circuits using hybrid superconducting-semiconducting nanowire josephson elements. *Phys. Rev. Lett.*, 115:127002, Sep 2015.

[28] Adrian Del Maestro, Timo Hyart, and Bernd Rosenow. Backscattering between helical edge states via dynamic nuclear polarization. *Phys. Rev. B*, 87(16):165440, 2013.

[29] MT Deng, CL Yu, GY Huang, Marcus Larsson, Philippe Caroff, and HQ Xu. Anomalous zero-bias conductance peak in a nb-insb nanowire-nb hybrid device. *Nano letters*, 12(12):6414–6419, 2012.

[30] Zhifeng Deng, Erhan Yenilmez, Josh Leu, J. E. Hoffman, Eric W. J. Straver, Hongjie Dai, and Kathryn A. Moler. Metal-coated carbon nanotube tips for magnetic force microscopy. *Applied Physics Letters*, 85(25), 2004.

[31] DA Dikin, M Mehta, CW Bark, CM Folkman, CB Eom, and V Chandrasekhar. Coexistence of superconductivity and ferromagnetism in two dimensions. *Physical Review Letters*, 107(5):056802, 2011.

[32] Lingjie Du, Ivan Knez, Gerard Sullivan, and R. R. Du. Observation of quantum spin Hall states in InAs/GaSb bilayers under broken time-reversal symmetry. *arxiv:1306.1925*.

[33] Christopher English, David Hamilton, Cesar Chialvo, Ion Moraru, Nadya Mason, and Dale Van Harlingen. Observation of non-sinusoidal current-phase relation in graphene Josephson junctions. *arXiv preprint arXiv:1305.0327*, 2013.

[34] A. Fête, S. Gariglio, A. D. Caviglia, J. M. Triscone, and M. Gabay. Rashba induced magnetoconductance oscillations in the $LaAlO_3$-$SrTiO_3$ heterostructure. *Phys. Rev. B*, 86:201105, 2012.

[35] Liang Fu and C. L. Kane. Josephson current and noise at a superconductor/quantum-spin-Hall-insulator/superconductor junction. *Phys. Rev. B*, 79(16):161408, 2009.

[36] Akira Furusaki, Hideaki Takayanagi, and Masaru Tsukada. Josephson effect of the superconducting quantum point contact. *Physical Review B*, 45(18):10563, 1992.

[37] Brian W Gardner, Janice C Wynn, Per G Björnsson, Eric WJ Straver, Kathryn A Moler, John R Kirtley, and Mark B Ketchen. Scanning superconducting quantum interference device susceptometry. *Review of Scientific Instruments*, 72(5):2361–2364, 2001.

[38] AA Golubov, M Yu Kupriyanov, and E Il'Ichev. The current-phase relation in Josephson junctions. *Reviews of Modern Physics*, 76(2):411, 2004.

[39] Christoph W Groth, Michael Wimmer, Anton R Akhmerov, and Xavier Waintal. Kwant: a software package for quantum transport. *New Journal of Physics*, 16(6):063065, 2014.

[40] Jill Guyonnet, Iaroslav Gaponenko, Stefano Gariglio, and Patrycja Paruch. Conduction at domain walls in insulating $pb(zr0.2ti_{0.8})o_3$ thin films. *Advanced materials*, 23(45):5377–5382, 2011.

[41] Sean Hart, Hechen Ren, Timo Wagner, Philipp Leubner, Mathias Mühlbauer, Christoph Brüne, Hartmut Buhmann, Laurens W Molenkamp, and Amir Yacoby. Induced superconductivity in the quantum spin hall edge. *Nature Physics*, 10(9):638–643, 2014.

[42] M. Z. Hasan and C. L. Kane. *Colloquium* : Topological insulators. *Rev. Mod. Phys.*, 82:3045–3067, Nov 2010.

[43] M. E. Huber, N. C. Koshnick, H. Bluhm, L. J. Archuleta, T. Azua, P. G. Bjornsson, B. W. Gardner, S. T. Halloran, E. A. Lucero, and K. A. Moler. Gradiometric micro-SQUID susceptometer for scanning measurements of mesoscopic samples. *Rev. Sci. Instr.*, 79(5):053704, 2008.

[44] B. Jalan, S. J. Allen, G. E. Beltz, P. Moetakef, and S. Stemmer. Enhancing the electron mobility of $SrTiO_3$ with strain. *Appl. Phys. Lett.*, 98:132102–132103, 2011.

[45] CL Jia, SB Mi, M Faley, U Poppe, J Schubert, and K Urban. Oxygen octahedron reconstruction in the $SrTiO_3/LaAlO_3$ heterointerfaces investigated using aberration-corrected ultrahigh-resolution transmission electron microscopy. *Physical Review B*, 79(8):081405, 2009.

[46] A. Joshua, J. Ruhman, S. Pecker, E. Altman, and S. Ilani. Gate-tunable polarized phase of two-dimensional electrons at the $LaAlO_3/SrTiO_3$ interface. *Proc. Natl Acad. Sci. USA*, 110:9633–9638, 2012.

[47] Beena Kalisky, Julie A Bert, Brannon B Klopfer, Christopher Bell, Hiroki K Sato, Masayuki Hosoda, Yasuyuki Hikita, Harold Y Hwang, and Kathryn A Moler. Critical thickness for ferromagnetism in $LaAlO_3/SrTiO_3$ heterostructures. *Nature communications*, 3:922, 2012.

[48] Beena Kalisky, Eric M Spanton, Hilary Noad, John R Kirtley, Katja C Nowack, Christopher Bell, Hiroki K Sato, Masayuki Hosoda, Yanwu Xie, Yasuyuki Hikita, et al. Locally enhanced conductivity due to the tetragonal domain structure in $LaAlO_3/SrTiO_3$ heterointerfaces. *Nature Materials*, 12(12):1091–1095, 2013.

[49] C. L. Kane and E. J. Mele. Quantum spin Hall effect in graphene. *Phys. Rev. Lett.*, 95:226801, 2005.

[50] C. L. Kane and E. J. Mele. Z2 topological order and the quantum spin Hall effect. *Phys. Rev. Lett.*, 95:146802, 2005.

[51] Jeehoon Kim, L Civale, E Nazaretski, N Haberkorn, F Ronning, A S Sefat, T Tajima, B H Moeckly, J D Thompson, and R Movshovich. Direct measurement of the magnetic penetration depth by magnetic force microscopy. *Superconductor Science and Technology*, 25(11):112001, 2012.

[52] K. v. Klitzing, G. Dorda, and M. Pepper. New method for high-accuracy determination of the fine-structure constant based on quantized Hall resistance. *Phys. Rev. Lett.*, 45:494–497, Aug 1980.

[53] I. Knez. *Transport Properties of Topological Phases in Broken Gap Indium Arsenide/Gallium Antimonide Based Quantum Wells*. PhD thesis, Rice University, 2012.

[54] Ivan Knez, RR Du, and Gerard Sullivan. Finite conductivity in mesoscopic Hall bars of inverted InAs/GaSb quantum wells. *Physical Review B*, 81(20):201301, 2010.

[55] Ivan Knez, Rui-Rui Du, and Gerard Sullivan. Evidence for helical edge modes in inverted InAs/GaSb quantum wells. *Phys. Rev. Lett.*, 107(13):136603, 2011.

[56] V. G. Kogan and J. R. Kirtley. Meissner response of superconductors with inhomogeneous penetration depths. *Phys. Rev. B*, 83:214521, Jun 2011.

[57] Markus König, Matthias Baenninger, Andrei G. F. Garcia, Nahid Harjee, Beth L. Pruitt, C. Ames, Philipp Leubner, Christoph Brüne, Hartmut Buhmann, Laurens W. Molenkamp, and David Goldhaber-Gordon. Spatially resolved study of backscattering in the quantum spin Hall state. *Phys. Rev. X*, 3:021003, Apr 2013.

[58] Markus König, Hartmut Buhmann, Laurens W. Molenkamp, Taylor Hughes, Chao-Xing Liu, Xiao-Liang Qi, and Shou-Cheng Zhang. The quantum spin Hall effect: Theory and experiment. *Journal of the Physical Society of Japan*, 77(3):031007, 2008.

[59] Markus König, Steffen Wiedmann, Christoph BrÃijne, Andreas Roth, Hartmut Buhmann, Laurens W. Molenkamp, Xiao-Liang Qi, and Shou-Cheng Zhang. Quantum spin hall insulator state in hgte quantum wells. *Science*, 318(5851):766–770, 2007.

[60] P Krogstrup, NLB Ziino, W Chang, SM Albrecht, MH Madsen, Erik Johnson, J Nygård, CM Marcus, and TS Jespersen. Epitaxy of semiconductor–superconductor nanowires. *Nature materials*, 2015.

[61] T. W. Larsen, K. D. Petersson, F. Kuemmeth, T. S. Jespersen, P. Krogstrup, J. Nygård, and C. M. Marcus. Semiconductor-nanowire-based superconducting qubit. *Phys. Rev. Lett.*, 115:127001, Sep 2015.

[62] Natalie Lezmy, Yuval Oreg, and Micha Berkooz. Single and multiparticle scattering in helical liquid with an impurity. *Phys. Rev. B*, 85:235304, Jun 2012.

[63] L. Li, C. Richter, J. Mannhart, and R. C. Ashoori. Coexistence of magnetic order and two-dimensional superconductivity at $LaAlO_3/SrTiO_3$ interfaces. *Nature Phys.*, 7:762–766, 2011.

[64] Tingxin Li, Pengjie Wang, Hailong Fu, Lingjie Du, Kate A Schreiber, Xiaoyang Mu, Xiaoxue Liu, Gerard Sullivan, Gábor A Csáthy, Xi Lin, et al. Observation of a helical luttinger liquid in InAs/GaSb quantum spin Hall edges. *Physical review letters*, 115(13):136804, 2015.

[65] Thomas M. Lippman and Kathryn A. Moler. Calculation of the effect of random superfluid density on the temperature dependence of the penetration depth. *Phys. Rev. B*, 85:104529, Mar 2012.

[66] Chaoxing Liu, Taylor L. Hughes, Xiao-Liang Qi, Kang Wang, and Shou-Cheng Zhang. Quantum spin hall effect in inverted type-II semiconductors. *Phys. Rev. Lett.*, 100(23):236601, 2008.

[67] Lan Luan. *MAGNETIC FORCE MICROSCOPY STUDIES OF UNCONVENTIONAL SUPERCONDUCTORS: SINGLE VORTEX MANIPULATION AND MAGNETIC PENETRATION DEPTH MEASUREMENTS*. PhD thesis, Stanford University, 2010.

[68] Lan Luan, Ophir M. Auslaender, Thomas M. Lippman, Clifford W. Hicks, Beena Kalisky, Jiun-Haw Chu, James G. Analytis, Ian R. Fisher, John R. Kirtley, and Kathryn A. Moler. Local measurement of the penetration depth in the pnictide superconductor $Ba(Fe_{0.95}Co_{0.05})_2As_2$. *Phys. Rev. B*, 81:100501, Mar 2010.

[69] Lan Luan, Thomas M. Lippman, Clifford W. Hicks, Julie A. Bert, Ophir M. Auslaender, Jiun-Haw Chu, James G. Analytis, Ian R. Fisher, and Kathryn A. Moler. Local measurement of the superfluid density in the pnictide superconductor $\mathrm{Ba}(\mathrm{Fe}_{1-x}\mathrm{Co}_x)_2\mathrm{As}_2$ across the superconducting dome. *Phys. Rev. Lett.*, 106:067001, Feb 2011.

[70] Eric Yue Ma, M Reyes Calvo, Jing Wang, Biao Lian, Mathias Mühlbauer, Christoph Brüne, Yong-Tao Cui, Keji Lai, Worasom Kundhikanjana, Yongliang Yang, et al. Unexpected edge

conduction in mercury telluride quantum wells under broken time-reversal symmetry. *Nature communications*, 6, 2015.

[71] Joseph Maciejko, Chaoxing Liu, Yuval Oreg, Xiao-Liang Qi, Congjun Wu, and Shou-Cheng Zhang. Kondo effect in the helical edge liquid of the quantum spin hall state. *Phys. Rev. Lett.*, 102(25):256803, 2009.

[72] J. Mannhart and D. G. Schlom. Oxide interfaces - an opportunity for electronics. *Science*, 327:1607–1611, 2010.

[73] AN Morozovska, EA Eliseev, MD Glinchuk, Long Qing Chen, SV Kalinin, and V Gopalan. Impact of free charges on polarization and pyroelectricity in antiferrodistortive structures and surfaces induced by a flexoelectric effect. *Ferroelectrics*, 438(1):32–44, 2012.

[74] Vincent Mourik, Kun Zuo, Sergey M Frolov, SR Plissard, EPAM Bakkers, and LP Kouwenhoven. Signatures of majorana fermions in hybrid superconductor-semiconductor nanowire devices. *Science*, 336(6084):1003–1007, 2012.

[75] Y. Naveh and B. Laikhtman. Magnetotransport of coupled electron-holes. *Europhys. Lett.*, 55(4):545, 2001.

[76] Fabrizio Nichele, Atindra Nath Pal, Patrick Pietsch, Thomas Ihn, Klaus Ensslin, Christophe Charpentier, and Werner Wegscheider. Insulating state and giant nonlocal response in an InAs/GaSb quantum well in the quantum Hall regime. *Phys. Rev. Lett.*, 112:036802, Jan 2014.

[77] Fabrizio Nichele, Henri J Suominen, Morten Kjaergaard, Charles M Marcus, Ebrahim Sajadi, Joshua A Folk, Fanming Qu, Arjan JA Beukman, Folkert K de Vries, Jasper van Veen, et al. Edge transport in the trivial phase of InAs/GaSb. *arXiv preprint arXiv:1511.01728*, 2015.

[78] K. Nilsson, A. Zakharova, I. Lapushkin, S. T. Yen, and K. A. Chao. Cyclotron masses and g-factors of hybridized electron-hole states in InAs/GaSb quantum wells. *Phys. Rev. B*, 74:075308, Aug 2006.

[79] Hilary Noad, Eric M Spanton, Katja C Nowack, Hisashi Inoue, Minu Kim, Tyler A Merz, Christopher Bell, Yasuyuki Hikita, Ruqing Xu, Wenjun Liu, et al. Enhanced superconducting transition temperature due to tetragonal domains in two-dimensionally doped $SrTiO_3$. *arXiv preprint arXiv:1605.08418*, 2016.

[80] M. Nonnenmacher, M. P. O'Boyle, and H. K. Wickramasinghe. Kelvin probe force microscopy. *Applied Physics Letters*, 58(25), 1991.

[81] Katja C. Nowack, Eric M. Spanton, Matthias Baenninger, Markus König, John R. Kirtley, Beena Kalisky, C. Ames, Philipp Leubner, Christoph Brüne, Hartmut Buhmann, Laurens W. Molenkamp, David Goldhaber-Gordon, and Kathryn A. Moler. Imaging currents in hgte quantum wells in the quantum spin Hall regime. *Nat. Mater.*, 12(9):787–791, 2013.

[82] A. Ohtomo and H. Y. Hwang. A high-mobility electron gas at the $LaAlO_3$/$SrTiO_3$ heterointerface. *Nature*, 427:423–426, 2004.

[83] SA Pauli, SJ Leake, B Delley, M Björck, CW Schneider, CM Schlepütz, D Martoccia, S Paetel, J Mannhart, and PR Willmott. Evolution of the interfacial structure of $LaAlO_3$ on $SrTiO_3$. *Physical review letters*, 106(3):036101, 2011.

[84] D. I. Pikulin and T. Hyart. Interplay of exciton condensation and the quantum spin Hall effect in InAs/GaSb bilayers. *Phys. Rev. Lett.*, 112:176403, Apr 2014.

[85] L. F. J. Piper, T. D. Veal, M. J. Lowe, and C. F. McConville. Electron depletion at inas free surfaces: Doping-induced acceptorlike gap states. *Phys. Rev. B*, 73:195321, May 2006.

[86] Xiao-Liang Qi and Shou-Cheng Zhang. Topological insulators and superconductors. *Reviews of Modern Physics*, 83(4):1057, 2011.

[87] Fanming Qu, Arjan J. A. Beukman, Stevan Nadj-Perge, Michael Wimmer, Binh-Minh Nguyen, Wei Yi, Jacob Thorp, Marko Sokolich, Andrey A. Kiselev, Michael J. Manfra, Charles M. Marcus, and Leo P. Kouwenhoven. Electric and magnetic tuning between the trivial and topological phases in InAs/GaSb double quantum wells. *Phys. Rev. Lett.*, 115:036803, Jul 2015.

[88] N. Reyren, S. Thiel, A. D. Caviglia, L. Fitting Kourkoutis, G. Hammer, C. Richter, C. W. Schneider, T. Kopp, A.-S. Ruetschi, D. Jaccard, M. Gabay, D. A. Muller, J.-M. Triscone, and J. Mannhart. Superconducting interfaces between insulating oxides. *Science*, 2007.

[89] Andreas Roth, Christoph Brüne, Hartmut Buhmann, Laurens W. Molenkamp, Joseph Maciejko, Xiao-Liang Qi, and Shou-Cheng Zhang. Nonlocal transport in the quantum spin Hall state. *Science*, 325(5938):294–297, 2009.

[90] Bradley J. Roth, Nestor G. Sepulveda, and Jr John P. Wikswo. Using a magnetometer to image a two-dimensional current distribution. *J. Appl. Phys.*, 65(1):361–372, 1989.

[91] Thomas L. Schmidt, Stephan Rachel, Felix von Oppen, and Leonid I. Glazman. Inelastic electron backscattering in a generic helical edge channel. *Phys. Rev. Lett.*, 108(15):156402, 2012.

[92] U. Schwingenschlögl and C. Schuster. Interface relaxation and electrostatic charge depletion in the oxide heterostructure $LaAlO_3/SrTiO_3$. *Europhys. Lett.*, 86:27005, 2009.

[93] J. F. Scott, E. K. H. Salje, and M. A. Carpenter. Domain wall damping and elastic softening in $SrTiO_3$: Evidence for polar twin walls. *Phys. Rev. Lett.*, 109:187601, 2012.

[94] Jan Seidel, Lane W Martin, Q He, Q Zhan, Y-H Chu, A Rother, ME Hawkridge, P Maksymovych, P Yu, M Gajek, et al. Conduction at domain walls in oxide multiferroics. *Nature materials*, 8(3):229–234, 2009.

[95] S. Seri and L. Klein. Antisymmetric magnetoresistance of the $SrTiO_3/LaAlO_3$ interface. *Phys. Rev. B*, 80:180410, 2009.

[96] T. Shibauchi, A. Carrington, and Y. Matsuda. A quantum critical point lying beneath the superconducting dome in iron pnictides. *Annual Review of Condensed Matter Physics*, 5(1):113–135, 2014.

[97] Ilya Sochnikov, Andrew J Bestwick, James R Williams, Thomas M Lippman, Ian R Fisher, David Goldhaber-Gordon, John R Kirtley, and Kathryn A Moler. Direct measurement of current-phase relations in superconductor/topological insulator/superconductor junctions. *Nano letters*, 13(7):3086–3092, 2013.

[98] Ilya Sochnikov, Luis Maier, Christopher A Watson, John R Kirtley, Charles Gould, Grigory Tkachov, Ewelina M Hankiewicz, Christoph Brüne, Hartmut Buhmann, Laurens W Molenkamp, et al. Nonsinusoidal current-phase relationship in josephson junctions from the 3d topological insulator hgte. *Physical review letters*, 114(6):066801, 2015.

[99] Eric M. Spanton, Katja C. Nowack, Lingjie Du, Gerard Sullivan, Rui-Rui Du, and Kathryn A. Moler. Images of edge current in InAs/GaSb quantum wells. *Physical Review Letters*, 113(2):026804, 2014.

[100] Massimiliano Stengel. First-principles modeling of electrostatically doped perovskite systems. *Physical review letters*, 106(13):136803, 2011.

[101] Anders Ström, Henrik Johannesson, and G. I. Japaridze. Edge dynamics in a quantum spin Hall state: Effects from rashba spin-orbit interaction. *Phys. Rev. Lett.*, 104(25):256804, 2010.

[102] Kyoichi Suzuki, Yuichi Harada, Koji Onomitsu, and Koji Muraki. Edge channel transport in the inas/gasb topological insulating phase. *Phys. Rev. B*, 87:235311, Jun 2013.

[103] DB Szombati, S Nadj-Perge, D Car, SR Plissard, EPAM Bakkers, and LP Kouwenhoven. Josephson ϕ_0-junction in nanowire quantum dots. *arXiv preprint arXiv:1512.01234*, 2015.

[104] Yoichi Tanaka, A. Furusaki, and K. A. Matveev. Conductance of a helical edge liquid coupled to a magnetic impurity. *Phys. Rev. Lett.*, 106:236402, Jun 2011.

[105] S. Thiel, G. Hammerl, A. Schmehl, C. W. Schneider, and J. Mannhart. Tunable quasi-two-dimensional electron gases in oxide heterostructures. *Science*, 313:1942–1945, 2006.

[106] D. J. Thouless, M. Kohmoto, M. P. Nightingale, and M. den Nijs. Quantized Hall conductance in a two-dimensional periodic potential. *Phys. Rev. Lett.*, 49:405–408, Aug 1982.

[107] H. Unoki and T. Sakudo. Electron spin resonance of fe3+ in $SrTiO_3$ with special reference to the 110 k phase transition. *J. Phys. Soc. Jpn*, 23:546–552, 1967.

[108] Jukka I Väyrynen, Moshe Goldstein, Yuval Gefen, and Leonid I Glazman. Resistance of helical edges formed in a semiconductor heterostructure. *Physical Review B*, 90(11):115309, 2014.

[109] Jukka I. Väyrynen, Moshe Goldstein, and Leonid I. Glazman. Helical edge resistance introduced by charge puddles. *Phys. Rev. Lett.*, 110:216402, 2013.

[110] Jing Wang, Biao Lian, and Shou-Cheng Zhang. Quantum anomalous Hall effect in magnetic topological insulators. *Physica Scripta*, 2015(T164):014003, 2015.

[111] X Wang, G Baskaran, ZQ Liu, J Huijben, JB Yi, A Annadi, A Roy Barman, A Rusydi, S Dhar, YP Feng, et al. Electronic phase separation at the $LaAlO_3/SrTiO_3$ interface. *Nature communications*, 2:188, 2011.

[112] Y. H. Wang, J. R. Kirtley, F. Katmis, P. Jarillo-Herrero, J. S. Moodera, and K. A. Moler. Observation of chiral currents at the magnetic domain boundary of a topological insulator. *Science*, 349(6251):948–952, 2015.

[113] Cenke Xu and Joel E Moore. Stability of the quantum spin Hall effect: Effects of interactions, disorder, and Z2 topology. *Physical Review B*, 73(4):045322, 2006.

[114] J. H. Xu, J. H. Miller, and C. S. Ting. Magnetic levitation force and penetration depth in type-ii superconductors. *Phys. Rev. B*, 51:424–434, Jan 1995.

[115] X. C. Zhang, K. Ortner, A. Pfeuffer-Jeschke, C. R. Becker, and G. Landwehr. Effective g factor of n-type HgTe/$Hg_{1-x}Cd_xTe$ single quantum wells. *Phys. Rev. B*, 69:115340, Mar 2004.

[116] Zhen Zhang and Jr. John T. Yates. Band bending in semiconductors: Chemical and physical consequences at surfaces and interfaces. *Chemical Reviews*, 112(10):5520–5551, 2012. PMID: 22783915.